



# Flow boiling in a vertical millimetric tube for upward, downward and microgravity conditions

Paul Ayegba

## ► To cite this version:

Paul Ayegba. Flow boiling in a vertical millimetric tube for upward, downward and microgravity conditions. Fluid Dynamics [physics.flu-dyn]. Institut National Polytechnique de Toulouse - INPT, 2022. English. NNT : 2022INPT0103 . tel-04248272

**HAL Id: tel-04248272**

**<https://theses.hal.science/tel-04248272>**

Submitted on 18 Oct 2023

**HAL** is a multi-disciplinary open access archive for the deposit and dissemination of scientific research documents, whether they are published or not. The documents may come from teaching and research institutions in France or abroad, or from public or private research centers.

L'archive ouverte pluridisciplinaire **HAL**, est destinée au dépôt et à la diffusion de documents scientifiques de niveau recherche, publiés ou non, émanant des établissements d'enseignement et de recherche français ou étrangers, des laboratoires publics ou privés.



Université  
de Toulouse

# THÈSE

En vue de l'obtention du

## DOCTORAT DE L'UNIVERSITÉ DE TOULOUSE

**Délivré par :**

Institut National Polytechnique de Toulouse (Toulouse INP)

**Discipline ou spécialité :**

Dynamique des fluides

---

**Présentée et soutenue par :**

M. PAUL AYEGBA

le lundi 12 septembre 2022

**Titre :**

Flow boiling in a vertical millimetric tube for upward, downward and microgravity conditions

---

**Ecole doctorale :**

Mécanique, Energétique, Génie civil, Procédés (MEGeP)

**Unité de recherche :**

Institut de Mécanique des Fluides de Toulouse ( IMFT)

**Directeurs de Thèse :**

MME CATHERINE COLIN

M. JULIEN SEBILLEAU

**Rapporteurs :**

M. DAVIDE DEL COL, UNIVERSITA DEGLI STUDI DI PADOVA

M. REMI REVELLIN, INSA LYON

**Membres du jury :**

M. CHRISTIAN RUYER-QUIL, UNIVERSITE DE SAVOIE CHAMBERY-ANNECY, Président

M. ANTOINE DU CLUZEAU, CEA SACLAY, Membre

M. JULIEN SEBILLEAU, TOULOUSE INP, Membre

MME CATHERINE COLIN, TOULOUSE INP, Membre

M. PASCAL LAVIEILLE, UNIVERSITE TOULOUSE 3, Membre



# Abstract

The goal of this work was to investigate the effect of gravity, wall heat flux and inlet conditions on several flow boiling quantities using both experimental and modelling approaches. Experimental measurements were carried out using two separate flow facilities (BRASIL and COSMO). Both facilities consisted of a vertical 6 mm sapphire tube coated externally with indium-tin-oxide (ITO) for Joule heating. The working fluid used for the experimental campaigns was HFE-7000. Upward ( $+1g$ ), downward ( $-1g$ ) and microgravity ( $\mu g$ ) flow boiling experiments were carried out over mass flux, heat flux and vapor quality ranges of  $50 \leq G \leq 400 \text{ kg/m}^2 \cdot \text{s}$ ,  $0 \leq q \leq 3 \text{ W/cm}^2$  and  $0 \leq x \leq 0.7$  respectively.

Bubbly, slug, churn, falling film (downward flow) annular flow patterns were observed for  $+1g$ ,  $\mu g$  and  $-1g$  flows. Mean bubble diameter was highest and bubble eccentricity lowest in  $\mu g$  relative to  $+1g$  and  $-1g$  due to the absence of buoyancy forces in  $\mu g$ . Measured void fraction was influenced by mass flux and was highest in downward flow and lowest in upward flow. The wall shear stress, interfacial shear stress and heat transfer coefficient generally increased with the wall mass flux, heat flux, and vapor quality. Wall shear stress and heat transfer coefficient were found to be higher in  $-1g$  relative to  $+1g$  flow. The heat transfer coefficient was generally higher in  $+1g$  relative to  $\mu g$ . Interfacial shear stress was found to be smaller in downward flow relative to upward flow due to lower vapor-liquid relative velocity in the former. Mean wave velocity and mean wave frequency showed significant dependence on the applied heat flux and flow orientation relative to gravity.

Semi-empirical and mechanistic models for predicting mean wave velocity, mean wave frequency, wall shear stress, interfacial friction factor and heat transfer coefficient were developed in this work and provided a good estimation of the experimental data within  $\pm 20\%$ . Furthermore, theoretical prediction of heat transfer coefficient for annular flow boiling were derived from eddy viscosity and diffusivity modelling providing a good estimation of both the heat transfer coefficient and liquid film thickness within  $\pm 15\%$  and  $\pm 20\%$  respectively.

# Résumé

Cette thèse s'intéresse aux effets de la gravité et du flux de chaleur pariétal sur l'ébullition convective de manière expérimentale et théorique. Les campagnes de mesures ont été réalisées sur deux montages expérimentaux (BRASIL et COSMO). Dans ces deux montages, la section d'essai est un tube vertical de saphir (de 6mm de diamètre intérieur) dans lequel circule du HFE-7000. Le tube est recouvert d'un dépôt d'ITO qui permet une chauffe par effet Joule. Des expériences en écoulement ascendant (+1g), descendant (-1g) et en microgravité ( $\mu g$ ) ont été réalisées pour des gammes de flux de masse, de flux de chaleur pariétaux et de titres thermodynamiques respectivement de  $50 \leq G \leq 400 \text{ kg/m}^2 \cdot \text{s}$ ,  $0 \leq q \leq 3 \text{ W/cm}^2$  and  $0 \leq x \leq 0.7$ .

Les régimes d'écoulement à bulles, poches-bouchons de type churn, en film tombant (pour un écoulement descendant) et annulaire ont été observés. Le diamètre moyen des bulles est plus grand avec des excentricités plus faibles pour les conditions de microgravité comparées aux écoulements ascendant et descendant, ce qui s'explique par l'absence de force de flottabilité en microgravité et du glissement des bulles. La fraction de taux de vide est influencée par le flux de masse et est plus importante pour les écoulements descendants que pour les ascendants. Les frottements pariétal et interfacial et le coefficient de transfert de chaleur augmentent le plus souvent avec le flux de masse, le flux de chaleur et le titre thermodynamique. Le frottement pariétal et le coefficient d'échange de chaleur sont plus élevés pour les écoulements descendants que pour les ascendants. Le coefficient de transfert de chaleur est le plus souvent plus important en écoulement ascendant qu'en microgravité. Le frottement interfacial est plus faible pour les écoulements descendants qu'ascendants ce qui s'explique par une plus faible vitesse relative entre phases dans le cas descendant. Les vitesses et fréquences moyennes des ondes dépendent significativement du flux de chaleur pariétal et de la gravité.

Des modèles mécanistiques et semi-empiriques pour prédire les vitesses et fréquences moyenne des ondes, les frottements pariétal et interfacial et le coefficient d'échange de chaleur ont été développés avec un bon accord avec les résultats expérimentaux ( $\pm 20\%$ ). De plus, une prédiction théorique, basée sur des modèles de viscosité et diffusivité turbulentes, permet de prédire le coefficient de transfert de chaleur et l'épaisseur de film liquide pour les écoulements annulaires avec des erreurs de  $\pm 15\%$  et  $\pm 20\%$  respectivement.

## Acknowledgements

I would like to thank my Supervisors Professor Catherine COLIN, Associate Professor Julien SEBILLEAU for their professional guidance and support all through my programme. They demonstrated professionalism and mastery of the subject area and spared no effort to ensure that high standards were met. They also helped me settle into the country and helped me handle the administrative procedures in the laboratory and the University. It was an interesting experience working with them and my knowledge of the subject area was greatly enhanced.

I wish to acknowledge the professional and technical support of Julien LEFORT, Gregory EHSES, Herve AYROLES, Frederic BERGAME, Laurent MOUNEIX, Ruddy SOERPARNO and all the Staff of Institut de Mécanique des Fluides de Toulouse, France. I also acknowledge the support and collaboration of Professor Jungho Kim and Dr Caleb HAMMER of the University of Maryland USA.

I would to thank Professor Davide DEL COL and Professor Remi REVELLIN who accepted to review my PhD Manuscript and the other members of the committee for taking part to the evaluation of my work, Professor Christian RUYER-QUIL, Docteur Antoine DU CLUZEAU and Associate Professor Pascal LAVIEILLE.

I would also like to acknowledge the Petroleum Technology Development Fund (PTDF) for the PhD grant funding provided to me from March 2019 to June 2022. I would also like to acknowledge Institut National Polytechnique de Toulouse for the PhD funding provided to me from June 2022 to September 2022. The European Space Agency (ESA) and the French Space Agency (CNES) through the GDR MFA are acknowledged for the financial support in the building of the experimental set-up.

My appreciation also goes to members of my family especially my wife, kids and siblings for their support. Without their support the programme would not have been a smooth ride. I also acknowledge the contributions of my friends and fellow PhD students of Institut de Mécanique des Fluides de Toulouse. Above all, I thank God Almighty for He made all what was accomplished possible. Thank God for His grace through the highs and lows of the programme and for good health.

# Table of Contents

## Contents

Abstract .....	ii
Acknowledgements .....	iv
Table of Contents .....	v
List of Figures .....	viii
List of Tables.....	xii
Nomenclature .....	xiii
Introduction .....	1
Chapter 1 .....	4
1.1 Fundamental description .....	5
1.1.1 Definition of two-phase flow parameters .....	5
1.1.2 Constitutive equations .....	6
1.1.3 Dimensionless groups .....	10
1.2 Two-Phase Models .....	12
1.2.1 Flow patterns in convective boiling.....	12
1.2.2 Gas velocity models.....	13
1.2.3 Bubble size evolution models .....	17
1.2.4 Wall shear stress models.....	17
1.2.5 Interfacial shear stress models .....	26
1.2.6 Interfacial wave structures models .....	28
1.2.7 Heat transfer coefficient models .....	28
1.3 Experimental studies on Two-Phase Flows.....	34
1.3.1 Experimental platforms .....	35
1.3.2 Effect of gravity on two-phase boiling flow .....	36
1.4 Conclusion.....	60

Chapter 2 .....	61
2.1 Experimental Setup .....	62
2.1.1 Hydraulic loop .....	63
2.1.2 Test section .....	67
2.1.3 Working fluid.....	68
2.2 Fluid Degassing and Filling of Loop.....	69
2.2.1 Degassing of working fluid .....	69
2.2.2 Filling of the loop .....	71
2.3 Experimental Measurements .....	71
2.3.1 Pressure measurement .....	72
2.3.2 Temperature measurement.....	73
2.3.3 Determination of void fraction .....	74
2.3.4 Flow visualisation.....	81
2.4 Data Reduction .....	82
2.4.1 Vapour quality .....	82
2.4.2 Wall shear stress .....	87
2.4.3 Interfacial shear stress.....	90
2.4.4 Heat transfer coefficient .....	91
2.4.5 Bubble geometry and wave structures .....	94
2.5 Parabolic Flight Experiments .....	97
2.6 Conclusion.....	101
Chapter 3 .....	102
3.1 Article on the Hydrodynamics of Upward and Downward Flow Boiling .....	103
3.2 Additional Results on Hydrodynamics of Upward and Downward Flow Boiling.....	134
3.2.1 Liquid entrainment in the vapour core of annular flow .....	134
3.2.2 Modelling of wave structures in annular flow .....	134

3.2.3 Modelling of Interfacial Friction Factor in Annular flow .....	137
3.3 Conclusion.....	138
Chapter 4.....	140
4.1 Mechanism of Heat Transfer in Upward and Downward Flow Boiling .....	141
4.3 Modelling of Heat Transfer Coefficient and Liquid Film Thickness in Annular Flow Boiling .....	144
4.4 Conclusion.....	190
Chapter 5.....	191
5.1 Flow Pattern, Flow Pattern Transition and Bubble Geometry in Normal and Microgravity .	192
5.1.1 Flow patterns in normal and microgravity.....	192
5.1.2 Flow pattern map and flow pattern transition.....	194
5.1.3 Bubble size distribution in normal and microgravity .....	197
5.1.4 Bubble size evolution in normal and microgravity.....	199
5.2 Void Fraction and Vapour Velocity in Microgravity .....	202
5.4 Heat Transfer Coefficient in Microgravity.....	210
5.4.1 Experimental results of heat transfer coefficient in microgravity .....	210
5.4.2 Modelling of heat transfer coefficient in microgravity and downward flow.....	214
5.4.3 Effect gravity level on measured heat transfer .....	218
5.5 Conclusion.....	222
Conclusion and Perspective.....	224
References .....	230

## List of Figures

Figure 1.1. Schematic drawing of control volume.....	7
Figure 1.2. Schematic drawing of flow boiling in vertical tube. ....	13
Figure 1.3. Illustration of upward annular flow. ....	17
Figure 1.4. Comparison of wall shear stress calculated using the homogenous model and various two-phase shear viscosity models for HFE7000 in a 6 mm diameter tube. ....	20
Figure 1.5. Comparison of various separated flow wall shear stress correlations for HFE7000 in a 6 mm diameter tube.....	26
Figure 1.6. Comparison of various correlations for predicting flow boiling heat transfer coefficient for HFE7000 in the tube of 6mm diameter. ....	33
Figure 1.7. Flow patterns, a. bubbly flow b. slug flow c. Falling film flow d. Annular flow.....	38
Figure 1.8. Flow pattern maps for upward boiling flows.....	41
Figure 1.9. Flow pattern maps for downward adiabatic flows.....	42
Figure 1.10. Evolution of average void fraction with vapour quality.....	43
Figure 1.11. Frictional pressure gradient at different gravity levels. ....	45
Figure 1.12. a. Space-time plots of flow structure, b. wave velocity versus vapour superficial velocity.....	46
Figure 1.13. Heat transfer evolution with mass and heat flux. ....	48
Figure 1.14. Evolution of heat transfer coefficient with vapour quality for various flow orientations relative to gravity. ....	48
Figure 1.15. Dominant force regime in flow boiling. ....	53
Figure 1.16. Gravity dependent ( $Fr < 4$ ) and gravity independent ( $Fr \geq 4$ ) regimes. ....	54
Figure 1.17. Gravity dependent and gravity independent flow boiling regimes.....	55
Figure 1.18. Gravity dependent regime for flow boiling heat transfer. ....	56
Figure 2.1. BRASIL experimental setup; data acquisition rack (left) and hydraulic loop (right). ....	63
Figure 2.2. COSMO experimental setup; data acquisition rack (left) and hydraulic loop (right). ....	63
Figure 2.3. Schematic illustration of the BRASIL experimental flow loop. ....	64
Figure 2.4. Schematic illustration of the COSMO experimental flow loop. ....	66
Figure 2.5. Schematic drawing of the test section of a. BRASIL b. COSMO experimental facility. ....	68
Figure 2.6. Picture and sketch of the boiler system. ....	70
Figure 2.7. Comparison between measured and theoretical saturation temperatures.....	70

Figure 2.8. Calibration curves of differential pressure transducers. ....	73
Figure 2.9. Calibration curves for various thermocouples and PT100 probes.....	74
Figure 2.10. Schematic drawing of void fraction probes.....	75
Figure 2.11. Measured capacitance versus time (Filling Data), BRASIL (top), COSMO (bottom). ....	76
Figure 2.12. Liquid capacitance versus temperature of electronics.....	78
Figure 2.13. Calibration curves of void fraction probes. ....	79
Figure 2.14. Geometry and field lines of 3D simulation of void fraction probes. ....	81
Figure 2.15. Scheme of both flow boiling loops.....	83
Figure 2.16. Change in enthalpy versus preheater power in the BRASIL loop.....	84
Figure 2.17. Heat loss versus logarithmic mean temperature difference.....	84
Figure 2.18. Change in enthalpy versus preheater power in the COSMO loop.....	85
Figure 2.19. Change in enthalpy versus Power to the ITO. ....	86
Figure 2.20. Illustration of total pressure determination from measured pressure drop. ....	89
Figure 2.21. Comparison between experimental friction factor and friction factor obtained with the Blasius correlation.....	90
Figure 2.22. a. Schematic drawing of the heated tube cross section, b. Illustration of axial locations of PT100 probes for wall temperature measurements. ....	92
Figure 2.23. Nusselt number versus Reynolds number for single-phase upward flow. ....	93
Figure 2.24. Parabolic flight trajectory. ....	98
Figure 2.25. Time evolution of mass flux, pressure and wall temperature under various gravity conditions in parabolic flight. ....	100
Figure 3.1: Liquid entrainment in the gas core of annular two-phase flow. ....	134
Figure 3.2: Comparison between measured and predicted mean wave velocity for upward and downward flow boiling. ....	135
Figure 3.3: Comparison between measured and predicted mean wave velocity for upward and downward flow boiling. ....	136
Figure 3.4: Interfacial friction factor ratio in downward flow. ....	138
Figure 4.1: Illustration of the various heat transfer regimes for upward flow boiling.....	142
Figure 4.2: Illustration of the various heat transfer regimes for downward flow boiling.....	143
Figure 5.1: Flow visualisation in the sapphire tube in normal and microgravity. ....	193
Figure 5.2: Flow visualisation in the visualisation test section in normal and microgravity.....	194
Figure 5.3: Flow pattern maps; a. microgravity, b. normal gravity. ....	195



Figure 5.4. Comparison of bubble size and bubble eccentricity between microgravity and normal gravity flows. ....	198
Figure 5.5. Comparison of bubble size and bubble eccentricity between microgravity and normal gravity flows.. ....	198
Figure 5.6. Bubble size evolution in microgravity and normal gravity flows.. ....	200
Figure 5.7. Bubble size evolution in microgravity and normal gravity flows.. ....	201
Figure 5.8: Measured void fraction at the outlet of the test sections. ....	203
Figure 5.9: Vapour velocity computed from measured void fraction versus mixture velocity. ....	204
Figure 5.10: Typical distance versus time diagram for $\mu g$ slug flow. ....	205
Figure 5.11: Gray scale plots of the tube cross section for $\mu g$ -slug flow. ....	205
Figure 5.12: Space-time diagram of tube cross section for $\mu g$ -slug flow. ....	206
Figure 5.13: Probability density function of Taylor bubble velocity for $\mu g$ slug flow. ....	207
Figure 5.14: Comparison between Taylor bubble velocity obtained from image processing and that computed using the measured void fraction. ....	207
Figure 5.15: Histogram of a. wave velocity, b. wave frequency in $\mu g$ -flow. ....	208
Figure 5.16: a-b. Comparison between mean wave velocity, liquid velocity and vapor velocity for $\mu g$ - and $+1g$ -flows obtained using the COSMO setup. c. Comparison between mean wave velocities in $+1g$ -flows determined using BRASIL and COSMO setups. ....	209
Figure 5.17: a-b. Comparison of mean wave frequency between for $\mu g$ - and $+1g$ -flows obtained using the COSMO setup, c. Comparison between mean wave frequency in $+1g$ -flows determined using BRASIL and COSMO setups. ....	210
Figure 5.18: Illustration of the various heat transfer regimes for microgravity flow boiling. ....	211
Figure 5.19: Measured heat transfer coefficient versus vapour quality at selected heat fluxes in microgravity. ....	212
Figure 5.20: Measured heat transfer coefficient versus vapour quality at selected heat fluxes in normal gravity. ....	213
Figure 5.21: Heat transfer coefficient versus vapour quality at selected heat fluxes in microgravity. ....	216
Figure 5.22: Heat transfer coefficient versus vapour quality at selected heat fluxes downward flow. ....	217
Figure 5.23: Comparison between heat transfer coefficient in normal and microgravity. ....	218
Figure 5.24: Ratio of heat transfer coefficient between $\mu g$ - and $+1g$ -flows. ....	219

Figure 5.25: Comparison between heat transfer coefficient among $+1g$ , $-1g$ and $\mu g$ -flows.. ..	220
Figure 5.26: Ratio of heat transfer coefficient between $-1g$ - and $+1g$ -flows.....	221

# List of Tables

Table 1.1. Selected dimensionless numbers used in the description of flow boiling .....	11
Table 1.2. Selected dimensionless number ranges used in the current work.....	12
Table 1.3. Two-phase homogenous mixture viscosity models .....	19
Table 1.4. Summary of investigations on heat transfer coefficient. ....	49
Table 1.5. Summary of the influence of gravity on various flow boiling quantities. ....	57
Table 2.1. Properties of HFE-7000 at 25°C and atmospheric pressure.....	69
Table 2.2. Mesh specification for 3D COMSOL simulation. ....	80
Table 2.3. Uncertainties in measured mass flux and preheater power.....	87
Table 2.4. Uncertainties in measured ITO power and wall heat flux .....	87
Table 2.5. Uncertainties in measured vapour quality.....	87
Table 2.6. Uncertainties in void fraction, frictional pressure drop, wall shear stress and heat transfer coefficient.....	91
Table 2.7. Uncertainties in vapour velocity, interfacial shear stress and interfacial friction factor. .	91
Table 2.8. Summary of test conditions for CNES PFC 161 microgravity parabolic flight campaign. .....	100
Table 3.1. Constants in Eq. 3.1 .....	135
Table 3.2. Constants in Eqs. 3.4 - 3.5 .....	136
Table 4.1: Dominant mechanism of heat transfer in upward flow boiling .....	142
Table 4.2: Dominant mechanism of heat transfer in downward flow boiling .....	143
Table 5.1. Model coefficients for $h_{2\phi}$ in normal and microgravity. ....	215
Table 5.2. Gravity dependence .....	222
Table 5.3. Gravity dependence .....	223

# Nomenclature

## Roman symbols

$A$	cross-section area	$m^2$
$A^+$	constant	$[-]$
$Bo$	Boiling number	$[-]$
$b$	constant	$[-]$
$C$	constant	$[-]$
$C_p$	specific heat at constant pressure	$J.K^{-1}.kg^{-1}$
$D$	diameter	$m$
$e$	rate of entrainment	$[-]$
$Fr$	Froude number	$[-]$
$f$	friction factor	$[-]$
$G$	mass flux	$kg.s^{-1}.m^{-2}$
$g$	acceleration due to gravity	$ms^{-2}$
$h$	heat transfer coefficient	$W.K^{-1}.m^{-2}$
$h_{l,v}$	latent heat of vaporisation	$J.kg^{-1}$
$j$	superficial velocity or imaginary unit	$m.s^{-1}$ or $[-]$
$K$	von Karman constant	$[-]$
$k$	thermal conductivity of sapphire tube	$W.m^{-1}.K^{-1}$
$L$	Length of the test section	$m$
$l^+$	dimensionless mixing length	$[-]$
$\dot{m}$	mass flow rate	$kg.s^{-1}$
$Nu$	Nusselt number	$[-]$
$n$	exponent of the interfacial damping function	$[-]$
$P$	pressure	$bar$
$Pr$	Prandtl number	$[-]$
$P_R$	Reduced pressure	$[-]$
$q$	heat flux	$W.m^{-2}$
$R$	radius	$m$
$Re$	Reynolds number	$[-]$
$r$	radial coordinate	$m$

$S$	perimeter	$m$
$Su$	Suratman number	$[-]$
$T$	temperature	$K$
$t$	time	$s$
$u$	mean velocity	$m.s^{-1}$
$u^*$	friction velocity	$m/s$
$V$	Volume	$m^3$
$We$	Weber number	$[-]$
$X$	Martinelli or laminarization parameter	$[-]$
$x$	Vapour quality	$[-]$
$y^+$	dimensionless distance from the wall	$[-]$
$y^*$	frictional distance from the wall	$m$
$z$	axis coordinate	$m$

### Greek symbols

$\alpha$	void fraction	$[-]$
$\delta$	liquid film thickness	$m$
$\varepsilon$	permittivity	$[-]$
$\varepsilon_m$	eddy viscosity	$m^2.s^{-1}$
$\phi$	Martinelli parameter	$[-]$
$\Gamma$	mass transfer	$kg.s^{-1}.m^{-3}$
$\lambda$	thermal conductivity	$W.m^{-1}.K^{-1}$
$\mu$	dynamic viscosity	$Pa.s$
$\nu$	kinematic viscosity	$m^2.s^{-1}$
$\rho$	density	$kg.m^{-3}$
$\sigma$	surface tension and dielectric constant	$N.m^{-1}$
$\tau$	shear stress	$Pa$
$\theta$	inclination	$degree$

### Subscripts

<i>A</i>	adiabatic
<i>cb</i>	convective boiling
<i>c</i>	core or critical
<i>elec</i>	electrical or electrode
<i>eff</i>	effective
<i>exp</i>	experimental
<i>fr</i>	frictional
<i>g</i>	gas
<i>i</i>	inner or interfacial
<i>k</i>	phase
<i>inlet</i>	inlet conditions
<i>l</i>	liquid phase
<i>lam</i>	laminar or laminarization
<i>lf</i>	liquid film
<i>lo</i>	liquid only
<i>m</i>	mixture
<i>meas</i>	measured
<i>NA</i>	non-adiabatic
<i>nb</i>	nucleate boiling
<i>o</i>	outer
<i>out</i>	outlet conditions
<i>ph</i>	preheater
<i>pred</i>	predicted
<i>sat</i>	saturated conditions
<i>sub</i>	subcooled conditions
<i>t</i>	total
<i>v</i>	vapor phase
<i>vo</i>	liquid only
<i>w</i>	wall
$\infty$	infinity

# Introduction

Two-phase flows are commonly encountered in chemical, nuclear and petroleum industries as well as in thermal management and transportation systems in normal-, reduced- and hyper-gravity conditions. Several engineering applications require the dissipation of significant amounts of heat and most of the current heat management systems rely on single-phase heat transfer. Recent improvements in the design and operation of thermal management systems seek to strike a balance between improved heat extraction and overall weight of the devices. One approach that has attracted significant research interests, is the use of two-phase vapour-liquid systems. Boiling thermal management systems take advantage of the latent heat of the fluid in heat extraction. Recent reports on thermal management systems have highlighted the importance phase change heat transfer for the effective deployment of long-term space devices (Lebon et al., 2019). Other benefits include; reduced pumping power due to lower mass flow rate requirements, isothermal cooling and reduced fluid volume requirements (Ohta et al., 2013). Despite its potential, boiling flow is characterized by a complex interplay of hydrodynamics, mass transfer, heat transfer and interfacial phenomena.

Flow boiling thermal management systems for space applications is a subject of interest to space agencies the world over. The potential of this can be seen in the Fission Power System (FPS) of NASA which has the capacity to deliver high power and low mass to power ratio (Chiaramonte and Joshi, 2004; Konishi and Mudawar, 2015). Space systems often experience varying conditions of gravity, ranging from microgravity to hypergravity, therefore thermal management systems are designed to accommodate these changes in gravity levels (Konishi and Mudawar, 2015). The primary effect of changes in gravity levels on two-phase flows is the effect of buoyancy consequent upon the difference in phase densities. This primary effect produces secondary effects such as changes in heat transfer coefficient, critical heat flux (CHF), flow patterns and flow pattern transition, wall and interfacial shear stresses, pressure gradient and void fraction (Colin et al., 1991; Narcy et al., 2014).

There is also the potential of significant improvement of terrestrial systems. Flow boiling applications are encountered in various earth applications such as in environmental applications, production of electricity in nuclear power plants, energy conservation, chemical, food and other process industries (Celata and Zummo, 2009a). In normal gravity, boiling flows are also sensitive to flow orientation relative to gravity and this effect remains a subject of interest (Kharangate et al., 2016; Konishi and Mudawar, 2015). Furthermore, modelling tools available for predicting two-phase flow

characteristics in normal gravity are often not robust enough and their applicable range are mostly constrained to ideal or over-simplified scenarios. Unlike gas-liquid adiabatic systems, flow boiling characteristics change significantly along the axial length and are dependent on the applied heat flux. For example, it has been reported that there may be significant difference between wall shear stress in adiabatic section of a boiling flow and in the boiling flows section itself, especially in the nucleate boiling regime (Layssac, 2018). Adequate understanding of the contributions of inertia, body forces, fluid viscosity and surface tension are still lacking in earth applications. Therefore, significant benefits can be derived from studies that seek to bridge these gaps.

Although significant research effort has been dedicated to flow boiling thermal management systems under varying gravity conditions, the underlining phenomena remains a subject of interest. A number of experimental and modelling studies have been successfully carried out which provide explanation to some of the observed flow boiling characteristics. However, practical difficulties involved and the limitations imposed by sophistication of instrumentations used in these studies have resulted in some conflicting reports on the influence of changes in gravity conditions on flow boiling.

Flow boiling research in microgravity started at IMFT in 2009 as part of the MAP program “Multiscale Analysis of Boiling” of the European Space Agency (ESA) and supported by the French Space Agency (CNES). The initial phase of the research included the building of Boiling Regimes in Annular and Slug flow in Low gravity (BRASIL) experimental loop and flow boiling experiments in upward flows during the PhD Theses of Narcy (2014) and Trejo-Peimbert (2018). The experimental flow loop was originally designed for vertical upward flow boiling experiments on earth and in microgravity conditions. It is equipped for the simultaneous determination of parameters such as pressure drop, void fraction, flow visualisation and parameters for the computation of heat transfer coefficient. In the current work, modification of the BRASIL loop was done to allow for downward flow experiments. Compact Small Scale Convection Loop (COSMO) was also built in 2021 during the Postdoctoral program of Paul Chorin for adiabatic two-phase flow experiments in normal and reduced gravity conditions. In the current work, the COSMO loop was modified to allow for flow boiling experiments in normal and microgravity conditions. The current study focuses on the investigation of flow boiling in both vertical upward and downward flow configurations in normal gravity as well upward microgravity flow. The core objective of this work is to carry out experimental and modelling study of flow boiling in the heated section of a vertical 6 mm ID tube under normal and microgravity conditions.



Chapter 1 of this thesis provides an overview of flow boiling mechanisms, parameters associated with flow boiling, fundamental balanced equations and classical models derived for the closure laws in these equations. It also outlines dimensionless numbers relevant to the description of flow boiling and a bibliographic survey of flow boiling experimental research with focus on gravity and heat flux effects on axisymmetric boiling flows. In Chapter 2, description of the experimental flow loops and the various diagnostics are provided. In addition, description of various measurement techniques and protocols as well as data reduction and error estimation are provided. Chapter 3 consists mainly of the results of experimental study and mechanistic modelling of the hydrodynamics of upward and downward flow boiling as published in one of our articles. The article provides selected experimental results of flow patterns, void fraction, wall shear stress, interfacial shear stress, heat transfer coefficient and wave structures in upward and downward flows along with the comparison with existing correlations. It also consists of proposed models of interfacial friction factor in upward flow, wall shear stress and heat transfer coefficient in both upward and downward flows. This chapter also consist of additional results on the modelling of interfacial friction factor, roll wave velocity and roll wave frequency. Chapter 4 consists mainly of the results of experimental study and theoretical modelling heat transfer coefficient and liquid film thickness in annular upward and downward flows as published in one of our articles. It also consists of a description of the various contributions to the total heat transfer coefficient. Chapter 5 provides experimental results of microgravity flow boiling along with comparison with upward flow experimental data in normal gravity. The results are limited to flow patterns, void fraction, vapor velocity, bubble characteristics and heat transfer coefficient. This chapter also consists of modelling of heat transfer coefficient for microgravity and downward flow boiling as well as a description of the effect of gravity on the heat transfer coefficient.

# **Chapter 1**

## **Overview of flow dynamics, heat transfer and modelling of flow boiling in pipes**

*This chapter begins with the presentation of fundamental equations and closure laws of two-phase axisymmetric flows in heated tubes along with relevant dimensionless numbers. This is followed by a description of flow patterns of boiling flows. Description of various models for parameters associated with boiling flows is then presented. Finally, a review of two-phase flows studies in reduced and normal gravity conditions is presented. The review focuses more on flow boiling and the review of adiabatic two-phase flow studies serves the purpose of comparison. The review highlights various trends observed by various investigators using different experimental facilities and for different gravity conditions.*

## 1.1 Fundamental description

One dimensional mass, momentum and energy balance equations for each phase can be used to describe the dynamics and heat transfer of two-phase axisymmetric flows in tubes. These phase-specific equations are coupled with jump equations which describes the heat and mass transfer across the interface of the phases.

### 1.1.1 Definition of two-phase flow parameters

The area occupied by each phase ( $A_k$ ) and the total cross-section of the flow ( $A = \sum A_k$ ) are important parameters in the description of two-phase flows and for the determination of closure laws. It is relevant in the definition of the mass flux ( $G$ ) which in terms of mass flow rate ( $\dot{m}$ ) is given as;

$$G = \frac{\dot{m}}{A} \quad 1.1$$

Other parameters of interest in flow boiling are vapour quality, void fraction, mean velocity and superficial velocity. The vapour quality is defined as the ratio of the vapour mass flow rate to the total mass flow rate flowing through the pipe and is given by;

$$x = \frac{\dot{m}_v}{\dot{m}} = \frac{\dot{m}_v}{\dot{m}_v + \dot{m}_l} \quad 1.2$$

where  $v$  and  $l$  stands for vapor and liquid respectively.

The void fraction is defined as the ratio of the pipe cross section occupied by vapour and is given by;

$$\alpha = \frac{A_v}{A_v + A_l} \quad 1.3$$

The mean in-situ velocity of each phase ( $u_k$ ) is defined as the ratio of the volumetric flow rate of a phase to the area occupied by that phase and is given by;

$$u_k = \frac{\dot{m}_k}{\rho_k A_k} \quad 1.4$$

where  $k$  stands for the phase that is  $v$  and  $l$  for vapor and liquid respectively

For each phase, the mean velocity is expressed as;

$$u_v = \frac{\dot{m}_v}{\rho_v A_v} = \frac{\dot{m}x}{\rho_v A \alpha} = \frac{Gx}{\rho_v \alpha} \quad 1.5$$

$$u_l = \frac{\dot{m}_l}{\rho_l A_l} = \frac{\dot{m}(1-x)}{\rho_l A (1-\alpha)} = \frac{G(1-x)}{\rho_l (1-\alpha)} \quad 1.6$$

The superficial velocity of each phase ( $j_k$ ) is the ratio of volumetric flow rate of each phase to the cross-sectional area of the pipe ( $A$ ) and is given by;

$$j_k = \frac{\dot{m}_k}{\rho_k A} \quad 1.7$$

$$j_v = \frac{\dot{m}_v}{\rho_v A} = \alpha u_v \quad 1.8$$

$$j_l = \frac{\dot{m}_l}{\rho_l A} = (1-\alpha)u_l \quad 1.9$$

The mixture velocity is the sum of vapour and liquid superficial velocities and is given by;

$$j = j_v + j_l \quad 1.10$$

### 1.1.2 Constitutive equations

Balanced equations for mass, momentum and energy can be written for each phase and at the interface for boiling flows in tube (Hewitt and Hall-Taylor, 1970; van P. Carey, 1992). The constitutive equations are integrated over a control volume (Figure 1.1).

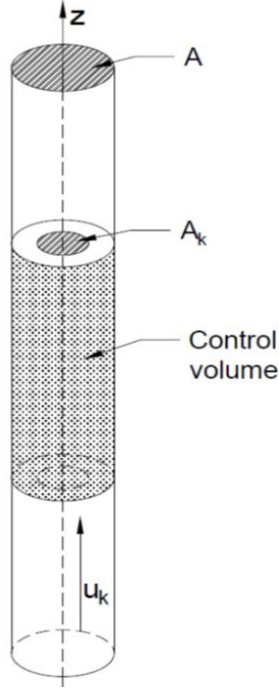


Figure 1.1. Schematic drawing of control volume.

**Mass balance:** for an impenetrable wall, the rate of change of mass of each phase in the mean direction of flow is determined by the mass transfer due to phase change ( $\Gamma_k$ ) exiting the control volume. It is expressed as;

$$\frac{\partial(\rho_k \alpha_k)}{\partial t} + \frac{\partial(\rho_k \alpha_k u_k)}{\partial z} = -\Gamma_k \quad 1.11$$

where  $z$  is the direction of mean flow,  $\rho_k$  is the density of the phase,  $t$  is time and  $u_k$  is the velocity of the phase in the mean flow direction.

**Momentum balance:** the changes in momentum of each phase within the control volume is determined by the sum of forces applied to the control volume. The balance equation for turbulent flow with interface travelling at velocity  $u_i$  is given by;

$$\begin{aligned} \frac{\partial(\rho_k \alpha_k u_k)}{\partial t} + \frac{\partial(\rho_k \alpha_k u_k^2)}{\partial z} \\ = \pm \rho_k \alpha_k g - \alpha_k \frac{\partial p_k}{\partial z} - (p_k - p_i) \frac{\partial \alpha_k}{\partial z} - \frac{\tau_{w,k} S_{w,k}}{A} - \frac{\tau_{ik} S_i}{A} - \Gamma_k u_i \end{aligned} \quad 1.12$$

where  $g$ ,  $S_{w,k}$  and  $S_i$  are acceleration due to gravity, wall perimeter wetted by phase  $k$  and perimeter of the interface respectively,  $\tau_{w,k}$  and  $p_k$  are wall shear stress and pressure in each phase,  $\tau_{ik}$  and  $p_i$

are interfacial shear stress and pressure at the interface. Assuming that capillary effect is negligible, the pressure in the tube cross section can be considered constant,  $p_k = p_i$ . Various simplifications may be applied to Eq. 1.12.

Momentum balance equation for mixtures: Adding the equations for each phase at steady state and substituting Eq. 1.5, Eq. 1.6 and  $4/D$  for  $u_v$ ,  $u_l$  and  $S_w/A$  gives;

$$G^2 \frac{d}{dz} \left[ \frac{(1-x)^2}{\rho_l(1-\alpha)} + \frac{x^2}{\rho_v\alpha} \right] = \pm \rho_m g - \frac{dp}{dz} - \frac{4\tau_w}{D} \quad 1.13$$

where  $\rho_m = \rho_v\alpha + \rho_l(1-\alpha)$  and the first term on the right-hand-side takes positive sign for downward flow and negative sign for upward flows.

Momentum balance equation for annular flow: in the case of annular flows, it is necessary to write separate momentum balance equations for the vapour and liquid phases. For the limiting case where it can be assumed that liquid entrainment in the gas core is negligible and  $S_i/A = 4\sqrt{\alpha}/D$ , the momentum balance equation for each is given by;

$$G^2 \frac{d}{dz} \left[ \frac{x^2}{\rho_v\alpha} \right] = \pm \rho_v\alpha g - \alpha \frac{dp}{dz} - \frac{4\sqrt{\alpha}\tau_i}{D} - \Gamma_v u_i \quad 1.14$$

$$G^2 \frac{d}{dz} \left[ \frac{(1-x)^2}{\rho_l(1-\alpha)} \right] = \pm \rho_l(1-\alpha)g - (1-\alpha) \frac{dp}{dz} - \frac{4\tau_w}{D} + \frac{4\sqrt{\alpha}\tau_i}{D} - \Gamma_l u_i \quad 1.15$$

where  $\tau_i = \tau_{iv} = -\tau_{il}$ . For the case of non-negligible liquid entrainment in the vapour core, the vapour flow carrying the liquid entrained droplet is commonly considered as homogenous, that is, the velocity of the entrained liquid is assumed to be equal to the velocity of the vapour core ( $u_v = u_{le}$ );  $\frac{Gx}{\rho_v\alpha} = \frac{G(1-x)e}{\rho_l\gamma}$ . Instead of writing 3 momentum balance equations, one for the vapour phase, one for the liquid film and one for the entrained droplet, only 2 equations can be written, one for the vapour core carrying droplets and one for the liquid film. In the following equations the effect of the droplet entrainment rate and redeposition has been integrated in a global interfacial shear stress:

$$G^2 \frac{d}{dz} \left[ \frac{x^2}{\rho_v\alpha + \rho_l\gamma} \right] = \pm (\rho_v\alpha + \rho_l\gamma)g - (\alpha + \gamma) \frac{dp}{dz} - \frac{4\sqrt{(\alpha + \gamma)}\tau_i}{D} - \Gamma_v u_i \quad 1.16$$

$$G^2 \frac{d}{dz} \left[ \frac{(1-x)^2}{\rho_l(1-\alpha-\gamma)} \right] = \pm \rho_l(1-\alpha-\gamma)g - (1-\alpha-\gamma) \frac{dp}{dz} - \frac{4\tau_w}{D} + \frac{4\sqrt{(\alpha+\gamma)}\tau_i}{D} - \Gamma_l u_i \quad 1.17$$

$\gamma = \frac{\rho_v}{\rho_l} \frac{1-x}{x} e$ ,  $\alpha$  and  $e = \frac{\dot{m}_{le}}{\dot{m}_l}$  is the entrainment rate of the droplets i.e., the liquid mass flow rate of the droplets over the total liquid mass flow rate.

**Energy balance:** the changes in energy of each phase is associated with the wall and interfacial heat fluxes, phase change and the mechanical work of pressure, viscous and buoyancy forces. For an open system, the total enthalpy balance can be written. The total enthalpy ( $h_{t,k}$ ) of phase ( $k$ ) is the sum of the enthalpy ( $h_k$ ), the kinetic energy and potential energy of the phase. The enthalpy balance equation is given by;

$$\begin{aligned} \frac{\partial(\rho_k \alpha_k h_{t,k})}{\partial t} + \frac{\partial(\rho_k \alpha_k u_k h_{t,k})}{\partial z} \\ = \rho_k \alpha_k g u_k + \alpha_k \frac{\partial p_k}{\partial t} + \xi \frac{\tau_{ik} S_{i,k}}{A} + \frac{q_{w,k} S_{w,k}}{A} + \frac{q_{i,k} S_{i,k}}{A} + \Gamma_k h_{k,sat} \end{aligned} \quad 1.18$$

$h_{k,sat}$  is the enthalpy of phase  $k$  at the interface assumed to be at saturation temperature,  $q_{w,i}$  and  $q_{w,k}$  are interfacial and wall heat flux respectively. The pressure variation with time, the work of gravity force and interfacial shear are considered negligible. Also, the contribution of kinetic energy and potential energy to the energy of the phase is considered negligible, therefore the total enthalpy ( $h_{t,k}$ ) of the phase is taken to be the enthalpy of the phase ( $h_k$ ).

The interfacial heat flux emanating from each of the phases is responsible for the energy variation associated with phase change.

$$(q_{i,v} + q_{i,l}) \frac{S_i}{A} = \Gamma_l h_{l,v} \quad 1.19$$

Adding the energy balance equation for each phase (Eq. 1.18) at steady state gives;

$$\frac{\partial[\rho_l(1-\alpha)u_l h_l]}{\partial z} + \frac{\partial(\rho_l \alpha u_v h_v)}{\partial z} = \frac{q_w S_w}{A} \quad 1.20$$

Eq. 1.20 is written with the assumption of negligible contribution of kinetic energy ( $h_{t,k} = h_k$ ), and negligible contribution of the work of the mechanical forces in Eq. 1.18.

$$h_k = Cp_k(T_k - T_{sat}) + h_{k,sat} \quad 1.21$$

Assuming vapour is at saturation temperature;

$$h_v = h_{v,sat}, h_l = Cp_l(T_l - T_{sat}) + h_{l,sat}, h_v - h_l = h_{l,v}$$

$$G[h_{l,v} + Cp_l(T_{sat} - T_l)]\frac{\partial x}{\partial z} + GCp_l(1 - x)\frac{\partial T_l}{\partial z} - \frac{4q_w}{D} = 0 \quad 1.22$$

Equations 1.11 to 1.22 consist of 15 variables 9 of which are secondary variables ( $S_i, S_{w,l}, \tau_{w,l}, \tau_{w,v}, \tau_i, q_{w,l}, q_{w,v}, q_{i,l}, I_l$ ) requiring closure laws to determine them. In the modelling of heat transfer and wall shear stress, for axisymmetric flows, global values of  $q_w$  and  $\tau_w$  are applied to the wall perimeter of  $\pi D$ , thereby reducing the number of secondary parameters for which closure laws are required to 6.

### 1.1.3 Dimensionless groups

Description of the various characteristics of flow boiling is better presented in terms of dimensionless numbers. This reduces the scale of each experiment and makes comparison with other experiments feasible. A number of dimensionless numbers are commonly used in the description of flow boiling. These dimensionless numbers are derived from system parameters. There are 16 independent parameters (12 independent dimensionless numbers) associated with flow boiling which are: liquid and vapour densities ( $\rho_l, \rho_v$ ), specific heat capacity of liquid and vapour ( $Cp_l, Cp_v$ ), thermal conductivities of liquid and vapour ( $k_l, k_v$ ), kinematic viscosity of the liquid and vapour ( $\nu_l, \nu_v$ ), saturation temperature ( $T_{sat}$ ) or pressure, surface tension ( $\sigma$ ) and latent heat of vaporisation of the fluid ( $h_{lv}$ ), experimental conditions such as mass flux ( $G$ ), tube diameter ( $D$ ), wall heat flux ( $q_w$ ), inlet vapour quality, ( $x_{in}$ ), liquid temperature ( $T_l$ ) and acceleration due to gravity ( $g$ ). Table 1.1 provides a summary of 12 dimensionless numbers that can be used to describe the current flow boiling study.



Table 1.1. Selected dimensionless numbers used in the description of flow boiling

Dimensionless number	Formula	Quantity ratio
$\Pi_1$	$\frac{\rho_v}{\rho_l}$	<i>density ratio</i>
$\Pi_2$	$\frac{Cp_v}{Cp_l}$	<i>specific capacity ratio</i>
$\Pi_3$	$\frac{v_v}{v_l}$	<i>kinematic viscosity ratio</i>
$\Pi_4$	$\frac{\lambda_v}{\lambda_l}$	<i>thermal conductivity ratio</i>
Boiling number ( $Bo$ )	$\frac{q_w}{Gh_{lv}}$	$\frac{\text{wall heat flux}}{\text{heat flux associated with phase change}}$
Nusselt number ( $Nu$ )	$\frac{q_w}{\lambda_l(T_w - T_l)}$	$\frac{\text{convection}}{\text{conduction}}$
Reynolds number of liquid ( $Re_l$ )	$\frac{j_l D}{v_l}$	$\frac{\text{inertia forces}}{\text{viscous forces}}$
Prandtl Number ( $Pr_l$ )	$\frac{Cp_l \mu_l}{\lambda_l}$	$\frac{\text{momentum diffusivity}}{\text{thermal diffusivity}}$
Mixture Froude Number ( $Fr$ )	$\frac{G}{\sqrt{\rho_m(\rho_l - \rho_v)gD}}$	$\frac{\text{inertia forces}}{\text{gravitational forces}}$
Weber number ( $We_v$ )	$\frac{\rho_v j_v^2 D}{\sigma}$	$\frac{\text{inertia forces}}{\text{surface tension}}$
Jakob number ( $Ja$ )	$\frac{Cp_l(T_w - T_{sat})}{h_{lv}}$	$\frac{\text{sensible heat}}{\text{latent heat}}$
Eotvos number ( $EO$ )	$\frac{(\rho_l - \rho_v)gD^2}{\sigma}$	$\frac{\text{gravity forces}}{\text{surface tension}}$

where  $\rho_m = \frac{1}{x/\rho_v + (1-x)/\rho_l}$ .

The order of magnitude of selected dimensionless numbers corresponding to the experimental conditions (Chapter 2) in the current work is provided in Table 1.2. These corresponds to mass flux, heat flux and vapour quality ranges of  $50 \leq G \leq 400 \text{ kg/m}^2\text{s}$ ,  $0 \leq q \leq 3 \text{ W/cm}^2$  and  $0 \leq x \leq 0.8$  respectively. In microgravity the residual gravity was assumed to be  $\approx 0.01g$ . Critical heat flux was not reached in the current work. The Reynolds number ranges covers both laminar and turbulent flows. The vapour Weber number reaches values high enough for destabilisation of the liquid film.

Table 1.2. Selected dimensionless number ranges used in the current work.

Dimensionless number	Experimental range
Boiling number ( $Bo$ )	$0 \leq Bo \leq 4 \times 10^{-3}$
Reynolds number of vapor ( $Re_v$ )	$2.5 \times 10^2 \leq Re_v \leq 7.5 \times 10^4$
Reynolds number of liquid ( $Re_l$ )	$2.2 \times 10^2 \leq Re_l \leq 7.0 \times 10^3$
Froude Number of mixture ( $Fr$ )	$0.01 \leq Fr \leq 3$ (1g), $0.1 \leq Fr \leq 12$ ( $\mu g$ )
Weber number of vapor ( $We_v$ )	$1.5 \times 10^{-2} \leq We_v \leq 8.0 \times 10^2$

## 1.2 Two-Phase Models

The determination of various terms in the momentum and energy balance equations require closure laws. These closure laws are often empirical correlations derived from experimental data and therefore their validity is often constrained to certain ranges of experimental conditions and also flow pattern.

### 1.2.1 Flow patterns in convective boiling

Below critical heat flux, flow patterns in vertical tubes can be broadly classified into bubbly, slug, churn, falling film (downward flow) and annular flow (Figure 1.2). Bubbly (Bb) flow regime is characterised by small bubbles with sizes less than the internal diameter of the tube and closure laws based on the homogenous models are often used to describe this flow regime. Bubble coalescence results in the formation of bullet-shaped Taylor bubbles and transition to slug or churn flow regime. The slug flow regime is characterised by bullet-shaped bubbles with typical length greater than the tube diameter while churn flow regime is a transitional flow regime between slug and annular flows characterised by significant flow fluctuations. The transition from bubbly directly to churn flow is also common, prompting the broad classification of the slug and churn flow regimes into intermittent or transitional flow regime. Taylor bubbles in slug flow regime and vapor pockets in churn flows have a drift velocity relative to the mean axial velocity of the flow and drift flux models are used to describe these flow regimes. Drift flux models may also be applied to bubbly flow regime where there is significant drift between the velocity of the bubbles and that of the continuous liquid phase. The falling film regime occur of downward concurrent flow and are characterized by low liquid and low/moderate vapor velocities with the vapor core surrounded by a falling liquid film along the wall

(Bhagwat and Ghajar, 2017). The liquid film is characterized by ripples and the interface was relatively smooth (no roll waves). The annular flow regime is characterized by high velocity vapor core and liquid film flowing along the wall. Roll waves may occur at the vapour-liquid interface in the annular flow and at high vapor qualities, interfacial stress-induced breakup of interfacial waves may result in liquid droplet entrainment in the vapor core. Separated flow models are used to determine closure laws for this flow regime.

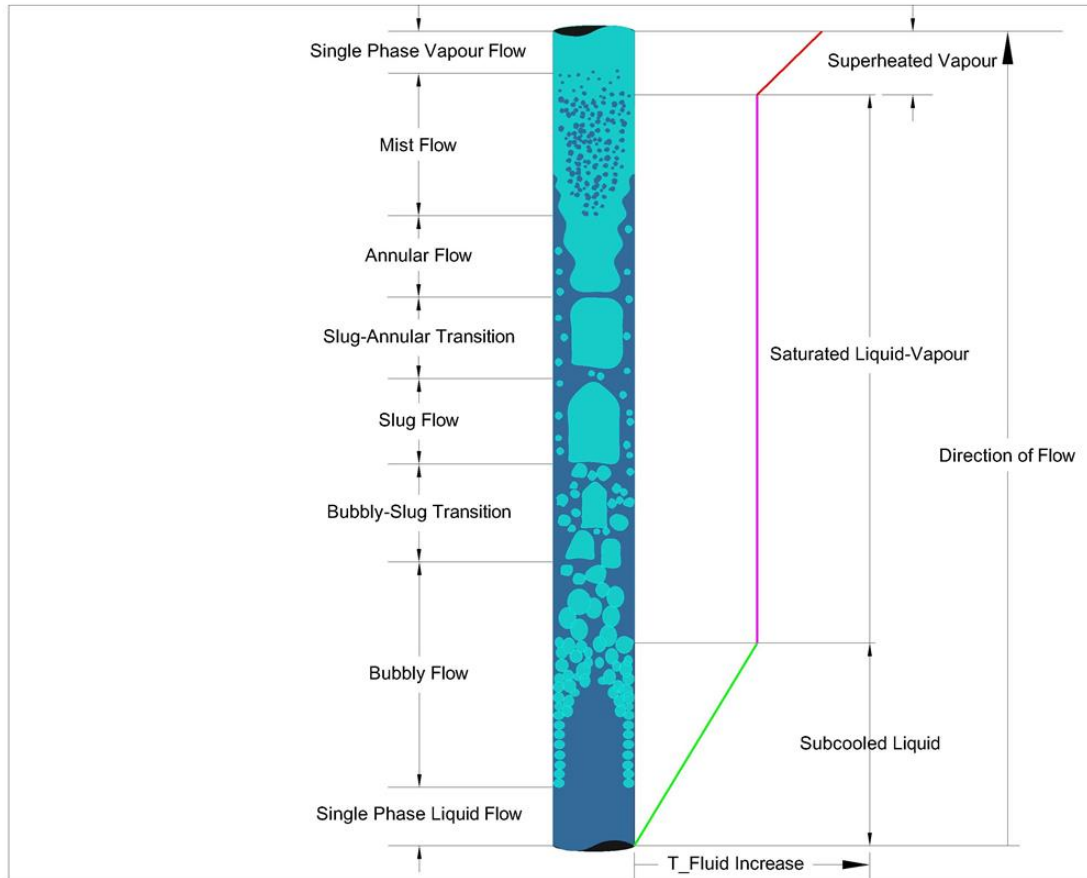


Figure 1.2. Schematic drawing of flow boiling in vertical tube showing flow pattern and temperature profile.

### 1.2.2 Gas velocity models

**Homogenous models:** homogenous models assume zero-slip velocity ( $u_l = u_v$ ) between the phases. Properties of the mixture are assumed to be the average property of the phases and so such models are generally valid where the drift velocity  $u_v - u_l$  is small by comparison to the liquid velocity. It may occur at high liquid flow rate or with properties of the phases close to each other. Several models have been proposed for mixture properties such as density and viscosity. A summary of various

models for determining the average shear viscosity was provided by Kim and Mudawar (2014). In the case of mixture density, an expression in common use is given by (Lamarsh, 1983);

$$\rho_m = \rho_l(1 - \alpha) + \rho_v \alpha \quad 1.23$$

The void fraction is obtained as follows;

$$u_l = u_v; \quad \frac{j_l}{(1 - \alpha)} = \frac{j_v}{\alpha}; \quad \alpha = \frac{j_v}{j_v + j_l} \quad 1.24$$

**Drift flux models:** where the relative velocity of the phases is significant, the homogenous models do not apply and closure laws for the drift velocity have to be derived. At moderate liquid velocities in the bubbly and slug flow regimes, significant drift is observed between the velocities of the phases due to buoyancy. Some early works in the development of drift flux models include those of Wallis, (1969); Zuber and Findlay (1965). The drift flux model is based on the premise that vapour velocity corresponds to the velocity at the centreline, which is higher than the mixture velocity, and there is a buoyancy-induced drift velocity ( $u_\infty$ ) between the phases. The relationship between vapour velocity and mixture velocity is given by;

$$u_v = C_o(j_v + j_l) + u_\infty \quad 1.25$$

where  $C_o$  is the distribution coefficient and is a function of the local vapour fraction and vapour velocity distribution. Expressions for drift velocity are generally adapted to flow patterns and include expressions as;

$$U_\infty = \begin{cases} 1.53 (g(\rho_l - \rho_v) \sigma / \rho_l^2)^{0.25} & \text{Bubbly flow (Harmathy, 1960)} \\ 0.35\sqrt{gD} & \text{Taylor bubble in vertical slug flow (Nicklin, 1962)} \end{cases} \quad 1.26$$

Several modifications to the drift flux model have been proposed. The various modifications have been tailored towards the prediction of void fraction which is calculated from vapour velocity,  $u_v$  by Eq. 1.27. A summary of selected drift flux models also extended to other flow patterns as annular flows is provided in Chapter 3 (Journal article: Table 2, pp110).

$$\alpha = \frac{j_v}{u_v} \quad 1.27$$

**Two-fluid models:** These models are based on the momentum balance equations for the liquid and the vapour phases. They are more generic and are often used for modelling two phase flows in the annular and stratified flow regimes. At steady state, the momentum balance equations for the vapour and liquid phase in a vertical annular flow are given by Eq. 1.28 and Eq. 1.29 respectively.

$$G^2 \frac{d}{dz} \left[ \frac{x^2}{\rho_v \alpha} \right] = \pm \rho_v \alpha g - \alpha \frac{dp}{dz} - \frac{4\sqrt{\alpha}\tau_i}{D} - \Gamma_v u_i \quad 1.28$$

$$G^2 \frac{d}{dz} \left[ \frac{(1-x)^2}{\rho_l(1-\alpha)} \right] = \pm \rho_l(1-\alpha)g - (1-\alpha) \frac{dp}{dz} - \frac{4\tau_w}{D} + \frac{4\sqrt{\alpha}\tau_i}{D} - \Gamma_l u_i \quad 1.29$$

To determine void fraction and total pressure gradient, closure laws are required for the wall and interfacial shear stresses. However, the void fraction (or liquid film thickness) calculated from these two momentum balance equations is very sensitive to the closure laws chosen for the wall and interfacial shear stresses. This explains why several correlations and models have been developed to calculate the void fraction in annular flow. One of such models is the void fraction model for separated flows proposed by Lockhart and Martinelli (1949) as a function of the two-phase multiplier ( $\phi_l$ ). The proposed model for void fraction is given by;

$$\alpha = 1 - \left( \frac{1}{\phi_l^2} \right)^{1/3} \quad 1.30$$

Awad and Muzychka (2014) developed a model for void fraction in circular pipes as a function of the Lockhart-Martinelli parameter ( $X$ ). It was assumed that both liquid and gas phases are in the turbulent regime as is often the case for large diameter pipes. They developed models for the lower and upper limits of void fraction ( $\alpha_{lower} \leq \alpha \leq \alpha_{upper}$ ) and proposed a void fraction correlation which is an average of these limiting values ( $\alpha_{average}$ ).

$$\alpha_{lower} = \frac{1}{1 + X^{16/19}} \quad 1.31$$

$$\alpha_{upper} = \frac{1}{1 + 0.28X^{0.71}} \quad 1.32$$

The Lockhart-Martinelli parameter ( $X$ ) for turbulent flows can be expressed as;

$$X = \left(\frac{1-x}{x}\right)^{7/8} \left(\frac{\rho_v}{\rho_l}\right)^{0.5} \left(\frac{\mu_l}{\mu_v}\right)^{1/8} \quad 1.33$$

A void fraction correlation for annular flow was developed by Cioncolini and Thome (2012a) given by;

$$\alpha = \frac{hx^n}{1 + (h-1)x^n} \quad 1.34$$

$$h = -2.129 + 3.129 \left(\frac{\rho_v}{\rho_l}\right)^{-0.2186}, \quad n = 0.3487 + 0.6513 \left(\frac{\rho_v}{\rho_l}\right)^{0.5150}$$

Void fraction obtained from separated flow models are used in the computation of liquid film thickness in the annular flow regime. In annular flow, the vapour core flows at the centre of the tube (or channel) while the liquid film flows along the wall. Liquid film thickness is dictated by a complex balance between interfacial shear stress, wall shear stress and weight of the liquid column along the wall. A simple illustration of annular upward flow is shown in Figure 1.1. In the case of negligible liquid entrainment in the gas core, the liquid film thickness is given by;

$$\delta = 0.5D(1 - \sqrt{\alpha}) \quad 1.35$$

Where the liquid entrainment is significant, determination of liquid film thickness is determined using;

$$\delta = 0.5D(1 - \sqrt{\alpha + \gamma}) \quad 1.36$$

$$\gamma = \frac{\rho_v}{\rho_l} \frac{1-x}{x} e \cdot \alpha \quad 1.37$$

The liquid entrainment  $e$  is given in terms of the core Weber number ( $We_c$ ) by Cioncolini and Thome (2012a) as;

$$e = (1 + 271.6We_c^{-0.8395})^{-2.209} \quad 1.38$$

$$We_c = \frac{\rho_c j_v^2 D}{\sigma} \quad (10 < We_c < 10^5) \quad 1.39$$

$$\rho_c = \frac{\frac{x}{\rho_v} + \frac{e(1-x)}{\rho_l}}{\frac{x}{\rho_v} + \frac{e(1-x)}{\rho_l}} \quad 1.40$$

$\rho_c$  is the density of the vapor core carrying liquid droplet. Due to implicit nature of Eqs. 1.38 to 1.40, the vapour density ( $\rho_v$ ) is used as an initial estimate for the core density ( $\rho_c$ ). This is then used to estimate the core Weber number ( $We_c$ ) and then the liquid entrainment ( $e$ ). The estimated liquid entrainment is then used to refine  $\rho_c$ . This iterative procedure is repeated until suitable convergence is attained.

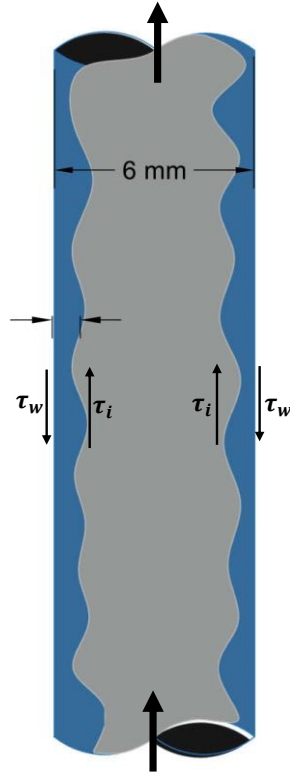


Figure 1.3. Illustration of upward annular flow.

### 1.2.3 Bubble size evolution models

Bubble size evolution along the test section results from, bubble compressibility, phase change, bubble coalescence and bubble nucleation. Various models for determining the various contributions to bubble size evolution have been proposed (Colin et al., 2004; Liao et al., 2011; Morel and Laviéville, 2008). A discussion of bubble size evolution is provided in Chapter 5.

### 1.2.4 Wall shear stress models

**Single-phase flows:** The expression for wall shear stress for single-phase incompressible flow in steady state is given by;

$$\tau_w = f \frac{\rho u^2}{2} \quad 1.41$$

where  $f$  is the fanning friction factor which is a function of the Reynolds number and pipe roughness. Approximate expressions for  $f$  in smooth pipe are given by the Poiseuille and Blasius correlations as follows;

$$f = \begin{cases} 16/Re & Re < 2000 \\ 0.0792Re^{-0.25} & 2000 \leq Re < 10^5 \end{cases} \quad 1.42$$

In two-phase flows, models for the prediction of wall shear stress are divided into two classes: homogenous flow models based on equivalent properties (viscosity, density) for the mixture and separate flow models considering wall shear stress for the liquid phase or the vapor phase alone, and an enhancement factor through a multiplier. Some examples of these 2 classes of models are presented hereafter.

**Homogenous flow models:** The expression for two-phase frictional pressure drop is analogous to that of single-phase flow with single-phase fluid properties replaced by effective mixture properties. The expression wall shear stress for homogenous model is given by;

$$\tau_{w\_2\phi} = f_{2\phi} \frac{\rho_{2\phi} (G/\rho_{2\phi})^2}{2} = f_{2\phi} \frac{G^2}{2\rho_{2\phi}} \quad 1.43$$

The frictional pressure gradient is therefore given by;

$$\left(\frac{dp}{dz}\right)_{fr} = \frac{4\tau_{w\_2\phi}}{D} = f_{2\phi} \frac{2G^2}{\rho_{2\phi}D} \quad 1.44$$

$$f_{2\phi} = \begin{cases} 16/Re_{2\phi} & Re_{2\phi} < 2000 \\ 0.0792Re_{2\phi}^{-0.25} & 2000 < Re_{2\phi} < 10^5 \end{cases} \quad 1.45$$

$$Re_{2\phi} = \frac{GD}{\mu_{2\phi}} \quad 1.46$$

where  $\rho_{2\phi} = \rho_l(1 - \alpha) + \rho_v\alpha$ ,  $\alpha = j_v/(j_v + j_l)$  and  $\mu_{2\phi}$  is determined using relevant correlations (Table 1.3). A comparison of wall shear stresses for a flow of HFE7000 in a 6mm diameter tube at  $G = 200 \text{ kg/m}^2\text{s}$  calculated using Eqs. 1.43, 1.45 and 1.46 and two-phase viscosity models given in



Table 1.3 is shown in Figure 1.4. Models of Owens (1961) and Cicchitti et al. (1960) gave higher prediction of wall shear stress over the entire range of vapour quality while models of Akers et al. (1958) and Beattie and Whalley (1982) gave higher predictions of wall shear only at high vapour quality. The other models gave similar prediction of wall shear stress over the entire range of vapour quality.

Table 1.3. Two-phase homogenous mixture viscosity models

Author(s)	Correlation
McAdams et al. (1942)	$\frac{1}{\mu_{2\phi}} = \frac{1}{\mu_v} + \frac{1-x}{\mu_l}$
Akers et al. (1958)	$\mu_{2\phi} = \frac{\mu_l}{\left[(1-x) + x\left(\frac{\rho_l}{\rho_v}\right)^{0.5}\right]}$
Cicchitti et al. (1960)	$\mu_{2\phi} = x\mu_v + (1-x)\mu_l$
Owens (1961)	$\mu_{2\phi} = \mu_l$
Dukler et al. (1964)	$\mu_{2\phi} = \frac{xv_v + (1-x)v_l}{\frac{x}{\rho_v} + \frac{(1-x)}{\rho_l}}$
Beattie and Whalley (1982)	$\mu_{2\phi} = w\mu_v + (1-w)(1+2.5w)\mu_l$ $w = \frac{x/\rho_v}{\frac{1}{\rho_l} + x\left(\frac{1}{\rho_v} - \frac{1}{\rho_l}\right)}$
Lin et al. (1991)	$\mu_{2\phi} = \frac{\mu_l\mu_v}{\mu_v + x^{1.4}(\mu_l - \mu_v)}$

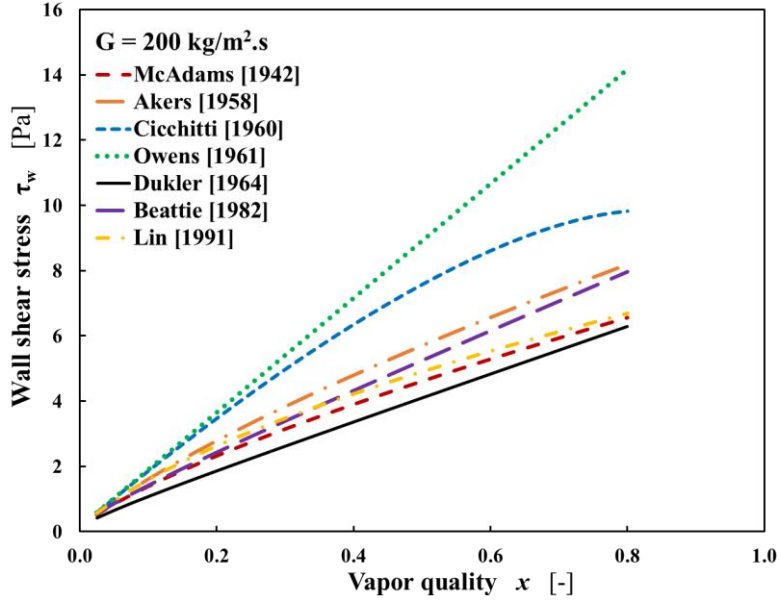


Figure 1.4. Comparison of wall shear stress calculated using the homogenous model and various two-phase shear viscosity models for HFE7000 in a 6 mm diameter tube.

**Separated flow models:** Separated flow models are more global and may be applied to all flow patterns. In separated flow models the interaction between the phases is taken into consideration and the properties of each phase is modelled rather than the property of the mixture. We begin by presenting separated flow models based on the liquid and vapour two-phase multipliers ( $\phi_l, \phi_v$ ), then models based on the liquid only and vapour only two-phase multipliers ( $\phi_{lo}, \phi_{vo}$ ) and finally we present other phenomenological models.

**Lockhart-Martinelli correlation:** This long-standing correlation forms the basis for other separated flow models and it is based on the assumption that the two-phase friction factor is related to the single-phase friction factor by a multiplier ( $\phi_k$ ) (Lockhart and Martinelli, 1949). The expression of frictional pressure gradient is given by;

$$\left(\frac{dp}{dz}\right)_{fr} = \frac{4\tau_{w-2\phi}}{D} = \phi_l^2 \left(\frac{dp}{dz}\right)_l = \phi_v^2 \left(\frac{dp}{dz}\right)_v \quad 1.47$$

$$\left(\frac{dp}{dz}\right)_l = -\frac{4}{D} f_l \frac{\rho_l j_l^2}{2} = -f_l \frac{2G^2(1-x)^2}{\rho_l D} \quad 1.48$$

$$\left(\frac{dp}{dz}\right)_v = -\frac{4}{D} f_v \frac{\rho_v j_v^2}{2} = -f_v \frac{2G^2 x^2}{\rho_v D} \quad 1.49$$

The Reynolds number for the calculation of friction factor is given by;

$$Re_l = \frac{G(1-x)D}{\mu_l}, \quad Re_v = \frac{GxD}{\mu_v} \quad 1.50$$

The two-phase multiplier is related to the Lockhart-Martinelli parameter ( $X$ ) given by;

$$X = \left[ \frac{\left(\frac{dp}{dz}\right)_l}{\left(\frac{dp}{dz}\right)_v} \right]^{0.5} \quad 1.51$$

The two-phase multipliers for liquid and vapour were represented by four different curves representing laminar-laminar ( $ll$ ), laminar-turbulent ( $lt$ ), turbulent-laminar ( $tl$ ) and turbulent-turbulent ( $tt$ ) liquid-vapour flow regimes. An approximate correlation for the profiles was given by Chisholm et al. (1967) (Eqs. 1.52 and 1.53);

$$\phi_l^2 = 1 + \frac{C}{X} + \frac{1}{X^2} \quad 1.52$$

$$\phi_v^2 = 1 + CX + X^2 \quad 1.53$$

The constant  $C$  for the four regimes are  $C_{ll} = 5$ ,  $C_{tl} = 10$ ,  $C_{lt} = 12$  and  $C_{tt} = 20$ .  $f_v$  and  $f_l$  are computed from Eq. 1.42.

The correlation of Lockhart and Martinelli (1949) is generally suited for  $\mu_l/\mu_v > 1000$  and  $G > 100 \text{ kg/m}^2\text{s}$ .

Awad and Muzychka (2014) developed rational bounds for two-phase frictional pressure gradient in circular pipes in terms of  $\phi_k$ ;  $(dp/dz)_{fr,lower} \leq (dp/dz)_{fr} \leq (dp/dz)_{fr,upper}$ .

The proposed correlations for lower and upper bounds for the liquid and vapour phases ( $k$ ) are;

$$\phi_{l,lower}^2 = \left[ 1 + \left( \frac{1}{X^2} \right)^{1/2.375} \right]^{2.375} \quad 1.54$$

$$\phi_{l,upper}^2 = \left[ 1 + \left( \frac{1}{X^2} \right)^{1/4} \right]^4 \quad 1.55$$

The two-phase multiplier and the Lockhart and Martinelli (1949) parameter (for turbulent liquid and turbulent vapour) may be expressed as;

$$\phi_l^2 = \frac{\left(\frac{dp}{dz}\right)_{fr}}{\left(\frac{dp}{dz}\right)_l} \quad 1.56$$

$$X_{tt} = \left(\frac{1-x}{x}\right)^{7/8} \left(\frac{\rho_v}{\rho_l}\right)^{0.5} \left(\frac{\mu_l}{\mu_v}\right)^{1/8} \quad 1.57$$

$$\left(\frac{dp}{dz}\right)_l = \frac{2G^2(1-x)^2}{\rho_l D} \quad 1.58$$

Combining Eqs. 1.54 to 1.58 gives expressions for frictional pressure gradient in the lower and upper bounds as follows;

$$\begin{aligned} \left(\frac{dp}{dz}\right)_{fr,lower} &= \frac{0.158G^{1.75}(1-x)^{1.75}\mu_l^{0.25}}{D^{1.25}\rho_l} \\ &\times \left[1 + \left(\frac{x}{1-x}\right)^{0.7368} \left(\frac{\rho_l}{\rho_v}\right)^{0.4211} \left(\frac{\mu_v}{\mu_l}\right)^{0.1053}\right]^{2.375} \end{aligned} \quad 1.59$$

$$\begin{aligned} \left(\frac{dp}{dz}\right)_{fr,lower} &= \frac{0.158G^{1.75}(1-x)^{1.75}\mu_l^{0.25}}{D^{1.25}\rho_l} \\ &\times \left[1 + \left(\frac{x}{1-x}\right)^{0.7368} \left(\frac{\rho_l}{\rho_v}\right)^{0.4211} \left(\frac{\mu_v}{\mu_l}\right)^{0.1053}\right]^{2.375} \end{aligned} \quad 1.60$$

$$\begin{aligned} \left(\frac{dp}{dz}\right)_{fr,average} &= \frac{0.079G^{1.75}(1-x)^{1.75}\mu_l^{0.25}}{D^{1.25}\rho_l} \\ &\times \left[ \left[1 + \left(\frac{x}{1-x}\right)^{0.7368} \left(\frac{\rho_l}{\rho_v}\right)^{0.4211} \left(\frac{\mu_v}{\mu_l}\right)^{0.1053}\right]^{2.375} \right. \\ &\left. + \left[1 + \left(\frac{x}{1-x}\right)^{0.4375} \left(\frac{\rho_l}{\rho_v}\right)^{0.25} \left(\frac{\mu_v}{\mu_l}\right)^{0.0625}\right]^4 \right] \end{aligned} \quad 1.61$$

A model was proposed by Chisholm (1973) which depends on the Chisholm parameter ( $Y$ ). The Chisholm parameter is given by;

$$Y = \left[ \frac{\left(\frac{dp}{dz}\right)_{lo}}{\left(\frac{dp}{dz}\right)_{vo}} \right]^{-0.5} \quad 1.62$$

$$\left(\frac{dp}{dz}\right)_{lo} = -f_{lo} \frac{2G^2}{\rho_l D} \quad 1.63$$

$$\left(\frac{dp}{dz}\right)_{vo} = -f_{vo} \frac{2G^2}{\rho_v D} \quad 1.64$$

$$\left(\frac{dp}{dz}\right)_{fr} = \frac{4\tau_{w,2\phi}}{D} = \phi_{lo}^2 \left(\frac{dp}{dz}\right)_{lo} = \phi_{vo}^2 \left(\frac{dp}{dz}\right)_{vo} \quad 1.65$$

$$Re_{lo} = \frac{GD}{\mu_l}, \quad Re_{vo} = \frac{GD}{\mu_v} \quad 1.66$$

$$\phi_{lo}^2 = 1 + (Y^2 - 1) [Bx^{(2-n)/2}(1-x)^{(2-n)/2} + x^{(2-n)}] \quad 1.67$$

where  $n$  is 1 for laminar flow and 0.25 for turbulent flow, and

$$B = \begin{cases} \frac{55}{\sqrt{G}} & 0 < Y < 9.5 \\ \frac{520}{Y\sqrt{G}} & 9.5 < Y < 28 \\ \frac{15000}{Y^2\sqrt{G}} & Y > 28 \end{cases} \quad 1.68$$

The Chisholm correlation is also suited for  $\mu_l/\mu_v > 1000$  and  $G > 100 \text{ kg/m}^2\text{s}$ . For  $\mu_l/\mu_v < 1000$ , Friedel (1979) proposed the following correlation;

$$\phi_{lo}^2 = C_1 + \frac{3.24C_2}{Fr^{0.045}We^{0.035}} \quad 1.69$$

where  $Fr$ ,  $We$ ,  $C_1$  and  $C_2$  are given by;  $Fr = \frac{G^2}{gD\rho_m^2}$ ,  $We = \frac{G^2D}{\sigma\rho_m}$ ,  $\rho_m = \left(\frac{x}{\rho_v} + \frac{1-x}{\rho_l}\right)^{-1}$ ,  $C_1 = (1-x)^2 + x^2 \left(\frac{\rho_l}{\rho_v}\right) \left(\frac{f_{vo}}{f_{lo}}\right)$  and  $C_2 = x^{0.78}(1-x)^{0.24} \left(\frac{\rho_l}{\rho_v}\right)^{0.91} \left(\frac{\mu_v}{\mu_l}\right)^{0.19} \left(1 - \frac{\mu_v}{\mu_l}\right)^{0.7}$  respectively.

$f_{lo}$  and  $f_{vo}$  are single-phase friction factors computed using  $Re_{lo}$  and  $Re_{vo}$  respectively.

An empirical correlation for the determination of frictional pressure gradient was also proposed by Muller-Steinhagen and Heck (1986) as a function of vapour quality (see journal article in Chapter 3, Eq. 18, pp114).

Cioncolini et al. (2009) proposed a correlation for predicting frictional pressure gradient in annular flows as a function of the vapour core Weber number ( $We_c$ ) given by;

$$\left(\frac{dp}{dz}\right)_{fr} = \frac{4\tau_{w,2\phi}}{D} = 2f_{2\phi} \frac{\rho_c j_c^2}{D} \quad 1.70$$

$$f_{2\phi} = 0.172We_c^{-0.372} \quad 1.71$$

$We_c$  is determined as outlined in Eqs. 1.37 to 1.40 and void fraction is determined using void fraction model of Woldeesemayat and Ghajar (2007) (journal article in Chapter 3, Table 2 pp110).

To provide better prediction of wall shear stress for adiabatic two-phase upward flow, Kim & Mudawar (2012b) proposed a modification to the constant ( $C$ ) in Eq. 1.52 (Chisholm et al., 1967). The modified correlation of Kim & Mudawar (2012b) is provided in Chapter 3 (journal article in Chapter 3, Eq. 19-23, pp115).

Klausner et al. (1990) was among the first to report an enhancement in frictional pressure gradient with increase in heat flux and associated this to turbulence enhancement in the liquid film. In general, higher wall shear stress have been reported boiling flows relative to adiabatic two-phase flow and the difference increases with wall heat flux (Kim and Mudawar, 2013a; Klausner et al., 1990; Layssac, 2018). To account for the effect of wall heat flux on the wall shear stress in flow boiling, Kim & Mudawar (2013b) proposed a modification to the constant ( $C_A$ ) in the model of Kim & Mudawar (2012b). This was done by introducing a function which depends on the boiling number ( $Bo$ ) and Weber number of the liquid ( $We_{lo}$ ) (journal article in Chapter 3, Eq. 24, pp116).

Cioncolini and Thome (2017) developed a correlation for predicting frictional pressure gradient in vertical tubes based on ‘momentum Weber number’ ( $We_m$ ), the weber number of the vapour core carrying liquid droplets. The proposed correlation for two-phase friction factor is given by;

$$f_{2\phi} = 0.2140We_m^{-0.3884} \quad 10^2 \leq We_m \leq 10^5 \quad 1.72$$

$$We_m = \frac{G^2 D}{\rho_m \sigma} \quad 1.73$$

$$\rho_m = \left[ \frac{(1-e)^2(1-x)^2x}{(1-\alpha)x\rho_l - e\alpha(1-x)\rho_v} + \frac{ex(1-x) + x^2}{\alpha\rho_v} \right]^{-1} \quad 1.74$$

where  $e$  is determined as outlined in Eqs. 1.37 to 1.40, the void fraction is determined using Eq. 1.34 and the frictional pressure gradient is given by;

$$\left( \frac{dp}{dz} \right)_{fr} = \frac{4\tau_{w-2\phi}}{D} = \frac{2f_{2\phi}G^2}{\rho_m D} \quad 1.75$$

A comparison of predicted wall shear stress using various correlations versus vapour quality for  $G = 200 \text{ kg/m}^2\text{s}$  is shown in Figure 1.5. The change in profile seen for the model of Lockhart and Martinelli (1949) corresponds to change from turbulent liquid ( $Re_l \geq 2000$ ) to laminar liquid ( $Re_l < 2000$ ) flow. Correlations of Lockhart and Martinelli (1949) and Awad and Muzychka (2014) give similar predictions of wall shear stress at higher vapour quality corresponding to laminar liquid and turbulent vapour flow. These two models also gave lower predictions of wall shear stress compared to the rest at high vapour quality. The correlation of Chisholm (1973) showed different trend compared to the rest. Correlations of Friedel (1979) and Muller-Steinhagen and Heck (1986) gave similar predictions of wall shear stress over the entire range of vapour quality and the predicted wall shear stresses were generally lower than those of Cioncolini et al. (2009) and Cioncolini and Thome (2017). Correlations of Cioncolini et al. (2009) and Cioncolini and Thome (2017) showed similar trends but the predicted wall shear stress was higher for Cioncolini and Thome (2017). We can see from this short review that even if the correlations have been developed for the same range of dimensionless numbers ( $Re_l, Re_v$ ) very large discrepancies in their predictions are pointed out.

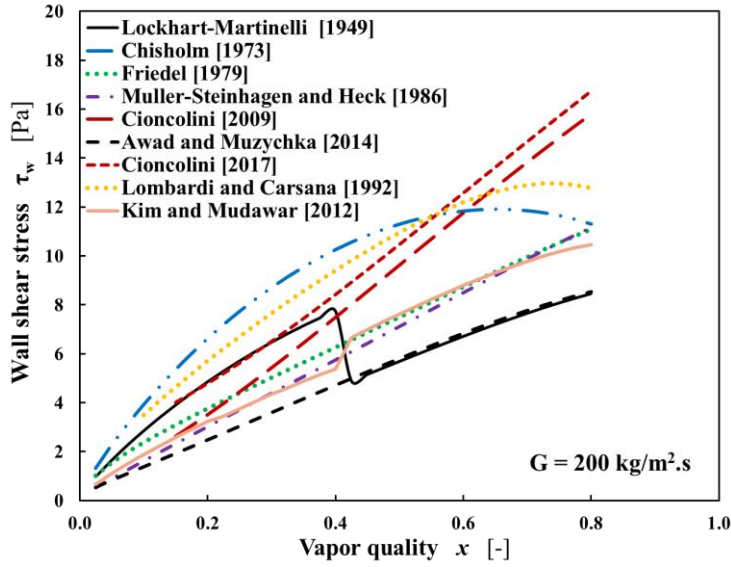


Figure 1.5. Comparison of various separated flow wall shear stress correlations for HFE7000 in a 6 mm diameter tube.

### 1.2.5 Interfacial shear stress models

Closure laws for interfacial shear stress are required for calculating pressure gradient and void fraction (or liquid film thickness) in two-phase models for annular flows. The interfacial shear stress is related to the interfacial friction factor by;

$$\tau_i = f_i \frac{\rho_v |u_v - u_i|^2}{2} - \frac{1}{2} \frac{(\bar{u}_v - u_i) \Gamma_{lv}}{2\pi r_i} \quad 1.76$$

Correlations for predicting interfacial friction factor and interfacial velocities are therefore required to compute the interfacial shear stress. For highly turbulent liquid film, the interfacial velocity ( $u_i$ ) is approximated by the velocity of the liquid film ( $u_l$ ),  $u_i = u_l$ . A few empirical and semi-empirical models have been proposed for the prediction of interfacial friction factor ( $f_i$ ). One of the early models is that of Wallis (1969) which was obtained from experiments inside a large diameter tube ( $D = 50 \text{ mm}$ ). In this model, it was assumed that the vapor core flow is fully turbulent and the roughness of the interface was equal to the liquid film thickness ( $\delta$ ). In this flow configuration, the friction factor of the vapor core ( $f_v$ ) flow is  $\approx 0.005$  and quite independent of the Reynolds number of the vapor. The model of Wallis (1969) is provided in Chapter 3 (journal article, Eq. 33, pp125). Using a similar flow configuration to Wallis (1969), Belt et al. (2009) proposed a correlation for interfacial friction factor (see journal article in Chapter 3, Eq. 34, pp125). Another correlation was proposed by Bousman



and Dukler (1993) for microgravity two-phase flow using data obtained inside a 12.7 mm diameter tube (Eq. 1.77).

$$\frac{f_i}{f_v} = 211.4 + 245.9\alpha \quad (0.70 \leq \alpha \leq 0.85) \quad 1.77$$

In these correlations, the interfacial friction factor is a function of the liquid film thickness alone. In the regime of transition between smooth and fully rough interface, Fore et al. (2000) highlighted the dependency of interfacial friction factor on both film thickness and Reynolds number of the gas phase. They introduced a function  $(1 + A/Re_v)$  to the correlation of Wallis (1969) to account for the Reynolds number dependence. Based on the approach of Fore et al. (2000), Narcy et al. (2014) proposed a correlation of interfacial friction factor from upward flow data obtained in the adiabatic section of a 6 mm ID tube (Eq. 1.78).

$$\frac{f_i}{f_v} = 1 + 18.3 \left[ \left( 1 + \frac{3 \times 10^5}{Re_v^{1.3}} \right) \left( \frac{\delta}{D} \right)^{0.1} - 0.89 \right] \quad 1.78$$

In general, the vapour phase is assumed to be turbulent and the friction factor of the vapour phase is given by;

$$f_v = 0.0792 Re_v^{-1/4} \quad 1.79$$

An empirical correlation for the determination of interfacial friction fraction in downward flow was proposed by Aliyu et al. (2016). The correlation was developed for adiabatic air-water flows and is based on experimentally determined pressure drop and liquid film thickness. The proposed correlation is given by;

$$\frac{f_i}{f_v} = 0.018 Re_v^{-0.27} \delta_v^{+1.35} \left( Fr_v \frac{\delta}{D} \right)^{-1.49} \quad 1.80$$

$$Fr_v = \frac{j_v}{\sqrt{gD}}, \delta_v^+ = \frac{\delta}{v_v} \sqrt{\frac{\tau_i}{\rho_v}}, \tau_i = \left( -\frac{dP}{dz} + \rho_c g \right) \frac{D-2\delta}{4}, \rho_c = (1 - \alpha_c)\rho_l + \alpha_c\rho_v$$

$\delta_v^+$  is the dimensionless liquid film thickness based on the gas or vapour properties,  $dP$  is the measured pressure drop,  $\delta$  is the measured liquid film thickness and  $Fr_v$  is the Froude number of the gaseous phase. The interfacial friction factor for this correlation is obtained by iteration using Eqs. 1.28, 1.76 and 1.80.

### 1.2.6 Interfacial wave structures models

Interfacial shear stress strongly depends on the wave parameters such as wave amplitude, wave velocity and wave frequency. Several studies were performed on the wave structure at the interface in annular flow in a goal to predict the entrainment rate of droplet. The droplet detachment is considered to mainly occurs at the crest of roll waves. Pearce (1979) proposed a correlation for the wave velocity for adiabatic two-phase upward flow (see journal article in Chapter 3, Eq. 36, pp127). Sekoguchi et al., (1985) proposed a correlation for predicting the frequency of disturbance waves in upward flow as a function of the Eötvös number ( $Eu$ ), Reynolds number of the liquid ( $Re_l$ ) and Froude number of the vapour ( $Fr_v$ ) (see journal article in Chapter 3, Eq. 38 pp127). These correlations will be compared to our experimental data in Chapter 3.

### 1.2.7 Heat transfer coefficient models

Single-phase forced convective heat transfer is predicted thanks to Nusselt number which depends on the Reynolds and Prandtl numbers. In single-phase laminar flow, the local Nusselt number is constant at constant wall heat flux or constant wall temperature (at fixed wall heat flux  $Nu = 4.36$  and at fixed wall temperature  $Nu = 3.66$ ).

**Single-phase flow correlations:** Typical correlations for single-phase Nusselt number include those of Gnielinski (1976) and Dittus and Boelter (1930). These correlations are generally valid for thermally developed flows over stated Reynolds and Prandtl number ranges. The correlation of Dittus and Boelter (1930) is given by;

$$Nu = 0.023Re^{0.8}Pr^{0.4} \quad (Re > 10^4, \quad 0.6 \leq Pr \leq 160) \quad 1.81$$

The correlation of Gnielinski (1976) is given by;

$$Nu = \frac{Pr(Re - 1000) \left( \frac{f}{2} \right)}{1 + 12.7(Pr^{2/3} - 1) \left( \frac{f}{2} \right)^{0.5}} \quad (3000 < Re < 5 \times 10^6, \quad 0.5 \leq Pr \leq 2000) \quad 1.82$$

$f$  is the fanning friction factor which is determined empirically according to Reynolds number and wall roughness ( $k/D$ ) using Colebrook and White (1937)'s correlation for turbulent flow (Eq. 1.83) or the Blasius approximation (Eq. 1.42).

$$\frac{1}{\sqrt{f}} = -4 \log \left( 2 \frac{k}{D} + \frac{9.35}{Re \sqrt{f}} \right) \quad 1.83$$

Correlations for correcting Nusselt number for cases where the flow is not thermally developed has also be developed. One of such correlations is that of Al-Arabi (1982) given by;

$$Nu_{\infty} = \frac{Nu_m}{\left[ 1 + \frac{(z/D)^{0.1} (0.68 + 3000/Re^{0.81})}{(z/D) Pr^{1/6}} \right]} \quad 1.84$$

where  $Nu_m$  is the measured Nusselt number and  $Nu_{\infty}$  is the Nusselt number for thermally developed flow,  $z$  being the abscissa in the tube from the beginning of the heated part.

**Flow boiling heat transfer:** In flow boiling, both bubble nucleation and mixing (forced convection) contribute to heat transfer, therefore, correlations for flow boiling heat transfer coefficient are often expressed as a weighted average of the contributions of each of these mechanisms. Nucleate boiling is dominant in bubbly and slug flow regimes and nucleate boiling heat transfer coefficient ( $h_{nb}$ ) decreases as flow transits from bubbly to annular flows due to suppression of bubble nucleation. Convective boiling is dominant in annular flows and the convective heat transfer coefficient ( $h_{cb}$ ) increases with vapour quality due to thinning of the annular liquid film (Kim and Mudawar, 2013b).

**Chen's correlation:** The correlation originally developed by Chen (1966) for saturated boiling is extended to subcooled boiling and takes the general form;

$$h = S \cdot h_{nb} + F \cdot h_l \quad 1.85$$

The first and second terms to the right are contributions from nucleate and convective boiling heat transfer.  $S$  is the suppression factor for nucleate boiling and  $F$  is the convective boiling enhancement factor which increases the contribution of convective boiling due to increase in vapour quality. Both  $F$  and  $S$  are functions of the Martinelli parameter for turbulent flows ( $X_{tt}$ ).

$$F(X_{tt}) = \begin{cases} 2.35 \left( 0.213 + 1/X_{tt} \right)^{0.736} & 1/X_{tt} > 0.1 \\ 1 & 1/X_{tt} < 0.1 \end{cases} \quad 1.86$$

$$S(X_{tt}) = \left[ 1 + 2.53 \times 10^{-6} \left( \frac{GD(1-x)F^{1.25}}{\mu_l} \right)^{1.17} \right]^{-1} \quad 1.87$$

$h_{nb}$  is obtained from nucleate pool boiling correlation of Forster and Zuber (1955) given by;

$$h_{nb} = 0.00122 \left[ \frac{Cp_l^{0.45} \lambda_l^{0.79} \rho_l^{0.49}}{\sigma^{0.5} \rho_v^{0.24} h_{lv}^{0.24} \mu_l^{0.29}} \right] (T_w - T_{sat})^{0.24} (p - p_{sat})^{0.75} \quad 1.88$$

where  $p$  is the saturation pressure corresponding to wall temperature  $T_w$ .

$h_l$  is determined from single-phase turbulent correlations such as those of Dittus and Boelter (1930) or Gnielinski (1976). Chen's correlation is applicable to deionised water, methanol, cyclohexane and pentane. For refrigerants (with Prandtl number  $Pr \gg 1$ ), Bennett and Chen (1980)'s recommended that the convective enhancement factor  $F$  is multiplied by  $Pr^{0.296}$ . Chen's correlation applies to saturated boiling, convective and axial flow, wall heat flux less than critical heat flux ( $q < CHF$ ) and vapour quality significantly less than 1 ( $x < 1$ ).

**Gungor and Winterton correlation:** Gungor and Winterton (1986) proposed a modified form of the Chen's correlation by replacing the convective enhancement factor  $F$  by a dimensionless expression which is a function of the boiling number ( $Bo$ ). The proposed correlation for the convective heat transfer coefficient is given by;

$$h_{cb} = h_l \left[ 1 + 3000Bo^{0.86} + \left( \frac{x}{1-x} \right)^{0.75} \left( \frac{\rho_l}{\rho_v} \right)^{0.14} \right] \quad 1.89$$

$h_l$  is determined using the superficial liquid velocity ( $j_l$ ) in the single-phase flow correlation.

Gungor's correlation is applicable to deionised water, refrigerants, ethylene and glycol. The correlation was developed for tube diameter in the range of  $2.95 \leq D \leq 32.00 \text{ mm}$  in horizontal, upward and downward channel flows. The correlation applies to saturated and subcooled boiling and system pressure in the range of  $1 \leq P_{system} \leq 202.6 \text{ mmHg}$ .

**Kandlikar correlation:** A correlation for saturated flow boiling in horizontal and vertical tubes was proposed by Kandlikar (1990) where it was assumed that the heat transfer coefficient is the larger value between the nucleate and convective heat transfer coefficients. The nucleate boiling heat

transfer coefficient is expressed as a function of boiling number ( $Bo$ ). The correlation for heat transfer coefficient is given by;

$$h = h_l [C_1 C_0^{C_2} + C_3 Bo^{C_4} F_K] \quad 1.90$$

$h_l$  is determined from single-phase turbulent correlations such as those of Dittus and Boelter (1930) or Gnielinski (1976).  $F_K$  is a constant which can be adapted to the working fluid and its value is between 1.2 and 1.4.  $C_0$  is the convection number, which determines the main contribution to the heat transfer and is given by;

$$C_0 = \left( \frac{1-x}{x} \right)^{0.8} \sqrt{\rho_v / \rho_l} \quad 1.91$$

For  $C_0 > 0.65$ ,  $C_1 = 0.6683$ ,  $C_2 = -0.2$ ,  $C_3 = 1058.0$ ,  $C_4 = 0.7$  and for  $C_0 < 0.65$ ,  $C_1 = 1.1360$ ,  $C_2 = -0.9$ ,  $C_3 = 667.2$ ,  $C_4 = 0.7$ .

Kandlikar's correlation applies to refrigerants, water, nitrogen and neon fluids; tube diameter range of  $4.6 \leq D \leq 32.0 \text{ mm}$ ; vapour quality range of  $0.001 \leq x \leq 0.987$ ; system pressure range of  $1.0 \leq P_{system} \leq 64.1 \text{ bar}$ ; and mass flux range of  $13 \leq G \leq 8179 \text{ kg/m}^2\text{s}$ .

**Liu and Winterton correlation:** Analysis of Liu and Winterton (1991) showed that the boiling number ( $Bo$ ) in the convective boiling heat transfer enhancement factor ( $F$ ) of previous correlations served the main purpose of enhancing forced convection with increasing vapour generation at the wall. This limits the application of these models to subcooled boiling. Liu and Winterton (1991) therefore proposed a model for heat transfer coefficient in which  $F$  was dependent on Prandtl number and independent of Boiling number. The correlation is given by;

$$h = \sqrt{(F h_l)^2 + (S h_{pool})^2} \quad 1.92$$

$h_l$  is determined from single-phase turbulent correlations such as those of Dittus and Boelter (1930) or Gnielinski (1976) using  $Re_{lo}$  (Eq. 1.66).

$$F = \left[ 1 + x Pr_l \left( \frac{\rho_l}{\rho_v} - 1 \right) \right]^{0.35} \quad 1.93$$

$$S = (1 + 0.055 F^{0.1} Re_l^{0.16})^{-1} \quad 1.94$$

$$h_{pool} = 55P_R^{0.12}q^{2/3}(-\log_{10} P_R)^{-0.55}M^{-0.5} \quad 1.95$$

$M$  is the molecular weight,  $P_R$  is the reduced pressure and  $h_{pool}$  is the nucleate boiling heat transfer coefficient of Cooper (1984). Liu's correlation is applicable to deionised water, refrigerants, ethylene and glycol. The correlation was developed for tube diameter in the range of  $2.95 \leq D \leq 32.00 \text{ mm}$ , in horizontal, upward and downward channel flows. The correlation applies to saturated and subcooled boiling and system pressure in the range of  $1 \leq P_{system} \leq 202.6 \text{ mmHg}$ .

**Kew and Cornwell correlation:** A correlation for heat transfer coefficient suited for flow boiling in the convective boiling dominant regime was proposed by Kew and Cornwell (1997). The heat transfer coefficient is a function of  $Re_{lo}$ ,  $Bo$  and vapour quality ( $x$ ) and is given by;

$$h = 30Re_{lo}^{0.857}Bo^{0.714}(1-x)^{0.143}\lambda_l/D \quad 1.96$$

Kew's correlation is applicable to refrigerants flowing in horizontal tube of diameter between 1.39 and 3.69 mm. The model can be applied to near-CHF conditions where partial dry-out occurs.

**Kim and Mudawar correlation:** A correlation was proposed by Kim and Mudawar (2013) after comparing several previous models and flow boiling data. Similar to previous models, the proposed model was developed by combining the contributions of nucleate and convective boiling. The model Kim and Mudawar (2013) is provided in Chapter 3 (journal article, Eqs. 30-32, pp120). This correlation is applicable to refrigerants flowing inside vertical tubes of diameter 4.5 to 6.50 mm with mass flux of 100 to 500 kg/m<sup>2</sup>s.

**Lu, Chen, Li and He Model:** Lu et al. (2017) proposed a modified version of Chen's model for flow boiling in vertical mini-channels. Unlike in Chen's model, where the convective heat transfer enhancement factor ( $F$ ) is a function of Martinelli parameter ( $X_{tt}$ ) alone, in this model,  $F$  is a function of both of Boiling number ( $Bo$ ) and Martinelli parameter ( $X_{tt}$ ). The idea here was to enhance the convective boiling term by the vapour generated in the layer adjacent to the wall. A confinement number term was also added to the nucleate boiling suppression factor ( $S$ ). The proposed model is given by;

$$h = \sqrt{((Fh_l)^2 + (Sh_{nb})^2)} \quad 1.97$$

$$F = 1 + 2.4 \times 10^4 Bo^{1.26} + 0.87 \left(1/X_{tt}\right)^{0.32}$$

$$h_{nb} = 0.00122 \left[ \frac{c p_l^{0.45} \lambda_l^{0.79} \rho_l^{0.49} g^{0.24}}{\sigma^{0.5} \rho_v^{0.24} h_{lv}^{0.24} \mu_l^{0.29}} \right] (T_w - T_{sat})^{0.24} (p - p_{sat})^{0.75}$$

$$S(X_{tt}) = \frac{1}{1 + 2.53 \times 10^{-6} \left( \frac{GD(1-x)F^{1.25}}{\mu_l} \right)^{1.14} + 1.75(N_{conf})^{0.3}}, \quad N_{conf} = \sqrt{\frac{\sigma}{g(\rho_l - \rho_v)D^2}}$$

Lu's correlation was developed for deionised water and applicable to tube diameters 2.15, 4.99 and 6.88 mm, vertical upward channel flow, saturated and subcooled boiling and mass flux range of  $300 \leq G \leq 1500 \text{ kg/m}^2\text{s}$ .

Figure 1.6 shows heat transfer coefficient in terms of vapour quality in a tube of 6 mm diameter with HFE7000 for the correlations presented above. For  $G = 50 \text{ kg/m}^2\text{s}$ , corresponding to laminar liquid flow and predominance of nucleate boiling, the predicted heat transfer coefficients for most of the correlations were fairly constant or decreased slightly with vapour quality. Furthermore, the correlations of Kandlikar (1990) and Lu et al. (2017), gave higher predictions relative to the other correlations. For  $G = 200 \text{ kg/m}^2\text{s}$ , corresponding to turbulent liquid flow and predominance of convective boiling, the predicted heat transfer coefficients fairly constant or increased with vapour quality. Furthermore, the correlation of Kandlikar (1990), gave higher predictions relative to the other correlations.

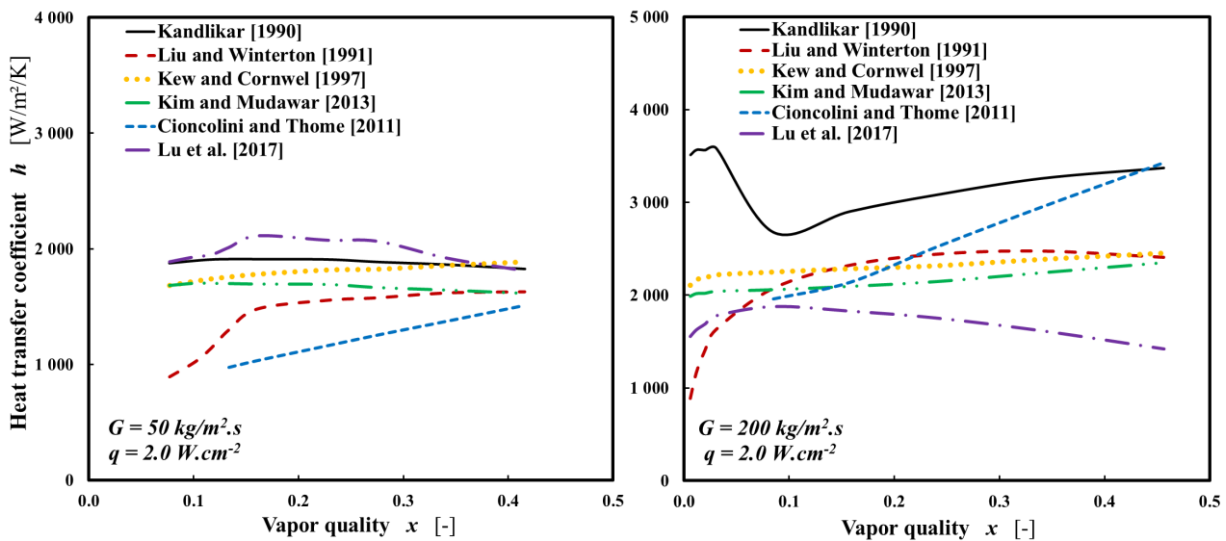


Figure 1.6. Comparison of various correlations for predicting flow boiling heat transfer coefficient for HFE7000 in the tube of 6mm diameter.

**Eddy viscosity models for annular flow:** A common approach in the prediction of saturated boiling heat transfer coefficient involves the use of eddy diffusivity in the liquid film. The heat transfer coefficient and the dimensionless temperature profile in the liquid film are predicted from Eq. 1.98 and Eq. 1.99 respectively.

$$h = \frac{q_w}{T_w - T_{sat}} = \frac{\rho_l C p_l u^*}{T_\delta^+} = \frac{\rho_l C p_l u^*}{\int_0^{\delta^+} \frac{q}{q_w} \left[ \frac{1}{Pr_l} \left( 1 + \frac{Pr_l}{Pr_t} \frac{\varepsilon_m}{\nu_l} \right) \right]^{-1} dy^+} \quad 1.98$$

$$T^+ = \int_0^{y^+} \frac{q}{q_w} \left[ \frac{1}{Pr_l} \left( 1 + \frac{Pr_l}{Pr_t} \frac{\varepsilon_m}{\nu_l} \right) \right]^{-1} dy^+ \quad 1.99$$

The dimensionless eddy viscosity ( $\varepsilon_m/\nu_l$ ) in Eqs. 1.98 and 1.99 are determined from theoretical (Chen et al., 2015; Fu and Klausner, 1997; Kim and Mudawar, 2014; Kim and Mudawar, 2013b, 2012b; Lee and Mudawar, 2019; Mudawwar and El-Masri, 1986; van DRIEST, 1956), or algebraic models (Cioncolini et al., 2009b; Cioncolini and Thome, 2011; Ohta, 2003). Details of theoretical eddy viscosity modelling is included in Chapter 4 (journal article). A heat transfer model was developed by Cioncolini and Thome (2011) from their algebraic eddy viscosity models (see journal article in Chapter 3, Eq. 27, pp120). Figure 1.6 shows heat transfer coefficient in terms of vapour quality for the correlation of Cioncolini and Thome (2011). In general, the heat transfer coefficient increased with vapour quality. The correlation is applicable to water, refrigerants and selected hydrocarbons, vertical and horizontal tube,  $1.03 \leq D \leq 14.4 \text{ mm}$ ,  $123 \leq G \leq 3925 \text{ kg/m}^2\text{s}$ ,  $0.19 \leq x \leq 0.94$ ,  $1.8 \leq q \leq 74 \text{ W/cm}^2$  and  $0.1 \leq P_{system} \leq 7.2 \text{ MPa}$ .

### 1.3 Experimental studies on Two-Phase Flows

Several investigations have been carried out to characterise flow boiling under different gravity conditions. These investigations have focused on the effects of gravity levels or flow orientation relative to earth-gravity on two-phase flow parameters such as bubble geometry, void fraction, heat transfer, pressure drop and interfacial wave structures. In general, both orientation to gravity and gravity levels have been shown to have significant influence on two-phase flows. Since the literature on two-phase flows and flow boiling in vertical pipe is very wide, this short review is far from being exhaustive and we have chosen to focus on the gravity effects on flow dynamics and heat transfers.



### 1.3.1 Experimental platforms

On ground, the effects of gravity have been studied by varying the orientation of the flow relative to gravity. In horizontal or inclined tubes, gravity tends to stratify the vapor/liquid flows or at least to induce some topological asymmetry. Even in a vertical configuration, experiments in upward ( $+1g$ ) and downward ( $-1g$ ) flow configurations point out significant differences in the flow hydrodynamics and heat transfers due to the gravity (Kharangate et al., 2016; Konishi and Mudawar, 2015). To investigate the effect of gravity levels on two-phase flows on ground, experiments have been carried out in centrifuges. Experiments in centrifuges provide hyper-gravity levels for long durations (Vlachou et al., 2019). Reduced gravity experiments have been carried out in drop tower, drop well, sounding rockets, parabolic flights and the international space station (ISS). These platforms provide different duration and levels of gravity. Drop towers and shafts produce gravity levels of  $\approx 10^{-5}g$  for a duration of 2 - 10 s by having the experimental setup undergo freefall above and below the ground level respectively. Sounding rockets produce high quality microgravity of  $\approx 10^{-5}g$  for a duration of 3 - 15 min during sub-orbital flights. Parabolic flights provide microgravity of the order of  $10^{-2}g$  for about 22 s. Although, drop towers and drop shafts provide high quality microgravity conditions, they have some disadvantages. These include, short duration of microgravity (resulting in the inability for the system to reach steady state), inability to manually interact with the setup during experimental runs, and requires several experimental runs to obtain sufficient data. Sounding rockets platform have limited experimental package carrying capacity. The key drawback in parabolic flights experiments is the low-quality microgravity and the *g-jitter* effect (the residual acceleration associated with flight manoeuvres). Compared to the aforementioned platforms, parabolic flights offer the following advantages; access by the experimentalist to the test facility; larger experimental package carrying capacity; and varying gravity test conditions ranging for microgravity to hyper-gravity. In recent time, experiments of the Japanese Space Agency JAXA have been performed for the study of flow boiling in a 4 mm diameter tube from 2017 to 2019. Experimental data are under evaluations (Inoue et al., 2021). A NASA experiment for studying flow boiling in a rectangular small channel has been launched to the ISS in August 2021 and should be operated until 2025 (Devahdhanush et al., 2022; Inoue et al., 2021). These experiments allow for the attainment of quasi-steady state conditions due to longer duration of microgravity. In the current work, the effect of gravity was investigated mainly on ground ( $+1g$  and  $-1g$ ) in addition to a limited range of experiments using parabolic flight (microgravity) with a new experimental device.

### **1.3.2 Effect of gravity on two-phase boiling flow**

Some literature reviews have been carried out which highlights the effect of gravity levels and flow orientation relative to gravity on two-phase flows. Ohta et al. (2002) highlighted key components of experimental facilities required for development of reliable reduced-gravity two-phase flow data base. Celata (2007) provided a brief review of the ground and microgravity experimental research of European Space Agency *ESA*. They highlighted the importance of parameters such as vapour quality and mass flux on microgravity heat transfer. Zhao (2010) summarised a series of flow boiling experiments carried out by the National Microgravity Laboratory/CAS (Chinese Academy of Science) involving ground tests and microgravity tests in drop towers and parabolic flight experiments. They proposed a semi-theoretical model based on Weber number for slug to annular flow transition. Di Marco (2012) analysed the influence of force fields on boiling performance under conditions of microgravity. They remarked that, consideration of flow patterns is essential for interpretation of various microgravity boiling behaviour. Baldassari and Marengo (2013)'s review focussed on defining suitable dimensionless numbers governing flow boiling in microchannel and microgravity. They highlighted the importance of Eötvös number which tends to zero when either gravity or channel diameter tends to zero. Narcy and Colin (2015) reviewed two-phase flows and flow boiling in tube experiments in microgravity and Konishi and Mudawar (2015) reviewed flow boiling investigations carried out in different flow orientations relative to gravity (horizontal, upward and downward flows).

#### **1.3.2.1 Bubble characteristics**

Bubble geometry results from a complex balance between buoyancy, surface tension, viscous and inertia forces (Bhagwat and Ghajar, 2017; Godbole et al., 2011). For a given fluid with constant surface tension, increase in liquid phase flow inertia (due to pressure gradient or gravity) promotes the detachment of nucleated bubbles from the wall. In general, the size of nucleated bubble at the heated wall have been reported to decrease with gravity levels from microgravity ( $0g$ ) through normal gravity ( $+1g$ ) to hyper-gravity ( $+1.8g$ ) (Lebon et al., 2019; Ma and Chung, 2001, 1998). Bubble size at detachment is also reported to reduce with mass flux and increase with heat flux depending on the level of subcooling (Lebon et al., 2019).

The size of entrained bubbles in the continuous liquid phase have also been reported to decrease with gravity levels from  $0g$  through  $+1g$  to  $+1.8g$  (Baltis et al., 2012; Celata and Zummo, 2009a; Luciani

et al., 2009; Narcy et al., 2014; Ohta, 1997; Westheimer and Peterson, 2001). Westheimer and Peterson (2001) further reported the absence of slug flow (or very large bubbles) in hyper-gravity conditions. In upward ( $+1g$ ), microgravity ( $0g$ ) and downward ( $-1g$ ) flows the drift velocities are positive, zero and negative respectively and the residence time of the bubbles in the bulk fluid increases from the former the latter. With increase in residence time of bubbles, there is increase in bubble size due to evaporation. The combination of buoyancy and liquid flow inertia influences the shape of bubbles (Bhagwat and Ghajar, 2012; Godbole et al., 2011). In normal gravity upward flow (concurrent buoyancy and pressure gradient forces), drift velocity is positive and entrained bubbles are disformed and elongated in the direction of flow (Figure 1.7.a-b). In microgravity flow (zero buoyancy force) there is zero drift between the phases and the entrained bubbles tend to be spherical (Figure 1.7.a-b). In normal gravity downward flow (opposing buoyancy and pressure gradient forces), the drift velocity is negative and the entrained bubbles also tend to elongate in the radial direction of the flow (Figure 1.7.a-b) (Lebon et al., 2019). It should be remarked that bubble size characteristics have also been strongly linked to degree of inlet subcooling (Lebon et al., 2019; Narcy et al., 2014; Saito et al., 1994).

Some investigations have been carried out with the view of classifying the dominant forces in flow boiling at various gravity levels (Baba et al., 2012; Ohta et al., 2013) and various flow orientation relative to gravity (Baba et al., 2012; Konishi and Mudawar, 2015). Such analyses were based on the Weber number ( $We$ ), Froude number ( $Fr$ ) and Bond number ( $Bo$ ) which represent ratios of inertia to surface tension, inertia to buoyancy and buoyancy to surface tension respectively. The focus of the aforementioned studies was on heat transfer coefficient and no conclusion on whether the same boundaries apply to bubble characteristics can be drawn. In general, the effect of gravity on bubble characteristics is reported to be negligible beyond certain critical vapour quality (Celata and Zummo, 2009) or mass flux (Narcy et al., 2014). Celata and Zummo (2009) reported a critical vapour quality of  $x \approx 0.3$  while Narcy et al. (2014) reported a critical mass flux of  $G = 540 \text{ kg/m}^2\text{s}$  for upward flow experiments carried out in 6 mm ID tubes.

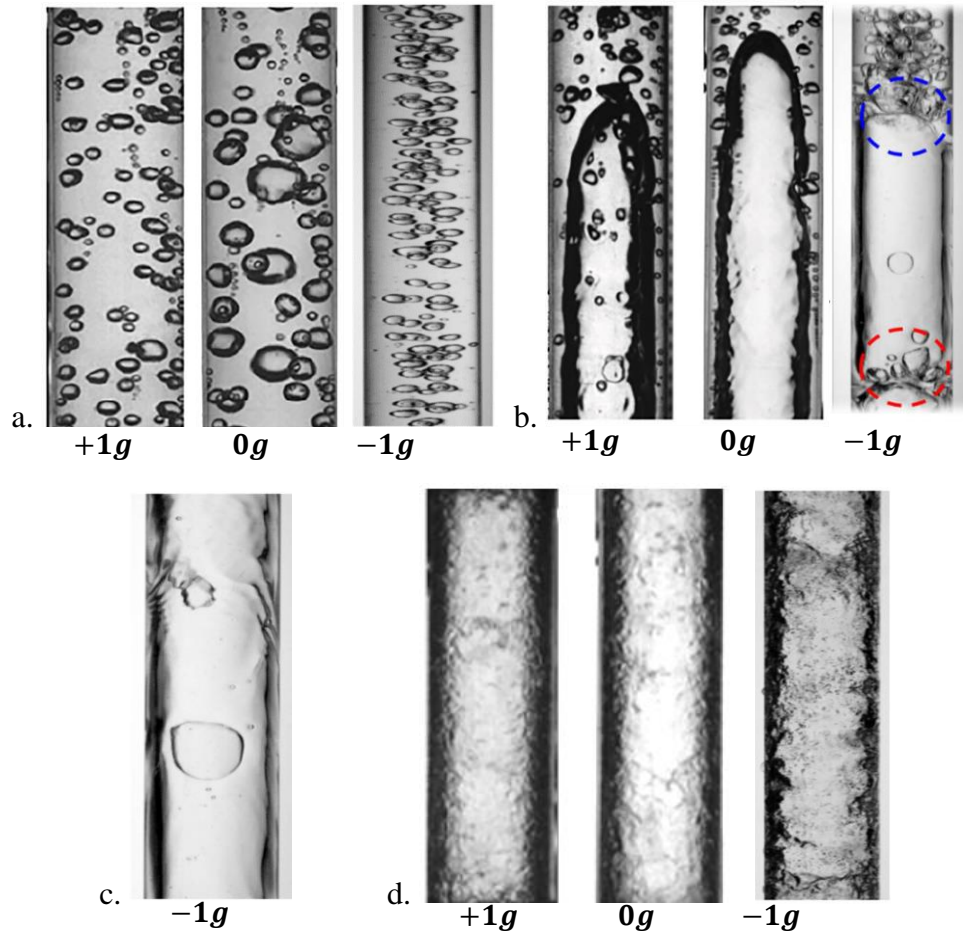


Figure 1.7. Flow patterns, a. bubbly flow b. slug flow c. Falling film flow d. Annular flow +1g and 0g (Narcy et al., 2014), -1g (Bhagwat and Ghajar, 2017).

### 1.3.2.2 Flow patterns and flow pattern transition

Bubble nucleation, bubble growth, bubble size at detachment and bubble coalescence all play significant roles in determining flow pattern and regime transition. Flow boiling flow pattern common to both normal- and micro-gravity in vertical tubes are bubbly flow, slug flow (or transitional flow), falling film flow (downward flow) and annular flow (Figure 1.7.). Bubbly flow occurs at low vapour quality especially at subcooled inlet conditions and low wall heat fluxes (Figure 1.7.a). Bubbles are nucleated at the heated wall (or enter at the inlet), grow in size (due to evaporation and/or coalescence), slide along the wall and detach (due to body force and liquid inertia). At higher wall heat flux or smaller subcooling more bubbles are nucleated at the wall. Transition to slug flow regime occurs when bubbles coalesce resulting in the formation of elongated cylindrical bubbles whose length increases with quality (Colin et al., 1991; Dukler et al., 1988). The elongated bubbles (Taylor bubbles) are bullet-shaped with smooth interface and their length scale is larger than pipe diameter

(Figure 1.7.b). Characteristics of the Taylor bubbles are similar in both normal ( $+1g$  and  $-1g$ ) and microgravity ( $0g$ ). However, the length of the Taylor bubble increases as drift velocity decrease from positive through zero to negative due to increase in residence time (evaporation). The smoothness of the interface of the Taylor bubbles increases in a similar way due to decrease in interfacial shear stresses from  $+1g$  through  $0g$  to  $-1g$ . Furthermore, the bubble nose becomes flatter due to changes in buoyancy relative to the mean flow from  $+1g$  to  $-1g$  (Godbole et al., 2011). The film thickness around the Taylor bubble is also dependent of gravity. The early detachment of bubbles in normal gravity ( $+1g$ ) relative to microgravity ( $0g$ ) results in higher concentration of small bubbles dispersed in the liquid surrounding the Taylor bubbles (Figure 1.7.b). Opposing gravity and pressure gradient forces inhibits bubble detachment from the wall in  $-1g$ -flow due to gravity. Furthermore, bubbles in the bulk fluid continue to grow in  $-1g$ -flow due to longer the residence time of the bubbles in the test section relative to  $+1g$ . Consequently, Taylor bubble size is generally larger in  $-1g$ -flow relative to  $+1g$ - and  $0g$ -flows. Transition from slug/churn to annular flow occurs when the inertia force in the Taylor bubbles overcomes the surface tension force at the bubble-liquid interface and surface tension draws the liquid to the wall. A thin liquid film forms on the wall and a vapour core occupies the centre of the tube (Figure 1.7.d). Roll waves (disturbance waves with amplitudes sometimes scaling with tube diameter) may also appear depending on the vapour quality (Dasgupta et al., 2017; Trejo-Peimbert et al., 2019). Though some conflicting reports exist, the liquid film thickness is mostly reported to be smaller in microgravity compared to normal gravity upward flow due to the effect of gravity on the liquid film. This would suggest an even thinner liquid film in downward flow. The smoothness (less roll waves) of the interface increases due to decrease in interfacial shear stresses from  $+1g$  through  $0g$  to  $-1g$  (Figure 1.7.d) (Bhagwat and Ghajar, 2012). In downward flow, if the liquid velocity ( $G/\rho_l$ ) at the entrance of the test section is lower than the bubble drift velocity, bubbles travel in opposite direction to the liquid and a steady state, flooding occurs. Under this condition, there is absence of bubbly and slug flow regimes and flooding results in the formation of the falling film regime. Falling-film regime is characterized by low liquid and low/moderate vapor velocities with the vapor core surrounded by a falling liquid film along the wall (Bhagwat and Ghajar, 2012; Godbole et al., 2011). The liquid film is characterized by ripples and the interface is relatively smooth (no roll waves) due to very low interfacial shear stresses. With increase in quality, transition from falling film to annular flow regime occurs. In the annular flow regime, liquid entrainment in the vapour core may also occur especially at high vapour quality and high mass fluxes. The frequency of

disturbance waves (where it is observed) depends on the interfacial shear stress which depends on the gravity conditions (Trejo-Peimbert et al., 2019).

Available models for predicting flow regime transitions include those based on critical void fraction, (Celata and Zummo, 2009a; Colin et al., 1991; Dukler et al., 1988; Mishima and Ishii, 1984; Usui, 1989), critical value of Weber number (Zhao and Rezkallah, 1993), Suratman number ( $Su = 1/Oh^2$ ,  $Oh = \sqrt{We}/Re$ ) (Jayawardena et al., 1997), bubble size evolution (Colin et al., 2008; Kamp et al., 2001; Takamasa et al., 2003). Celata and Zummo (2009a) provided flow pattern maps, which were representative of their microgravity data collected in a 6 mm tube (Figure 1.8a). Due to limited power available, annular flow was not observed in that work. Bubbly-slug flow transition occurred at higher void fraction than the 0.45 proposed by Dukler and co-workers (solid line in Figure 1.8a) in their gas-liquid adiabatic microgravity flow experiments. For boiling flow, they proposed a void fraction at bubbly-slug transition in microgravity of 0.74 and this was derived from the sphere-packing theory which underlines the arrangement of non-overlapping identical sphere in a volume. Beyond this limit, bubble coalesce resulting in the formation of Taylor bubbles. The maximum packing for spheres is given by;

$$\beta = \pi/3\sqrt{2} = 0.74048 \quad 1.100$$

A similar void fraction ( $\alpha \approx 0.7$ ) at bubbly-slug transition was reported in the Thesis of Narcy (2014) in both normal and microgravity. In that work, slug to annular flow pattern transition was reported at vapour quality of  $x_c \approx 0.14$ . Flow pattern maps which are representative of data (+1g and 0g) collected in 6 mm ID tube was also provided (Figure 1.8b). Bubbly-slug and slug-annular transition boundaries based on critical vapour qualities of  $x_c = 0.05$  and  $x_c = 0.14$  respectively was also proposed (Figure 1.8b). For +1g adiabatic flows, Mishima and Ishii (1984), proposed a bubbly-slug transition criteria from which was derived from the drift flux model of Ishii (1977) (see journal article in Chapter 3, Table 2, pp110). They also proposed criteria for slug-churn flow regime transition (Eq. 1.101). Their proposed slug-churn transition boundary coincided with their proposed slug-annular transition boundary at higher mass flux.

$$\alpha \geq 1 - 0.813 \left\{ \frac{(C_0 - 1)j + 0.35 \sqrt{\frac{(\rho_l - \rho_v)gD}{\rho_l}}}{j + 0.75 \sqrt{\frac{(\rho_l - \rho_v)gD}{\rho_l}} \left[ \frac{(\rho_l - \rho_v)gD^3}{\rho_l v_l^2} \right]^{1/18}} \right\}^{0.75} \quad 1.101$$

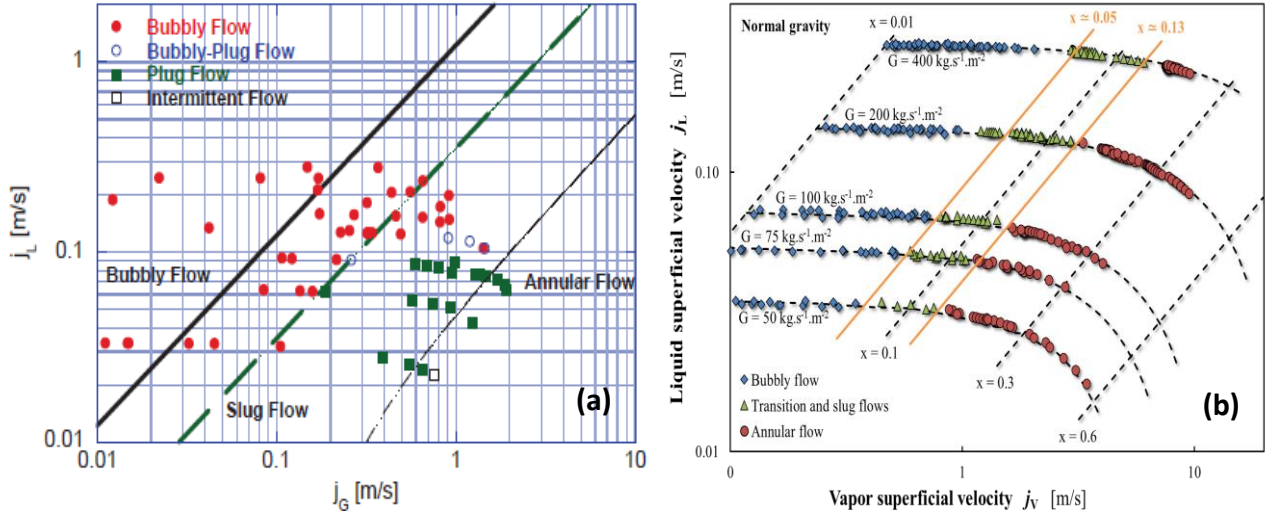


Figure 1.8. Flow pattern maps for upward boiling flows; a.  $0g$  (Celata and Zummo, 2009b), b.  $+1g$  (Narcy et al., 2014).

A few modelling studies have been carried out on the criteria for bubbly-slug transition in adiabatic gas-liquid downward flows (Bhagwat and Ghajar, 2015; Martin, 1976; Usui, 1989). Others proposed transition boundaries based on flow visualizations (Almabrok et al., 2016; Bhagwat and Ghajar, 2017). Usui (1989) proposed a criterion for bubbly-slug transition using the drift flux model (Eq. 1.25) with negative drift velocity ( $u_{\infty}$ ) as given by Harmathy (1960) (Eq. 1.26) (Figure 1.9a). A criterion for slug-falling film regime transition was proposed by Usui (1989) (Eq. 1.102). He also proposed a criterion for transition from falling film/slug flow to annular flow (Eq. 1.103). Bhagwat and Ghajar (2017) proposed flow pattern map in downward flow from flow visualisation obtained in 12.5 mmID tube (Figure 1.9b).

$$Fr_l = \left( K_1 - \frac{K_2}{Eo} \right)^{23/18} \quad 1.102$$

where  $K_1 = 0.92$ ,  $K_2 = 7$ ,  $Fr_l = \frac{j_l}{\sqrt{gD(\rho_l - \rho_v)/\rho_l}}$  and  $Eo = gD^2(\rho_l - \rho_v)/\sigma$ .

$$Fr_l = 2.5(j_v/j_l)^{-2/3} \quad 1.103$$

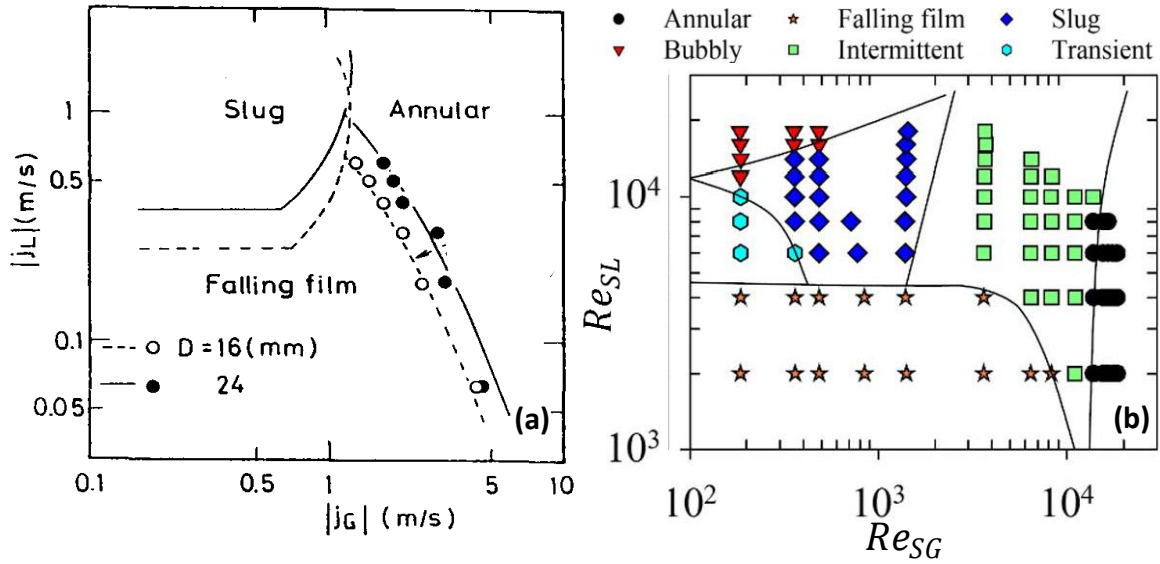


Figure 1.9. Flow pattern maps for downward adiabatic flows; a. (Usui, 1989), b. (Bhagwat and Ghajar, 2017).

### 1.3.2.3 Void fraction

At constant liquid and gas superficial velocities in the bubbly and slug flow regimes, void fraction increases from  $+1g$  through  $0g$  to  $-1g$  due to changes in residence time (evaporation) of bubbles in the test section. Brutin et al. (2013) reported higher void fraction in microgravity compared to hypergravity at low mass flux and low to moderated heat fluxes. For  $G = 124 \text{ kgs}^{-1}\text{m}^{-2}$  and  $q \leq 20 \text{ kWm}^{-2}$ , the difference between the void fraction in  $0g$  and  $1.8g$  increased from inlet to outlet and the evolution of void fraction in both cases were fairly linear. At higher heat flux, the void fraction characteristics remained qualitatively the same except for the non-linear evolution of void fraction. The difference in void fraction for both gravity levels was associated with difference in bubble size and bubble coalescence frequency. The higher void fraction in  $0g$  also yielded thinner annular liquid film at the wall compared to  $1.8g$  thereby influencing the two-phase heat transfer characteristics. Narcy et al. (2014) and Trejo-Peimbert et al. (2019) reported lower void fraction (Figure 1.10a) and larger annular liquid film thickness in normal gravity ( $+1g$ ) than in microgravity.



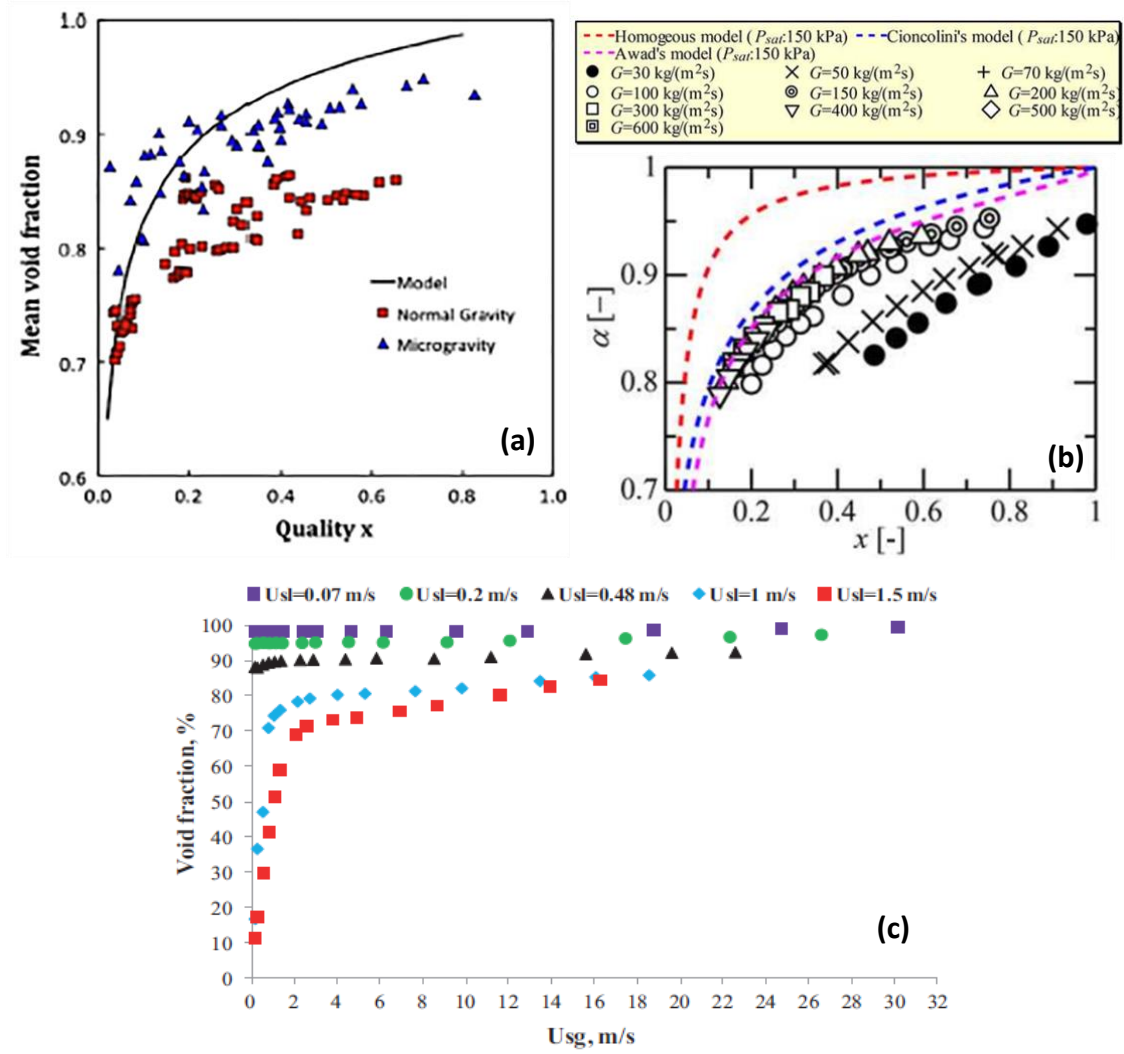


Figure 1.10. Evolution of average void fraction with vapour quality. a.  $+1g$  and  $0g$  (Narcy et al., 2014), b.  $+1g$  (Gomyo and Asano, 2016), c.  $-1g$  (Almabrok et al., 2016) .

Void fraction is also dependent on mass flux or mixture Reynolds number for  $+1g$  and  $-1g$  (Almabrok et al., 2016; Bhagwat and Ghajar, 2012; Gomyo and Asano, 2016). This is due to the contribution of the drift velocity ( $u_{\infty}$ ) to void fraction as given in the drift flux model (Eq. 1.25). At constant vapour quality, void fraction increases with mass flux in upward flow and decreases with mass flux in downward flows. The dependence of void fraction on mass flux becomes negligible at high mass fluxes or high vapour quality. Measurements of void fraction using capacitance probes were carried out for upward flow in 0.5, 1.1, 2.0 and 4.0 mmID tubes by Gomyo and Asano (2016). The mass flux range was  $30 < G < 600 \text{ kg}/(\text{m}^2\text{s})$  and the fluid used was FC-72. They reported a strong dependence of void fraction on mass flux (Figure 1.10b). Almabrok et al. (2016) measured the

void fraction of air-water downward flow in a 101.6 *mmID* tube. They reported a dependence of void fraction on liquid superficial velocity at constant gas superficial velocity (Figure 1.10c).

### 1.3.2.3 Pressure drop and shear stresses

Accurate determination of flow boiling pressure drop is important for understanding of the effect of gravity on flow boiling. Pressure drop in flow boiling is a combination of frictional, gravitational and acceleration components. In horizontal and microgravity conditions the gravitational term is negligible and at low to moderate heat fluxes, in short test sections, the changes in the acceleration component may be negligible. Gravity, however, induces phase stratification in horizontal flows for  $+1g$  and  $+1.8g$ . Fang et al., 2012 and Fang and Xu (2013) carried out reviews of two-phase frictional pressure drop investigations in normal and microgravity conditions. In general, for horizontal flows, frictional pressure gradient ( $dp_F$ ) was reported to be higher in microgravity than in normal gravity (Chen et al., 1991; Colin et al., 1991; Colin and Fabre, 1995; Heppner et al., 1975). According to Hurlbert et al. (2004) annular adiabatic two-phase frictional pressure drop varies as a function of  $1/g^{0.39}$ . In vertical upward adiabatic two-phase flow, Zhao and Rezkallah (1995) report similar two-phase frictional pressure gradient in both  $0g$  and  $+1g$ , while Han and Gabriel (2006) reported that  $dp_{F_{0g}} < dp_{F_{1g}}$  at high mass flux and  $dp_{F_{0g}} > dp_{F_{1g}}$  at low mass flux.

Studies of the effect of flow orientation relative to gravity or gravity level on flow boiling pressure drop have also received attention. Kharangate et al. (2016) carried out pressure drop measurements in upward, downward and horizontal channel ( $5.0\text{ mm} \times 2.5\text{ mm}$ ) using FC-72 as working fluid. The reported equivalent total pressure drops in upward and downward flows were greater than that of horizontal flow. Brutin et al. (2013) carried out flow boiling experiments in rectangular channel of  $6 \times 0.454\text{ mm}^3$  (hydraulic diameter  $0.84\text{ mm}$ ) using HFE-7100 as working fluid. Heating was done using a  $0.4\text{ mm}$  copper wire inside a cement rod of dimension  $16 \times 10 \times 70\text{ mm}$  and heat flux and mass flux were in the range  $15 \leq q \leq 55\text{ kWm}^{-2}$  and  $30 \leq G \leq 248\text{ kgs}^{-1}\text{m}^{-2}$ . They reported increased frictional pressure drop with increase in gravity level and this was associated with decrease in void fraction with gravity level which results in increased liquid volume fraction and subsequently enhanced frictional pressure gradient (Figure 1.11). In  $1.8g$ , the frictional pressure gradient was about 1.3 times that of  $1g$ , while it was half of that value in  $\mu g$ . Narcy (2014) carried out measurement of pressure drop in flow boiling but in an adiabatic section of the experimental setup and also computed wall and interfacial shear stresses. Frictional pressure gradients in both microgravity and normal

gravity increased with vapour quality. At low mass flux, where gravity effect was prevalent, the frictional pressure drop was higher in normal gravity compared to microgravity. At higher mass flux, both frictional pressure losses converge. The implication of these results is higher wall shear stresses in normal gravity relative to microgravity at low mass fluxes. At high mass flux, there was inadequate data from which to draw a conclusion on the effect of gravity on wall shear stress. However, the limited data showed limited influence of gravity on wall shear stress for mass fluxes above  $200 \text{ kg/m}^2\text{s}$  (Narcy, 2014). It has been reported that there is significant difference between wall shear stress in adiabatic section of a boiling flow and that in the heated section itself, especially in the nucleate boiling regime (Layssac, 2018). Bubble nucleation at the heated wall in boiling flows alters the velocity profile close to the wall which in turn modifies the wall shear stress. Quantification of the effect of wall heat flux on wall shear stress is limited. Furthermore, data on frictional pressure gradient in the diabatic section of downward flows are lacking in literature.

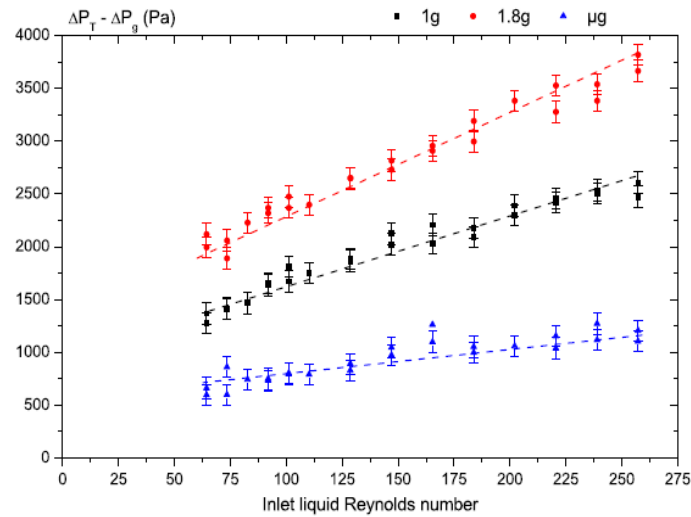


Figure 1.11. Frictional pressure gradient at different gravity levels (Brutin et al., 2013).

Gravity also influences interfacial shear stresses due to changes in relative velocity of the phases. In the parabolic flight flow boiling experiments of Ohta (1997), they reported an increased transparency in the liquid film of annular flow regime in microgravity and attributed this to lower shear stresses relative to normal and hypergravity. At low heat flux and high vapour quality in the annular flow regime, it was stated that the influence of shear forces on the liquid film exceeds that of gravity thereby suppressing gravitation effect on the hydrothermal characteristics. At all mass fluxes ( $50 - 400 \text{ kg/m}^2\text{s}$ ) and vapour quality ( $0 - 0.8$ ), Narcy (2014) reported higher interfacial shear stress in normal gravity upward flow compared to microgravity.

### 1.3.2.4 Disturbance (roll) waves

Interfacial structures in annular two-phase flows are linked to the interfacial shear stress. Parameters of interest such as wave velocity, wave frequency and wave amplitude have mainly been investigated in adiabatic gas-liquid flows (Azzopardi, 1986; Barbosa et al., 2003; Dasgupta et al., 2017) for the prediction of liquid droplet entrainment. Measurement of wave parameters in flow boiling are limited especially in downward flows. In characterising the disturbance waves associated with annular flows, Trejo-Peimbert et al. (2019) reported higher wave velocity and lower wave frequency in microgravity ( $0g$ ) compared to normal gravity ( $+1g$ ). The lower wave velocity in  $+1g$  can be attributed to the downward pull of gravity on the roll waves in  $+1g$  resulting in reduced wave velocity. The lower wave frequency in  $0g$  relative to  $+1g$  is due to lower interfacial shear stress in the former. In the work of Trejo-Peimbert et al. (2019), velocity and frequency of disturbance waves were obtained from space-time plots of flow visualisation at the centreline of the tube (Figure 1.12a). Similar report of higher wave velocity in  $0g$  relative to  $+1g$  was reported by Asano et al. (2019) (Figure 1.12b).

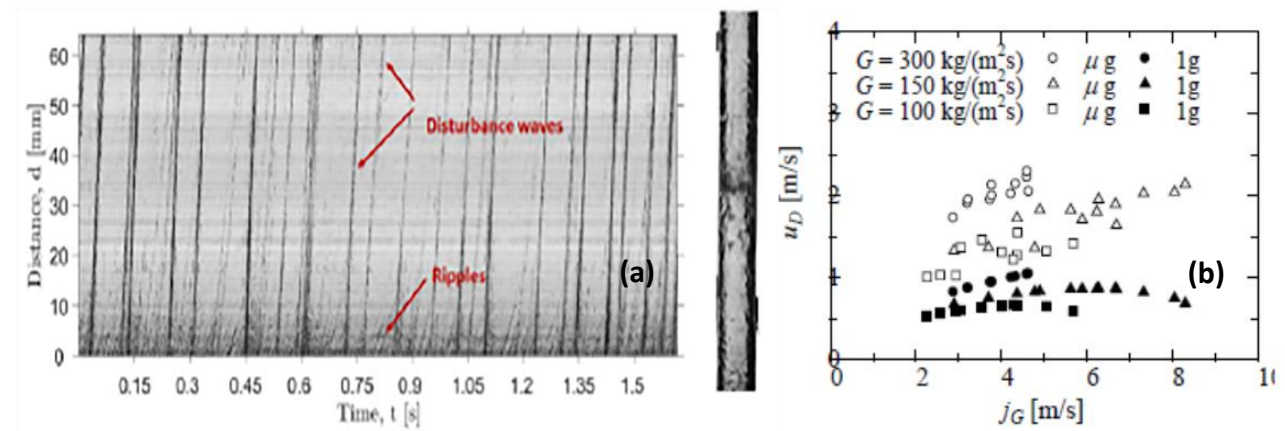


Figure 1.12. a. Space-time plots of flow structure, right: corresponding flow visualisation (Trejo-Peimbert et al., 2019), b. wave velocity versus vapour superficial velocity (Asano et al., 2019).

### 1.3.2.5 Flow boiling heat transfer

Heat transfer under various gravity conditions has been studied in both subcooled and saturated boiling conditions. Review articles provide very useful correlations and data in the nucleate and convective boiling regimes (Cioncolini and Thome, 2011; Kandlikar, 1990; Kim and Mudawar, 2013b). In general, parametric studies have focussed on the evolution of heat transfer coefficient with mass flux, heat flux, and vapour quality. Regardless of the flow configuration relative to gravity or gravity level, it has been established that heat transfer effectiveness increases with mass flux

(Figure 1.13). Though most of the reported experimental data show increased heat transfer with increase in mass flux, the trend of this increase differs in various reports, even for the same flow pattern. Available experimental data for vertical upward flow suggest that flow boiling heat transfer also increases with wall heat flux (Figure 1.13), especially in the nucleate boiling regime (Baba et al., 2012; Lebon et al., 2019; Narcy, 2014). Below critical heat flux and in the convective boiling dominant regime, saturated flow boiling heat transfer generally increases with vapour quality and this behaviour becomes independent of flow direction at higher vapour quality and low heat flux (Baba et al., 2012; Konishi and Mudawar, 2015; Lebon et al., 2019). The increased heat transfer with increase in vapour quality is the result of higher turbulent mixing and thinner annular liquid film. Overall, existing data suggest that the dependence of flow boiling heat transfer on either of these parameters is implicit.

In the subcooled and/or nucleate boiling regime(s) reports on the effect of flow direction relative to gravity on flow boiling heat transfer are limited. In the work of Baba et al. (2012), which was done using FC-72 inside 0.51 mm tube, higher heat transfer coefficient was reported in downward flows relative to upward flows  $h_{-1g} > h_{+1g}$  (Figure 1.14). Kharangate et al. (2016), in their channel (5.0 mm  $\times$  2.5 mm) flow measurements, using FC-72, reported equivalent heat transfer coefficient in both upward and downward flows  $h_{-1g} \approx h_{+1g}$ . With regards to the effect of gravity levels, available results are rather conflicting. Luciani et al. (2009, 2008) and Lui et al. (1994) reported higher heat transfer coefficient in 0g relative to +1g in their parabolic flight and ground experiments ( $h_{0g} > h_{1g}$ ). Similar result was reported by Baltis et al., (2012) for  $G \geq 150 \text{ kg/m}^2\text{s}$  ( $D = 6 \text{ mm}$ ,  $h_{0g} > h_{1g}$ ). However, they reported lower heat transfer coefficient in 0g relative to +1g for  $G \leq 100 \text{ kg/m}^2\text{s}$ . On the other hand, Ohta (1997) and Saito et al. (1994) both reported similar heat transfer in 0g and +1g ( $h_{0g} \approx h_{1g}$ ). Other investigations reported higher heat transfer coefficient in +1g relative to 0g (Celata, 2007; Konishi et al., 2015; Trejo-Peimbert et al., 2019).

In the saturated and/or convective boiling regime(s), the limited studies report little or no influence of gravity on the heat transfer coefficient. While Baba et al. (2012) reported slightly higher heat transfer in downward flow relative to upward flow, Kharangate et al. (2016) reported similar heat transfer coefficient in both flow directions ( $h_{-1g} \approx h_{+1g}$ ). They also reported equivalent heat transfer coefficient for all inclinations for  $G \geq 800 \text{ kg/m}^2\text{s}$ . With respect to the effect of gravity levels on heat transfer in the convective boiling dominant regime, Celata (2007) and Luciani et al. (2009, 2008)

reported similar heat transfer in  $0g$  and  $+1g$  ( $h_{0g} \approx h_{1g}$ ). However, Ohta (1997) reported lower heat transfer coefficient in microgravity relative to normal gravity.

Table 1.4 provides a summary of selected works showing the influence of various parameters and gravity on flow boiling heat transfer. In general, the heat transfer coefficient is influenced by mass flux, heat flux, vapour quality and gravity.

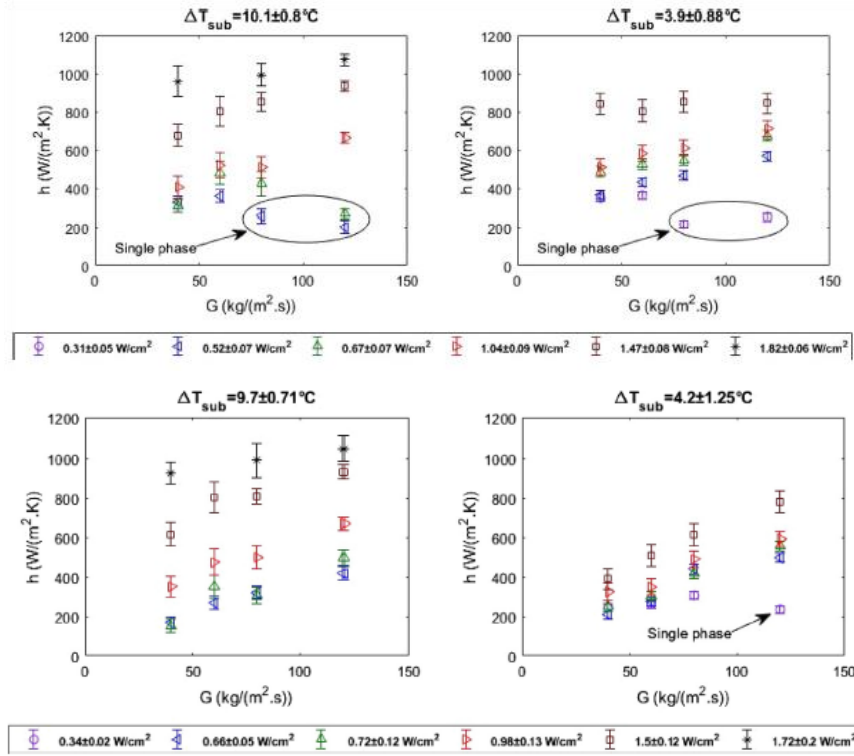


Figure 1.13. Heat transfer evolution with mass and heat flux  $+1g$  (top),  $0g$  (bottom): (Lebon et al., 2019).

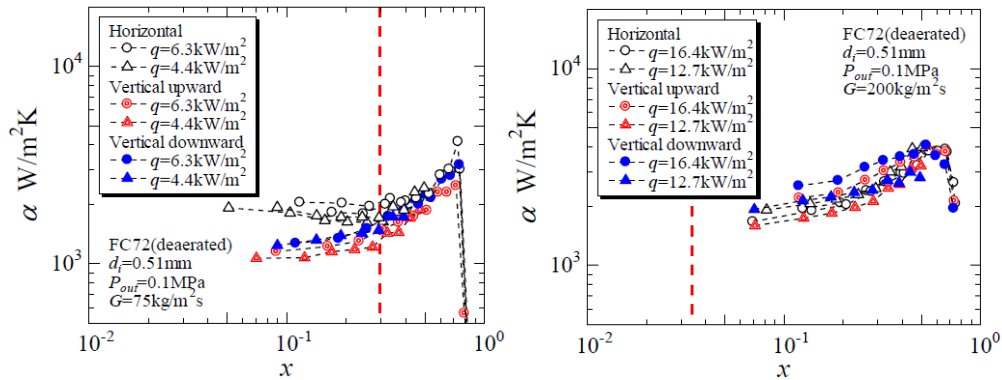


Figure 1.14. Evolution of heat transfer coefficient with vapour quality for various flow orientations relative to gravity (Baba et al., 2012).

Table 1.4. Summary of investigations on heat transfer coefficient.

Author(s)	Test fluid and test section	Test conditions	Calculated Froude and Reynolds number	Heat transfer coefficient (h)			
				Mass flux	Heat flux	Vap. qual.	Gravity (g)
(Lui et al., 1994)	R113; vertical pipe flow; $D = 12 \text{ mm}$ ; parabolic flight and ground experiments	$230 \leq G \leq 840 \text{ kg/m}^2\text{s}$ ; $q = 1.7 \text{ W/cm}^2$ ; subcooled boiling	$0.44 \leq Fr_{lo} \leq 1.62$ $5,000 \leq Re_{lo} \leq 20,000$	-	-	-	$h_{0g} > h_{1g}(NB)$
(Saito et al., 1994)	Distilled water; horizontal channel flow; $25 \times 25 \text{ mm}$ ; parabolic flight and ground experiments	$36 \leq G \leq 250 \text{ kg/m}^2\text{s}$ ; $5.3 \leq q \leq 18.6 \text{ W/cm}^2$ ; subcooled boiling	Horizontal flow	$\updownarrow$	$\uparrow$	$\uparrow$	$h_{0g} \approx h_{1g}(NB)$
(Ohta, 1997)	R113; vertical upward flow; $D = 8 \text{ mm}$ ; parabolic flight and ground experiments	$150 \leq G \leq 600 \text{ kg/m}^2\text{s}$ ; $0.5 \leq q \leq 15 \text{ W/cm}^2$ ; subcooled and saturated boiling	$0.35 \leq Fr_{lo} \leq 1.41$ $2,400 \leq Re_{lo} \leq 10,000$	-	-	-	$h_{0g} \approx h_{1g}(NB)$ $h_{0g} < h_{1g}(CB)$
(Celata, 2007)	Test fluid, FC-72; vertical upward pipe flow; $D = 2, 4, \text{ and } 6 \text{ mm}$ ; parabolic flight ground experiments	$47 \leq G \leq 570 \text{ kg/m}^2\text{s}$ ; $4.8 \leq q \leq 10 \text{ W/cm}^2$ ; subcooled boiling	$0.11 \leq Fr_{lo} \leq 2.5$ $200 \leq Re_{lo} \leq 8,000$	-	-	-	$h_{0g} < h_{1g}(NB)$ $h_{0g} \approx h_{1g}(CB)$
(Luciani et al., 2009, 2008)	Test fluid, HFE-7100; vertical upward channel flow; $D_h = 0.49, 0.84, 1.18 \text{ mm}$ ; parabolic flight ground experiments	$900 \leq G \leq 21000 \text{ kg/m}^2\text{s}$ ; $q \leq 3.3 \text{ W/cm}^2$ ; subcooled and saturated boiling	Microchannel	-	-	$\downarrow$	$h_{0g} > h_{1g}(NB)$ $h_{0g} \approx h_{1g}(CB)$

(Baltis et al., 2012)	Test fluid, FC-72; vertical upward pipe flow; $D = 2, 4, \text{ and } 6 \text{ mm}$ ; parabolic flight and ground experiments	$47 \leq G \leq 570 \text{ kg/m}^2\text{s}$ ; $4.8 \leq q \leq 10 \text{ W/cm}^2$ ; subcooled boiling	$0.11 \leq Fr_{lo} \leq 2.5$ $200 \leq Re_{lo} \leq 8,000$	-	-	-	$h_{0g} < h_{1g} (G < 100 \text{ kg/m}^2\text{s})$ $h_{0g} \geq h_{1g} (G \geq 150 \text{ kg/m}^2\text{s})$ (NB)
(Baba et al., 2012)	Test fluid, FC-72; vertical upward and vertical downward flow; $D = 0.51 \text{ mm}$ ; ground experiments	$50 \leq G \leq 200 \text{ kg/m}^2\text{s}$ ; $0.26 \leq q \leq 1.6 \text{ W/cm}^2$ ; subcooled and saturated boiling	Microchannel	↑	↑	↑	$h_{-1g} > h_{+1g}$ (NB and CB)
(Narcy et al., 2014)	Test fluid, HFE-7000; vertical upward pipe flow; $D = 6 \text{ mm}$ ; parabolic flight and ground experiments	$50 \leq G \leq 400 \text{ kg/m}^2\text{s}$ ; $0.5 \leq q \leq 3.5 \text{ W/cm}^2$ ; subcooled and saturated boiling	$0.15 \leq Fr_{lo} \leq 1.22$ $880 \leq Re_{lo} \leq 7,200$	↑	↑	↑	$h_{0g} < h_{1g} \text{ (NB)}$ $h_{0g} \approx h_{1g} \text{ (CB)}$
(Konishi et al., 2015)	Test fluid, FC-72; horizontal channel flow; $5.0 \times 2.5 \text{ mm}$ ; parabolic flight	$220 \leq G \leq 3350 \text{ kg/m}^2\text{s}$ ; $5 \leq q \leq 40 \text{ W/cm}^2$ ; subcooled boiling	$0.87 \leq Fr_{lo} \leq 13.7$ $1,200 \leq Re_{lo} \leq 20,000$	↑	↓	-	$h_{0g} \leq h_{1g} \text{ (NB)}$
(Kharangate et al., 2016)	Test fluid, FC-72; vertical upward and vertical downward flow; $5 \times 2.5 \text{ mm}$ channel; ground experiments	$180 \leq G \leq 2030 \text{ kg/m}^2\text{s}$ ; $8 \leq q \leq 20 \text{ W/cm}^2$ ; subcooled and saturated boiling	$0.71 \leq Fr_{lo} \leq 8.0$ $1,000 \leq Re_{lo} \leq 12,000$	↑	↑	↑	$h_{-1g} \approx h_{1g}$ (NB and CB)
(Iceri et al., 2017)	Test fluid, perfluoro-hexane; horizontal flow; $D = 4 \text{ mm}$ ; parabolic flight	$115 \leq G \leq 323 \text{ kg/m}^2\text{s}$ ; $0.32 \leq q \leq 4.1 \text{ W/cm}^2$ ; subcooled boiling	Horizontal flow	↑	↓	-	$h_{0g} \geq h_{1g}$ $\geq h_{1.8g} \text{ (NB)}$



(Lebon et al., 2019)	Test fluid, HFE-7000; vertical upward pipe flow; $D = 6 \text{ mm}$ ; parabolic flight	$40 \leq G \leq 120 \text{ kg/m}^2\text{s}$ ; $0.25 \leq q \leq 1.85 \text{ W/cm}^2$ ; subcooled boiling	$0.12 \leq Fr_{lo} \leq 0.36$ $700 \leq Re_{lo} \leq 2,100$	↑	↑	-	$h_{0g} < h_{1g}$ $< h_{1.8g}(NB)$
(Trejo-Peimbert et al., 2019)	Test fluid, HFE-7000; vertical upward pipe flow; $D = 6 \text{ mm}$ ; parabolic flight and ground experiments	$50 \leq G \leq 400 \text{ kg/m}^2\text{s}$ ; $0.5 \leq q \leq 3.0 \text{ W/cm}^2$ ; subcooled and saturated boiling	$0.15 \leq Fr_{lo} \leq 1.22$ $880 \leq Re_{lo} \leq 7,200$	↑	-	↑	$h_{0g} < h_{1g}(NB)$ $h_{0g} \approx h_{1g}(CB)$
↑ Increase   ↓ Decrease   ↕ Increased and/or decreased   - Effect not reported							

To examine the effect of gravity on heat transfer coefficient, the Froude ( $Fr_{lo} = \sqrt{G^2/\rho_l^2 gD}$ ) and Reynolds number ( $Re_{lo} = GD/\mu_l$ ) ranges for selected studies in vertical millimetric tubes/channels were calculated from the flow conditions as well as the fluid properties (Table 1.3). Although the  $Fr_{lo}$  and  $Re_{lo}$  were not sufficient to classify the reported heat transfer into gravity-dependent and gravity-independent regimes, gravity dependence was mainly reported in the nucleate boiling (NB) dominant regime even at high value of  $Fr_{lo}$  close to 13 reported in Konishi et al. (2015). The reported results suggest that, for  $Fr_{lo} \leq 13.7$ , if the heat flux (or wall superheat) is high enough for heterogenous nucleation at the wall, the heat transfer may show some degree of gravity dependence. However, at sufficiently high  $Fr_{lo}$ ,  $Re_{lo}$  or  $x$ , the mean diameter and frequency of detaching bubbles has been reported to become independent of gravity (Celata and Zummo, 2009). This has led some researchers to propose criteria for gravity-dependence based on the mixture Froude number (Baba et al., 2012; Ohta et al., 2013; Reynolds, 1964)

Reynolds (1964), defined the boundary between body force dominated and inertia force dominated at mixture Froude number of  $Fr = 1$  (Eq. 1.104); the boundary between surface tension dominated and inertia dominated at mixture Weber number of  $We = 1$ ; and the boundary between surface tension dominated and body force dominated at Bond number of  $Bo = 1$  (Figure 1.15). In this regime classification,  $Fr > 1$  correspond to gravity-independent regime. More recent studies have reported gravity dependence at higher mixture Froude number. Baba et al. (2012) defined the boundary between body force dominated and inertia force dominated at mixture Froude number of  $Fr = 4$  (Eq. 1.104); the boundary between surface tension dominated and inertia dominated at mixture Weber number of  $We = 5$ ; and the boundary between surface tension dominated and body force dominated at Bond number between  $0.033 \leq Bo \leq 0.55$ . According to them, the effect of flow orientation relative to gravity on flow boiling heat transfer is negligible for  $Fr \geq 4$  (Figure 1.15).

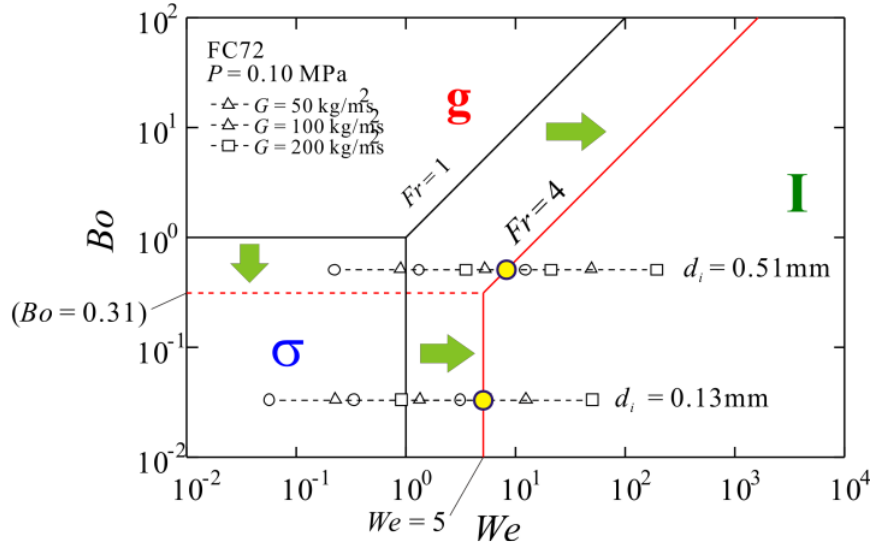


Figure 1.15. Dominant force regime in flow boiling (Baba et al., 2012).

$$Fr = \sqrt{\frac{We}{Bo}} = \frac{G}{\sqrt{\rho_m(\rho_l - \rho_v)gD}} \quad 1.104$$

where  $\rho_m = \frac{1}{x/\rho_v + (1-x)/\rho_l}$ ,  $Bo = \frac{(\rho_l - \rho_v)gD^2}{\sigma}$  and  $We = \frac{G^2 D}{\rho_m \sigma}$

Figure 1.16 show plots of calculated mixture Froude number versus vapour quality for selected fluids flowing inside 6 mmID tubes. Going by the criteria of Baba et al. (2012) (i.e.  $Fr \geq 4$ ), the lowest mass flux and corresponding quality for which gravity effect become negligible are  $G \geq 400 \text{ kg/m}^2\text{s}$ ,  $x = 0.8$  (HFE7000),  $G \geq 600 \text{ kg/m}^2\text{s}$ ,  $x = 0.6$  (FC72),  $G \geq 400 \text{ kg/m}^2\text{s}$ ,  $x = 0.7$  (R113),  $G \geq 100 \text{ kg/m}^2\text{s}$ ,  $x = 0.6$  (Water).

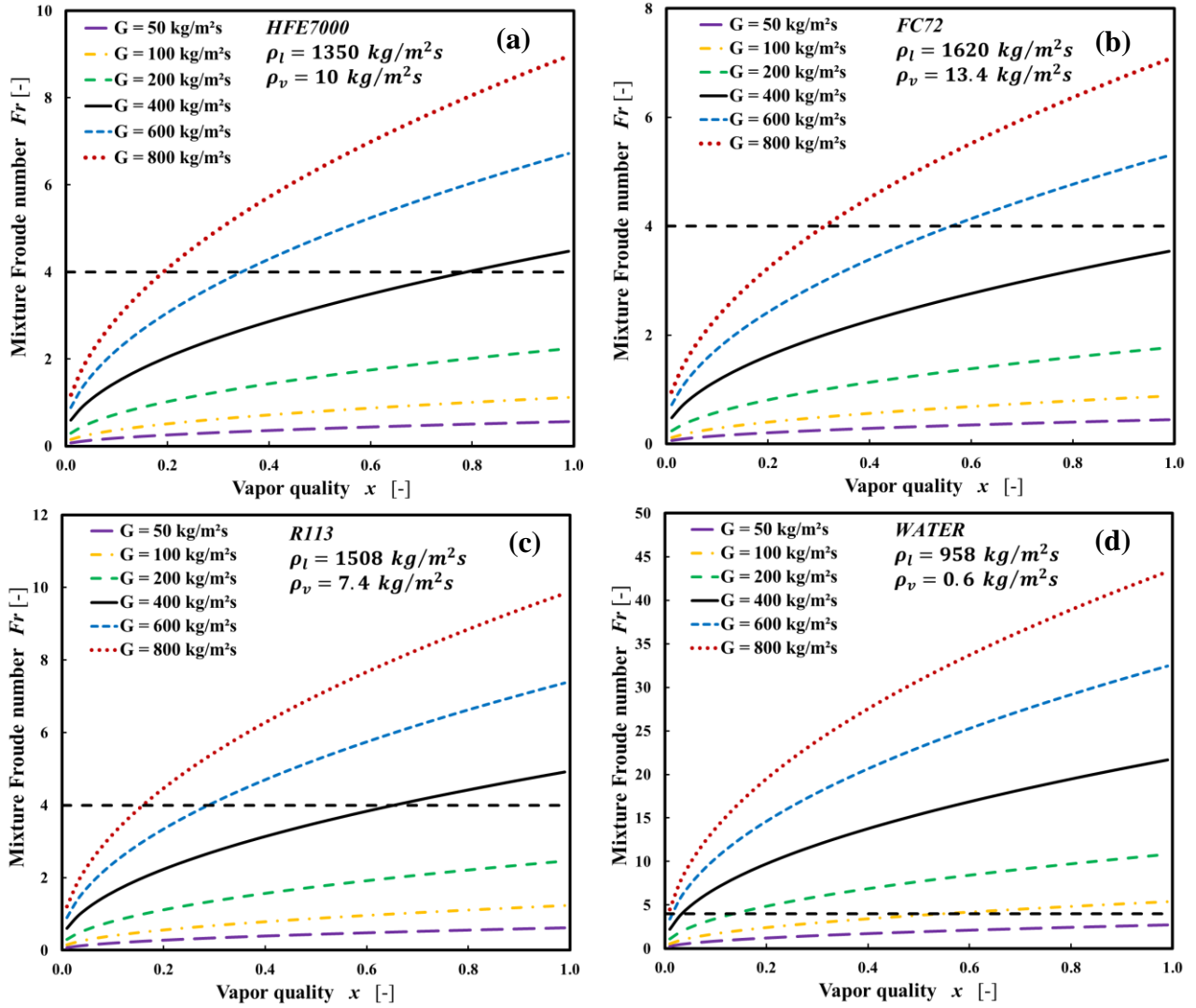


Figure 1.16. Gravity dependent ( $Fr < 4$ ) and gravity independent ( $Fr \geq 4$ ) regimes.

Ohta et al. (2013) proposed a flow boiling regime map based on experimental observations from selected studies (Figure 1.17). Gravity dependence was reported mainly in the nucleate boiling (NB) regime and at low to intermediate mass fluxes. Interestingly, clear conclusion on the effect of gravity could only be drawn at low heat flux and moderate vapour quality.

		Low $x$	Moderate $x$	High $x$
High $G$		NB	TFC	TFC
Low $G$	High $q$	NB	NBA	NBA
	Low $q$	NB	TFC	TFC
Extremely low $G$		NB	NBA	NBA

$G$	: Mass velocity
$x$	: Vapor quality
$q$	: Heat flux
NB	: Nucleate Boiling
TFC	: Two-phase Forced Convection
NBA	: Nucleate Boiling in Annular film






	: Gravity effect on liquid-vapor behavior
	: Possible gravity effect on liquid-vapor behavior
	: Gravity effect on heat transfer
	: Possible gravity effect on heat transfer
	: No gravity effect on liquid-vapor behavior and heat transfer

Figure 1.17. Gravity dependent and gravity independent flow boiling regimes (Ohta et al., 2013).

Lebon et al. (2019) proposed a regime map based on their experimental observations and measurement in  $+1g$ ,  $0g$  and  $-1g$  which shows gravity-dependent and gravity-independent regimes (Figure 1.18). For a given mass flux, a transition from gravity-dependent to gravity-independent region occurs if some threshold value of heat flux is attained. In the proposed map, there is an increase in the range of heat flux conditions of the gravity-dependent regime with decrease in subcooling. This was attributed to the increased buoyancy force associated with the larger bubbles observed at lower subcooling.

In conclusion, for the commonly used thermal fluids and at low to moderate wall heat flux ( $q \leq 15 \text{ W/cm}^2$ ), the transition criteria of  $Fr = 4$  provides a good estimate of boundary between gravity-dependent and gravity-independent flow boiling regimes (Baba et al., 2012). However, with increase in heat flux, the effect of gravity levels is negated at much lower values of  $Fr$  (Lebon et al., 2019; Ohta et al., 2013).

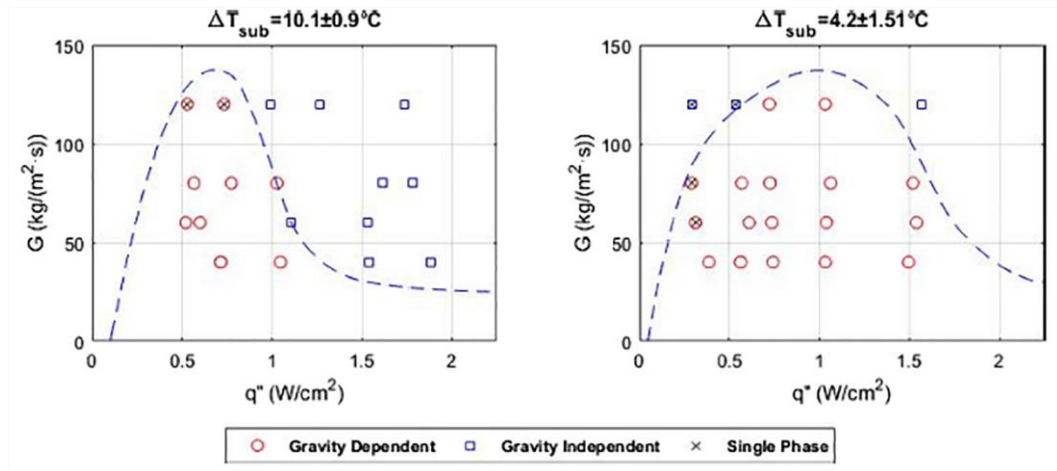


Figure 1.18. Gravity dependent regime for flow boiling heat transfer (Lebon et al., 2019).

### 1.3.2.6 Summary of the influence of gravity on flow boiling

A summary of literature survey on the influence of gravity on flow boiling is provided in Table 1.5 along with some remarks.

Table 1.5. Summary of the influence of gravity on various flow boiling quantities.

Parameter	Authors	Main conclusions	Remarks
Bubble characteristics	Ohta (1997) Ma and Chung (1998, 2001) Westheimer and Peterson (2001) Celata and Zummo (2009) Luciani et al. (2009) Godbole et al. (2011) Bhagwat and Ghajar (2012) Baltis et al. (2012) Narcy et al. (2014) Lebon et al. (2019)	<ul style="list-style-type: none"> <li>The size of nucleated and entrained bubbles generally decreased with increase in gravity levels.</li> <li>Bubble size was generally higher in downward flow (<math>-1g</math>) relative to upward flow (<math>+1g</math>).</li> <li>The effect of gravity level was limited to low mass flux and/or vapor quality.</li> </ul>	<ul style="list-style-type: none"> <li>Inadequate and inconsistent reports on the bubble and slug characteristics.</li> </ul>
Flow patterns	Martin, (1976) Usui et al. (1989) Colin et al. (1991) Dukler et al. (1988) Celata and Zummo (2009) Godbole et al. (2011) Bhagwat and Ghajar (2012, 2017)	<ul style="list-style-type: none"> <li>Similar flow patterns of bubbly, intermittent and annular occurs for gravity levels of <math>\mu g</math>, <math>+1g</math> &amp; <math>+1.8g</math>.</li> <li>An additional flow pattern called falling-film regime occurs in <math>-1g</math> flow.</li> </ul>	<ul style="list-style-type: none"> <li>Inconsistent reports on the criteria of flow pattern transition in flow boiling.</li> </ul>

	Narcy et al. (2014)		
Void fraction	Bhagwat and Ghajar (2012) Brutin et al. (2013) Narcy et al. (2014) Trejo-Peimbert et al. (2019)	<ul style="list-style-type: none"> <li>• Void fraction increases from <math>+1g</math> through <math>0g</math> to <math>-1g</math>.</li> <li>• Void fraction increases with <math>G</math> in <math>+1g</math>-flow and decreases with <math>G</math> in <math>-1g</math>-flow.</li> </ul>	<ul style="list-style-type: none"> <li>• Limited investigations.</li> <li>• No available thresholds of gravity dependence.</li> </ul>
Wall and interfacial shear stresses	Zhao and Rezkallah (1995) Ohta (1997) Han and Gabriel (2006) Brutin et al. (2013) Narcy (2014) Kharangate et al. (2016) Layssac (2018)	<ul style="list-style-type: none"> <li>• The influence of gravity level on wall shear stress depends on flow conditions.</li> <li>• Similar wall shear stress was reported in <math>+1g</math>- and <math>-1g</math>-flows.</li> <li>• The interfacial shear stress increases with gravity level.</li> </ul>	<ul style="list-style-type: none"> <li>• Inconsistent reports and limited experimental and modelling studies particularly on the effect of flow orientation.</li> </ul>
Wave structures	Asano et al. (2019) Trejo-Peimbert et al. (2019)	<ul style="list-style-type: none"> <li>• Mean roll wave velocity decreased with gravity level.</li> <li>• Mean roll wave frequency increased with gravity level.</li> </ul>	<ul style="list-style-type: none"> <li>• Limited experimental and modelling studies particularly on the effect of flow orientation relative to gravity.</li> </ul>
Heat transfer coefficient	Lui et al. (1994) Ohta (1997) Celata (2007) Baltis et al. (2012) Baba et al. (2012) Narcy et al. (2014)	<ul style="list-style-type: none"> <li>• Majority of investigations reports increase in heat transfer coefficient with gravity level.</li> <li>• Higher or equivalent heat transfer coefficient was reported in <math>-1g</math>-flow relative to <math>+1g</math>-flow.</li> </ul>	<ul style="list-style-type: none"> <li>• Inconsistent reports and limited experimental and modelling studies.</li> <li>• Limited investigations on the criteria for gravity dependence.</li> </ul>



	<p>Konishi et al. (2015)</p> <p>Kharangate et al. (2016)</p> <p>Trejo-Peimbert et al. (2019)</p> <p>Lebon et al. (2019)</p>	<ul style="list-style-type: none"> <li>• Gravity dependence was more pronounced in the nucleate boiling regime.</li> <li>• Gravity influence was limited to some threshold values of mixture Froude number or wall heat flux.</li> </ul>	
--	---	--	--

## 1.4 Conclusion

*An overview of flow boiling along with fundamental equations, closure laws and dimensionless numbers relevant to flow boiling was presented in the chapter. Available models for predicting flow pattern transition, void fraction, wall shear stress, interfacial shear stress, wave structures and heat transfer in upward, downward and microgravity flow boiling was also presented in this chapter. Furthermore, a non-exhaustive review of literature for two-phase flows with phase change in reduced and normal gravity conditions was presented.*

*The review highlighted the limited experimental and modelling studies of flow boiling, particularly in downward and microgravity flow conditions. The review also highlighted lack of consistency among available data sets and existing models as well as the lack of experimental measurements in the heated test section. Most of the studies report only partial data: heat transfer coefficient but no wall shear stress or void fraction data at the same time. In these conditions it is difficult to provide a modelling of the physical mechanisms. To bridge the gap in experimental data, two flow boiling loops were developed at IMFT in 2010 (BRASIL) and 2021 (COSMO) and were used in the current work. Systematic experiments with the same test section, the same parameters (flow rate, heat fluxes, qualities, subcooling, pressure range) are performed in upward, downward flows and in microgravity conditions. Description of these experimental facilities is provided in the next chapter.*

## Chapter 2

### Experimental Setup and Measurement Techniques

*This chapter begins with the description of the BRASIL (Boiling Regimes in Annular and Slug flow In Low gravity) and Compact Small Scale Convection Loop (COSMO) experimental setup. This is followed by a description of the measurement techniques, data reduction and error estimation.*

## 2.1 Experimental Setup

In this work, most of the ground experiments were done using BRASIL (Boiling Regimes in Annular and Slug flow In Low gravity) flow loop (Figure 2.1). This setup was previously used by Narcy (2014) and Trejo-Peimbert (2018) for flow boiling experiments in upward flow configuration in  $+1g$  and  $\mu g$  conditions. In the current work, modifications were made to the setup to enable both  $+1g$  and  $-1g$  flow boiling experiments. Some ground ( $+1g$ ) and parabolic flight ( $\mu g$ ) experiments were also carried using COSMO (Compact Small Scale Convection Loop) flow loop (Figure 2.2).

Both experimental setups were designed for flow boiling experiments in millimetric tubes. They consist of two sub-systems each: a hydraulic loop with control and metering instrumentation for pressure, temperature, void fraction and mass flux measurements; and an air system that uses bellows to set and maintain the pressure in the hydraulic loop. This is the constant pressure volume compensator (Figure 2.1 and Figure 2.2). The bellow(s) also provide compensation for volume changes within the hydraulic loop resulting from heated liquid expansion and/or vapour generation. Data acquisition was done using National Instrument Data Acquisition (NI-DAQ) device at frequency of 100 Hz. A LabVIEW VI (virtual interface) was configured for simultaneous acquisition of input voltage to the channels of the DAQ hardware. The inputs to the DAQ are outputs from the various devices and measurement instrumentation such as thermocouples, pressure transducers, flow meters, heaters, pump etc. The LabVIEW VI was configured so that real-time data of all essential parameters was possible and safe limits were not exceeded. In the case of COSMO, camera framerate controls were also implemented on the LabVIEW VI.

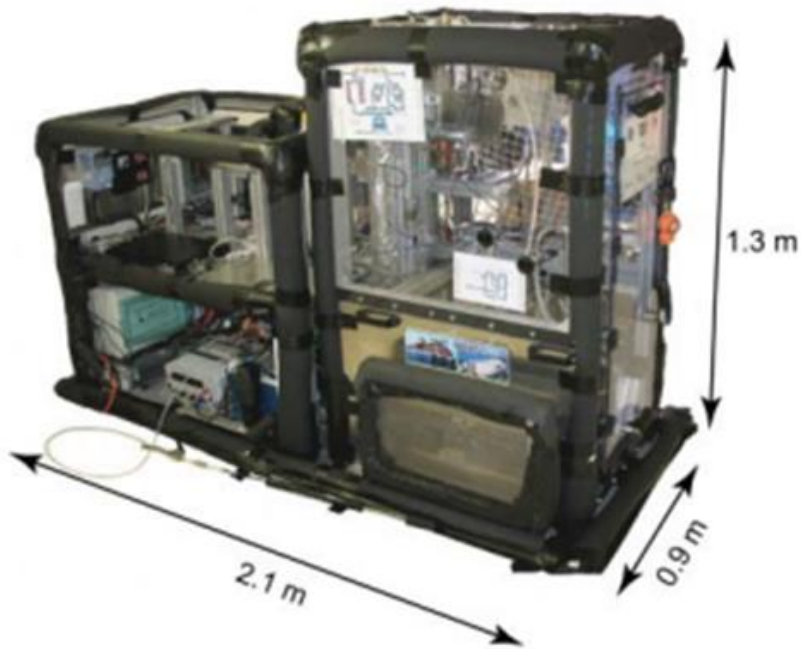


Figure 2.1. BRASIL experimental setup; data acquisition rack (left) and hydraulic loop (right).

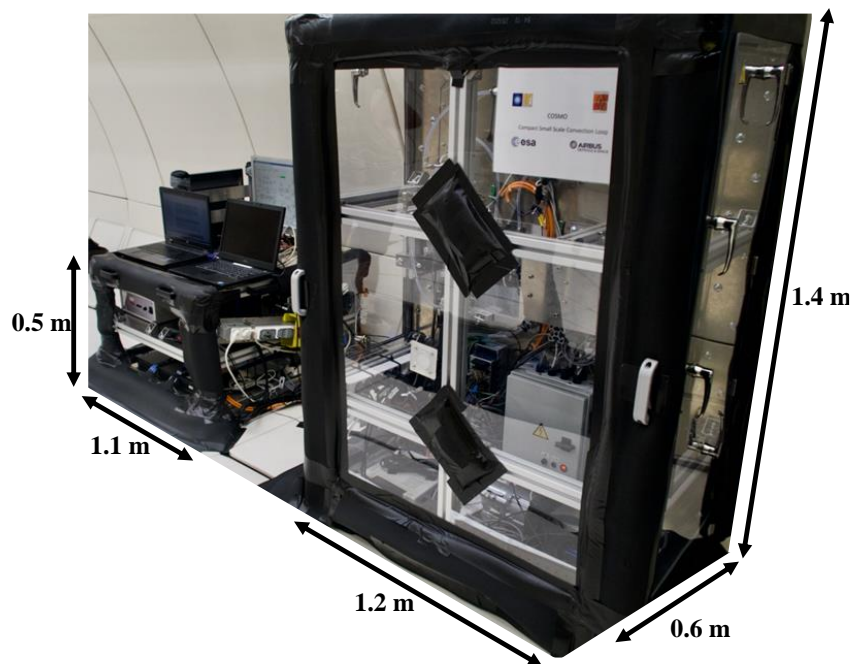


Figure 2.2. COSMO experimental setup; data acquisition rack (left) and hydraulic loop (right).

### 2.1.1 Hydraulic loop

A schematic drawing of the hydraulic loop of BRASIL is shown in Figure 2.3. Instrumentations along the loop include; a volumetric gear pump (L21755 Micropump with a DC-305A motor and maximum

flow rate of  $3.5 \text{ L/min}$ ) for fluid circulation and flow rate adjustment, PID for maintaining setpoint values, a Coriolis flowmeter for measuring mass flowrate and various temperature and pressure sensors installed along the loop. The flow meter employs the Coriolis effect for the determination of mass flowrate and has a quoted accuracy of 0.5% FS. The loop also consists of two preheating columns (85 cm long each) which are connected in series and fitted internally with heating coils. The power source to the preheaters was QVR320 and has a power regulator. In the preheater, fluid heating was done to attain desired liquid temperature or two-phase vapour quality at the inlet of the test section. Up to 900 W heating power was available at the preheater. The accuracy of the voltage and current supplies to the heating elements are  $\pm 45 \text{ mV}$  and  $\pm 30 \text{ mA}$  respectively. Suitable lagging was provided for the preheaters to minimise heat losses. Temperature measurements of the fluid inside the preheaters ( $TLH1, TLH2$ ) and at the surface of the heating elements ( $T_{exH1}, T_{3H1}$ ) were done at two locations using thermocouples. These measurements provide means of ensuring the safety limits are maintained. Manual pressure control may be implemented with the use of a bike pump/air-purge valve connected to the constant pressure volume compensator.

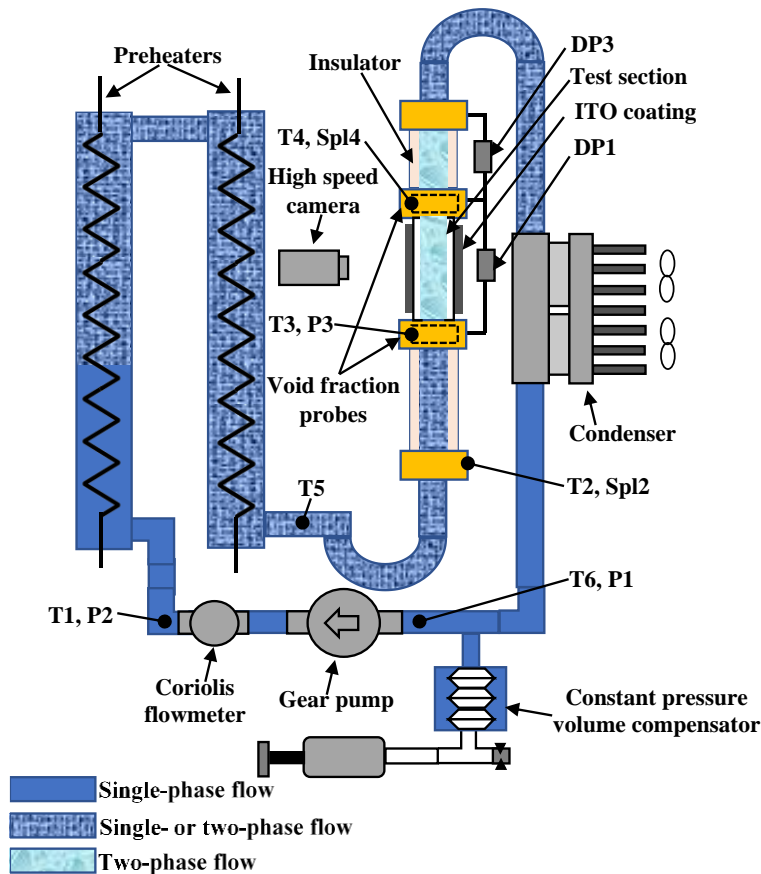


Figure 2.3. Schematic illustration of the BRASIL experimental flow loop.

Schematic drawings of the hydraulic loop of COSMO are shown in Figure 2.4. The loop consists of a positive displacement pump (micro-annular gear pump model mzt-7265 from HNP Mikrosysteme with mass flux range of  $20 \leq G \leq 150 \text{ kg/m}^2\text{s}$ ) for fluid circulation and flow rate adjustment, PID for maintaining setpoint values, a Coriolis flowmeter (M14 model from Bronkhorst) for measuring mass flowrate and various temperature and pressure sensors installed along the loop. The flow meter has a quoted accuracy of 1.0% FS. The loop also consists of two preheaters which are connected in series upstream and downstream of an assembly of two elbows and a straight horizontal tube. Preheater 1 (PH1) was built and certified (leakage free) by Airbus DS. The heating length was 120 mm, the total length was 210 mm and its weight was about 1.5 kg. The liquid passes through a grid of parallel ducts whose dimensions are chosen to maintain constant total cross section of the flow from the inlet to the outlet. Four flat heating elements are attached to each side of PH1. These electrical elements are MINCO Thermofoil heaters model HK6908. Each heating element can provide up to 24.4 W. The four elements were connected to one power module which can deliver up to 35 V and 3 A (105 W maximum). Preheater 2 (PH2) provides heat by Joule effect with three heating wires wrapped around the copper tube. The heating wires were connected to a direct current electrical supply dedicated to the two pre-heaters. The model of the heating wires is SEA 15/150 (length 500 mm and diameter 1 mm) from Thermocoax and can sustain up to 200 W through a 35 V electrical supply. Each of the heating wires is controlled autonomously in order to create independent heating sections. The copper tube was 320 mm long, 6 mmID and 10 mmOD. It was covered by a Kapton (polyimide) layer and the Kapton layer was covered with foam which provided both thermal and electrical isolations. In the PH1, fluid heating was done to attain desired single phase liquid temperature while in PH2, fluid heating was done to attain either the desired single phase liquid temperature or two-phase vapour quality. The temperature rises of PH1 and PH2 are limited by the presence of thermo-switches set at 80°C and 125/125/145°C respectively. The CoSmo loop was designed with size, power consumption and weight constraints for a possible accommodation in the European Drawer Rack 2 (EDR2) of the International Space Station. So, the range of flow rate, power is lower than for the BRASIL experimental set-up. Due to the size constraint, the distance between the elbows and the Preheater 2 and test section is limited. The hydrodynamics of the single-phase flow downstream the second elbow (at the location of Preheater 2) has been studied in a specific experiment by PIV measurement of the velocity field and numerical simulation using OpenFoam. Dean vortices are produced in the elbows and are damped downstream. A decay length is determined from experiments and simulations. After this length, the single-phase flow retrieves its axisymmetric.

This is the reason why the Preheater 2 has been split into 3 parts and for bubbly flow at low quality only the third part of the Preheater 2 is used to generate the bubbles. The first and second parts of the preheater 2 are used for higher qualities, for which the residual Dean vortices has a lower impact. The preheater 1 is only used to heat up the liquid after the flow meter and boiling incipience is avoided to prevent liquid-vapour stratification in the elbows between the 2 preheaters.

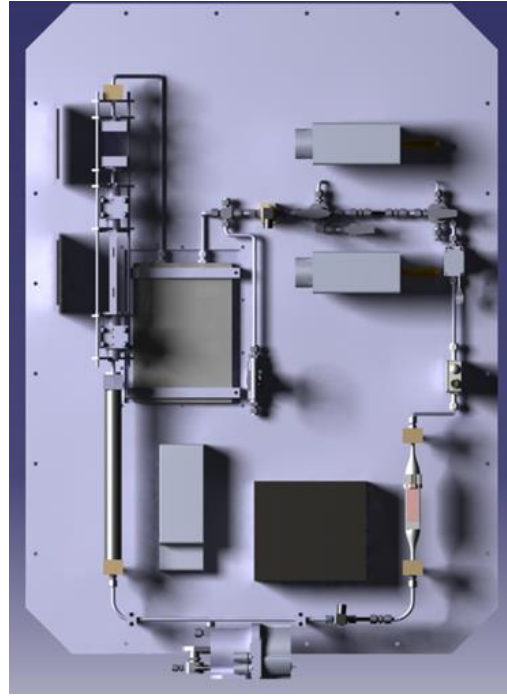
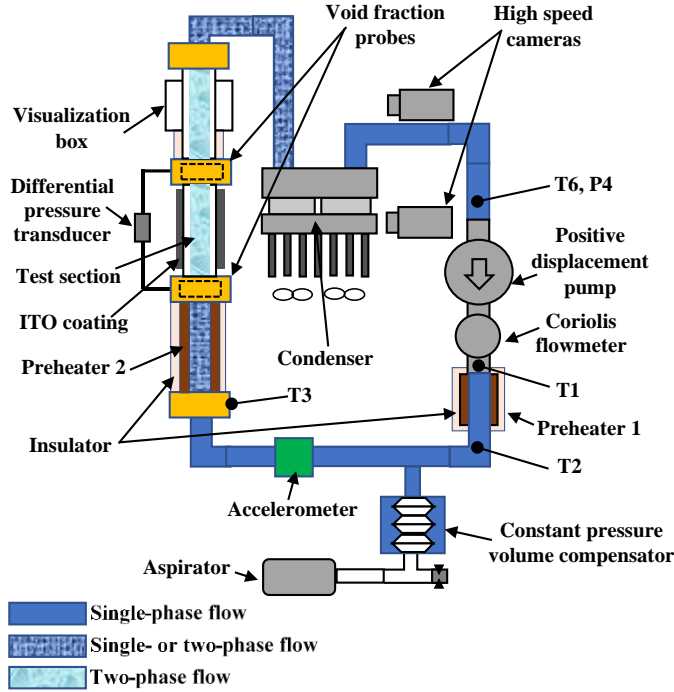


Figure 2.4. Schematic illustration of the COSMO experimental flow loop.

The current work involves the determination of flow boiling pressure drop, flow pattern, void fraction and heat transfer coefficient in a vertical tube of  $6\text{ mmID}$  and  $8\text{ mmOD}$  in  $+1g$ ,  $-1g$  and  $0g$  using HFE-7000 as working fluid. Preheated single-phase liquid or two-phase vapour-liquid flow enters the Sapphire tube test section (Figure 2.5) at pressures which can be varied from 1 to 2 bar ( $34^\circ\text{C} < T_{sat} < 54^\circ\text{C}$ ). Over this pressure range a mass flux in the range of  $40\text{ kg}\cdot\text{m}^{-2}\text{s}^{-1} < G < 500\text{ kg}\cdot\text{m}^{-2}\text{s}^{-1}$  can be attained in the loop. Pressure variations resulting from heating and phase changes also occurs. Further heating of the fluid was done by resistive heating using ITO coating on the outer wall to which a voltage source is connected. Vapour quality at the outlet of the test section is determined from an enthalpy balance on the heated tube. In general, an outlet vapour quality of up to 0.9 can be attained in both BRASIL and COSMO setups depending on the mass flux. Fluid exiting the test section is condensed and cooled to the desired temperature at the inlet of the pump using



Peltier module(s) in the condenser. In the case of BRASIL, the two condensers consisted of 4 cold plates, 9 Peltier modules per plate connected to fins (heat sinks) and fans for removing heat from the Peltier modules. In the case of COSMO, the condenser consisted of one cold plate (model CP30) from Boyd Corporation and 8 Peltier modules (model RC12-9) from Marlow. Peltier module power regulation was automated and driven by a PID which sets the liquid temperature at the pump inlet. The pump inlet temperatures were set to  $\leq T_{sat} - 10^{\circ}C$ . In this study, mass fluxes of 50, 75, 100, 200 and 400  $kg.m^{-2}s^{-1}$  were studied using BRASIL (+1g and -1g) and mass fluxes of 50, 75, 100 and 150  $kg.m^{-2}s^{-1}$  were investigated using the COSMO setup (+1g and 0g).

### 2.1.2 Test section

In both experimental setups, the test section consisted of a vertical transparent sapphire tube (surface roughness of 0.3 – 0.5  $nm RMS$ ) of 6  $mmID$  long and 1  $mm$  thick, coated externally with ITO for Joule heating (Figure 2.5). The thickness of the ITO coating was 100 nm, the coated length was about 180 mm and range of heat flux was  $0 < q < 3 W.cm^{-2}$ . The coating did not affect the transparency of the tube significantly and so visual observation of flow patterns was possible using high-speed cameras. Void fraction probes (capacitance probes) were connected at the inlet and outlet of the test section. The void fraction probes were made using polyether ether ketone (PEEK) material. In the case of BRASIL, two adiabatic sections made of stainless-steel tubes were connected, one each, to the ends of the void fraction probes. The adiabatic sections also have an internal diameter of 6  $mm$  each and lengths of approximately 200  $mm$  and 150  $mm$  before and after the sapphire tube respectively. The adiabatic sections were lagged to minimise heat losses. In the case of COSMO, PH2 made of copper was connected upstream of the test section and an adiabatic section made of glass was connected downstream of the test section. Both sections had internal diameters of 6  $mm$  and PH2 had a length of 320  $mm$ . In both setups, the tube sections before the sapphire tube provide a flow development and the post-sapphire tube adiabatic sections provide a means for measuring adiabatic two-phase pressure drop. In the case of COSMO, the downstream adiabatic section also included visualisation section. The visualization section consists of a circular borosilicate glass tube of 6  $mmID$  and 80  $mm$  long surrounded by a rectangular visualization box of 90  $mm$  length and 30  $mm$  width made up of PMMA windows. Two elastic tubes are connected to the visualization box for the purpose of filling and maintaining the pressure inside the box. The visualization box serves to reduce optical distortion close to the wall. In the case of BRASIL, a flexible hose was connected between the preheater and the adiabatic section upstream of the test section and another between the

adiabatic section downstream of the test section and the condenser. These connections were to enable easy inversion of the test section for the purpose of upward and downward flow experiments. The hoses were lagged to minimise heat losses.

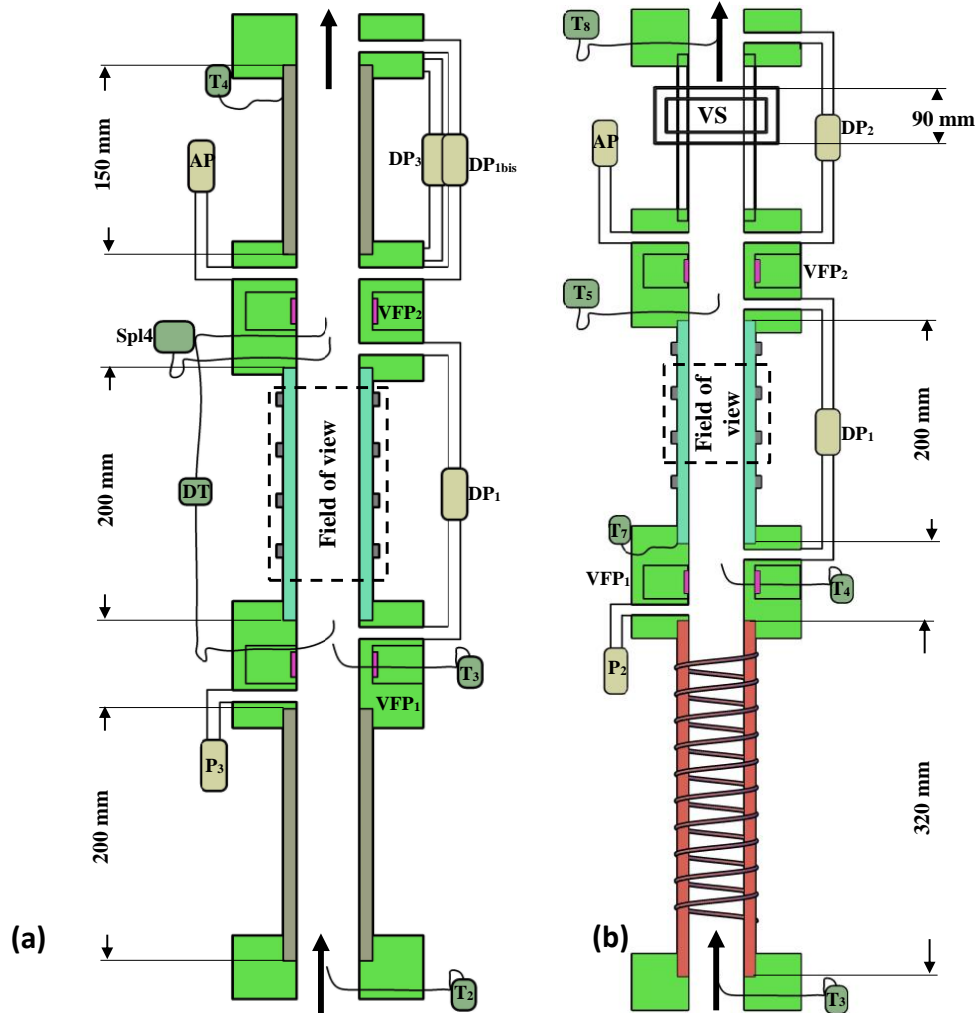


Figure 2.5. Schematic drawing of the test section of a. BRASIL b. COSMO experimental facility.

### 2.1.3 Working fluid

The working fluid used was 1-methoxyheptafluoropropane ( $C_3F_7OCH_3$ ) refrigerant, commonly called HFE-7000. It finds applications in cooling reactors in the processing industries as well as automated test equipment (ATE) and wafer processing equipment in the semiconductor industry which requires low temperatures. The choice of fluid was based on its thermophysical properties which makes it suitable for both ground and parabolic flight experiments under conditions of limited heating power. The properties of this segregated hydrofluoroethers (HFE) that makes it suitable for

this study include; non-flammability, low toxicity and dielectric. Average properties of the test fluid are given in Table 2.1.

Table 2.1. Properties of HFE-7000 at 25°C and atmospheric pressure

Property	Value
Molecular weight	200g/mol
Saturation temperature	34°C
Liquid density	1400 $kg/m^3$
Vapour density	8 $kg/m^3$
Thermal conductivity	0.075 $W/m^2K$
Kinematic Viscosity	$3.2 \times 10^{-7} m^2/s$
Specific Heat	1300 $J/kg.K$
Surface Tension	0.0124 $N/m$
Latent Heat of Vaporization	130 $kJ/kg$

## 2.2 Fluid Degassing and Filling of Loop

A brief description of the procedure followed in degassing the working fluid and filling the loop is provided in this section.

### 2.2.1 Degassing of working fluid

The working fluid was degassed using a boiler before it was used to fill the experimental loops. The boiler is fitted internally with 3 cartridges with 1000 W heating capacity. Two thermal switches (73°C) are connected in series along the electrical supply and attached to the wall of the boiler (Figure 2.6). The power supply to the boiler is provided by 230Vac. A glass column condenser was connected to the top of the boiler and this column was connected to a cold-water container. The fluid was first superheated inside the boiler, then the valve connecting the boiler to the column condenser was open slightly to allow non-condensable gasses to exit the boiler. Parts of the working fluid that exit the boiler along with the non-condensable gasses is recondensed in the column condenser and returned to the boiler. During degasification, the pressure and temperature of the fluid was measured. The degasification process was repeated several times until the theoretical boiling curve was achieved. Figure 2.7 shows results of three separate degasification campaigns carried out over the course of this

work. A good agreement was found with the theoretical boiling curve. The small deviation in case 3 was due to some minor physical deformation of the PT100 used for temperature measurement which resulted in changes in the resistance of the probe.

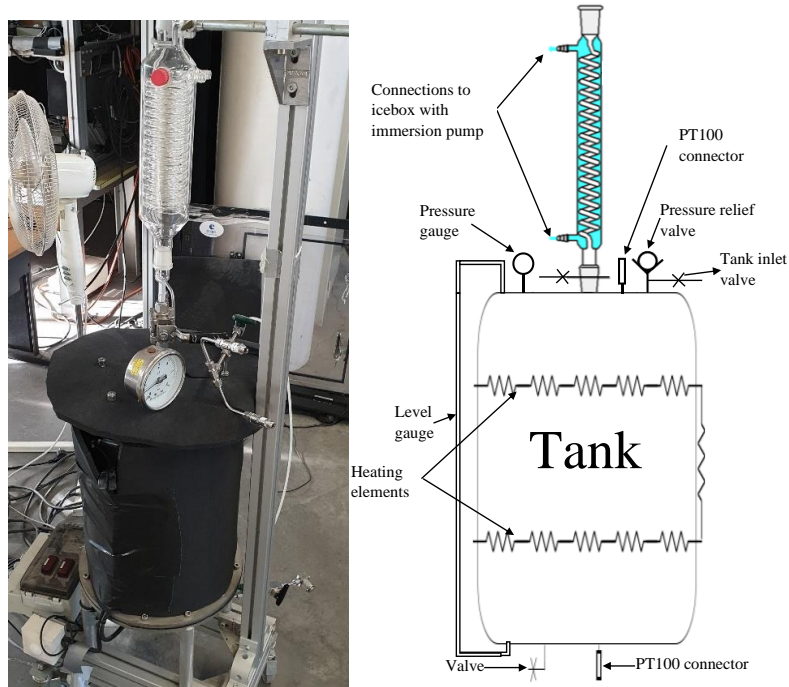


Figure 2.6. Picture and sketch of the boiler system.

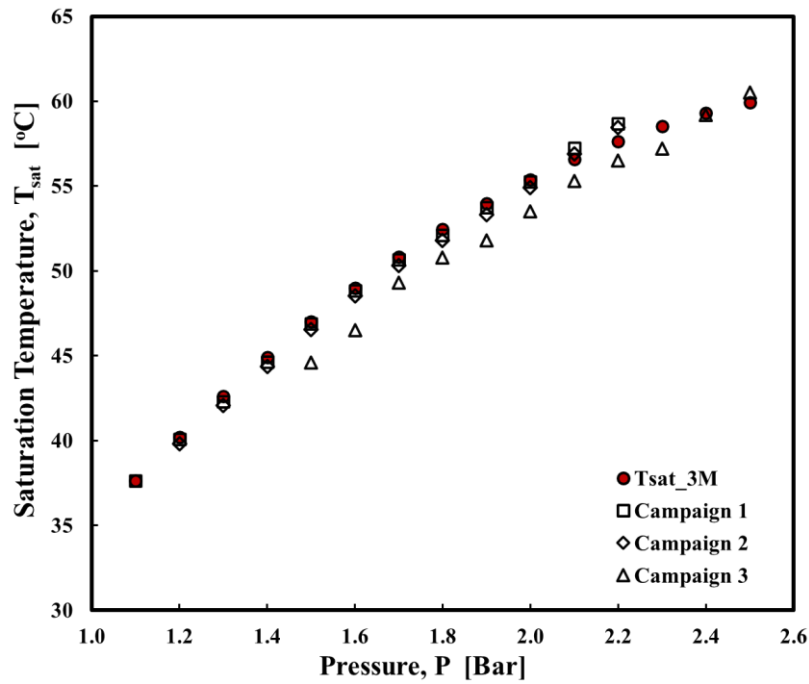


Figure 2.7. Comparison between measured and theoretical saturation temperatures.

### 2.2.2 Filling of the loop

The loop was first filled with air to a pressure of around 2 bar and leakage test was carried out. The loop was then vacuumed and further leakage test was carried out. The loop was considered leak free when the absolute pressure remains below 0.02 mbar during one hour. The degassed fluid in the boiler was superheated so as to create a significant pressure gradient between the boiler and the experimental loop. Filling of the loop was carried out using tube and valve connectors. Care was taken to balance the pressure on the air and liquid side of the bellow during filling. The hydraulic loop was generally maintained at around 1.2 bar. This is to minimise the possibility of non-condensable gasses gaining entrance into the loop. Notwithstanding, small amounts of non-condensable gasses may find its way into the loop over time thereby changing the saturation temperature of the working fluid. Consequently, over the course of various experimental campaigns, the saturation temperature of the working fluid inside the loop was measured at various locations along the test section.

### 2.3 Experimental Measurements

This investigation involved the measurement of several primary parameters necessary to describe flow boiling in circular millimetric tubes and also for the computation of secondary parameters. The measured parameters include; temperature, pressure and capacitance. The measurements of each of these parameters are associated with a degree of uncertainty due to the accuracy of the measurement devices. Therefore, the measured parameter ( $X$ ) is stated as the sum of its mean value ( $X_{mean}$ ) and its measurements accuracy ( $\delta X$ ). Some of the computed parameters are; fluid properties, vapour quality, void fraction, wall shear stress, interfacial shear stress and heat transfer coefficient. The uncertainties ( $\delta P$ ) associated with each of these computed parameters ( $P$ ) are given by;

$$\delta P(A, B, C, \dots) = \sqrt{\left(\frac{\partial P}{\partial A} \delta A\right)^2 + \left(\frac{\partial P}{\partial B} \delta B\right)^2 + \left(\frac{\partial P}{\partial C} \delta C\right)^2 + \dots} \quad 2.1$$

Geometric parameters such as tube diameters and tube length also introduce uncertainties to the computed parameters. In this work, the uncertainties in tube diameter and length are as follows;

$$D_i = 6 \text{ mm} \pm 0.05 \text{ mm}$$

$$D_o = 8 \text{ mm} \pm 0.05 \text{ mm}$$

$$L = 200 \text{ mm} \pm 0.1 \text{ mm}$$

### 2.3.1 Pressure measurement

Absolute and differential pressure measurements were carried out at relevant sections of the loop. Absolute pressure measurements were done using Keller PAA21 pressure transducers with measurement range and accuracy of  $0 - 5 \text{ bars}$  and  $\pm 0.25 \text{ mbar}$  respectively. These transducers provide means for measuring pressures at the different sections of the loop which are used for determining saturation temperature and for computing fluid properties. Differential pressure measurements were done using Validyne differential pressure (DP) transducers (model P305D). The output of the DP transducers are voltage values which are linearly proportional to the differential pressure across its membrane. In the case of BRASIL, 3 DP transducers were used, two of which were connected across the downstream adiabatic section ( $DP_{1bis\_BS}$  and  $DP_{3\_BS}$ ) and the third was connected across the sapphire (heated) tube section ( $DP_{1\_BS}$ ). For COSMO, 2 DP transducers were used, one each across the sapphire tube ( $DP_{1\_CM}$ ) section and the downstream adiabatic section ( $DP_{2\_CM}$ ). Specifications for the DP transducers (Figure 2.5) are;

$$DP_{1\_BS} (= DP_{2\_CM}): n^{\circ} 28,56 \text{ cmH}_2\text{O (Full Scale)}, \delta DP = \pm 2.8 \text{ mmH}_2\text{O}$$

$$DP_{3\_BS}: n^{\circ} 28,56 \text{ cmH}_2\text{O (FS)}, \delta DP = \pm 2.8 \text{ mmH}_2\text{O}$$

$$DP_{1bis\_BS} : n^{\circ} 30,86 \text{ cmH}_2\text{O (FS)}, \delta DP = \pm 4.3 \text{ mmH}_2\text{O}$$

$$DP_{1\_CM} (= DP_{1BS\_downward \text{ flow}}): n^{\circ} 30,86 \text{ cmH}_2\text{O (FS)}, \delta DP = \pm 4.3 \text{ mmH}_2\text{O}$$

where the subscripts *BS* and *CM* stands for BRASIL and COSMO respectively. Calibration of all the DP transducers were carried out and result of calibration of  $DP_{1\_BS} (= DP_{2\_CM})$  and  $DP_{1\_CM} (= DP_{1BS\_downward \text{ flow}})$  are shown in Figure 2.8 while that of  $DP_{3\_BS}$  and  $DP_{1bis\_BS}$  are shown in the Appendix section.

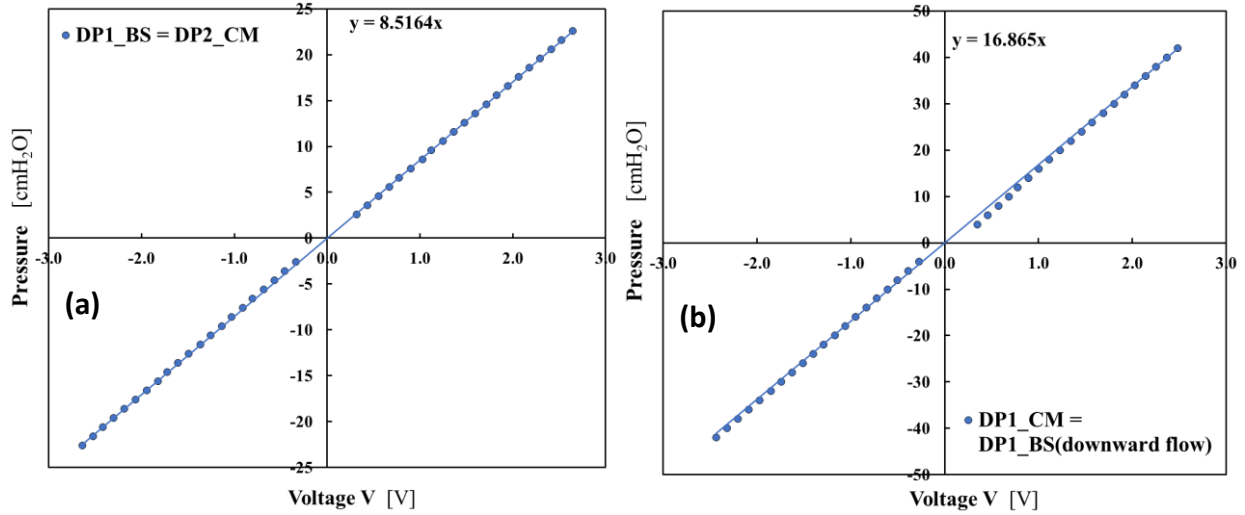


Figure 2.8. Calibration curves of differential pressure transducers.

### 2.3.2 Temperature measurement

**BRASIL:** Temperature measurements were done using K-type and T-type thermocouples as well as PT100 probes. Fluid temperature measurements corresponding to  $T_1, T_2, T_3, T_4, T_5$  and  $T_6$  were done using K-type thermocouples. These thermocouples are provided with cold-junction compensation on the NI-DAQ and have a stated accuracy of  $\pm 0.25^\circ\text{C}$ . Due to the possibility of small temperature difference along the sapphire tube, high precision in temperature measurements across this section is required. Two T-type thermocouples were connected at the inlet and outlet of the sapphire tube section (one serving as cold junction and the other as hot junction on the NI-DAQ) for measuring temperature difference across this section. The stated accuracy of the T-type thermocouple was  $\pm 0.1^\circ\text{C}$ . Fluid temperatures were also measured using PT100 probes at the inlet of the upstream adiabatic section (*Spl2*) and at the outlet of the sapphire tube section (*Spl4*). The stated accuracy of the PT100 probes was  $\pm 0.1^\circ\text{C}$ .

**COSMO:** Temperature measurements were done using K-type thermocouples and PT100 probes. Fluid temperature measurements corresponding to  $T_1, T_2, T_5, T_6$  and  $T_8$  were done using K-type thermocouples. Fluid temperatures were also measured using PT100 probes at the inlet ( $T_3$ ) and outlet ( $T_4$ ) of PH2.

In both setups, pairs of wall temperatures were also measured at 4 axial distances from the inlet to the sapphire tube using PT100 probes. The thermocouples and PT100 probes used for liquid temperature measurements were all calibrated in a thermal bath before use. The thermal bath used was Isotech

thermal bath with stated accuracy of  $\pm 0.05^\circ\text{C}$ . The calibration curves are shown in Figure 2.9.

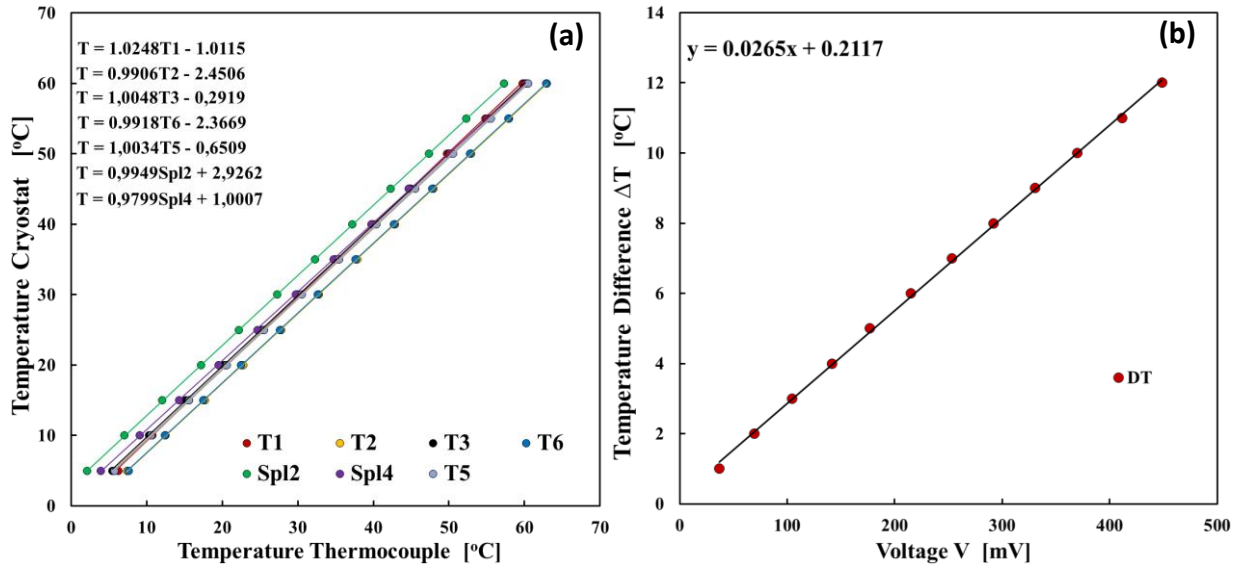


Figure 2.9. Calibration curves for various thermocouples and PT100 probes.

### 2.3.3 Determination of void fraction

Determination of void fraction is essential for closure laws in the momentum balance equation as well as to calculate the mean liquid/vapour velocity and the liquid film thickness in annular flow. Techniques for measuring void fraction are mainly based on fluid conductance or fluid capacitance (Canière et al., 2007; Ceccio and George, 1996; Gardenghi et al., 2020). In this study, conductance probes were not suitable for void fraction measurement owing to the fact that the test fluid used is a dielectric fluid. Capacitance probes developed in-house at IMFT were used in this study for void fraction measurements. Both experimental setups contain two capacitance probes, they are used for void fraction measurements at the inlet and outlet of the test section (Figure 2.10). The measurement principle is based on determination of electrical impedance ( $Z$ ) which is given by;

$$1/Z = 1/R + 2 \pi j f C \quad 2.2$$

The term on the left-hand-side is the impedance term, the first term on the right-hand-side is the resistive/conductive term while the second term is the capacitive term, with the capacitance  $C$ , the frequency  $f$ , and the imaginary unit  $j$  ( $j^2 = -1$ ). For an equivalent parallel plate capacitor, the capacitance is given by;



$$C = \frac{\varepsilon_0 \varepsilon_r A}{d} \quad 2.3$$

where  $\varepsilon_0$  is the permittivity of vacuum,  $\varepsilon_r$  is the relative permittivity of the medium,  $d$  is the distance between the plates (electrodes) and  $A$  is the surface area of the plates.

Applying a high frequency ( $f$ ) across two parallel capacitors between which a dielectric fluid with very low conductivity flows makes the resistive term negligible compared to the capacitive term. The impedance term is now essentially a function of the capacitive term in Eq. 2.2. For two-phase flows in between parallel capacitor plates, the measured capacitance is therefore proportional to the volume fraction of each phase. An excitation frequency of 31.6 kHz was applied across two parallel capacitors in each of the void fraction probes (VFP). The basic design of the VFPs in both setups is shown in Figure 2.10. The measuring and guard electrodes are all of dimension 10 x 10 x 1 mm and the spacing between parallel electrodes is 10 mm. The electrode configuration, overall design and various modifications are based on previous reviews and testing of the void fraction probes. The main difference between the VFPs in the two experimental setups is the size of the PEEK material. The dimension of the PEEK materials used for the VFPs on BRASIL was 6 mmID, 60 mmOD and 120 mm length while that of COSMO was 6 mmID, 30 mmOD and 90 mm.

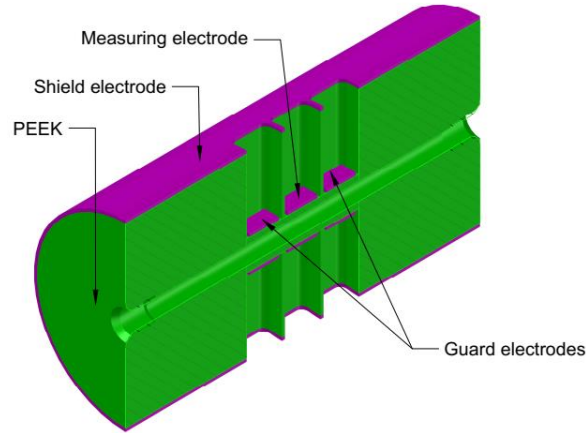


Figure 2.10. Schematic drawing of void fraction probes.

Calibration of the capacitance probes was done using HFE7000 liquid and Teflon rods of various diameters (mimicking annular flow with different vapour core diameters). The Teflon rods were used in place of the actual vapour and has permittivity close to that of HFE7000 vapour. The permittivity of the various materials are as follows;

- HFE7000 liquid: 7.4
- HFE7000 vapour: 1.4
- Teflon rod: 2.1
- PEEK: 3.2
- Air: 1

The sensitivity of the VFPs was measured as the difference in capacitance between the liquid and the vapour phases. For this calibration, the sensitivity is given as the difference between the capacitance of HFE7000 liquid and Teflon rod given by;

$$\Delta C = C_l - C_v \quad 2.4$$

For BRASIL, the measured sensitivities of VFP1 and VFP2 were approximately 0.24 and 0.235 pF respectively while for COSMO they were 0.164 and 0.31 respectively. Figure 2.11 show plots of measured capacitances versus time during the process of filling each loop with HFE7000.

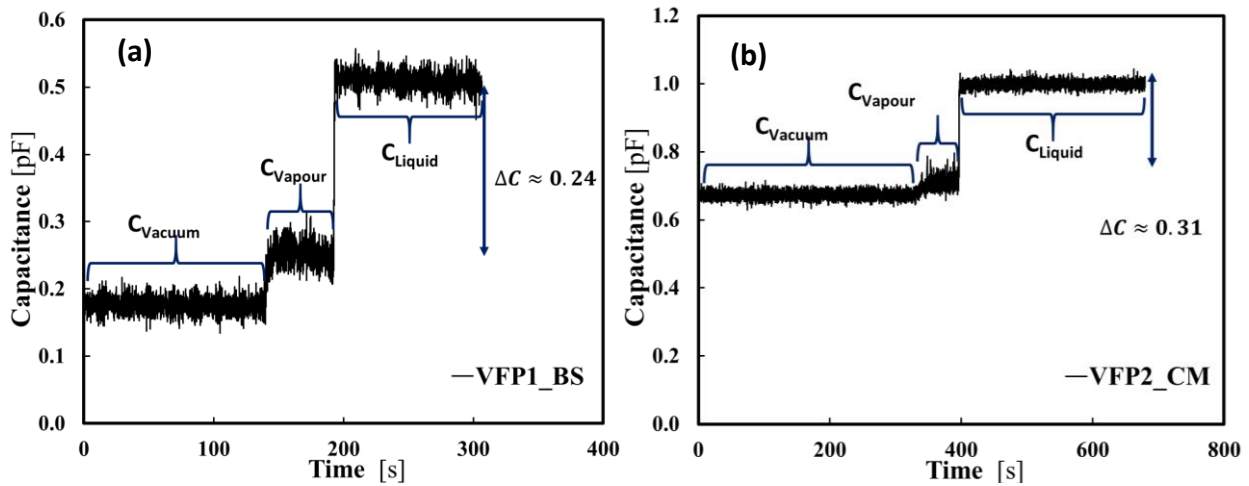


Figure 2.11. Measured capacitance versus time (Filling Data), BRASIL (top), COSMO (bottom).

Considering the difference in permittivity between the Teflon rod and HFE7000 vapour, measured capacitance ( $C$ ) is presented in reduced form as follows:

$$C^* = \frac{C - C_v}{C_l - C_v} \quad 2.5$$

where  $C$ ,  $C_v$ ,  $C_l$  and  $C^*$  are measured capacitance, capacitance of Teflon rod, capacitance of liquid and reduced capacitance respectively.

The diameters of Teflon rods used were 3.34, 4.42, 5.24, 5.54 and 6.00 *mm* corresponding to void fractions of 30.99, 54.27, 76.27, 85.25 and 100% respectively. Effort was made to ensure precise measurements of the diameters of Teflon rods used as small errors in diameter measurement could result in significant shift in the calibration curves. Several runs were carried out for each Teflon rod inserted into HFE7000 liquid. In between each measurement, the capacitance of all-liquid and all-vapour (6 mm Teflon) were measured to determine any possible deviation due to possible changes in the temperature of the electronics. The capacitance of the liquid ( $C_l$ ) was recorded along with the temperature of the electronics ( $T_{elect}$ ). Measured liquid capacitance increased with the temperature of the electronics. A straight line provided a good fit between liquid capacitance and the temperature of the electronics, particularly with the void fraction probes used in the BRASIL experimental setup (Figure 2.12). Measured capacitance ( $C$ ) was corrected using corresponding temperature of the electronics. It should be remarked that, liquid capacitance and temperature measurements were also taken during the actual two-phase experiments. Time series measurement of capacitances are recorded for all the measurement runs and average values computed. Data for the first 1-2 seconds were omitted from the averaging as it sometimes took a couple of seconds for measurements to reach steady state. The same procedure was followed in calibrating all the void fraction probes and the results are shown in Figure 2.13. Calibration results of VFP1 and VFP2 were in good agreement particularly with the BRASIL probes. The full-scale measurement accuracy was determined from the maximum amplitude of oscillation ( $\delta C_l$ ) and the average value for the all-liquid measurement of each VFP. The estimated accuracy of the void fraction probes used in the current work was  $\delta C_l / C_l \approx 6\%$ .

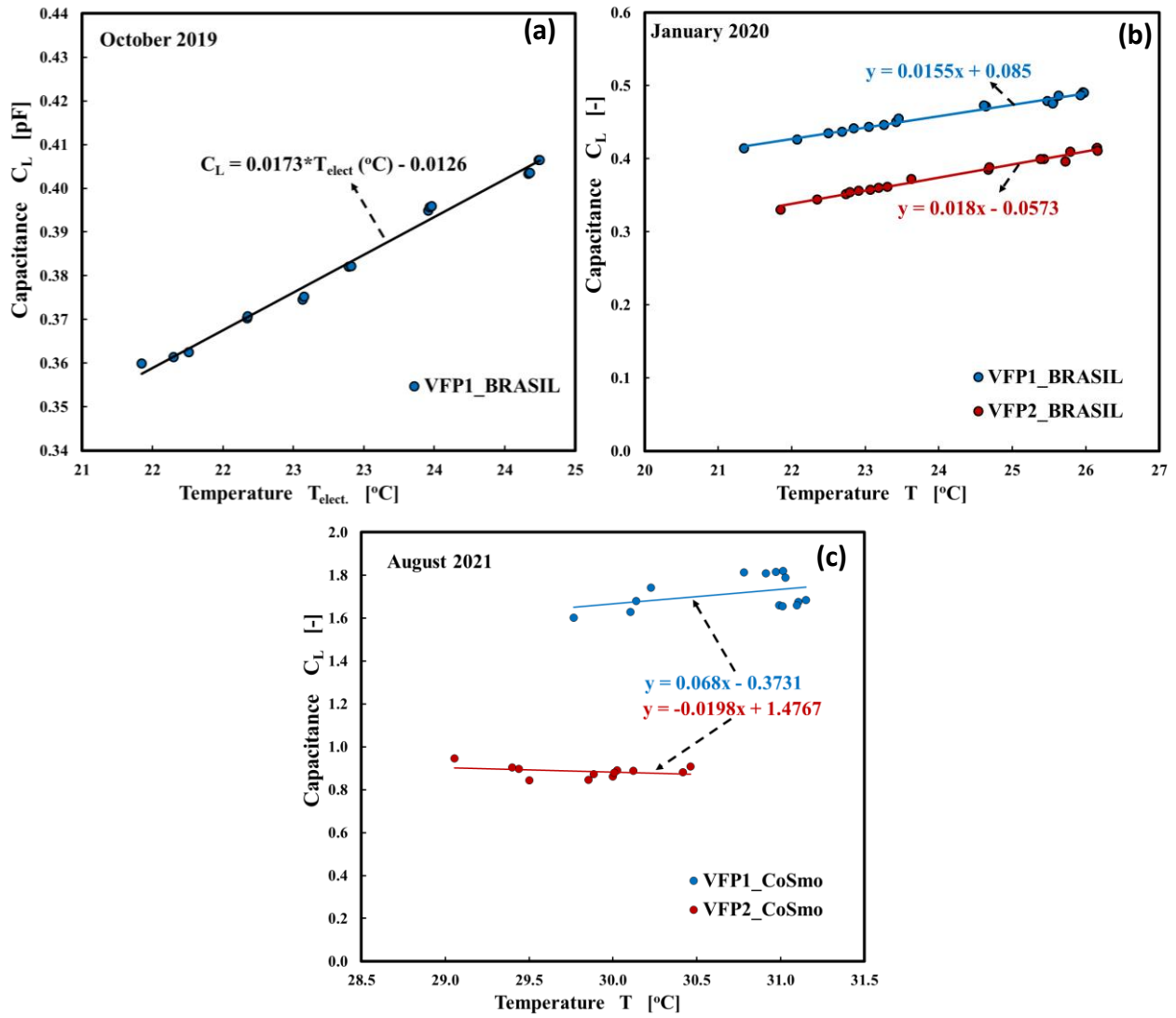


Figure 2.12. Liquid capacitance versus temperature of electronics.

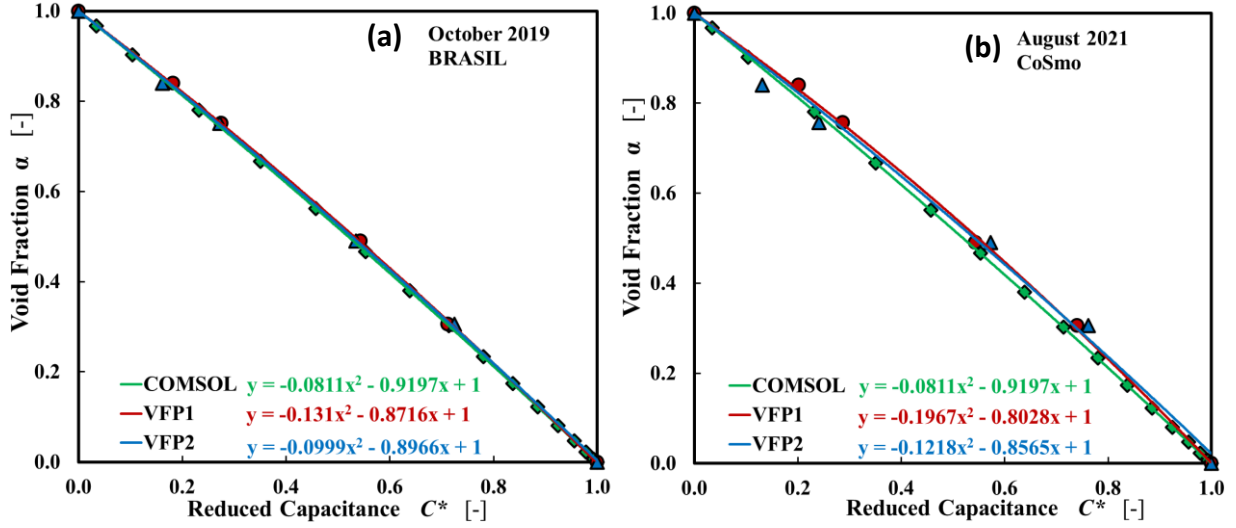


Figure 2.13. Calibration curves of void fraction probes: VFP 1 and VFP2 represent experimental calibrations done using Teflon rods, while COMSOL refers to results of 3D simulation carried out using COMSOL Multiphysics 5.3a.

To validate the results of the calibration, a 3D model was developed with COMSOL Multiphysics 5.3a using dielectric properties of HFE7000 liquid and vapour phases as well as dielectric properties of the PEEK (Figure 2.14).

In the simulation of parallel plate capacitors, the polarization is proportional to the electric field and the electric field displacement ( $D$ ) is given by;

$$D = \epsilon_0 \epsilon_r E \quad 2.6$$

where  $\epsilon_0$  is the permittivity of vacuum,  $\epsilon_r$  is the relative permittivity of the dielectric material and  $E$  ( $V/m$ ) is the electric field intensity. In the case of 2D simulation, Eq. 2.6 can be expressed as;

$$-nD = \epsilon_0 \epsilon_r \frac{V_{ref} - V}{d_s} = \rho_s \quad 2.7$$

where  $V_{ref}(V)$  is the reference voltage (5 V),  $V(V)$  is the ground voltage (0 V),  $d_s$  (m) is the thickness of the dielectric material (distance between parallel plates),  $n(-)$  is the outward normal from the surface of the reference electrode and  $\rho_s(C/m^2)$  is the electric charge density. Eq. 2.7 can be expressed in terms of 2D capacitance as follows;

$$C(Farad) = \frac{\epsilon_0 \epsilon_r A}{d_s} = \frac{-nD}{V_{ref} - V} \cdot A \quad 2.8$$

In the case of 3D capacitor simulation;

$$\rho_v \left( \frac{C}{m^3} \right) = \nabla \cdot D = \nabla \cdot (\epsilon_0 \epsilon_r E) \quad (E = -\nabla \cdot V) \quad 2.9$$

In the 3D simulation, a terminal voltage ( $V_{ref}$ ) of 5 V was applied which corresponds to the applied terminal voltage of the VFPs used in the current work. Meshing of the electrostatic domain was done using physics-controlled mesh with extra-fine element. Mesh specifications is shown in Table 2.2. A reference impedance ( $Z_{ref}$ ) of 50 ohms was used for the simulation. 3D simulations of both bubbly and annular flow scenarios were carried out (Figure 2.14). Experimental calibration and Simulation results were quite consistent (Figure 2.13).

Table 2.2. Mesh specification for 3D COMSOL simulation.

Parameter	Value
Maximum element size	4.27 mm
Minimum element size	0.183 mm
Maximum element growth rate	1.35
Curvature factor	0.3
Resolution of narrow regions	0.85

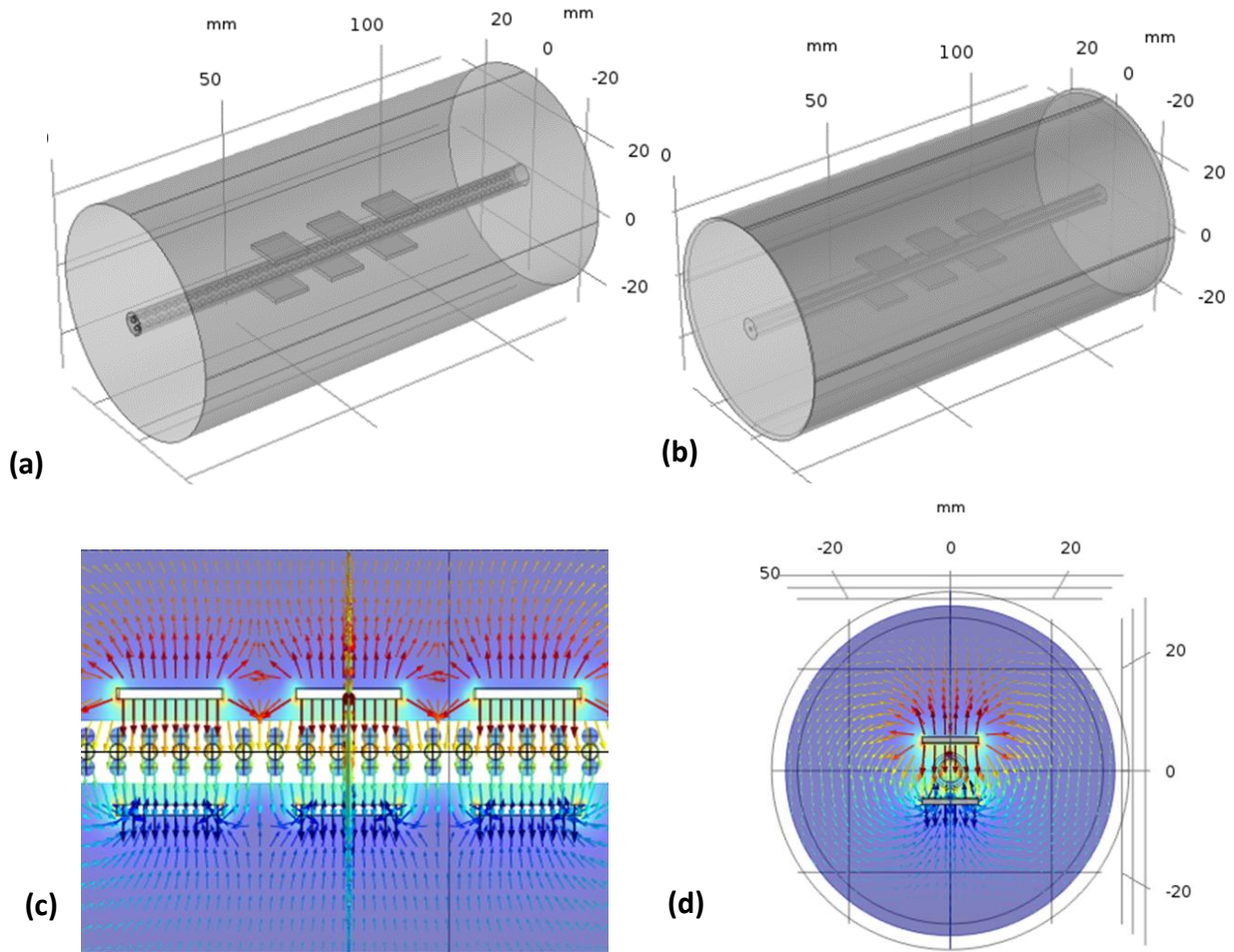


Figure 2.14. Geometry and field lines of 3D simulation of void fraction probes, bubbly flow (left), annular flow (right).

### 2.3.4 Flow visualisation

Flow visualisation for upward and downward flows were carried out on the BRASIL experimental setup using two different high-speed cameras (PCO Dimax,  $2000 \times 2000$  pixels and PCO1200HS,  $1200 \times 1000$  pixels) with spatial resolutions of  $12 \text{ pix/mm}$  ( $168 \text{ mm}$  field of view,  $FoV$ ) and  $8 \text{ pix/mm}$  ( $160 \text{ mm}$   $FoV$ ). Visualisation of nearly the entire tube at a frequency of  $1.0$  or  $1.4 \text{ kHz}$  enabled the observation of the evolution of flow pattern and wave structures from the inlet to outlet of the heated section.

In the case of COSMO, two high speed cameras (both PCO1200HS) with resolutions of  $18 \text{ pix/mm}$  (heated test section,  $71 \text{ mm}$   $FoV$ ) and  $39.5 \text{ pix/mm}$  (adiabatic visualisation section,  $32.4 \text{ mm}$   $FoV$ ) were used. In the heated section, flow visualisation carried out at  $400 \text{ Hz}$  was used to determine the flow patterns for  $(+1g)$  and  $(0g)$ . In the downstream adiabatic section, flow visualisation carried out

at 400 Hz was used to determine bubble geometry (+1g and 0g) and velocity of Taylor bubbles (0g). The visualisation section was surrounded by a rectangle box filled with HFE-7100 to minimise optical distortion. The choice of fluid used in the visualisation box was because it has the same refractive index ( $n = 1.35$ ) as the working fluid (HFE-7000) but higher saturation temperature ( $61^\circ\text{C}$  at 1 bar). Calibration was done using target grid of point which were regularly spaced at 0.125 mm apart as well as a thin needle of 0.5 mm diameter. Almost no optical distortion was observed and it was possible to identify the inner and outer edges of the tube.

## 2.4 Data Reduction

The measured parameters such as temperature, pressure and void fraction were used to compute parameters such as vapour quality, liquid film thickness, wall shear stress, interfacial shear stress and heat transfer coefficient. It was assumed that the uncertainties in fluid properties are negligible.

### 2.4.1 Vapour quality

In both experimental setups, the fluid at the inlet of the sapphire tube section was either at subcooled or saturated conditions. For saturated inlet conditions, the inlet quality ( $x_{in}$ ) was determined from the enthalpy balance in the preheater, flexible hose (BRASIL) and adiabatic section upstream (BRASIL) of the sapphire tube (Figure 2.15). For COSMO, preheater here refers to PH2. The enthalpy balance between the inlet to the preheater and the inlet to the sapphire tube is given by;

$$\frac{P_{ph\_eff}}{(\pi D^2/4)} = G(1 - x_{in})Cp_l T_{in} + Gx_{in}h_v - GCp_l T_{in,ph} \quad 2.10$$

For saturated conditions at the inlet to the sapphire tube;

$$Cp_l T_{in} = h_{l,sat} \text{ and } h_{v,sat} - h_{l,sat} = h_{lv}$$

$$x_{in} = \frac{4P_{ph\_eff} - GCp_l \pi D^2 (T_{in} - T_{in,ph})}{G\pi D^2 h_{lv}} \quad 2.11$$

**BRASIL:** Combined heat losses in the preheater, connecting hose and adiabatic section upstream of the sapphire tube section results in difference between the actual preheater power ( $P_{preheat}$ ) and the effective preheater power ( $P_{ph\_eff} = \Delta H_{preheat}$ ). Heat loss estimation was done by comparing the changes in enthalpy of the fluid with the actual preheater power at different flow rates in single-phase



flow. Plots of change in enthalpy versus preheater power are shown in Figure 2.16. The result shows that heat loss was a function of mass flux and the heat loss decreased with increase in mass flux for the same preheater power. This was because, for the same preheater power, the liquid temperature at the outlet of the preheater decreased with mass flux. Heat loss also changed with ambient conditions, being less in the summer (Figure 2.16b). Effort to correlate the heat losses to fluid and ambient temperatures are shown in Figure 2.17. The heat losses appear to be well correlated with the logarithmic mean temperatures in the various sections within an accuracy of  $\pm 20\%$ . Error in preheater power was estimated from the accuracy of the root mean square values of voltage ( $U_{rms}$ ) and current ( $I_{rms}$ ).

$$\delta P_{ph} = \sqrt{(U_{rms}\delta I_{rms})^2 + (I_{rms}\delta U_{rms})^2} \quad 2.12$$

$$\delta I_{rms} = \pm 10 \text{ mA}, \delta U_{rms} = \pm 45 \text{ mV}$$

Uncertainties in the inlet quality mass flux and mass flow rate are given by;

$$\delta x_{in} = \left\{ \left[ \frac{4\delta P_{ph}}{G\pi D^2 h_{lv}} \right]^2 + \left[ \frac{-4P_{ph}\delta G}{G^2\pi D^2 h_{lv}} \right]^2 + \left[ \frac{-8P_{ph}\delta D}{G\pi D^3 h_{lv}} \right]^2 + \left[ \frac{-Cp_l\delta T}{h_{lv}} \right]^2 \right\}^{0.5} \quad 2.13$$

$$\delta G = \sqrt{\left( \frac{4}{\pi D^2} \delta \dot{m} \right)^2 + \left( \frac{-8\dot{m}}{\pi D^3} \delta D \right)^2}, \quad \delta \dot{m} = 0.5\% \times \dot{m} \quad 2.14$$

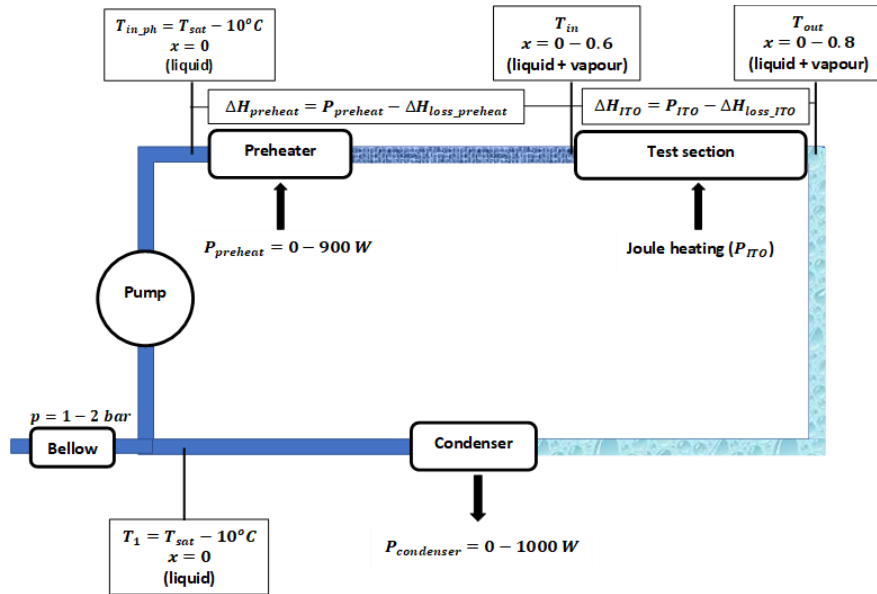


Figure 2.15. Scheme of both flow boiling loops

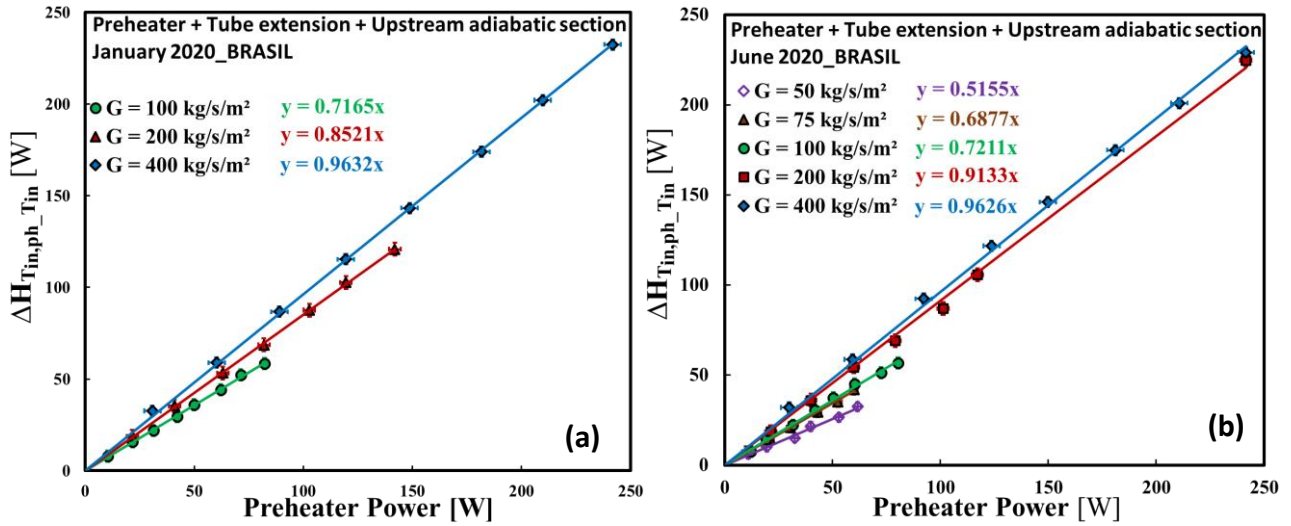


Figure 2.16. Change in enthalpy versus preheater power in the BRASIL loop.

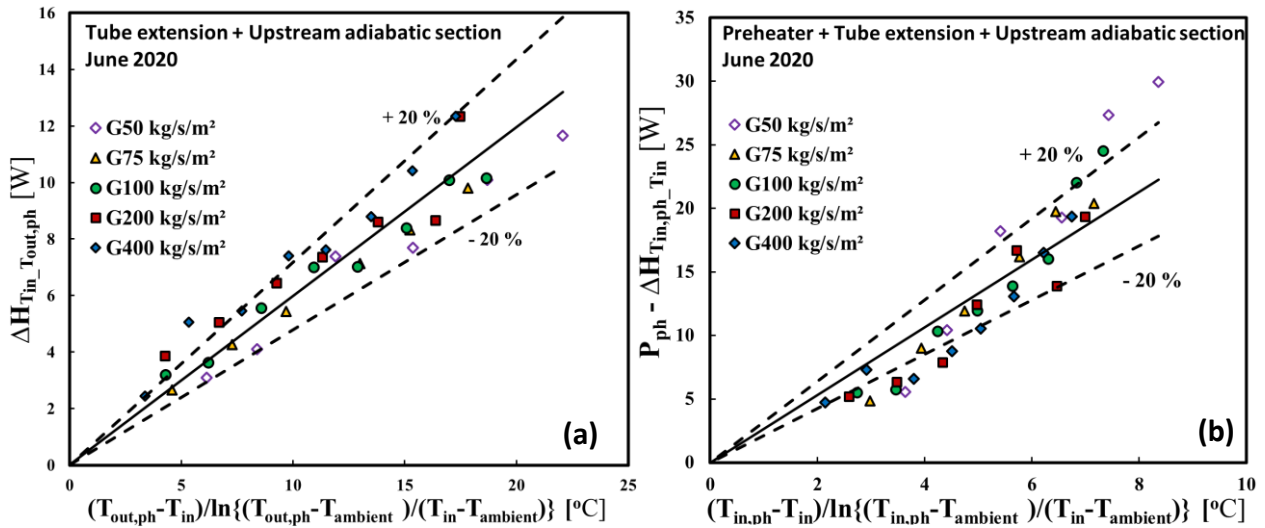


Figure 2.17. Heat loss versus logarithmic mean temperature difference.

**COSMO:** Similar procedure was followed to estimate heat losses in this loop. The heat losses also showed mass flux dependence and ambient temperature dependence particularly for lower mass fluxes (Figure 2.18). It should be remarked that the onset of bubble formation was reached at a much lower preheater power in COSMO compared to BRASIL. This is due to the difference in preheater types used in the two experimental setups. In COSMO, nucleation at the inner wall of the copper tube (PH2) resulted in bubble formation at low preheater power. The main advantage of this preheater is its low thermal inertia which allows the fluid to attain thermal equilibrium at a much shorter time relative to the preheater used in the BRASIL setup. We can remark that the heat losses are comparable in the 2 experiments BRASIL and COSMO.

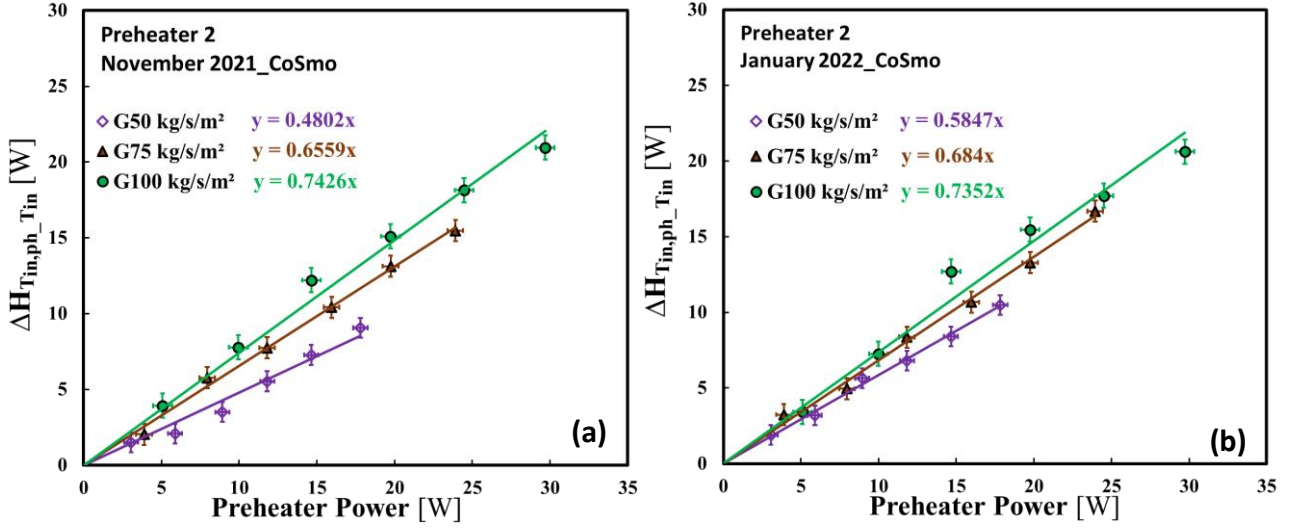


Figure 2.18. Change in enthalpy versus preheater power in the COSMO loop.

The quality ( $x_z$ ) at an axial position ( $z$ ) downstream of the inlet of the sapphire tube section was obtained from enthalpy balance between the inlet of the sapphire tube and that position.

$$x_z = x_{in} + \frac{\left[ \frac{4q_{eff} \times z}{GD} - Cp_l(T_z - T_{in}) \right]}{h_{lv} + Cp_l(T_{sat} - T_z)} \quad 2.15$$

At subcooled inlet conditions  $x_{in} = 0$  and at saturated inlet conditions  $T_z = T_{in} = T_{sat}$ ,  $Cp_l(T_z - T_{in}) = 0$ ,  $Cp_l(T_{sat} - T_z) = 0$ . For subcooled inlet conditions the temperature evolution between the inlet and outlet of the sapphire tube section is assumed to be linear. The mean vapour quality along the heated tube section was obtained by numerical integration of the local values over the tube length.

$$x = \frac{1}{L} \int_0^L x_z dz \quad 2.16$$

The effective wall heat flux ( $q_{eff}$ ) is obtained from the difference in applied heat flux ( $q$ ) and estimated heat loss in the sapphire tube section. Heat loss in the sapphire tube section was obtained from the enthalpy balance of single-phase flow for various mass fluxes. Plots of change in liquid enthalpy versus applied wall heat flux is shown in Figure 2.19. The heat loss in the sapphire tube section was also a function of ambient conditions.

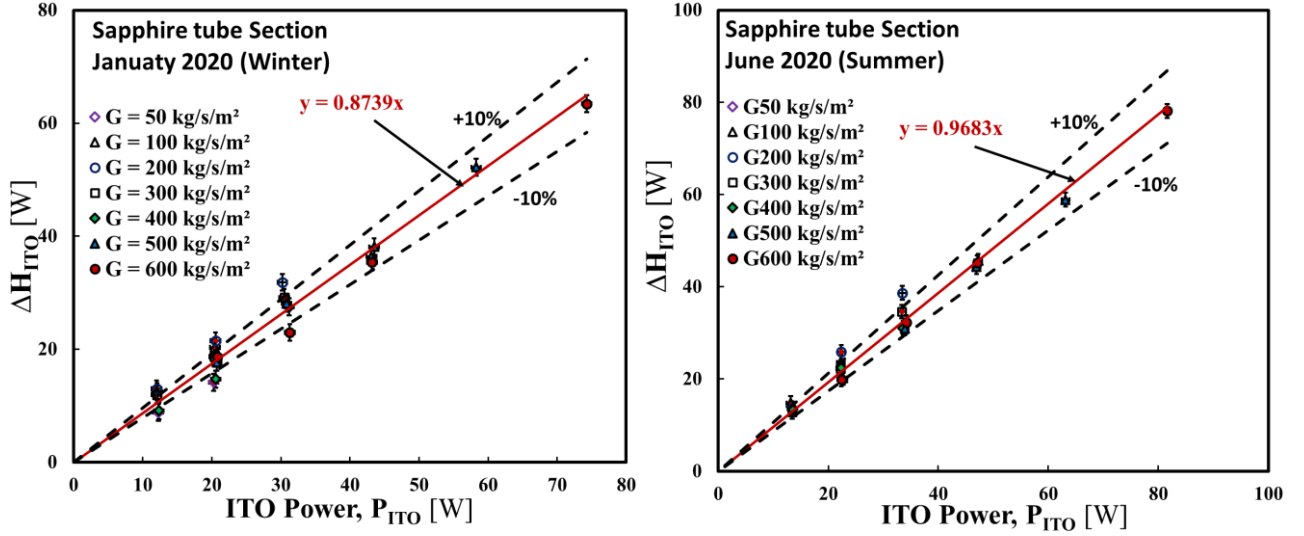


Figure 2.19. Change in enthalpy versus Power to the ITO.

$$q_{eff} = \frac{P_{ITO}}{\pi DL} \eta \quad \eta = 0.87, 0.97 \quad 2.17$$

where  $\eta$  is estimated from the plot of  $\Delta H_{ITO}$  versus  $P_{ITO}$  with an estimated accuracy of 10%.

The error in vapour quality at the outlet of the sapphire tube section is given by;

$$\begin{aligned} \delta x_{out} = \delta x_{in} + & \left\{ \left[ \frac{4L\delta q_{eff}}{GD[h_{lv} + Cp_l(T_{sat,meas} - T_z)]} \right]^2 + \left[ \frac{4q_{eff}\delta L}{GD[h_{lv} + Cp_l(T_{sat,meas} - T_z)]} \right]^2 \right. \\ & + \left[ \frac{-4Lq_{eff}\delta G}{G^2D[h_{lv} + Cp_l(T_{sat,meas} - T_z)]} \right]^2 \\ & \left. + \left[ \frac{-8Lq_{eff}\delta D}{GD^2[h_{lv} + Cp_l(T_{sat,meas} - T_z)]} \right]^2 + \left[ \frac{-Cp_l\delta T}{h_{lv} + Cp_l(T_{sat,meas} - T_z)} \right]^2 \right\}^{0.5} \end{aligned} \quad 2.18$$

$$q_{eff} = \sqrt{\left( \frac{\delta P_{ITO}}{\pi DL} \right)^2 + \left( \frac{-P_{ITO}\delta D}{\pi D^2 L} \right)^2 + \left( \frac{-P_{ITO}\delta L}{\pi D L^2} \right)^2} \quad 2.19$$

$$\delta P_{ITO} = \sqrt{(U_{ITO}\delta I_{ITO})^2 + (I_{ITO}\delta U_{ITO})^2} \quad 2.20$$

$$\delta I_{ITO} = \pm 10 \text{ mA}, \delta U_{ITO} = \pm 30 \text{ mV}$$

Table 2.3. Uncertainties in measured mass flux and preheater power.

<b>G (kg/m<sup>2</sup>s)</b>	<b><math>\dot{m}</math> (kg/s)</b>	<b><math>\delta\dot{m}</math> (kg/s)</b>	<b><math>\delta G</math> (kg/m<sup>2</sup>s)</b>	<b><math>U_{ph\_rms}</math> (V)</b>	<b><math>I_{ph\_rms}</math> (A)</b>	<b><math>P_{ph}</math> (W)</b>	<b><math>\delta P_{ph}</math> (W)</b>	<b><math>\delta P_{ph}</math> (%)</b>
50	1.41E-03	7.07E-06	0.87	62	1.20	75	1.88	2.51
75	2.12E-03	1.06E-05	1.31	80	1.58	127	2.41	1.89
100	2.83E-03	1.41E-05	1.74	97	1.92	188	2.94	1.56
200	5.65E-03	2.83E-05	3.48	125	1.92	241	3.78	1.56
400	1.13E-02	5.65E-05	6.96	137	2.58	354	4.11	1.16

Table 2.4. Uncertainties in measured ITO power and wall heat flux

<b><math>U_{ITO}</math> (V)</b>	<b><math>I_{ITO}</math> (A)</b>	<b><math>P_{ITO}</math> (W)</b>	<b><math>\delta P_{ITO}</math> (W)</b>	<b><math>q_{ITO}</math> (W)</b>	<b><math>\delta q_{ITO}</math> (W)</b>
59	0.27	15	0.59	3992	180
84	0.38	31	0.84	7999	264
102	0.46	46	1.02	11758	331
119	0.55	65	1.19	16402	400
132	0.61	80	1.32	20178	455
145	0.67	97	1.45	24346	514

Table 2.5. Uncertainties in measured vapour quality.

<b>G kg/m<sup>2</sup>.s</b>	<b><math>P_{ph}</math> [W]</b>	<b><math>\delta x_{in}</math> [-]</b>	<b><math>x_{in}</math> [-]</b>	<b><math>q</math> [W/cm<sup>2</sup>]</b>	<b><math>\delta x_{out}</math> [-] Low <math>x_{in}</math></b>	<b><math>\delta x_{out}</math> [-] High <math>x_{in}</math></b>	<b><math>x_{out}</math> [-] Low <math>x_{in}</math></b>	<b><math>x_{out}</math> [-] High <math>x_{in}</math></b>
50	59	1.25E-02	0.11	0.5	1.72E-02	2.11E-02	0.20	0.36
50	87	1.64E-02	0.27	1.0	1.93E-02	2.33E-02	0.28	0.43
75	72	9.80E-03	0.07	1.0	1.48E-02	1.86E-02	0.19	0.35
75	117	1.37E-02	0.23	3.0	2.03E-02	2.41E-02	0.39	0.56
100	126	1.09E-02	0.13	1.0	1.50E-02	1.85E-02	0.22	0.37
100	178	1.45E-02	0.28	3.0	1.90E-02	2.25E-02	0.37	0.53
200	241	9.89E-03	0.11	1.0	1.29E-02	1.65E-02	0.16	0.34
200	368	1.35E-02	0.29	3.0	1.45E-02	1.81E-02	0.25	0.42

Parameters computed from vapour quality include, superficial velocities and mean velocities. The uncertainties associated with all the computed parameters are determined according to Eq. 2.1.

## 2.4.2 Wall shear stress

The wall shear stress in the sapphire tube section is obtained from the momentum balance equation

for the mixture and given by;

$$\frac{dP}{dz} = -\frac{4}{D}\tau_w - \rho_m g \sin \theta - G^2 \frac{d}{dz} \left[ \frac{(1-x_z)^2}{\rho_l(1-\alpha_z)} + \frac{x_z^2}{\rho_v\alpha_z} \right] \quad 2.21$$

$$\frac{dP}{dz} = -\frac{4}{D}\tau_w - [\rho_l(1-\alpha_z) + \rho_v\alpha_z]g \sin \theta - G^2 \frac{d}{dz} \left[ \frac{(1-x_z)^2}{\rho_l(1-\alpha_z)} + \frac{x_z^2}{\rho_v\alpha_z} \right] \quad 2.22$$

Assuming constant fluid properties, integrating Eq. 2.22 from 0 to  $L$ , gives;

$$\begin{aligned} \frac{\Delta P}{L} = & -\frac{4}{D}\tau_w - [\rho_l(1-\alpha) + \rho_v\alpha]g \sin \theta \\ & - \frac{G^2}{L} \left[ \left( \frac{(1-x_{out})^2}{\rho_l(1-\alpha_{out})} + \frac{x_{out}^2}{\rho_v\alpha_{out}} \right) - \left( \frac{(1-x_{in})^2}{\rho_l(1-\alpha_{in})} + \frac{x_{in}^2}{\rho_v\alpha_{in}} \right) \right] \end{aligned} \quad 2.23$$

Where  $\tau_w$  is an average value of the wall shear stress along the length  $L$  and:

$$\alpha = \frac{1}{L} \int_0^L \alpha_z dz \quad 2.24$$

To obtain  $\alpha_z$ , measured void fraction at the outlet ( $\alpha_{out}$ ) of the heated tube was plotted versus the computed outlet ( $x_{out}$ ) vapour quality and a fitting was proposed. The fitted curve was used to compute the local void fraction ( $\alpha_z$ ) along the heated tube section corresponding to the local vapour quality ( $x_z$ ).

In a closed loop the total pressure drop term is the difference between the static pressures at points  $P_{in}$  and  $P_{out}$  in Figure 2.20. The measured differential pressure as provided by the deformation of the membrane of the differential pressure transducer is given by;

$$\Delta P_m = P_+ - P_- \quad 2.25$$

The total pressure drop is given by;

$$\Delta P = P_{out} - P_{in} = (P_- - \rho_l g H_-) - (P_+ - \rho_l g H_+) \quad 2.26$$

$$\Delta P = P_{out} - P_{in} = -(\Delta P_m + \rho_l g L \sin \theta) \quad 2.27$$

$\sin \theta$  is 1 for vertical upward flow and  $-1$  for vertical downward flow.



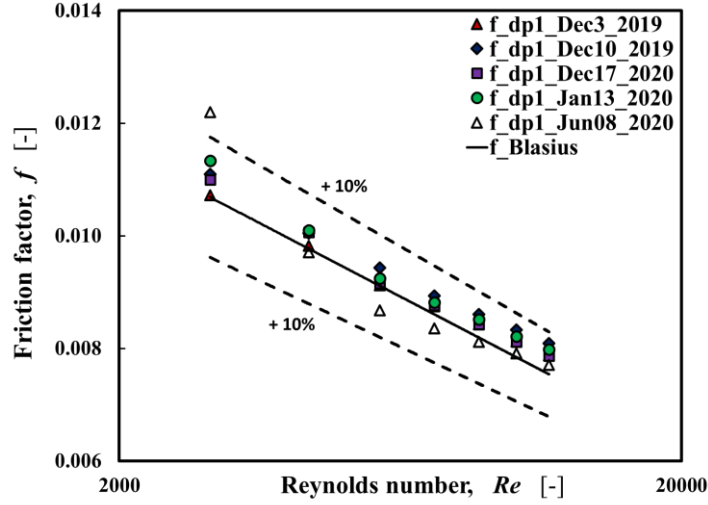


Figure 2.21. Comparison between experimental friction factor and friction factor obtained with the Blasius correlation.

### 2.4.3 Interfacial shear stress

The interfacial shear stress along the heated section of the tube in annular flow was obtained from the momentum balance equation for the vapour phase considering that it also includes the contribution of the interfacial mass transfer (Eq. 2.31).

$$\alpha_z \frac{dP}{dz} = -\frac{4\sqrt{\alpha_z}\tau_i}{D} - \rho_v \alpha_z g \sin \theta - G^2 \frac{d}{dz} \left[ \frac{x_z^2}{\rho_v \alpha_z} \right] - \Gamma_v u_i \quad 2.31$$

$$\frac{dP}{dz} = -\frac{4}{D\sqrt{\alpha_z}}\tau_i - \rho_v g \sin \theta - \frac{G^2}{\alpha_z} \frac{d}{dz} \left[ \frac{x_z^2}{\rho_v \alpha_z} \right] - \Gamma_v u_i \quad 2.32$$

Assuming constant fluid properties, integrating Eq. 2.32 from 0 to  $L$  gives;

$$\frac{\Delta P}{L} = -\frac{4}{D\sqrt{\alpha}}\tau_i - \rho_v g \sin \theta - \frac{G^2}{\alpha L} \left[ \frac{x_{out}^2}{\rho_v \alpha_{out}} - \frac{x_{in}^2}{\rho_v \alpha_{in}} \right] - \Gamma_v u_i \quad 2.33$$

where  $\alpha$  and  $\Delta P$  are determined from Eq. 2.24 and Eq. 2.27 respectively and the last term on the right-hand-side is often negligible. The uncertainty in the calculation of  $\tau_i$  is computed according to Eq. 2.1 using  $\delta D$ ,  $\delta x$  and  $\delta \alpha$ .



Table 2.6. Uncertainties in void fraction, frictional pressure drop, wall shear stress and heat transfer coefficient.

$\alpha$ [-]	$\delta\alpha$ [-]	$\delta\Delta P_f$ (Pa)	$\Delta P_f$ (Pa)	$\delta\tau_w$ (Pa) $\alpha = 0.3$	$\delta\tau_w$ (Pa) $\alpha = 0.7$	$\delta\tau_w$ (Pa) $\alpha = 0.9$	$\tau_w$ (Pa)	$q$ [W/cm <sup>2</sup> ]	$T_w - T_L$ [°C]	$\delta h$ [W/m <sup>2</sup> K]
0.3	0.018	64	500	0.48	0.91	1.14	3.1	0.5	5	229
0.7	0.042	139	1500	0.88	1.17	1.36	9.4	1.5	10	158
0.9	0.054	177	2500	1.36	1.57	1.71	15.6	3.0	18	114

Table 2.7. Uncertainties in vapour velocity, interfacial shear stress and interfacial friction factor.

$x$ [-]	$\alpha$ [-]	$\delta u_v$ [-]	$u_v$ [-]	$\Delta P_m$ (Pa)	$\delta\tau_i$ [-]	$\tau_i$ [-]	$\delta f_i$ [-]	$f_i$ [-]	$\delta f_i$ [%]
0.31	0.87	0.15	1.7	2586	0.34	3.4	4.45E-02	0.32	14.0
0.35	0.89	0.16	1.9	2630	0.34	3.1	3.49E-02	0.25	14.1
0.29	0.87	0.20	2.4	2498	0.34	3.7	2.32E-02	0.18	13.1
0.39	0.90	0.25	3.1	2312	0.35	4.3	1.46E-02	0.11	12.8
0.32	0.87	0.28	3.5	2441	0.34	4.0	1.14E-02	0.09	12.4
0.41	0.89	0.33	4.3	2144	0.35	4.9	8.60E-03	0.07	11.8
0.31	0.91	0.51	6.5	1681	0.39	8.1	6.01E-03	0.06	9.4
0.35	0.91	0.56	7.2	1282	0.42	8.9	5.27E-03	0.06	9.5

#### 2.4.4 Heat transfer coefficient

In both experimental setups, determination of inner wall heat transfer coefficient ( $h_i$ ) was done at four (4) axial locations along the heated tube section. Schematic drawing of the tube cross section is shown in Figure 2.22a and a schematic drawing showing the 4 locations where  $h_i$  was measured is shown in Figure 2.22b. In each of the 4 locations, a pair of PT100 probe was attached at opposite ends of the wall and used for measuring outer wall temperature ( $T_{ow}$ ). Fluid temperature measurement was done at the inlet and outlet of the sapphire tube using thermocouple  $T_3$  and PT100 probe *Sp14* respectively. In the case of BRASIL, measurement of differential fluid temperature was also done using T-type thermocouple. Fluid temperature at the 4 axial locations were determined by linear interpolation between inlet and outlet fluid temperatures. The heat transfer coefficient at the inner wall can be obtained from an energy balance between the fluid and the inner wall as follows;

$$h_i(T_{iw} - T_{i\infty}) = [q_{ow} - h_e(T_{ow} - T_{e\infty})] \frac{R_o}{R_i} \quad 2.34$$

$T_{iw}$ ,  $T_{ow}$ ,  $T_{i\infty}$ , and  $T_{e\infty}$  are inner wall, outer wall, fluid and ambient air temperatures respectively.  $R_i$

and  $R_o$  are inner and outer tube radii,  $q_{ow}$  is the applied wall heat flux while the term  $h_e(T_{ow} - T_{e\infty})$  is the heat loss to the surrounding. The method used for estimating heat losses in this work have been described earlier and the term in the square bracket (Eq. 2.34) is the effective wall heat flux ( $q_{eff}$ ). Applying the conduction equation to the heated tube wall gives;

$$T_{ow} - T_{iw} = q_{eff} \ln\left(\frac{R_o}{R_i}\right) \frac{R_o}{k} \quad 2.35$$

where  $k(= 22 \text{ W/mK})$  is the thermal conductivity of sapphire tube. Combining Eqs. 2.34 and 2.35 gives;

$$h_i = \frac{q_{eff}}{T_{ow} - T_{i\infty} - \ln\left(\frac{R_o}{R_i}\right) \frac{R_i}{k} q_{eff}} \quad 2.36$$

The uncertainty associated with the calculated heat transfer coefficient is given by;

$$\delta h_i = \left[ \left( \frac{\delta q_{eff}(T_{ow} - T_{i\infty})}{T_{ow} - T_{i\infty} - \ln\left(\frac{R_o}{R_i}\right) \frac{R_o}{k} q_{eff}} \right)^2 + \left( \frac{-q_{eff} \delta T_{ow}}{\left( T_{ow} - T_{i\infty} - \ln\left(\frac{R_o}{R_i}\right) \frac{R_o}{k} q_{eff} \right)^2} \right)^2 + \left( \frac{q_{eff} \delta T_{i\infty}}{\left( T_{ow} - T_{i\infty} - \ln\left(\frac{R_o}{R_i}\right) \frac{R_o}{k} q_{eff} \right)^2} \right)^2 \right]^{0.5} \quad 2.37$$

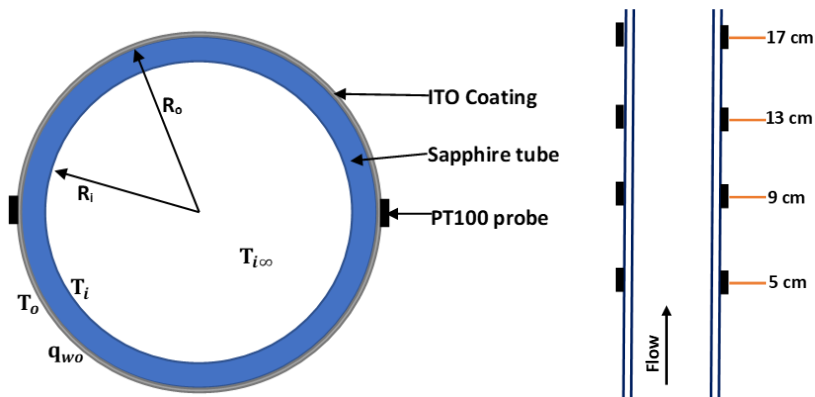


Figure 2.22. a. Schematic drawing of the heated tube cross section, b. Illustration of axial locations of PT100 probes for wall temperature measurements.

Single-phase measurements at moderate wall heat flux were carried out to provide validation for the

measurement technique. The measured single-phase Nusselt number ( $Nu$ ) was compared to Gnielinski (1976)'s correlation (Eq. 1.82). Figure 2.23a shows measurement obtained the 4 axial locations along the tube without correction for thermal development or heat losses. As expected, the Nusselt numbers were higher than that predicted by Gnielinski (1976)'s correlation. Figure 2.23b shows the experimental Nusselt number after correction with (Al-Arabi, 1982)'s correlation. After correction for thermal development, most of the experimental Nusselt numbers at various axial locations were within  $\pm 15\%$  of the (Gnielinski, 1976)'s correlation. Figure 2.23c shows experimental Nusselt number after correction for both thermal development and heat losses. Again, most of the experimental data were within  $\pm 15\%$  of the (Gnielinski, 1976)'s correlation. This provides validation to the experimental technique.

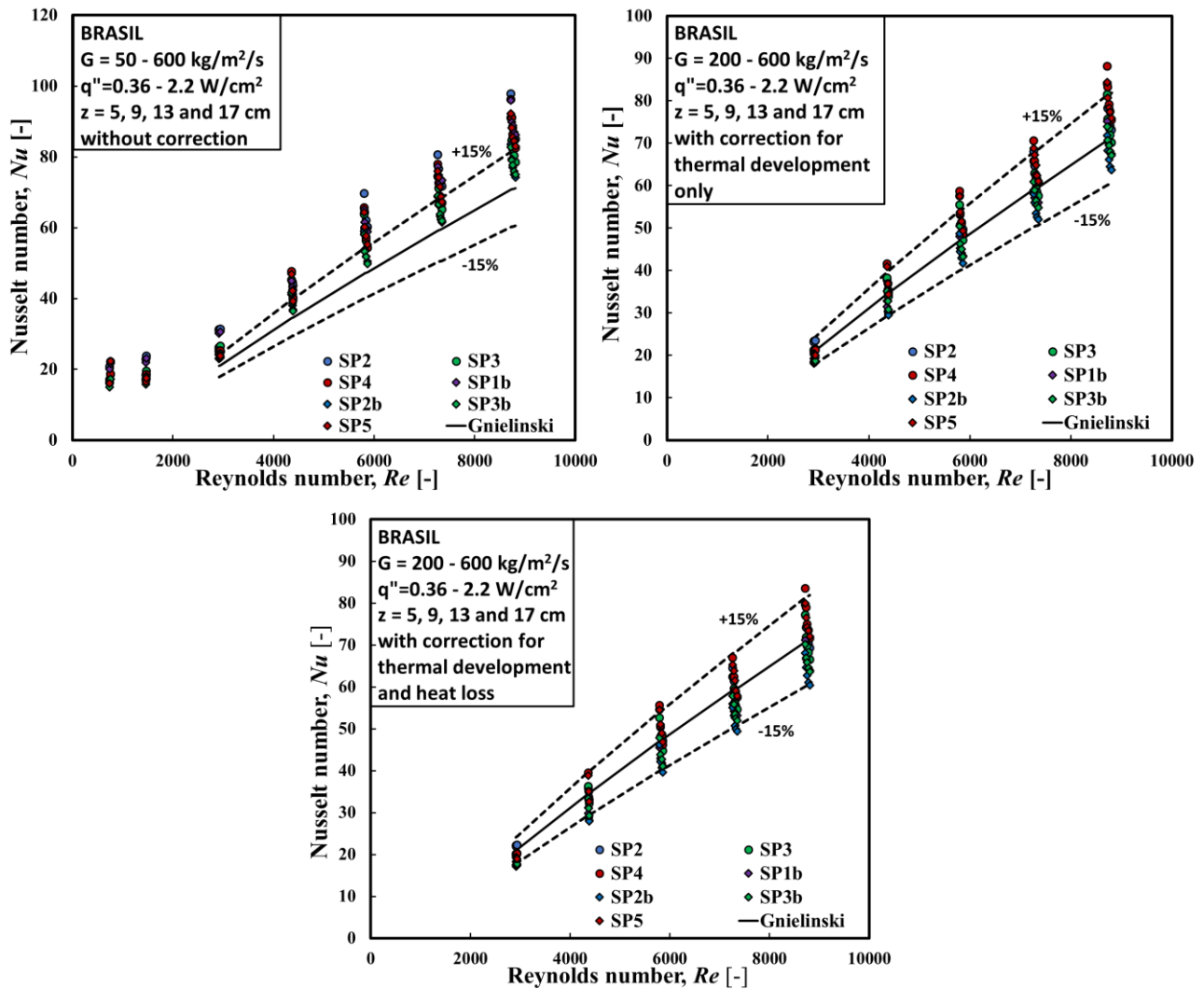


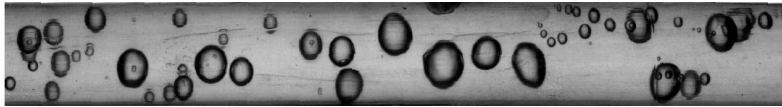
Figure 2.23. Nusselt number versus Reynolds number for single-phase upward flow.

### 2.4.5 Bubble geometry and wave structures

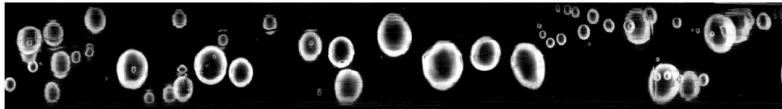
MATLAB image processing toolbox was used for determining the mean bubble diameter and eccentricity in the visualisation section of the COSMO setup ( $\mu g$ ). This was done by the detection of bubble contours. The characterization of interface structures and Taylor bubble velocity were performed by image processing of high-speed visualizations and especially of the analysis of space-time diagrams. Wave velocity and frequency were determined in the heated section for both experimental setups ( $+1g, -1g, \mu g$ ) while Taylor bubble velocity was determined in the visualisation section of the COSMO setup ( $\mu g$ ).

The following steps were followed in the determination of bubble size and bubble eccentricity (this is a measure of the non-circularity of bubbles and its value is 0 for a circle and 1 for straight line);

1. Edge detection of the tube exterior walls.



2. Image masking using background image (single phase flow image).



3. Image adjustments (contrasting and brightening).
4. Image binarization.



5. Filling of holes and general image morphing.



6. Contour detection.

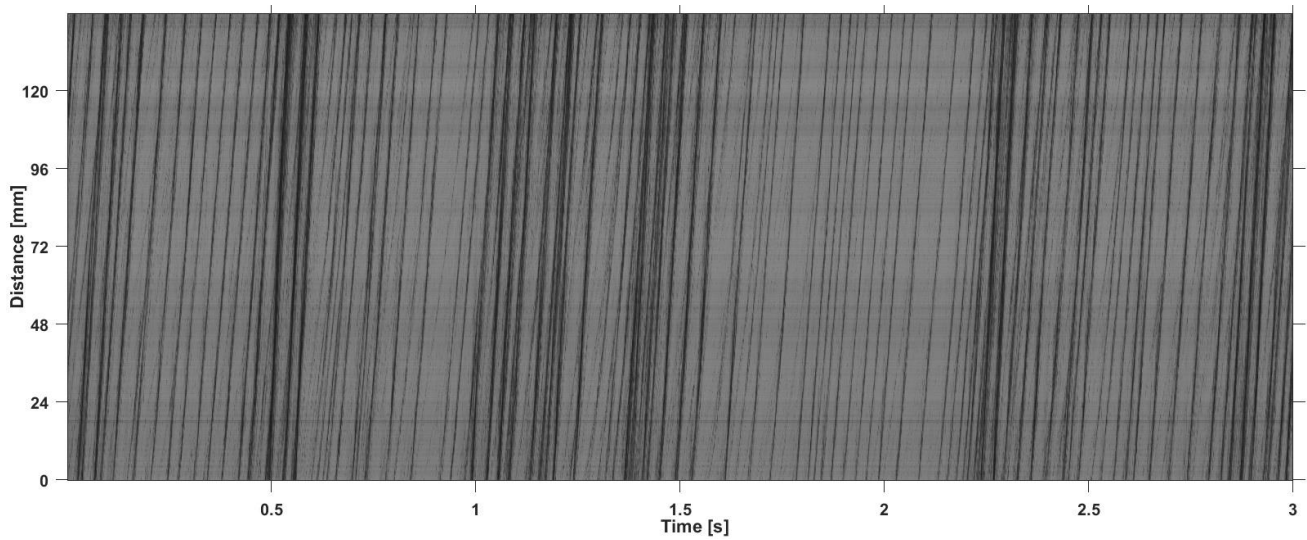


7. Determination of the equivalent bubble diameter and bubble eccentricity. The equivalent bubble diameter is the diameter of a circle with the same area as the bubble, returned as a scalar and computed as  $(\sqrt{4 \times Area/\pi})$ . Where, *Area* is the actual number of pixels

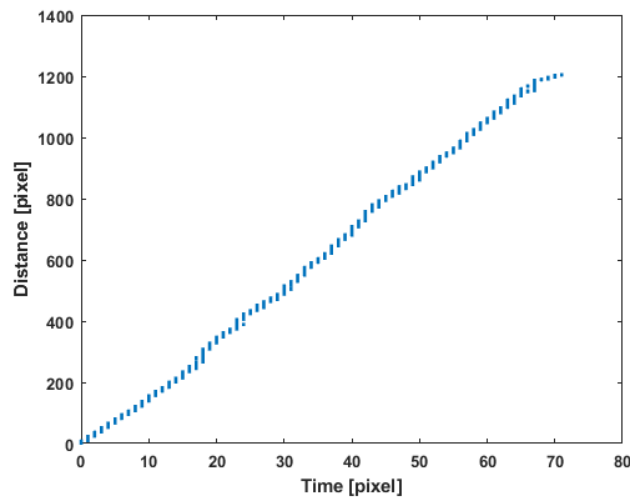
corresponding to the bubble, returned as a scalar. The eccentricity is the ratio of the distance between the foci of the ellipse and its major axis length. The value is between 0 and 1. (0 and 1 are degenerate cases. An ellipse whose eccentricity is 0 is actually a circle, while an ellipse whose eccentricity is 1 is a line segment). The major axis length, is the length (in pixels) of the major axis of the ellipse that has the same normalized second central moments as the bubble, returned as a scalar.

The following steps were followed in determining the Taylor bubble and wave velocity;

1. Edge detection of the tube exterior walls (see above).
2. Extraction and time-sequencing of the tube centreline images (space-time diagrams).



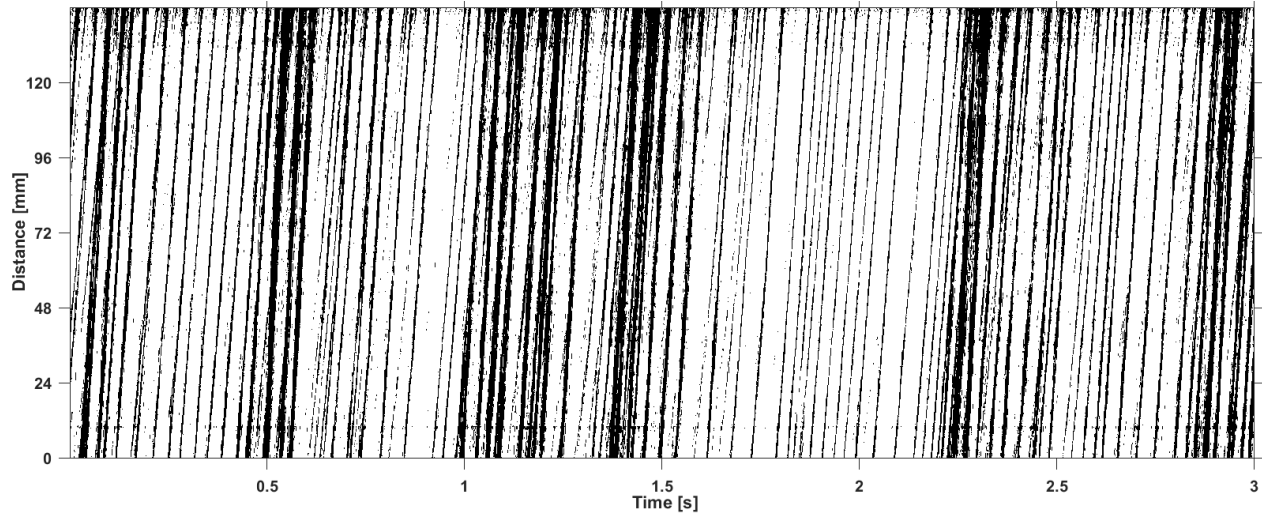
3. Search for maximum lag (time step) of axial displacement of waves.



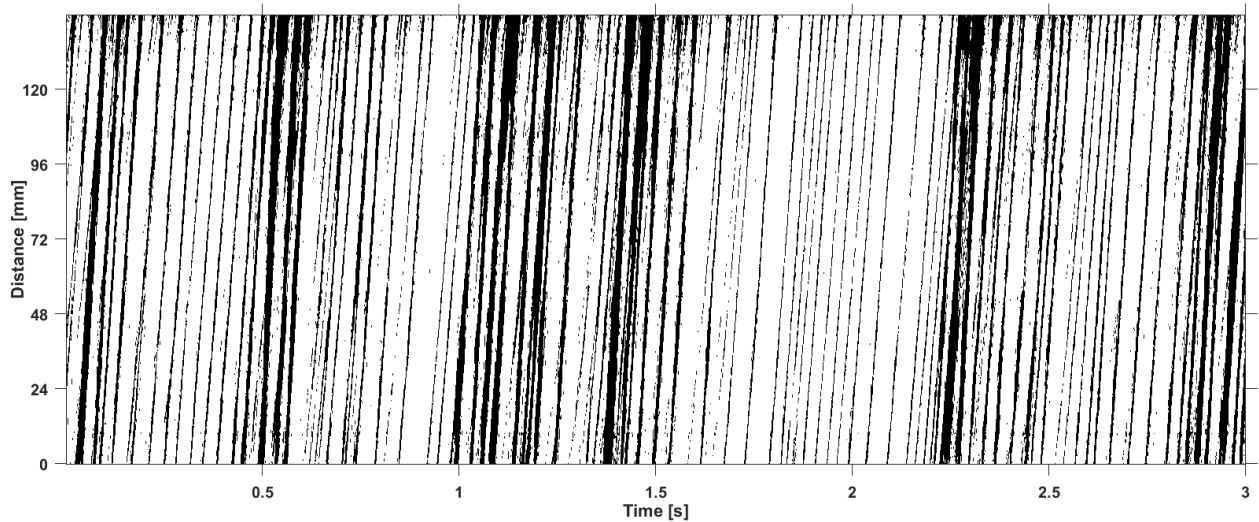
4. Determination of the slope from the axial displacement and time lag.
5. Calculation of the velocity.

The following steps were followed in the determination of wave frequency;

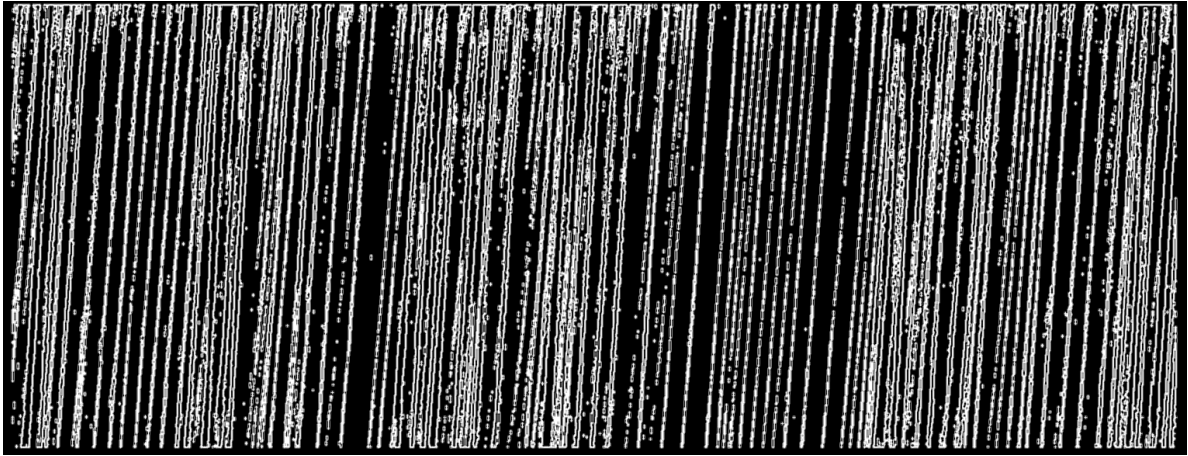
1. Edge detection of the tube exterior walls (see above).
2. Extraction and time-sequencing of the tube centreline images (see above).
3. Image binarization of space-time diagrams.



4. Image morphing (erode, dilate and fill).



5. Search for edges of roll waves (edges of black lines in the space-time diagrams).



6. Determination of minimum spacing between successive waves.
7. Calculation of the wave frequency.

## 2.5 Parabolic Flight Experiments

In this study, some experiments were carried out in microgravity (near weightless) conditions during the CNES PFC 161 parabolic flight campaign in Bordeaux-Merignac airport France from 20<sup>th</sup> September 2021 to 1<sup>st</sup> October 2021. Parabolic flights provide a platform for short-term scientific study in reduced gravity as well as a platform for functionality test of instrumentation and facilities prior to their deployment for long-term space projects. Parabolic flights are the only sub-orbital platform that allows the experimentalists to interact directly with their experimental facility during the reduced gravity phase of the experiments.

Experiments were carried out onboard the Airbus A310 ZERO-G aircraft. The aircraft and parabolic flight campaigns are managed by Novespace in collaboration with the French Space Agency (CNES) and the European Space Agency (ESA). The aircraft simulates various gravity levels ranging from  $0g$  through  $+1g$  to  $1.8g$  during a series of parabolic manoeuvres. The interval between the start of two consecutive manoeuvres was 3 *mins* which consisted of 1.15 *mins* between the start and end of each parabola and 1.45 *mins* between the end of one parabola and the start of the next parabola. During the parabolic manoeuvres, the pilots have to minimise the lift force and also balance the drag force with the engine thrust. A parabolic manoeuvre included;

- a horizontal steady flight phase lasting about 1.45 *mins* during which the aircraft simulates  $+1g$ . This period was mostly used to adjust experimental conditions and record data from the preceding parabola.

- a pull-up flight phase where the nose of the aircraft is pulled up from  $0^\circ$  gradually to around  $+47^\circ$  and the aircraft ascends during the pull-up. This phase last for about 24 s and the gravity level during this phase is typically around  $+1.8g$ .
- an injection phase where the pilot reduces the engine thrust to the minimum required to compensate for air-drag and the free fall trajectory. The injection starts when the nose of the aircraft is at around  $+47^\circ$  and the injection phase, which also corresponds to the  $\mu g$ -phase last for about 22 s.
- A pull-out phase which starts at  $-45^\circ$  to  $0^\circ$  where the nose the aircraft descends until it returns to its initial horizontal steady flight mode. The gravity level during the pull-out phase is typically around  $+1.8g$  and lasts for about 22 s.
- There is a transition phase immediately before and immediately after of the  $\mu g$ -phase each lasting about 3 s.

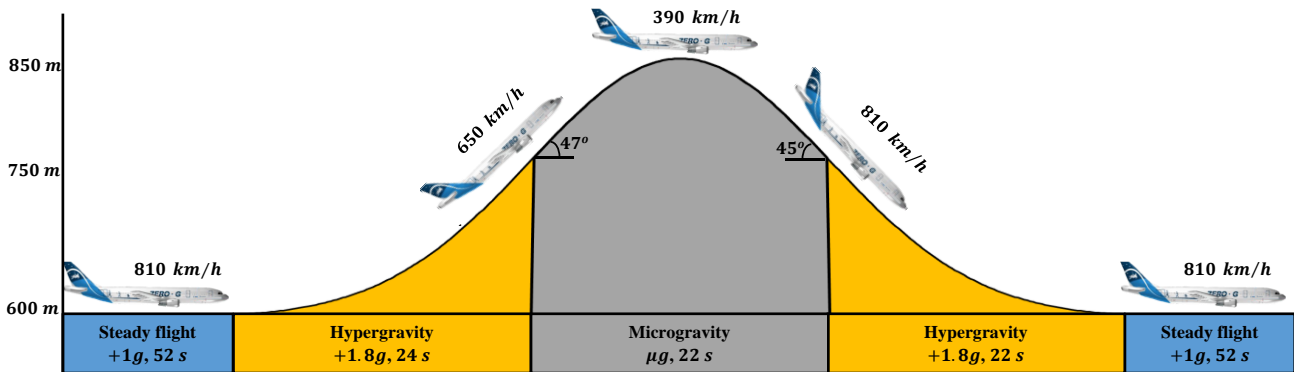


Figure 2.24. Parabolic flight trajectory.

A series of 93 parabolas (31 each day) were done over a 3-day flight campaign. During each parabola, the fluid was allowed to circulate in the loop at set conditions of mass flux, heat flux and preheater power. Data acquisition for all parameters commenced just before the pull-up phase (hypergravity) except for flow visualisation and void fraction measurements which commenced just after the pull-up phase (or start of  $\mu g$ -phase). After each parabola, LabVIEW data and camera recording were saved into the CPU. The same procedure was followed for all the parabolas. Typically, between 3 and 4 persons were required to manage the experimental setup and carryout measurements. Constant communication was maintained between the experimentalists to ensure experiments went according to plan and with minimum problems.



Some challenges and constraints are associated parabolic flight experiments in general and the CNES PFC 161 parabolic flight campaign in particular. These include:

- Parabolic flight campaigns are constrained by limited measurement time and limited number of experiments. The microgravity phase is restricted to around 22 s and the number of parabolas is limited which reduces the number of different measurements that can be carried out and limits the number of runs for each measurement condition.
- The experimental loop for parabolic flight campaign is required to be compact and below a certain weight limit. This limits the length of the preheater and test section and consequently the establishment length. This size limitation also factors into component selection such as pump and flow meter which can be used in the setup. In the case of CNES PFC 161 parabolic flight campaign, pump failure occurred in some of the runs.
- Another constraint is the significant restrictions imposed by the parabolic flight managers on to protect the experimentalists. The hydraulic loop must be leak-proof and the structural framework of the loop must be able to withstand bending at hypergravity conditions. These limit the ability of the experimentalists to access the interior parts of the loop in the event of problems. In the case of CNES PFC 161 parabolic flight campaign, bubble entrapment in the pressure lines occurred quite frequently during the  $\mu g$ -phase of measurements.
- Parabolic flight campaigns also have significant restrictions to power supply and maximum temperature limits. In general, fluids with low saturation temperatures are required and only limited heat flux can be applied at the test section.
- The sudden changes in gravity levels have significant influence on flow parameters such as pressure, flow rate and flow establishment. The volumetric pump and the use of PID ensured that fairly constant flowrate was achieved throughout the parabola. In the case of CNES PFC 161 parabolic flight campaign, pressure regulation was achieved only to a limited extent by PID. The wall temperature of the sapphire tube also slightly evolved during the parabola but quickly stabilised in microgravity. Special care was taken in the averaging of the data ensuring that a steady state was reached.

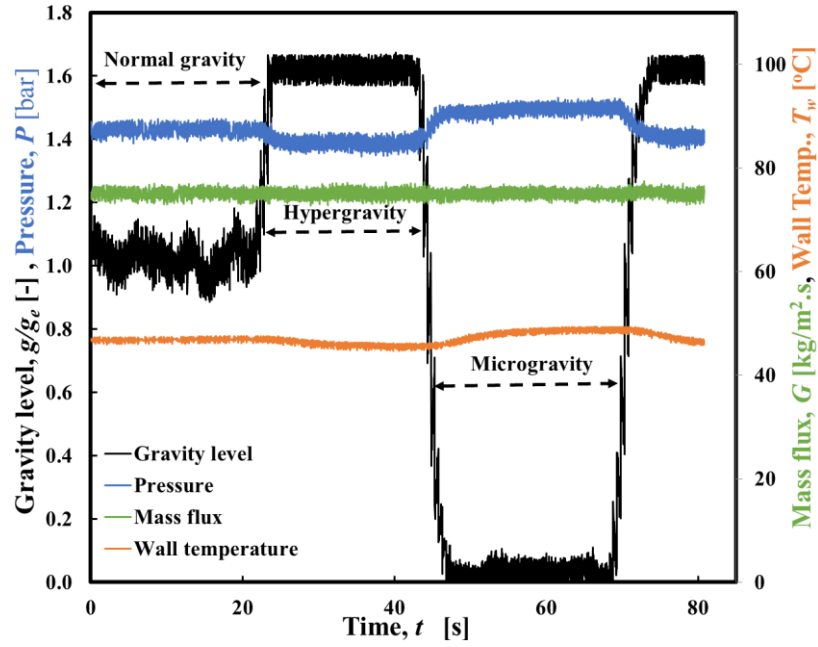


Figure 2.25. Time evolution of mass flux, pressure and wall temperature under various gravity conditions in parabolic flight.

The experimental conditions investigated during the CNES PFC 161 parabolic flight campaign is summarised in Table 2.8.

Table 2.8. Summary of test conditions for CNES PFC 161 microgravity parabolic flight campaign.

Mass flux	Power supply to preheater 2, $ph2$ (W)	Subcooled Temp. or quality at the inlet of test section, $ts$	Heat flux and Maximum quality at the outlet of the test section
50 kg/m <sup>2</sup> .s	0 10 28 53 135	$T_{Sub\_in\_ts} \approx 10^{\circ}C \pm 1.5^{\circ}C$ $T_{Sub\_in\_ts} \approx 5^{\circ}C \pm 1.5^{\circ}C$ $x_{in\_ts} \approx 0.05 \pm 0.025$ $x_{in\_ts} \approx 0.2 \pm 0.025$ $x_{in\_ts} \approx 0.3 \pm 0.025$	$q_w \approx 0.5, 1.0, 1.5 W/cm^2$ $x_{out\_max} \approx 0.7$
75 kg/m <sup>2</sup> .s	0 14 41 80 176	$T_{Sub\_in\_ts} \approx 10^{\circ}C \pm 1.5^{\circ}C$ $T_{Sub\_in\_ts} \approx 5^{\circ}C \pm 1.5^{\circ}C$ $x_{in\_ts} \approx 0.05 \pm 0.025$ $x_{in\_ts} \approx 0.2 \pm 0.025$ $x_{in\_ts} \approx 0.3 \pm 0.025$	$q_w \approx 0.5, 1.0, 1.5, 2.0 W/cm^2$ $x_{out\_max} \approx 0.7$
100 kg/m <sup>2</sup> .s	0 18 53 107	$T_{Sub\_in\_ts} \approx 10^{\circ}C \pm 1.5^{\circ}C$ $T_{Sub\_in\_ts} \approx 5^{\circ}C \pm 1.5^{\circ}C$ $x_{in\_ts} \approx 0.05 \pm 0.025$ $x_{in\_ts} \approx 0.2 \pm 0.025$	$q_w \approx 0.5, 1.0, 1.5, 2.0 W/cm^2$ $x_{out\_max} \approx 0.5$

	124	$x_{in\_ts} \approx 0.3 \pm 0.025$	
$150 \text{ kg/m}^2\text{s}$	0	$T_{Sub\_in\_ts} \approx 10^{\circ}\text{C} \pm 1.5^{\circ}\text{C}$	$q_w \approx 0.5, 1.0, 1.5, 2.0 \text{ W/cm}^2$ $x_{out\_max} \approx 0.3$
	81	$T_{Sub\_in\_ts} \approx 5^{\circ}\text{C} \pm 1.5^{\circ}\text{C}$	
	124	$x_{in\_ts} \approx 0.2 \pm 0.025$	
$1.2 \text{ bar} \leq P_2 = P_{in\_ts} \leq 1.4 \text{ bar}, 30^{\circ}\text{C} \leq T_3 = T_{in\_ph2} \leq 35^{\circ}\text{C}, T_{in\_pump} = T_6 \leq 25^{\circ}\text{C}$			

## 2.6 Conclusion

*The two flow boiling loops used in this work were built at IMFT with the aim of carrying out experiments in upward, downward and microgravity flow conditions. The flow facilities were equipped with advanced diagnostics to enable the determination of two-phase parameters such as void fraction, flow pattern, wave structures, wall shear stress, interfacial shear stress and heat transfer coefficient. Some of the diagnostics included capacitance void fraction probes, high speed cameras, thermocouples, Pt100 temperature probes, absolute pressure sensors and differential pressure transducers. The various diagnostics were carefully calibrated and single-phase flow validation tests were carried to increase confidence of measurements. The experimental facilities were used on ground for upward and downward flow experiments and on-board a Zero-G aircraft for microgravity experiments. Experimental measurements were focussed on the heated test section with the view of bridging the research gap in this area. Although these two loops were not built specifically in the frame of this PhD thesis, they were strongly modified for the present study (downward flow for BRASIL, implementation of a flow boiling test section for Cosmo) and a special care was devoted to validation of the measurement technics and quantification of errors. The experimental results are presented in the following chapters along with comparisons with existing models and development of new models.*

## **Chapter 3**

### **Results of Hydrodynamics of Upward and Downward Flow Boiling**

*This section mainly consists of a long article we recently published in International Journal of Multiphase flows with extended results on hydrodynamics of flow boiling in upward and downward flows. The experimental results presented in the article include; flow pattern, void fraction, wave structures, wall and interfacial shear stresses as well as heat transfer coefficient. The experimental results are also compared with relevant correlations and new correlations were also proposed in the article. The article is followed by additional results such as the modelling of wave structures and interfacial friction factor in downward flow, that were not part of the article.*

## 3.1 Article on the Hydrodynamics of Upward and Downward Flow Boiling

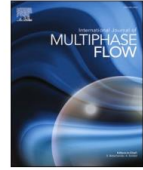
International Journal of Multiphase Flow 153 (2022) 104120



Contents lists available at ScienceDirect

International Journal of Multiphase Flow

journal homepage: [www.elsevier.com/locate/ijmulflow](http://www.elsevier.com/locate/ijmulflow)



# Hydrodynamics of vertical upward and downward flow boiling in a millimetric tube

Paul Onubi Ayegba, Julien Sebilliau, Catherine Colin\*

Institut de Mécanique des Fluides de Toulouse – Université de Toulouse – CNRS-INPT-UPS, Allée Camille Soula, 31400, Toulouse, France

### ARTICLE INFO

#### Keywords:

Flow boiling  
Wall shear stress  
Heat transfer coefficient  
Interfacial friction factor  
Wave structures  
Flow visualization

### ABSTRACT

Upward and downward vapor-liquid vertical flows inside a vertical 6 mm sapphire tube was investigated using HFE-7000 as working fluid. The goal was to investigate the effect of flow direction and wall heating on two-phase parameters such as flow pattern, wall shear stress ( $\tau_w$ ), interfacial shear stress ( $\tau_i$ ) and interfacial wave structures. The mass flux, heat flux and vapor quality ranges were  $50 \leq G \leq 400 \text{ kg/m}^2 \cdot \text{s}$ ,  $0 \leq q \leq 3 \text{ W/cm}^2$  and  $0 \leq x \leq 0.7$  respectively. Bubbly, slug, churn, annular flow patterns were observed in upward and downward flows. A falling film regime occurred in downward flow at low mass fluxes. Void fractions were higher in downward flow than in upward flow due to gravity effect, and were in good agreement with drift flux models of the literature. The wall shear stress increased with the wall heat flux due to the bubble nucleation at the wall. Following a similar approach to Kim and Mudawar (2013b), a correlation for the wall shear stress taking into account the forced convection and the bubble nucleation was derived and provided a good estimation of the experimental data within  $\pm 20\%$ . From image processing of the high-speed visualizations, velocities ( $U_w$ ) and frequencies ( $F_w$ ) of the disturbance waves in annular flow were measured. The interfacial shear stress was found to directly depend of the product  $U_w \times F_w$  and a prediction of the interfacial friction factor was proposed in flow boiling for both upward and downward flows.

### 1. Introduction

Two-phase flows are commonly encountered in chemical, nuclear and petroleum industries as well as other engineering applications. Recent improvements in the design and operation of thermal management systems have sort to strike a balance between improved heat dissipation and overall weight of the devices. One approach that has attracted significant research interests is the use of phase-change heat transfer. Boiling thermal management systems take advantage of the latent heat in phase change (Enoki et al., 2020; Kim and Mudawar, 2014). Boiling flow is, however, characterized by a complex interplay of hydrodynamics, mass transfer, heat transfer and interfacial phenomena. At low mass flux, boiling flows are also sensitive to gravity and the effect of gravity on such flows remains a subject of interest (Kharangate et al., 2016; Konishi and Mudawar, 2015). In horizontal or inclined tubes, gravity tends to stratify the vapor/liquid flows or at least to induce some topological asymmetry. Even in a vertical configuration, experiments at  $+1g$  (upward flow) and  $-1g$  (downward flow) point out significant differences in the flow hydrodynamics and heat transfers due to the

gravity (Kharangate et al., 2016; Konishi and Mudawar, 2015). A comparison of these two configurations provides useful information on the gravitational effects on two-phase flows.

Numerous studies of vertical two-phase flow patterns have been performed under adiabatic (Taitel et al. 1980, Mishima and Ishii, 1984; Bhagwat and Ghajar, 2017, 2014) and boiling (Chen et al., 2006; Enoki et al., 2020) conditions. These flow patterns include mainly bubbly, intermittent (slug and churn), falling-film (only in downward-inclined flow) and annular flows. Two-phase flow characteristics, such as bubble size and shape in bubbly flow or the liquid film thickness in annular flow have been shown to be influenced by both the flow direction (Bhagwat and Ghajar, 2012) and the gravity level (Narcy et al., 2014). Transition between the various flow patterns have also been investigated for both adiabatic (Taitel et al. 1980, Wu et al., 2017) and boiling two-phase flows. Bubbly-slug transition is due to bubble coalescence (Colin et al., 1996) and most bubbly-slug transition criteria have been based on a critical value of the void fraction (Mishima and Ishii, 1984; Usui, 1989). Studies have also shown important differences between bubbly-slug transition in fully-developed adiabatic flow and developing

\* Corresponding author.

E-mail address: [catherine.colin@imft.fr](mailto:catherine.colin@imft.fr) (C. Colin).

<https://doi.org/10.1016/j.ijmulflow.2022.104120>

Received 5 January 2022; Received in revised form 19 April 2022; Accepted 4 May 2022

Available online 6 May 2022

0301-9322/© 2022 Elsevier Ltd. All rights reserved.

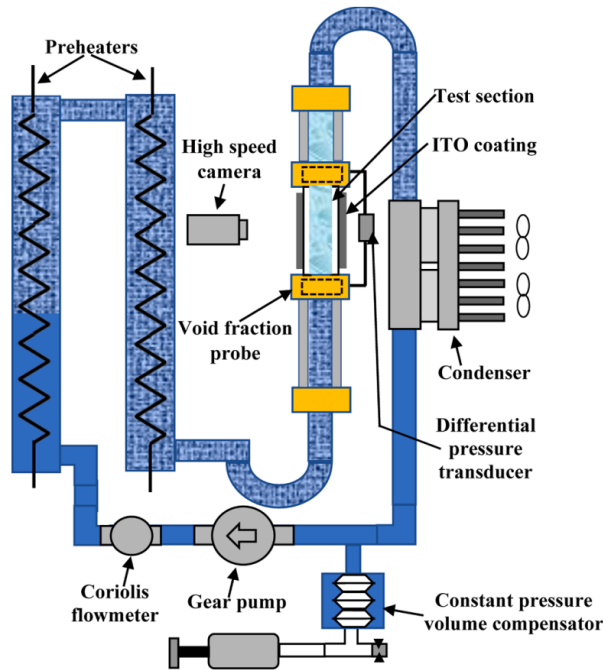


Fig. 1. Experimental set-up.

boiling flow (Celata and Zummo, 2009; Narcy et al., 2014). Several intermittent-annular flow transition criteria based on void fraction, Weber number of the vapor core and Froude number of the liquid have been proposed (Mishima and Ishii, 1984; Taitel et al., 1980; Usui, 1989; Wu et al., 2017). Most of the studies of flow patterns and flow pattern transition have focused on adiabatic (upward and downward) or boiling upward two-phase flow. There are very limited investigations on flow pattern and flow pattern transitions in downward flow boiling. However downward flow are also of interest for some applications including tubular co-current and counter current heat exchangers and distillation processes involving downward falling film flow.

Void fraction ( $\alpha$ ) is important for the determination of the vapor velocity ( $U_v = j_v/\alpha$ ,  $j_v$  being the superficial vapor velocity) in bubbly/slug flows and for the estimation of the liquid film thickness in annular flows. Techniques for measuring void fraction are mainly based on fluid conductance or fluid capacitance (Canière et al., 2007; Ceccio and George, 1996; Gardenghi et al., 2020). The evolution of void fraction with superficial gas velocity or quality have been shown to be sensitive to gravity (Almabrok et al., 2016; Bhagwat and Ghajar, 2012; Narcy et al., 2014). This is due to the changes in drift velocity ( $U_{\infty}$ ) with gravitational acceleration in bubbly and slug flow regimes and the liquid film thickness in annular flow. Measurements of void fraction in downward boiling flow are limited.

Experimental measurements of wall shear stress ( $\tau_w$ ) in two-phase flow have been focused on adiabatic flows or on the adiabatic section of boiling flows (Dalkilic et al., 2008; Khodabandeh, 2005; Maqbool et al., 2012). Several correlations and models have been developed based on the compilation of extensive experimental pressure drop data (Lockhart and Martinelli, 1949; Muller-Steinhagen and Heck, 1986; Cioncolini and Thome, 2017; Kim and Mudawar, 2014). Fewer measurements of the wall shear stress have been performed on diabatic test section. It has been reported that there is significant difference between wall shear stress in adiabatic section of a boiling flow and in the boiling flows section itself, especially in the nucleate boiling regime (Layssac, 2018). Bubble nucleation at the heated wall in boiling flows alters the velocity profile close to the wall which in turn modifies the wall shear

stress. Quantification of the effect of wall heat flux on wall shear stress is limited (Kim and Mudawar, 2013b). Most of the existing models for the wall shear stress do not account for the effect of wall heat flux. Furthermore, wall heat transfer is linked to the friction velocity ( $u^* = \sqrt{\tau_w/\rho_l}$ ) and accurate measurement of wall shear stress in the heated tube section provides bases for the development of models for predicting wall heat transfer (Cioncolini and Thome, 2011).

The interfacial shear stress ( $\tau_i$ ) is of a great importance in the dynamics of annular flows. At the time of this report, the authors are not aware of any experimental data on interfacial shear stress in the heated section of boiling flows. Data reported in the literature on the measurement of interfacial shear stress concerns adiabatic flows (Asali et al., 1985; Fore et al., 2000; Fukano and Furukawa, 1998; Narcy et al., 2014). This is particularly the case with downward boiling flow. However, there is significant data on interfacial shear stress measurements in the adiabatic section of boiling flows. Models for predicting the interfacial friction factor ( $f_i$ ) have been focussed on two-phase flows at very high gas Reynolds number ( $Re_g \geq 30,000$ ,  $f_g \approx 0.005$ ) (Belt et al., 2009; Wallis, 1969). Under such flow conditions, the interfacial friction factor is a function of the liquid film thickness ( $\delta$ ) alone. At lower gas Reynolds number, the turbulent gas flow is not fully developed and Fore et al. (2000) demonstrated that the interfacial friction factor was a function of both the liquid film thickness and the Reynolds number of the gas core flow. They proposed modifications to the model of Wallis (1969) to account for the gas Reynolds number dependence. Interfacial shear stress strongly depends on the wave parameters such as wave amplitude, wave velocity and wave frequency. These parameters have mainly been investigated in adiabatic gas-liquid flows (Azzopardi, 1986; Barbosa et al., 2003; Dasgupta et al., 2017) for the prediction of liquid droplet entrainment. Measurement of wave parameters in flow boiling are limited especially in downward flows. Experimental data on wave parameters provides bases for developing or improving models for predicting interfacial friction factor. Models and correlations linking wave parameters to interfacial friction factor are also limited in the literature. Such models could provide a means of quantifying the interfacial friction factor from easily accessible data.

In flow boiling, numerous studies focused on the measurements and modelling of heat transfer. Review articles provide very useful correlations based on analysis of very large experimental data bases in the convective boiling regime (Cioncolini and Thome, 2011) and in the convective and nucleate boiling regimes (Kandlikar, 1990; Kim and Mudawar, 2013a).

The reviewed literature shows that there is limited data on downward flow boiling. It also shows limited data on the effect of bubble nucleation on wall and interfacial shear stresses in both upward and downward flows. This work therefore focusses on the hydrodynamics of flow boiling in the heated section of a vertical 6 mm internal diameter tube for both upward and downward flows. The paper begins with a description of the experimental facility, measurement techniques used and data reduction methods applied. This is followed by the presentation of experimental results; flow visualization, void fraction, wall shear stress, interfacial shear stress and structure of the liquid film in annular flow. The experimental results are also compared with existing and proposed correlations.

All the data presented in this manuscript are provided as a supplementary material.

## 2. Experimental setup and measurement techniques

### 2.1. Hydraulic loop

The experimental setup used for this work was designed for flow boiling experiments in millimetric tubes (Fig. 1). The working fluid used was 1-methoxyheptafluoropropane ( $C_3F_7OCH_3$ ) refrigerant, commonly called HFE-7000. Liquid HFE-7000 was first pumped by a gear pump



**Table 1**  
Test conditions.

	Upward flow	Downward flow
$1.2 \leq P \leq 1.5 \text{ bar}$	$15 \leq \Delta T_{\text{sub}} \leq 5^\circ\text{C}$ , $0 \leq x_{\text{in}} \leq 0.3$	$15 \leq \Delta T_{\text{sub}} \leq 5^\circ\text{C}$ , $0 \leq x_{\text{in}} \leq 0.3$
$G \approx 50 \text{ kg/m}^2\text{s}$	$q_w = 0.5, 1.0, 1.5$ and $2.0 \text{ W/cm}^2$	$q_w = 0.5, 0.75, 1.0$ and $1.5 \text{ W/cm}^2$
$G \approx 75 \text{ kg/m}^2\text{s}$	$q_w = 0.75, 1.0, 1.25, 1.5$ and $2.0 \text{ W/cm}^2$	$q_w = 0.50, 0.75, 1.0, 1.5$ and $2.0 \text{ W/cm}^2$
$G \approx 100 \text{ kg/m}^2\text{s}$	$q_w = 1.0, 1.5, 2.0, 2.5$ and $3.0 \text{ W/cm}^2$	$q_w = 0.75, 1.0, 1.25, 1.5$ and $2.0 \text{ W/cm}^2$
$G \approx 200 \text{ kg/m}^2\text{s}$	$q_w = 1.0, 1.5, 2.0, 2.5$ and $3.0 \text{ W/cm}^2$	$q_w = 1.0, 1.5, 2.0, 2.5$ and $3.0 \text{ W/cm}^2$
$G \approx 400 \text{ kg/m}^2\text{s}$	$q_w = 1.0, 1.5, 2.0, 2.5$ and $3.0 \text{ W/cm}^2$	$q_w = 1.0, 1.5, 2.0, 2.5$ and $3.0 \text{ W/cm}^2$

(L21755 Micropump, with the DC-305A motor) and the liquid flow rate was measured using a Coriolis flow meter. The liquid was then preheated using two pre-heaters connected in series. Preheated single-phase liquid or two-phase vapor-liquid flow entered a 22 cm long vertical adiabatic section located just upstream of the test section. The adiabatic section was made of stainless steel which was insulated and this section enabled the flow to fully develop. The flow then entered the test section at pressures which can be varied from 1 to 2 bar ( $34^\circ\text{C} < T_{\text{sat}} < 54^\circ\text{C}$ ) and a mass flux in the range of  $40 \text{ kg.m}^{-2}\text{s}^{-1} < G < 400 \text{ kg.m}^{-2}\text{s}^{-1}$  can be attained in the loop. The test section consisted of a vertical transparent sapphire tube of 6 mm ID, 200 mm long and 1 mm thick, coated externally with ITO for Joule heating. The thickness of the ITO coating was 100 nm and the coated length was 180 mm. The coating was transparent allowing flow visualization with a high-speed camera. Vapor quality at the outlet of the test section was determined by enthalpy balance along the test section and in general an outlet vapor quality of up to 0.9 is attainable in the loop. Fluid exiting the test section was condensed and cooled to the desired temperature at the inlet of the pump using two PID-controlled Peltier modules in the condenser. The pump inlet temperature was set to  $\leq T_{\text{sat}} - 10^\circ\text{C}$ . Table 1 provides a summary of test conditions at the inlet of the test section along with the nominal heat flux at the test section. Three experimental runs were carried out for each condition provided in Table 1. This experimental set-up allowed the determination of void fraction, vapor velocity, wall shear stress, interfacial shear stress and heat transfer coefficient in a vertical tube of 6 mm ID and 8 mm OD in upward and downward vertical flow configurations. Analysis of images obtained from high-speed visualization was also used in this work to describe the flow patterns and interfacial structures in annular flow.

## 2.2. Measurement techniques

Various measurement instruments were used to acquire data and these included flow meter, differential pressure transducers, absolute pressure transmitters, thermocouples, PT100 temperature probes, void fraction probes and a high-speed camera. The flow meter employs the Coriolis effect for the determination of mass flowrate with a quoted accuracy of 0.5% FS (full scale). Differential pressure measurements were done using a Validyne differential pressure (DP) transducer (model P305D,  $56 \text{ cmH}_2\text{O}$  (FS),  $\delta DP = \pm 2.8 \text{ mmH}_2\text{O}$ ). Absolute pressure measurements were done using Keller PAA21 pressure transducers with measurement range and accuracy of 0–5 bars and  $\pm 0.25 \text{ mbar}$  respectively. These transducers provide means for measuring pressures at the different sections of the loop which were used for determining saturation temperature and for computing fluid properties. Fluid temperature measurements at various sections of the loop were done using K-type thermocouples with a stated accuracy of  $\pm 0.25^\circ\text{C}$ . Two T-type thermocouples (accuracy  $\pm 0.1^\circ\text{C}$ ) were also connected at the inlet and outlet of the sapphire tube section for measuring temperature difference across this section. Fluid temperatures were also measured using PT100 probes (accuracy  $\pm 0.1^\circ\text{C}$ ) at the inlet of the upstream adiabatic section and at the outlet of the sapphire tube section. Pairs of outer wall temperatures were also measured at four axial distances from the inlet of the sapphire tube using PT100 probes. Additional details of each of these can be found in Nancy et al. (2014). Two capacitance probes at the inlet and outlet of the test section gave access to the void fraction (see Nancy et al., 2014). The sensitivity of the capacitance probes was  $\approx 0.24 \text{ pF}$  and their measurement accuracy was estimated at  $\approx 6\%$ . The accuracy of the different parameters resulting from data reduction are evaluated in the Appendix. Flow visualization was carried using a high-speed camera (PCO Dimax,  $2000 \times 2000$  pixels) with a spatial resolution of  $\approx 12 \text{ pix/mm}$ . Visualisation of the entire tube section at a frequency of 1.0 and 1.4 kHz enabled the observation of the evolution of flow pattern and wave characteristics from the inlet to outlet of the heated section.

## 2.3. Data reduction

### 2.3.1. Vapor quality and heat transfer

The fluid at the inlet of the test section was either at subcooled or saturated conditions. The inlet quality ( $x_{\text{in}}$ ) was determined from the enthalpy balance across the preheater, connecting section (flexible hose) and adiabatic section (insulated stainless steel) upstream of the test section. The enthalpy balance between the inlet of the preheater and the inlet of the test section is given by Eq. 1.

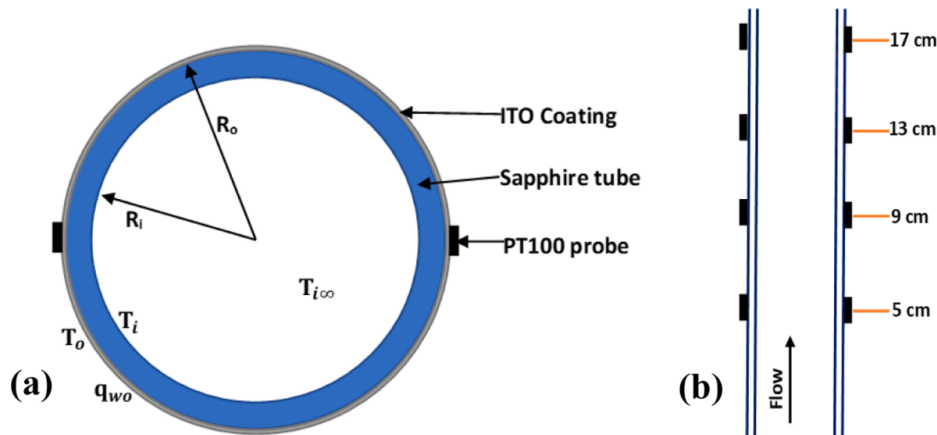


Fig. 2. a. illustration of the heated tube cross section, b. illustration of axial locations of PT100 probes for wall temperature measurements.

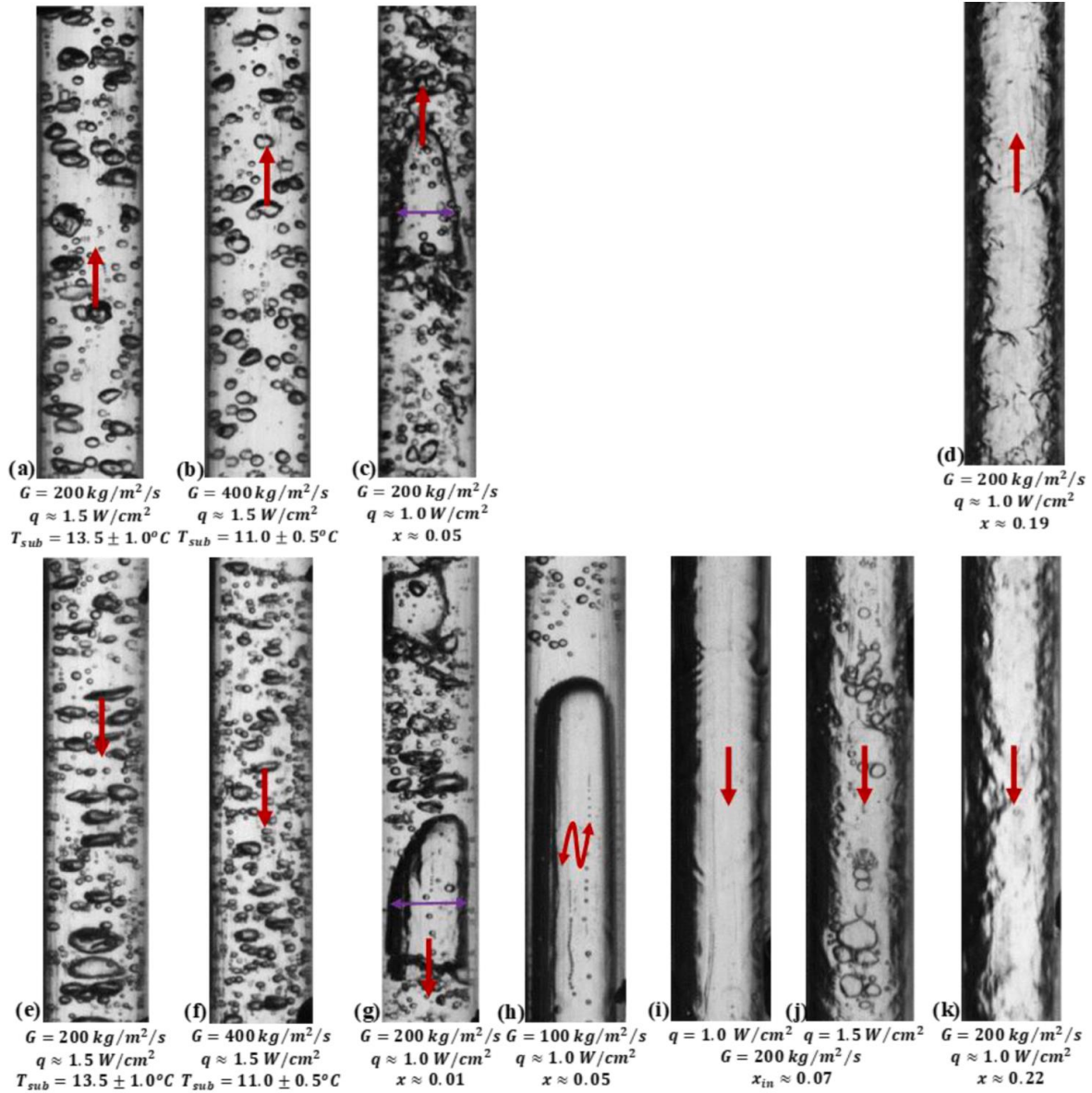


Fig. 3. Flow visualization in upward and downward flows: a-b. upward bubbly flow, c. upward intermittent flow, d. upward annular flow, e-f. downward bubbly flow, g-h. downward intermittent flow, i-j. downward falling film flow and k. downward annular flow. Red arrows indicate the direction of vapor flow.

$$\frac{P_{ph-eff}}{(\pi D^2/4)} = G(1-x_{in})Cp_l T_{in} + Gx_{in}h_v - GCp_l T_{in,ph} \quad (1)$$

where  $T_{in}$  and  $x_{in}$  are the temperature and the quality at the inlet of the test section,  $T_{in,ph}$  is the temperature at the inlet of the preheater,  $P_{ph-eff}$  is the preheater power after correction for heat losses, which is the effective power transmitted to the fluid (see [Narcy et al., 2014](#)).  $G$  is the total mass flux,  $h_v$  is the enthalpy of the vapor and  $Cp_l$  is the specific heat capacity of the liquid. For saturated conditions at the inlet of the test section;  $Cp_l T_{in} = h_{l,sat}$ ,  $h_v = h_{v,sat}$  and  $h_{v,sat} - h_{l,sat} = h_{lv}$ ,  $h_{l,sat}$  and  $h_{v,sat}$  being the enthalpy of liquid and vapor at saturation:

$$x_{in} = \frac{4P_{ph-eff} - GCp_l \pi D^2 (T_{in} - T_{in,ph})}{G\pi D^2 h_{lv}} \quad (2)$$

The quality ( $x_z$ ) at an axial position ( $z$ ) in the test section ( $z = 0$  at the

entrance) was obtained from the enthalpy balance between the inlet of the test section and the position  $z$ .

$$x_z = x_{in} + \frac{\left[ \frac{4q_{eff} \times z}{GD} - Cp_l (T_z - T_{in}) \right]}{h_{lv} + Cp_l (T_{sat} - T_z)} \quad (3)$$

At subcooled inlet conditions,  $x_{in} = 0$  and at saturated inlet conditions  $T_z = T_{in} = T_{sat}$ ,  $Cp_l (T_z - T_{in}) = 0$ ,  $Cp_l (T_{sat} - T_z) = 0$ . For subcooled inlet conditions the temperature evolution between the inlet and outlet of the sapphire tube section was assumed to be linear. The effective wall heat flux ( $q_{eff}$ ) was obtained from the difference in applied heat flux ( $q$ ) and estimated heat loss in the test section (see [Narcy et al., 2014](#)).

Calculation of inner wall heat transfer coefficient ( $h_i$ ) was done at four (4) axial locations along the heated tube section. Schematic draw-



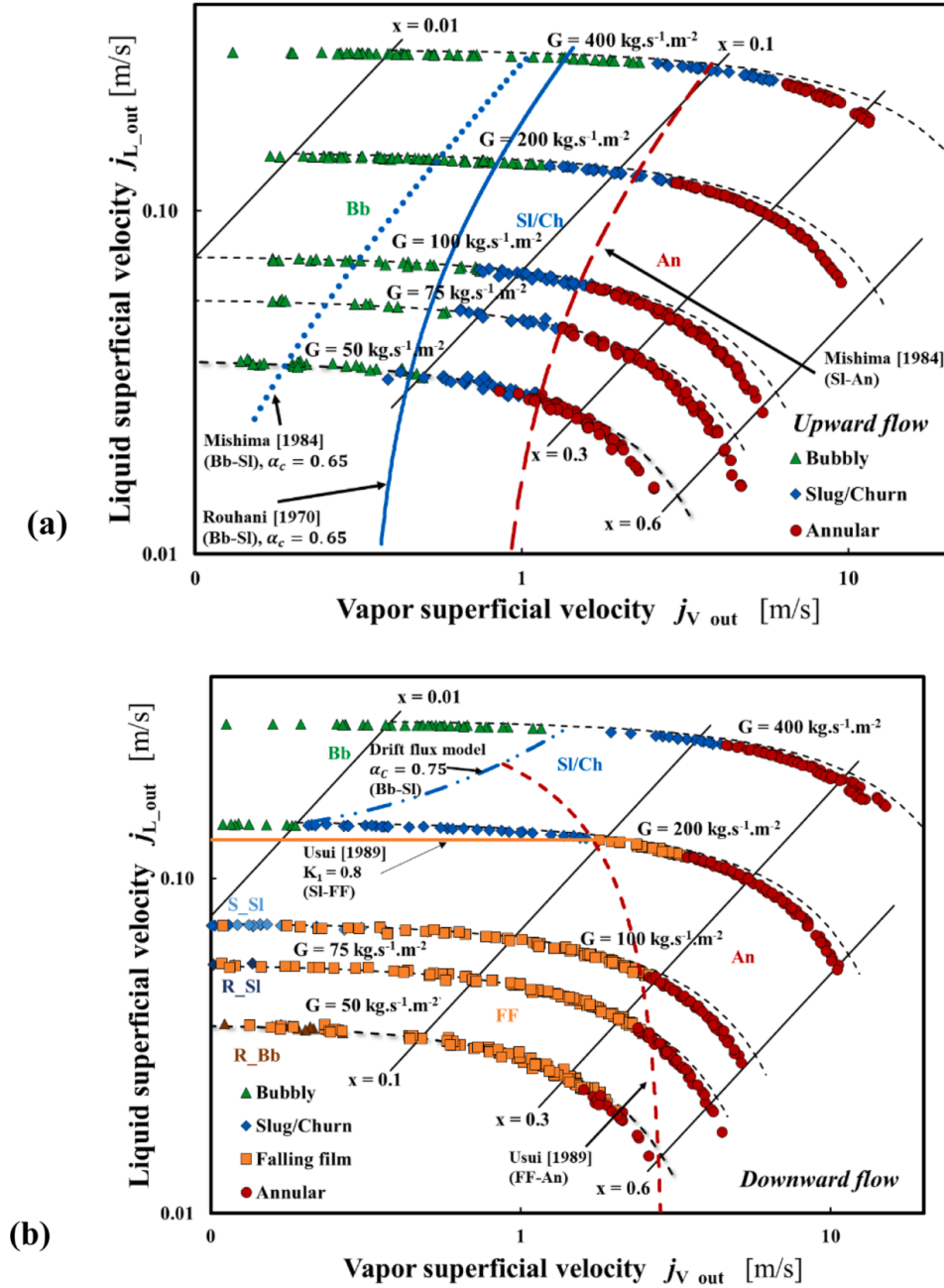


Fig. 4. Flow pattern maps for a. upward flow, b. downward flow. Bb (bubbly flow), Sl (slug flow), Ch (churn flow), An (annular flow), FF (falling film flow), S\_Sl (stagnant or oscillating slug flow), R\_Sl (reverse slug flow), R\_Bb (reverse Bb).

ing of the tube cross section is shown in Fig. 2a and a schematic drawing showing the 4 locations where  $h_i$  was calculated is shown in Fig. 2b. The heat transfer coefficient at the inner wall can be obtained from an energy balance between the fluid and the inner wall as follows;

$$h_i = \frac{q_{eff}}{T_{ow} - T_{i\infty} - \ln\left(\frac{R_o}{R_i}\right) \frac{R_o}{k} q_{eff}} \quad (4)$$

where  $k$  is the thermal conductivity of sapphire tube,  $R_o$  and  $R_i$  are the outer and inner tube radii of the sapphire tube,  $T_{ow}$  and  $T_{i\infty}$  are the outer

wall temperature and the liquid bulk temperature.

Single-phase measurements at moderate wall heat flux were carried out to provide validation for the measurement technique. The measured single-phase Nusselt number ( $Nu$ ) was compared to Gnielinski's correlation (1976). After correction with Al-Arabi's correlation (1982) for entrance effect and correcting for heat loss, most of the experimental Nusselt numbers at various axial locations were within  $\pm 15\%$  of Gnielinski's correlation (see Appendix, Fig. A1). This provides validation of the experimental technique.

### 2.3.2. Wall and interfacial frictions

The wall shear stress was obtained from the momentum balance equation of the mixture (Eq. 5).

$$\frac{dP}{dz} = -\frac{2}{R}\tau_w - \rho_m g \sin\theta - G^2 \frac{d}{dz} \left[ \frac{(1-x)^2}{\rho_l(1-\alpha)} + \frac{x^2}{\rho_v\alpha} \right] \quad (5)$$

where  $P$ ,  $\tau_w$ ,  $g$ ,  $\alpha$ ,  $x$ ,  $\theta$ ,  $\rho_v$  and  $\rho_l$  are the pressure, wall shear stress, acceleration due to gravity, void fraction, vapor quality, the tube inclination to the horizontal, vapor density and liquid density, respectively.  $\theta = 90^\circ$  in upward flow and  $-90^\circ$  in downward flow and mixture density is given by  $\rho_m = \rho_l(1-\alpha) + \rho_v\alpha$ . The first, second and third terms of the RHS of Eq. 5 are the frictional, gravitational and acceleration pressure gradients, respectively. In the current work, the acceleration term was generally non-negligible for non-adiabatic measurements and zero for adiabatic flow measurements. This term is calculated from the measurements of the void fractions and qualities at the inlet and outlet of the test section. The measured void fraction at the outlet of the tube was used to obtain a relationship between void fraction and vapor quality. The local void fraction ( $\alpha(z)$ ) at various axial locations along the test section was determined from this relationship. The gravitational pressure drop in Eq. 5 was obtained by numerical integration of  $(\rho_l(1-\alpha) + \rho_v\alpha)g \sin\theta$  along the length of the test section with fluid properties assumed constant.

Differential pressure measurements were carried out for single-phase flows for the purpose of validating the measurement techniques. The experimental single-phase wall friction factor was obtained using;

$$f_w = -\frac{dP}{dz} \frac{D\rho_l}{2G^2} \quad (6)$$

and was in good agreement with the Blasius correlation for turbulent flows ( $f_w = 0.0792Re^{-0.25}$ ) within  $\pm 10\%$  (see Appendix, Fig. A1).

The interfacial shear stress ( $\tau_i$ ) was obtained from the momentum balance of the vapor phase (Eq. 7) using measured pressure drop and void fraction. Eq. 7 is written with the assumption of negligible liquid entrainment in the gas core. In the current work, the difference introduced by this assumption was always less than 2% (Narcy et al., 2014). The interfacial friction factor ( $f_i$ ) was obtained from Eq. 8 and it is often scaled by the friction factor of the vapor core turbulent flow above a smooth interface given Eq. 9.

$$\alpha \frac{dp}{dz} = -\rho_v \alpha g \sin\theta - G^2 \frac{d}{dz} \left[ \frac{x^2}{\rho_v\alpha} \right] - \frac{4\sqrt{\alpha}\tau_i}{D} \quad (7)$$

$$f_i = \frac{2\tau_i}{\rho_v(U_v - U_l)^2} \quad (8)$$

$$f_v = 0.0792Re_v^{-0.25} \quad \left( Re_v = \frac{U_v D}{\nu_v} \right) \quad (9)$$

## 3. Results and discussion

### 3.1. Flow visualization and pattern maps

Flow visualizations were carried out at various two-phase flow conditions ranging from subcooled to saturated boiling for both upward and downward flows (Fig. 3). The observed flow patterns for upward flow were categorized into bubbly, intermittent (slug, churn and other transitions flows) and annular flow regimes for  $50 \leq G \leq 400 \text{ kg/m}^2\text{s}$ . The observed flow patterns in downward flow were categorized into bubbly, intermittent, falling-film and annular flow regimes.

Bubbly flow was observed for subcooled inlet conditions. The bubble diameter and the aspect ratio (mean radial to mean axial diameter) of the bubbles were significantly larger in downward flow particularly at  $G \leq 200 \text{ kg/m}^2\text{s}$  (Fig. 3a and 3e). The slower bubble velocity in downward flow led to a longer residence time and a higher rate of

coalescence. These differences, between upward and downward flow, become less obvious at higher mass flux where mixture velocity become dominant in comparison with the relative velocity (Fig. 3b and f). Bubbly flow regime was observed for all mass fluxes in upward flow but was only observed at  $G \geq 200 \text{ kg/m}^2\text{s}$  in downward flow. For  $G = 200 \text{ kg/m}^2\text{s}$ , the liquid velocity ( $G/\rho_l$ ) at the entrance of the test section is of order of magnitude of the bubble drift velocity ( $U_\infty$ ) which is around  $0.15 \text{ m/s}$ .

Fig. 3c and g show slug flow regime in upward and downward flow respectively. The main difference between slug flow in upward and downward flows is the shape of the bubbles. The cap of the Taylor bubbles in upward flow was sharper with a smaller curvature radius of the bubble nose relative to downward flow. In downward flow, the bubble nose is relatively flat (or distorted), with a larger radius of curvature and a thinner liquid film around the bubble. This is due to the longer mean residence time of the bubble in the heated tube section in downward flow, which led to a higher evaporation of the liquid film. The observations are consistent with that of Bhagwat and Ghajar (2017). At  $G = 100 \text{ kg/m}^2\text{s}$ , stagnated or oscillating Taylor bubbles were observed in downward flow (Fig. 3h).

Falling-film regime was observed for  $G \leq 200 \text{ kg/m}^2\text{s}$  and was characterized by low liquid and low/moderate vapor velocities with the vapor core surrounded by a falling liquid film along the wall (Fig. 3i-j). The liquid film was characterized by ripples and the interface was relatively smooth (no roll waves). At heat fluxes  $q \geq 1.5 \text{ W/cm}^2$ , nucleate boiling was observed in the liquid film (Fig. 3j). At saturated conditions in both upward and downward flows, annular flow regime was observed (Fig. 3c and k). The annular flow regime was characterized by high velocity vapor core and liquid film flowing along the wall. Roll waves were observed in the annular flow and at high vapor qualities, interfacial stresses induced breakup of interfacial waves resulting in liquid droplet entrainment in the vapor core. The same flow patterns were observed in adiabatic two-phase flow (Bhagwat and Ghajar, 2017) except for the effect of bubble nucleation at the wall which is specific to boiling flows. Observed flow patterns in upward flow are also consistent with the report of Narcy et al. (2014). Some flow visualizations are showed in the supplementary material.

The observed flow patterns were presented in flow pattern maps in terms of liquid and vapor superficial velocities ( $j_l$ ,  $j_v$ ) for both upward (Fig. 4a) and downward (Fig. 4b) flows. Bubbly to intermittent flow regime transition occurred at higher void fraction in downward flow relative to upward flow. Furthermore, flow patterns in upward and downward flows become similar at significantly high flow rate ( $G \geq 400 \text{ kg/m}^2\text{s}$ ).

In upward flow, bubbly to intermittent flow regime transition occurred for measured values of the void fraction of about 0.65 ( $0.64 \leq \alpha_c \leq 0.67$ ). This value of critical void fraction at bubbly-intermittent flow transition is in agreement with other flow boiling experiments in upward flow where  $\alpha_c$  of about 0.7 was reported (Celata and Zummo, 2009; Narcy et al., 2014). Applying  $\alpha_c = 0.65$  in the drift flux models of Ishii (1977) (see Mishima and Ishii (1984)) and Rouhani and Axelsson (1970), gave bubbly-intermittent flow transition boundaries shown in Fig. 4a as dotted line and solid line respectively. These drift flux models are given in Table 1 and  $x_c$  is given by Eq. 10. The model of Rouhani and Axelsson (1970) gave a reasonable prediction of the bubbly-intermittent flow transition boundary particularly at lower mass fluxes.

$$x_c = \frac{\frac{G}{\rho_l} + \frac{U_\infty}{C_0}}{\frac{G(1-C_0\alpha_c)}{\rho_v C_0 \alpha_c} + \frac{G}{\rho_l}} \quad (10)$$

In downward flow, co-current bubbly and slug flows were observed for  $G \geq 200 \text{ kg/m}^2\text{s}$  and bubbly-slug transition occurred at void fraction of  $\approx 0.75$ . A few modelling studies have been carried out on the criteria for bubbly-slug transition in adiabatic gas-liquid downward flows (Bhagwat and Ghajar, 2015; Martin, 1976; Usui, 1989). Others proposed

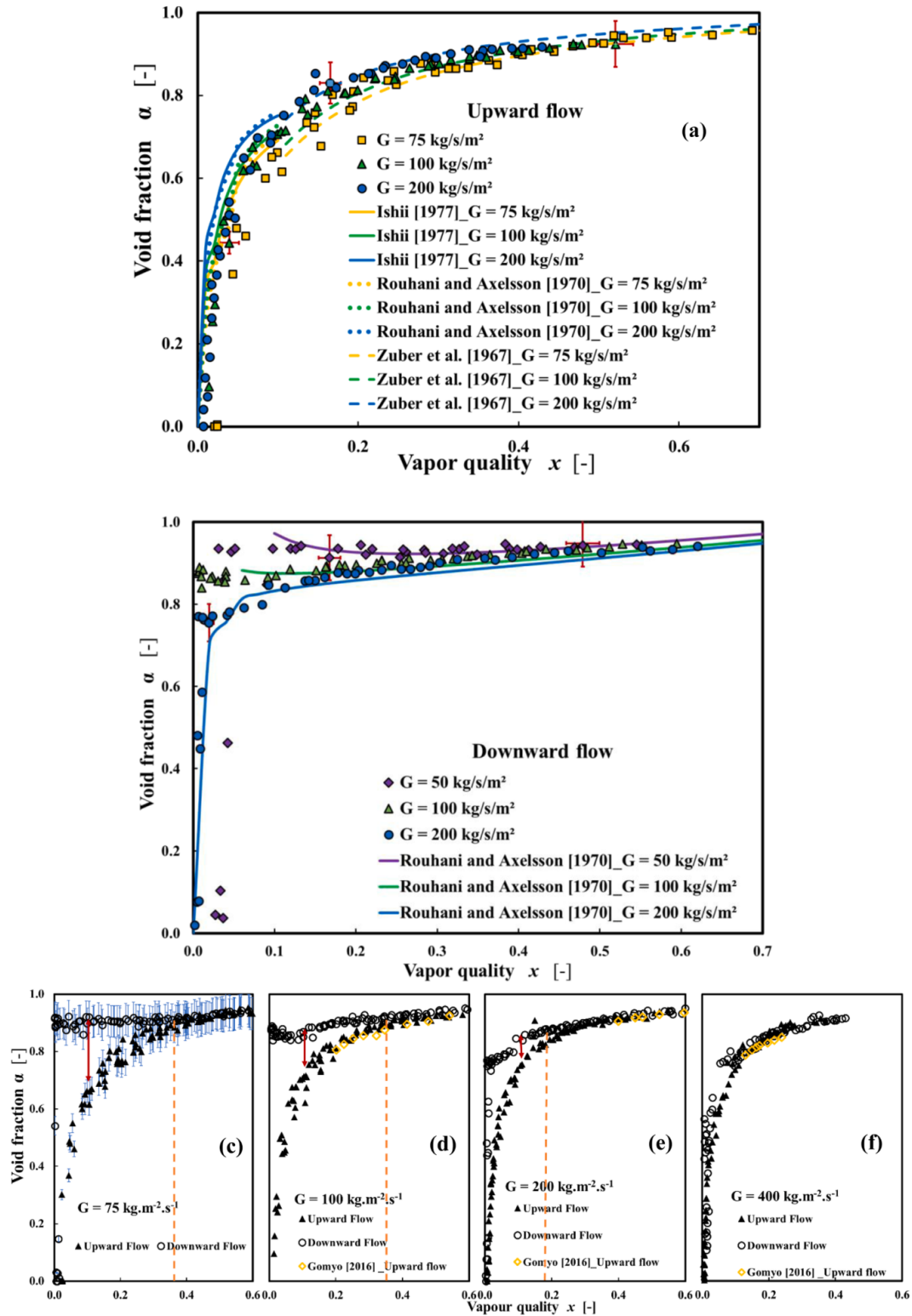


Fig. 5. Void fraction versus vapor quality in upward and downward flows and comparison with selected models. Error bars were only put at selected point to improve readability.

**Table 2**  
Selected void fraction correlations.

Author	Correlation for drift velocity or void fraction
(Bhagwat and Ghajar, 2014)	$U_{\infty} = (0.35\sin\theta + 0.45\cos\theta)\sqrt{\frac{gD(\rho_l - \rho_v)}{\rho_l}(1 - \alpha)^{0.5}C_2C_3C_4}$ <p>where <math>\theta</math> is measured from horizontal and expressions for determining <math>C_{0.1}</math>, <math>C_2</math>, <math>C_3</math>, and <math>C_4</math> can be found in (Bhagwat and Ghajar, 2014)</p> $C_0 = \frac{1 - (\rho_v/\rho_l)^2}{1 + (Re_{20}/1000)^2} + \frac{1 + C_{0.1}}{1 + (1000/Re_{20})^2}$
(Ishii, 1977)	$\begin{cases} U_{\infty} = \sqrt{2} \left[ \frac{\sigma g(\rho_l - \rho_v)}{\rho_l^2} \right]^{0.25} (1 - \alpha)^{1.75} & \text{Bubbly flow} \\ U_{\infty} = \sqrt{2} \left[ \frac{\sigma g(\rho_l - \rho_v)}{\rho_l^2} \right]^{0.25} & \text{Churn flow} \end{cases}$ $C_0 = 1.2 - 0.2\sqrt{\rho_v/\rho_l}$
(Rouhani and Axelsson, 1970)	$U_{\infty} = \pm 1.18 \left[ g\sigma \left( \frac{\rho_l - \rho_v}{\rho_l^2} \right) \right]^{0.25}$ $C_0 = \begin{cases} 1 + 0.2(1 - x) \cdot (gD\rho_l^2/G^2)^{0.25} & \text{for } \alpha \leq 0.25 \\ 1 + 0.2(1 - x) & \text{for } \alpha > 0.25 \end{cases}$
(Zuber et al., 1967)	$U_{\infty} = 23 \sqrt{\frac{\mu_l G(1 - x)}{\rho_l \mu_l D}}, C_0 = 1.0$
(Woldesemayat and Ghajar, 2007)	$\alpha = \frac{j_v}{j_v \left[ 1 + \left( \frac{j_l}{j_v} \right) \left( \frac{\rho_v}{\rho_l} \right)^{0.1} \right] + 2.9 \left[ \frac{g\sigma(1 - \cos\theta)(\rho_l - \rho_v)}{\rho_l^2} \right]^{0.25} (1.22 + 1.22\sin\theta) \frac{P_{atm}}{P}}$
(Cioncolini and Thome, 2012)	$\alpha = \frac{hx^n}{1 + (h - 1)x^n} \text{ where } \begin{cases} h = -2.129 + 3.129 \left( \frac{\rho_v}{\rho_l} \right)^{-0.2186} \\ n = 0.3487 + 0.6513 \left( \frac{\rho_v}{\rho_l} \right)^{0.5150} \end{cases}$

transition boundaries based on flow visualizations (Almabrok et al., 2016; Bhagwat and Ghajar, 2017). Usui (1989) proposed a criterion for bubbly-slug transition using the drift flux model (Eq. 11) approach with  $\alpha_c = 0.175$ ,  $C_0 = 1.2$  and  $u_{\infty}$  given by Eq. 12. The proposed transition boundary falls outside of the plot range of Fig. 4b. The reason for this is the significantly lower mean value of  $\alpha_c$  used in that work. With a value of  $\alpha_c = 0.75$  (current work), and same values of  $C_0$  and  $U_{\infty}$  as Usui (1989), the drift flux model gave a good estimation of the bubbly-slug transition (Fig. 4b).

$$\alpha = \frac{j_v}{C_0(j_v + j_l) + u_{\infty}} \quad (\text{Driftfluxmodel}) \quad (11)$$

$$U_{\infty} = -1.53 \left[ \frac{\sigma \cdot g \cdot (\rho_l - \rho_v)}{\rho_l^2} \right]^{1/4} \quad (12)$$

With an increase in mass flux (50→400 kg/m<sup>2</sup>s), intermittent to annular flow regime transition was observed at slightly higher void fraction (0.78→0.84) in upward flow. Mishima and Ishii (1984) proposed criteria for slug-churn flow regime transition (Eq. 13). Their proposed slug-churn transition boundary coincided with their proposed slug-annular transition boundary at higher mass flux. Their proposed slug-churn transition criteria gave a good prediction of our observed intermittent-annular flow transition except at the highest mass flux. (Mishima and Ishii, 1984)

$$\alpha \geq 1 - 0.813 \left\{ \frac{(C_0 - 1)j + 0.35 \sqrt{\frac{(\rho_l - \rho_v)gD}{\rho_l}}}{j + 0.75 \sqrt{\frac{(\rho_l - \rho_v)gD}{\rho_l}} \left[ \frac{(\rho_l - \rho_v)gD^3}{\rho_l^3} \right]^{1/18}} \right\}^{0.75} \quad (13)$$

In downward flow, slug-falling film ( $G \leq 200 \text{ kg/m}^2\text{s}$ ), slug-annular ( $G = 400 \text{ kg/m}^2\text{s}$ ) and falling film-annular ( $G \leq 200 \text{ kg/m}^2\text{s}$ ) flow regime transitions were observed. In a number of downward flow studies, slug-falling film regime transition is defined by a region of constant liquid superficial velocity (Almabrok et al., 2016; Bhagwat and Ghajar, 2017; Usui, 1989). A criterion for slug-falling film regime

transition was proposed by Usui (1989) (Eq. 14). The proposed transition boundary slightly over-predicts the observed transition boundary in the current work. However, substituting a value 0.8 (in place of 0.92) for  $K_1$  in Eq. 14 provided a good estimation of the observed slug-falling film regime transition (Fig. 4b). Usui (1989) also proposed a criterion for transition from falling film/slug flow to annular flow (Eq. 15). The proposed model over-predicts and under-predicts the transition boundary in the current work at low and high mass fluxes respectively (Fig. 4b – dashed line) (Usui, 1989).

$$Fr_l = \left( K_1 - \frac{K_2}{Eo} \right)^{23/18} \quad (14)$$

where  $K_1 = 0.92$ ,  $K_2 = 7$ ,  $Fr_l = \frac{j}{\sqrt{gD(\rho_l - \rho_v)/\rho_l}}$  and  $Eo = gD^2(\rho_l - \rho_v)/\sigma$  (Usui, 1989).

$$Fr_l = 2.5(j_v/j_l)^{-2/3} \quad (15)$$

Overall, the accuracy of prediction of flow pattern and transition in the heated section of boiling flows appears to depend on the accuracy of measurement of the local void fraction at any axial location. For short-length millimetric tubes (as with the current work), the void fractions corresponding to the various transition boundaries were generally higher than the corresponding void fraction at transition for fully developed adiabatic gas-liquid flows.

### 3.2. Void fraction and liquid film thickness

Results of measured void fraction in upward and downward flows are presented on plots of void fraction versus vapor quality. Fig. 5a shows measured void fraction versus vapor quality at the outlet of the heated tube section in upward flow. The measured void fraction increased with mass flux for  $x \leq 0.3$  and this trend is in agreement with some commonly used void fraction models (Ishii, 1977; Rouhani and Axelsson, 1970; Zuber et al., 1967). The measured void fractions were also in agreement with recent void fraction measurement of Gomyo and Asano (2016) obtained inside a tube of 4 mm ID with vapor-liquid FC-72 as



**Table 3**  
Mean absolute error for various void fraction correlations.

Model/Correlation ( $G = 50 - 400 \text{ kg/m}^2\text{s}$ )	Upward flow (MAE %)	Downward flow (MAE %)
Rouhani and Axelsson (1970) (IN/AN)	15.7	2.8
Ishii (1977) (IN)	27.0	
Bhagwat and Ghajar (2014) (IN/AN)	9.6	5.2
Woldeesemayat and Ghajar (2007) (IN/AN)	6.8	
Zuber et al. (1967) (AN)	2.5	
Cioncolini and Thome (2012) (AN)	5.4	

IN – intermittent flow, AN – annular flow

working fluid (Fig. 5d-f). Two common approaches are generally used in void fraction modelling: drift flux approach (Bhagwat and Ghajar, 2014; Rouhani and Axelsson, 1970; Woldeesemayat and Ghajar, 2007; Zuber et al., 1967) and separated flow approach (Lockhart and Martinelli, 1949). A review of various models for predicting the void fraction of flows in various orientations at earth gravity conditions can be found elsewhere (Bhagwat and Ghajar, 2014, 2012). Selected correlations are provided in Table 2. The model of Zuber et al. (1967) provided a good prediction of the experimental data in the range of void fraction  $0.6 \leq \alpha \leq 1.0$  corresponding to intermittent and annular flow regimes while the models of Rouhani and Axelsson (1970) and Ishii (1977) gave good predictions of the experimental data in the range of void fraction  $0.1 \leq \alpha < 0.6$  corresponding to bubbly and intermittent flow regimes (Fig. 5a). The model of Woldeesemayat and Ghajar (2007) gave a good prediction of the measured void fraction in the intermittent and annular flow regimes. The void fraction correlation of Cioncolini and Thome (2012) provided a good estimation of the experimental data for  $x \geq 0.3$ . This correlation gave poor prediction at lower quality because the model was developed for annular two-phase flows. Table 3 provides a summary of mean absolute error for selected void fraction models.

In downward flow, high values of the void fraction ( $> 0.8$ ) were recorded at low vapor quality for  $G \leq 100 \text{ kg/m}^2\text{s}$  which corresponds to falling film regime and the disappearance of the bubbly co-current flow regime (Fig. 5b). In contrast to upward flow, measured void fraction decreased with increase in mass flux or liquid superficial velocity especially in the bubbly and intermittent flow regimes. This is associated with the decrease in residence time of the vapor with increase in mass

flux. The general trend of measured void fraction and its mass flux dependence are consistent with other investigations for adiabatic gas-liquid downward flows (Almabrok et al., 2016; Bhagwat and Ghajar, 2012). A common approach to void fraction modelling in downward flows is the drift flux model approach with a negative drift velocity (Bhagwat and Ghajar, 2012; Usui and Sato, 1989). Fig. 5b show comparison of measured void fraction with the model of Rouhani and Axelsson (1970). The model provided a good prediction of measured void fraction for  $G \leq 200 \text{ kg/m}^2\text{s}$  both in magnitude and trend.

Fig. 5c-f show comparison between measured void fraction in upward and downward flow. The void fractions in downward flow were generally higher than those of upward flow for  $x \leq 0.3$  and the difference in void fraction diminishes with both mass flux and vapor quality. The results are consistent with flow visualization and the difference in void fraction is directly linked to gravity effect with a longer residence time of the vapor phase in the test section in downward flow relative to upward flow.

The liquid film thickness ( $\delta$ ) in the falling film and annular flow regimes were calculated from the measured void fraction using Eq. 16. In the current work, for  $G \leq 400 \text{ kg/m}^2\text{s}$ , the contribution of liquid entrainment to the calculated liquid film thickness was negligible as shown by Nancy et al. (2014), using the model of Cioncolini et al. (2009) to estimate the droplet entrainment rate. Namely for the highest mass flux  $G = 400 \text{ kg/m}^2\text{s}$  and quality of  $x = 0.4$ , the liquid entrainment rate  $e = 0.2$ . Thus the difference in the estimation of the film thickness with and without entrainment is 0.1%, much below the uncertainty in the film thickness measurement itself. Fig. 6a and b show calculated film thickness in upward and downward flows respectively. Film thickness decreased with vapor quality as well as mass flux in upward flow. In downward flow, film thickness decreased with vapor quality but increased with mass flux. Predicted void fraction in the annular flow regime using models of Zuber et al. (1967) (upward flow) and Rouhani and Axelsson (1970) (downward flow) were also used to estimate the liquid film thickness according to Eq. 16. The predicted liquid film thickness agrees favorably with experimental results (Fig. 6). The mean absolute error for both models are 14.9% (Zuber et al. (1967) – upward flow) and 16.1% (Rouhani and Axelsson (1970) – downward flow).

$$\delta = 0.5D(1 - \sqrt{\alpha}) \quad (16)$$

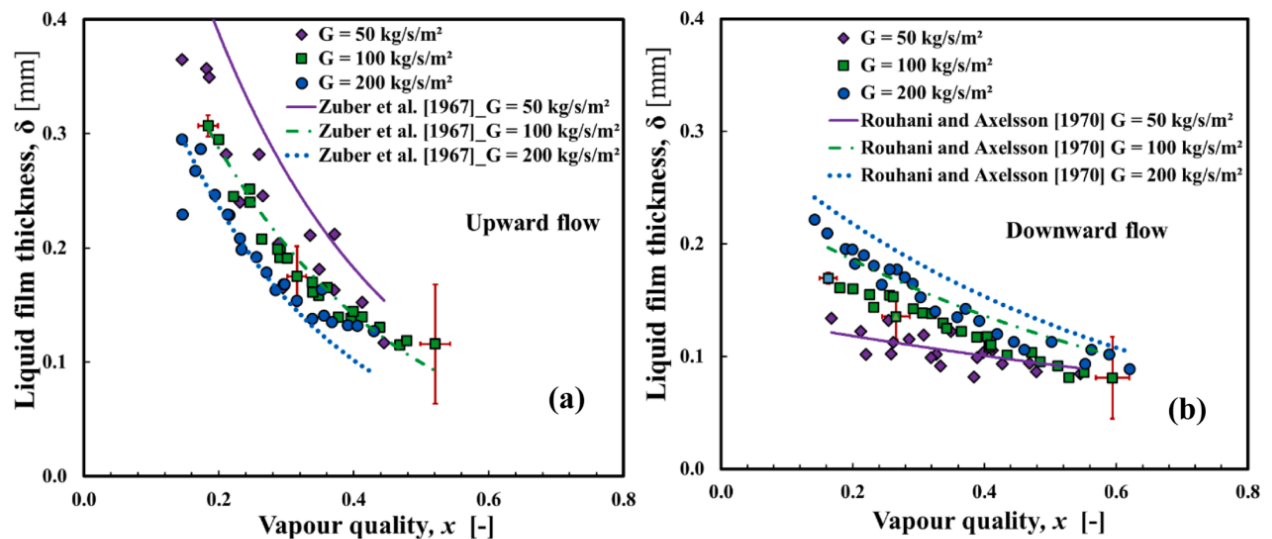


Fig. 6. Liquid film thickness versus vapor quality, a. upward flow, b. downward flow.

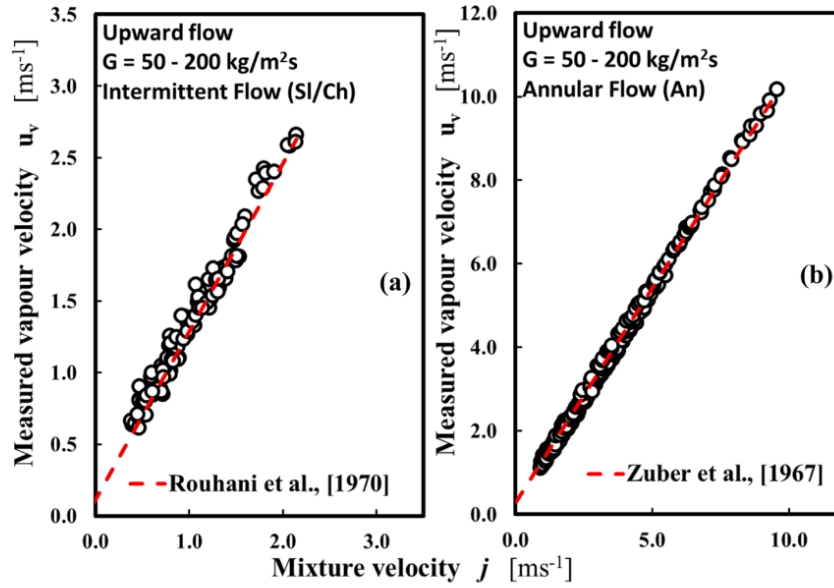


Fig. 7. Vapor velocity versus mixture velocity in upward flow.

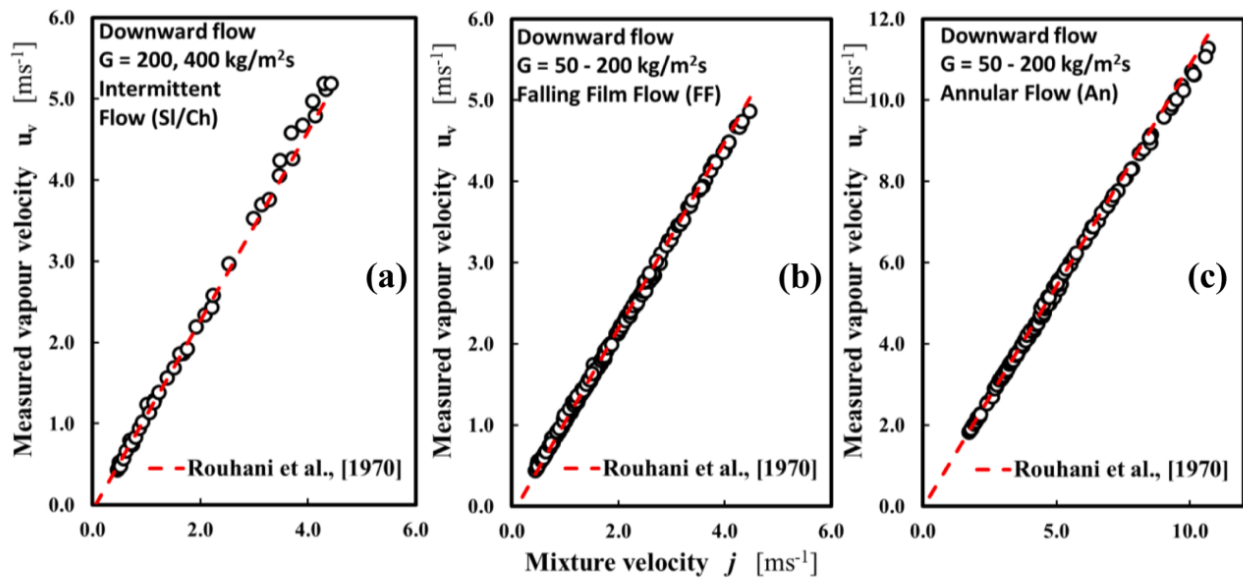


Fig. 8. Vapor velocity versus mixture velocity in downward flow.

### 3.3. Vapor velocity

Measured void fraction at the outlet of the heated test section was used to compute vapor velocity in both upward and downward flows over a wide range of quality corresponding to subcooled and saturated boiling regimes. Figs. 7 and 8 show computed vapor velocity versus mixture velocity for upward and downward flows respectively. Due to lack of precision in the quality for very low values of the quality corresponding to bubbly flow, only vapor velocities corresponding to intermittent, falling film (downward flow) and annular flow are presented. Fig. 7a and b show vapor velocity in the intermittent and annular flow regimes respectively along with comparison with relevant models. A good agreement can be seen between experimental and predicted

vapor velocity, although the data showed higher dispersion in the intermittent flow regime. Fig. 8a-c show computed vapor velocity versus mixture velocity in downward flow for intermittent, falling film and annular flow regimes respectively along with comparison with the model of Rouhani and Axelsson (1970). Good agreement is seen between experimental and predicted vapor velocity for all flow regimes and vapor quality.

### 3.4. Wall shear stress and heat transfer coefficient

Results of measured heat transfer coefficient and wall shear stress for flow boiling under various conditions of inlet vapor quality, heat flux and mass flux are presented in terms of mean vapor quality for both

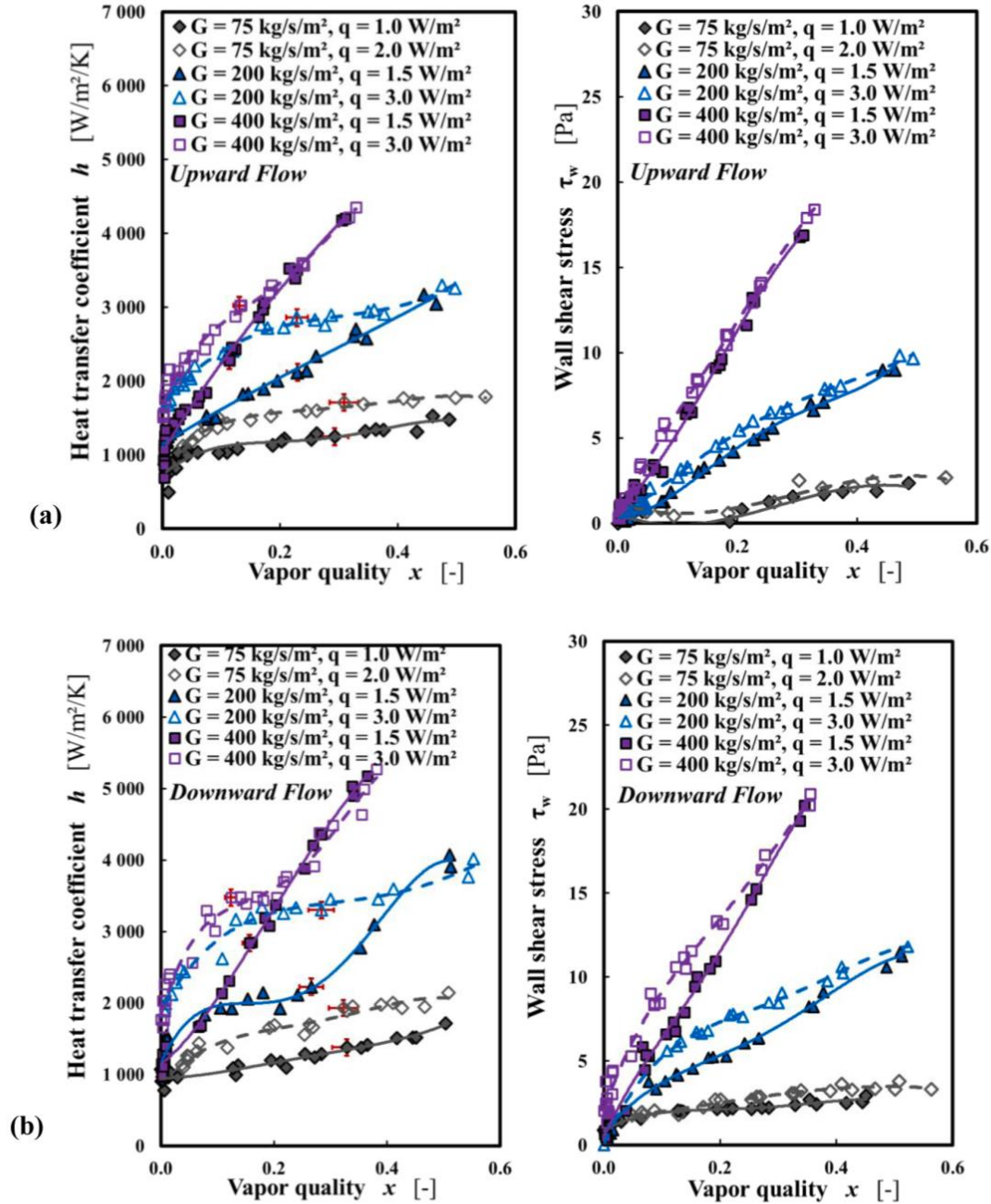


Fig. 9. Evolutions of the heat transfer coefficient and wall shear stress for different mass and heat fluxes, a. upward flow, b. downward flow; heat transfer coefficient (left), wall shear stress (right). The lines are polynomial fits that provide trends: upward flow (solid lines), downward flow (dashed lines).

upward and downward flows (Fig. 9). The heat transfer coefficient and wall shear stress increased with both vapor quality and mass flux in both upward and downward flows. Both the heat transfer coefficient and wall shear stress also increased with the wall heat flux for the same mean vapor quality in both upward and downward flows. This heat flux dependence was predominant in the nucleate boiling regimes; nucleate boiling (NB), nucleate boiling in the falling-film (NBFF) and nucleate boiling in the annular flow (NBA). This is consistent with recent reports in flow boiling (Kim and Mudawar, 2013b, 2013a; Layssac, 2018). In most of the experiments, except for  $G = 400 \text{ kg/m}^2\text{s}$ , bubble nucleation at the wall was observed from the flow visualizations. These

observations are in agreement with the measured values of the wall temperature  $T_w$  that are larger than the temperature for the onset of nucleated boiling  $T_{w\_ONB}$  given by Davis and Anderson (1966):

$$(T_w)_{ONB} = T_{sat} + \frac{8\sigma q_{ONB} T_{sat}}{h_{lv} \lambda_l \rho_l} \quad (17)$$

The nucleated bubbles at the wall seem to act as a roughness at the wall leading to an increase of the velocity gradient of liquid near the wall and an increase of the friction velocity. The effect of heat flux was generally higher in downward flow relative to upward flow. This is likely due to longer residence time of nucleated bubbles attached at the



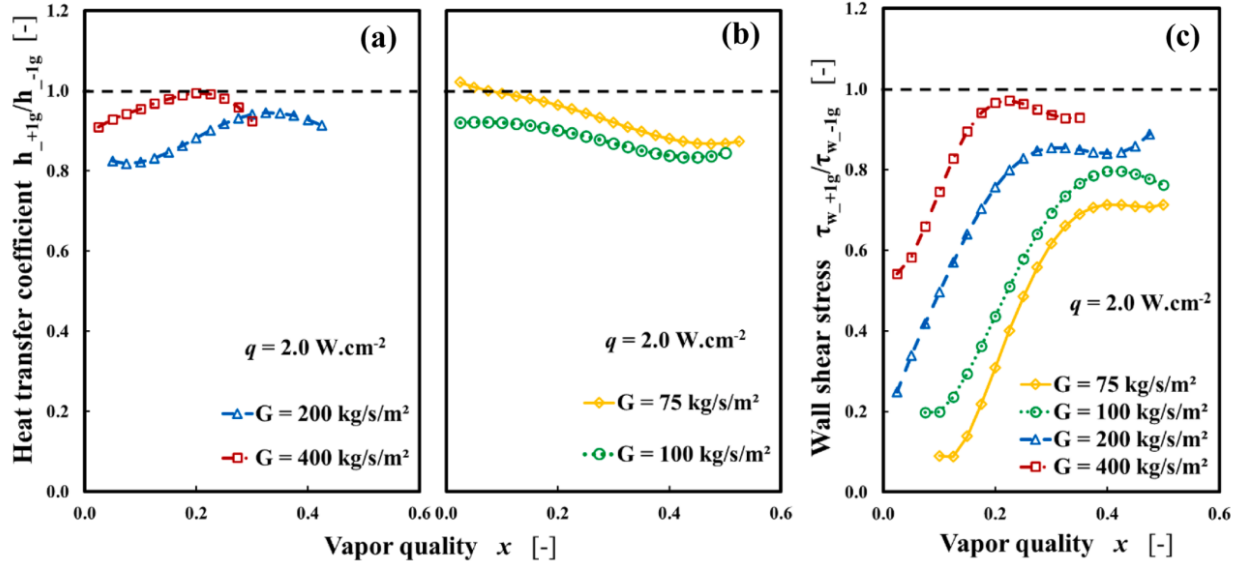


Fig. 10. a-b. Ratio of heat transfer coefficient in +1g (upward flow) to heat transfer coefficient in -1g (downward flow), c. Ratio of wall shear stress in +1g to wall shear stress in -1g.

Table 4

Ratio of heat transfer coefficient and wall shear stress between upward and downward flows for  $q = 1.0$  and  $2.0 \text{ W/cm}^2$ .

Heat transfer coefficient				
Mass flux	$q = 1.0 \text{ W/cm}^2$		$q = 2.0 \text{ W/cm}^2$	
	$x = 0.10$	$x = 0.35$	$x = 0.10$	$x = 0.35$
$G = 75 \text{ kg/m}^2/\text{s}$	1.10	0.96	0.99	0.90
$G = 100 \text{ kg/m}^2/\text{s}$	0.99	1.03	0.92	0.85
$G = 200 \text{ kg/m}^2/\text{s}$	1.00	0.94	0.82	0.94
$G = 400 \text{ kg/m}^2/\text{s}$	—	—	0.96	0.92
Wall shear stress				
Mass flux	$q = 1.0 \text{ W/cm}^2$		$q = 2.0 \text{ W/cm}^2$	
	$x = 0.10$	$x = 0.35$	$x = 0.10$	$x = 0.35$
$G = 75 \text{ kg/m}^2/\text{s}$	0.20	0.72	0.09	0.69
$G = 100 \text{ kg/m}^2/\text{s}$	0.19	0.76	0.20	0.77
$G = 200 \text{ kg/m}^2/\text{s}$	0.56	0.89	0.5	0.85
$G = 400 \text{ kg/m}^2/\text{s}$	—	—	0.75	0.93

wall in downward flow which in turn increases the time-averaged apparent roughness at the wall relative to upward flow. Namely, in upward flow drag force and buoyancy force are in the same direction and promote the bubble detachment whereas in downward flow they are in the opposite direction. The range of mixture velocity over which the effect of heat flux was significant was also wider in downward flow relative to upward flow. This is attributed to the wider range of mixture velocity for which nucleate boiling regimes (NB, NBFF and NBA) occurred in downward flows relative to upward flow. Overall, there was a strong coupling between the wall shear stress and wall heat transfer in both upward and downward flows. Modelling results on the wall shear stress and heat transfer coefficient will be discussed in the next sections.

Fig. 10 and Table 4 provide comparisons between heat transfer coefficient in upward and downward flow at constant heat flux and selected mass fluxes along with the corresponding wall shear stress. At constant heat flux, both the heat transfer coefficient and wall shear stress

were generally higher in downward flow. This is linked to the higher liquid velocity in downward flow relative to upward flow. In the case of wall shear stress, the ratio increased with increase in mass flux and vapor quality (Fig. 10c). This trend was replicated for measured heat transfer coefficient for  $G = 200$  and  $400 \text{ kg/m}^2/\text{s}$  (Fig. 10a), while the reverse was the case at lower mass flux (Fig. 10b). As inertia becomes dominant compared to gravity ( $G = 400 \text{ kg/m}^2/\text{s}$ ,  $x \geq 0.15$ ), heat transfer coefficient and wall shear stress in upward and downward flows become comparable. For  $G = 400 \text{ kg/m}^2/\text{s}$ , the Froude number  $Fr = G^2/\rho_l^2 g D = 1.34$ . This number is lower than 1 for  $G \leq 200 \text{ kg/m}^2/\text{s}$ .

#### 3.4.1. Modelling of wall shear stress for non-boiling vapor-liquid two-phase flow

At saturated inlet conditions, the fluid enters the test section as vapor-liquid two-phase flow. The saturated boiling regime corresponds mostly to annular flow with limited range of intermittent flow. With no heat flux applied to the test section, the wall shear stress corresponds to adiabatic two-phase flow. The wall shear was generally higher in downward flow for  $G \leq 200 \text{ kg/m}^2/\text{s}$  (See Fig. A2 in Appendix).

The adiabatic data were compared to correlations of Muller-Steinhagen and Heck (1986) Eq. 18 and Kim & Mudawar (2012) (Eqs. 19–23). Both correlations gave similar predictions over the range of test conditions and gave good prediction the measured data within  $\pm 30\%$ . However, the correlations underpredicted the measured wall shear stress in both upward and downward flows for  $G \leq 200 \text{ kg/m}^2/\text{s}$  and provided good estimation of the measured data at  $G = 400 \text{ kg/m}^2/\text{s}$  (Fig. 11). To improve model performance, modification of the correlation of Kim & Mudawar (2012) was proposed by introducing the Martinelli parameter ( $X$ ) and small modifications to the coefficients in their expression for  $C_A$  (see Table 5). The proposed correlation provided good prediction of the measured wall shear stress over the measurement range in both upward and downward flows. Although, the correlation for downward flow underpredicted the measured data for  $G < 100 \text{ kg/m}^2/\text{s}$ .

$$\left(\frac{dp}{dz}\right)_{fr} = F(1-x)^{1/3} + Bx^3 \quad (18)$$



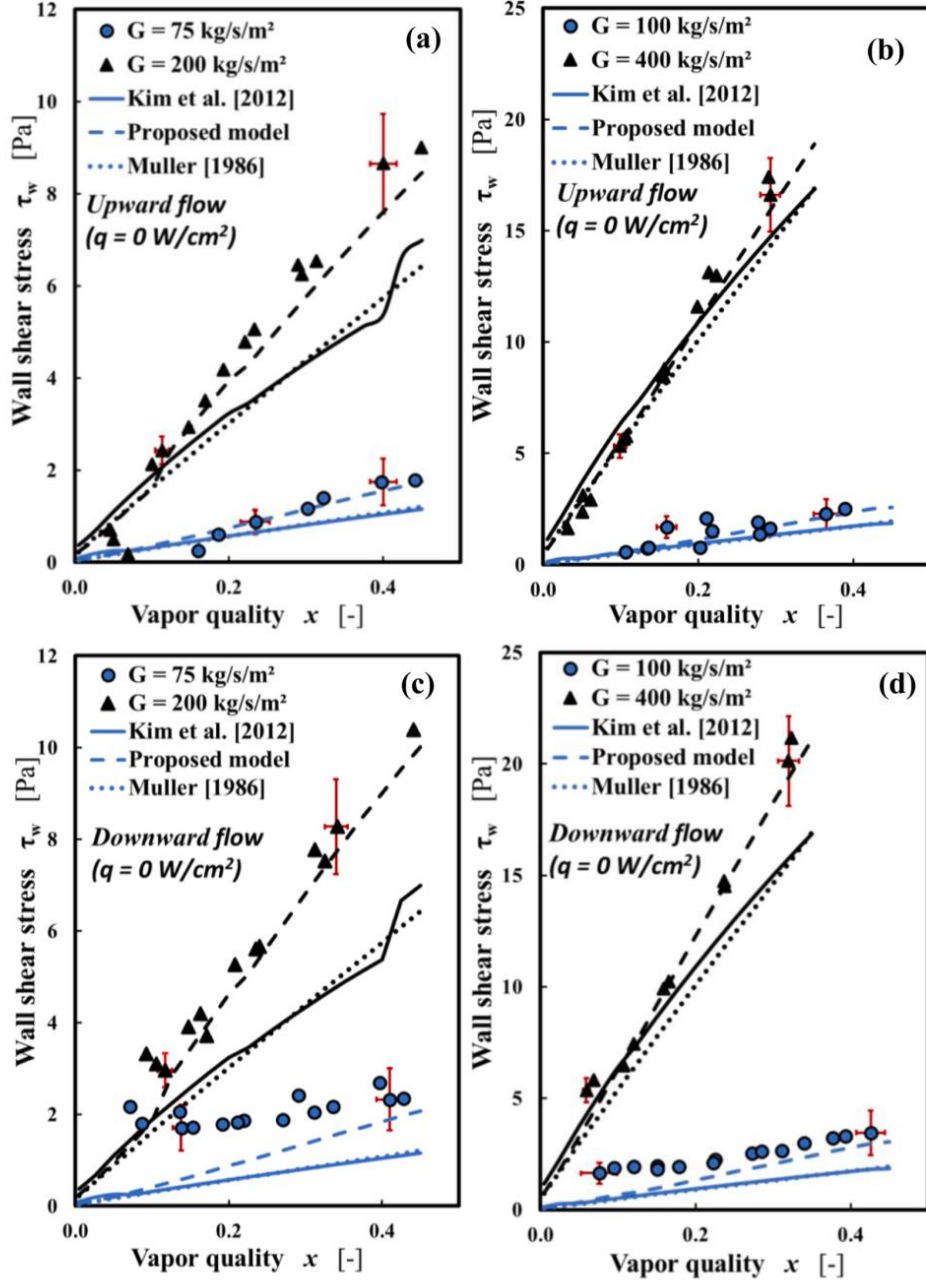


Fig. 11. Comparison between measured wall shear stress for non-boiling two-phase flow with predicted wall shear stress obtained from selected correlations.

where  $F = A + 2(B - A)x$ ,  $A = \left(\frac{dp}{dz}\right)_{lo}$ ,  $B = \left(\frac{dp}{dz}\right)_{vo}$ ,  $\left(\frac{dp}{dz}\right)_{lo} = -f_{lo} \frac{2G^2}{\rho_l D}$ ,

$$\left(\frac{dp}{dz}\right)_{vo} = -f_{vo} \frac{2G^2}{\rho_v D}$$

$$\left(\frac{dp}{dz}\right)_{fr} = \frac{4\tau_{w-2\phi}}{D} = \phi_l^2 \left(\frac{dp}{dz}\right)_l \quad (19)$$

$$\phi_l^2 = 1 + \frac{C_A}{X} + \frac{1}{X^2} \quad (20)$$

$$X = \left[ \left(\frac{dp}{dz}\right)_l / \left(\frac{dp}{dz}\right)_v \right]^{0.5} \quad (21)$$

$$\left(\frac{dp}{dz}\right)_l = -\frac{4}{D} f_l \frac{\rho_l \bar{u}_l^2}{2} = -f_l \frac{2G^2(1-x)^2}{\rho_l D} \quad (22)$$

$$\left(\frac{dp}{dz}\right)_v = -\frac{4}{D} f_v \frac{\rho_v \bar{u}_v^2}{2} = -f_v \frac{2G^2 x^2}{\rho_v D} \quad (23)$$

### 3.4.2. Modelling of wall shear stress in flow boiling (non-adiabatic)

Measured wall shear stress in upward and downward flow boiling

**Table 5**  
Expressions for  $C_A$  and  $f_k$ .

Kim & Mudawar (2012)	$f_k = \begin{cases} 16Re_k^{-1} & Re_k < 2000 \\ 0.079Re_k^{-0.25} & 2000 \leq Re_k < 20000 \\ 0.046Re_k^{-0.2} & Re_k \geq 20000 \end{cases}$
	$C_A = \begin{cases} 0.39Re_{lo}^{0.03}Su_{vo}^{0.1}(\rho_l/\rho_v)^{0.35}, & Re_l \geq 2000, Re_v \geq 2000 \\ 8.7 \times 10^{-4}Re_{lo}^{0.17}Su_{vo}^{0.1}(\rho_l/\rho_v)^{0.14}, & Re_l \geq 2000, Re_v < 2000 \\ 0.001559Su_{vo}^{0.1}(\rho_l/\rho_v)^{0.36}, & Re_l \geq 2000, Re_v < 2000 \\ 3.5 \times 10^{-5}Re_{lo}^{0.44}Su_{vo}^{0.1}(\rho_l/\rho_v)^{0.5}, & Re_l < 2000, Re_v < 2000 \end{cases}$
Proposed corr. (A) for upward flow	$f_k = \begin{cases} 16Re_k^{-1} & Re_k < 1500 \\ 0.079Re_k^{-0.25} & 1500 \leq Re_k < 20000 \\ 0.046Re_k^{-0.2} & Re_k \geq 20000 \end{cases}$
	$C_A = \begin{cases} 0.33Re_{lo}^{0.03}Su_{vo}^{0.1}(\rho_l/\rho_v)^{0.35}(1/X^{0.22}), & Re_l \geq 3000, Re_v \geq 3000 \\ 0.40Re_{lo}^{0.03}Su_{vo}^{0.1}(\rho_l/\rho_v)^{0.35}(1/X^{0.27}), & Re_l < 3000, Re_v \geq 3000 \end{cases}$
Proposed corr. (A) for downward flow	$C_A = \begin{cases} 0.38Re_{lo}^{0.03}Su_{vo}^{0.1}(\rho_l/\rho_v)^{0.35}(1/X^{0.22}), & Re_l \geq 3000, Re_v \geq 3000 \\ 0.47Re_{lo}^{0.03}Su_{vo}^{0.1}(\rho_l/\rho_v)^{0.35}(1/X^{0.30}), & Re_l < 3000, Re_v \geq 3000 \end{cases}$

where  $k$  stands for liquid (l) or vapor (v),  $Re_l = \frac{G(1-x)D}{\mu_l}$ ,  $Re_{lo} = \frac{GD}{\mu_l}$ ,  $Re_v = \frac{GxD}{\mu_v}$ ,  $Re_{vo} = \frac{GD}{\mu_v}$ ,  $Su_{vo} = \frac{\rho_v \sigma D}{\mu_v^2}$ .

were also compared to selected models for adiabatic flows two-phase flows Fig. 12). The models of Muller-Steinhagen and Heck (1986) (Eq. 18) and Kim & Mudawar (2012) (Eqs. 19–23) generally under-predicted the wall shear stress for  $G \leq 200 \text{ kg/m}^2\text{s}$  especially for downward flows. Although, these models provided good predictions of the wall shear stress at  $G = 400 \text{ kg/m}^2\text{s}$ , they failed to highlight the heat flux dependence of the wall shear stress. This is expected, considering the fact that the models were developed for adiabatic two-phase flows. In comparison, the proposed model (Proposed corr. (A)-upward flow" in Table 4) for adiabatic two-phase flow gave better prediction of the wall shear stress over the entire range of mass fluxes. However, this correlation also failed to capture the effect of heat flux on the wall shear stress. Other models were also tested and mean absolute errors for all the models tested is provided in Table 6.

To account for the effect of wall heat flux on the wall shear stress in flow boiling, Kim & Mudawar (2013b) proposed a modification to the constant ( $C_A$ ) in the model of Kim & Mudawar (2012). This was done by introducing a function which depends on the boiling number ( $Bo$ ) and Weber number of the liquid ( $We_{lo}$ ) (Eq. 24).

$$C_{NA} = \begin{cases} C_A [1 + 60We_{lo}^{0.32}Bo^{0.78}] & Re_l \geq 2000 \\ C_A [1 + 530We_{lo}^{0.52}Bo^{1.09}] & Re_l < 2000 \end{cases} \quad (24)$$

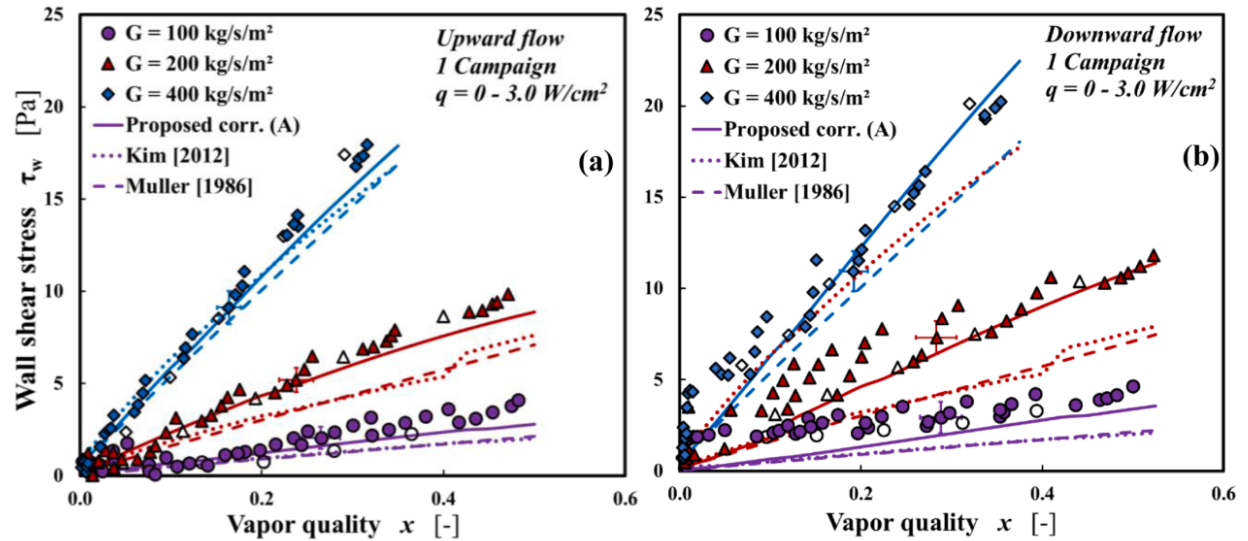
$$We_{lo} = \frac{G^2 D}{\rho_l \sigma}, \quad Bo = \frac{q_w}{Gh_{lv}}$$

Fig. 13a provides a comparison between predicted and measured wall shear stresses for upward flow boiling. The correlation provided good predictions of the measured wall shear stress over a limited range of data and also highlighted the dependence of wall shear stress on heat flux. The model overpredicted the wall shear stress at  $G = 400 \text{ kg/m}^2\text{s}$  and underpredicted the wall shear stress at  $G = 75 \text{ kg/m}^2\text{s}$ . More importantly, in the inertia dominant regime, measured data showed a suppression of the effect of wall heat flux. This suppression increased with both mass flux and vapor quality for  $Re_l \geq 1500$ . This trend in the experimental data is consistent with the conditions necessary for bubble nucleation at the wall. The model of Kim & Mudawar (2013b), failed to capture this trend (not shown for conciseness). Due to the above limitations to the model, a modification to the model was proposed in the

**Table 6**  
Mean absolute error for selected wall shear stress models.

Model/Correlation	Upward (MAE %)	Downward (MAE %)
Lockhart and Martinelli (1949)	62.9	69.5
Friedel (1979)	70.4	65.1
Muller-Steinhagen and Heck (1986)	49.1	64.2
Cicchitti et al. (1960)	48.0	62.8
Cioncolini et al. (2009)	34.0	33.9
Cioncolini and Thome (2017)	32.0	22.7
Kim & Mudawar (2012b)	37.2	50.8
Kim & Mudawar (2013b)	32.9	37.6
Proposed corr. (A)	26.3	30.3
Proposed corr. (NA)	17.0	18.8

A – adiabatic, NA – flow boiling (non-adiabatic)



**Fig. 12.** Wall shear stress versus vapor quality for vapor-liquid upward flow (left) and downward flow (right) along with comparison with selected models; adiabatic flow (open symbols), boiling flow (closed symbols).

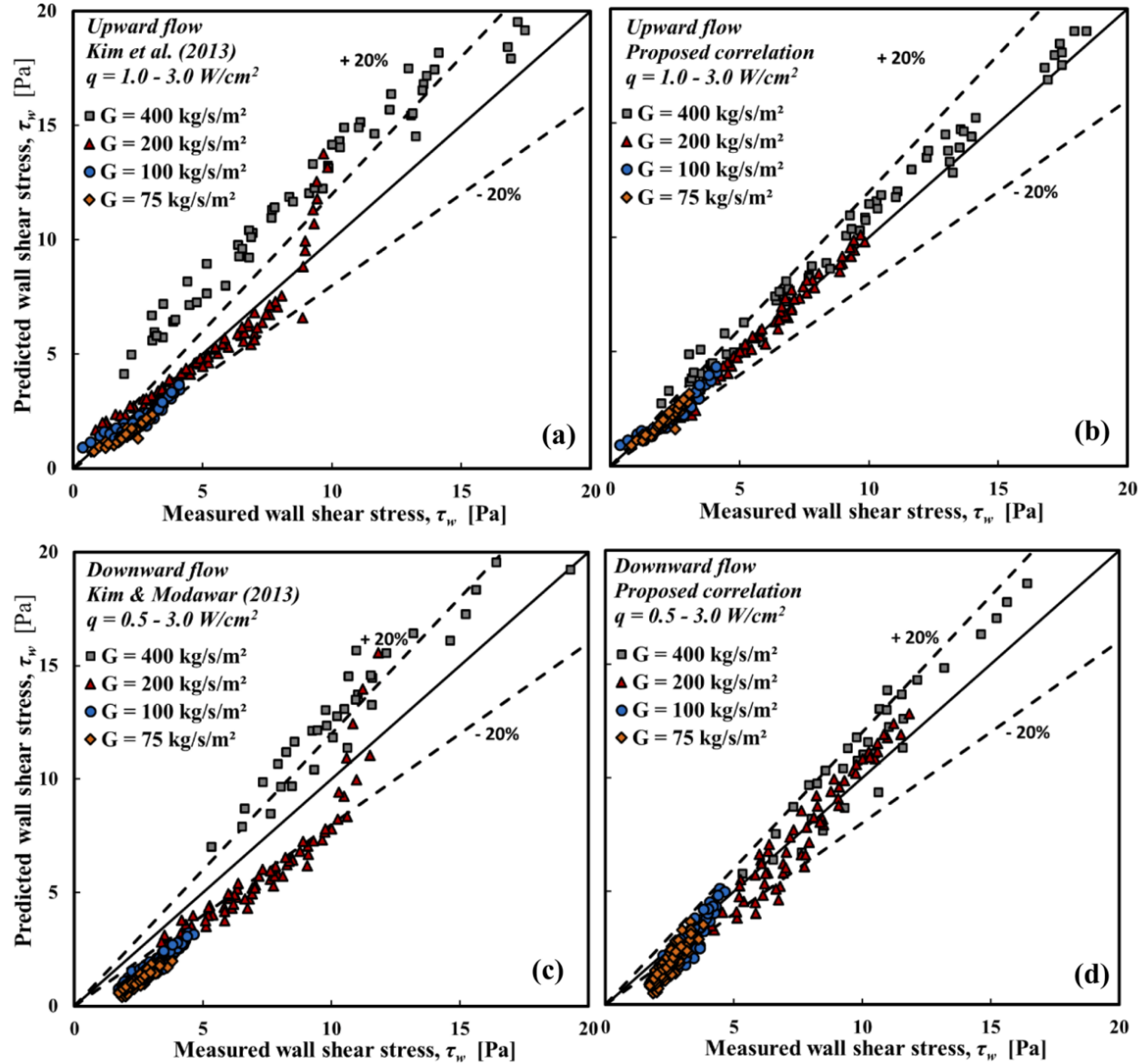


Fig. 13. Comparison between measured and predicted wall shear stress in upward (top) and downward flow boiling: (a & c) model of Kim & Mudawar (2013b), (b & d) proposed correlation.

current work. In the proposed correlation,  $C_A$  is determined according to “Proposed corr. (A)-upward flow” in Table 5. To account for the reduced heat flux dependence with increasing vapor quality, for  $Re_l \geq 1500$ , the Weber number of the liquid ( $We_{lo}$ ) was replaced with liquid Weber number determined with the superficial velocity ( $We_l$ ). Modifications were also done to the coefficients in Eq. 24 to give a better description of the heat flux dependence. The proposed correlation for  $C_{NA}$  is given by Eq. 25. Fig. 13b show comparisons between predicted and measured wall shear stresses in upward flow boiling. The correlation provided good predictions of the measured wall shear stress over the entire range of measurement. Furthermore, the proposed model recovered the trend of the measured data (not shown for conciseness). The mean square error for the model of Kim & Mudawar (2013b) and that for the proposed correlation are given in Table 6 above.

$$C_{NA} = \begin{cases} C_A [1 + 30We_l^{0.32}Bo^{0.78}] & Re_l \geq 1500 \\ C_A [1 + 320We_{lo}^{0.52}Bo^{1.09}] & Re_l < 1500 \end{cases} \quad (25)$$

$$\text{where } We_l = \frac{G^2(1-x)^2D}{\rho_l\sigma}$$

As described earlier, the measured wall shear stress was generally higher in downward flow relative to upward flow and so modifications were made to coefficients of  $C_{NA}$  proposed for upward flow (Eq. 25). In the proposed correlation for  $C_{NA}$  in downward flow,  $C_A$  is determined according to “Proposed corr. (A)-downward flow” in Table 5. The proposed correlation is given by Eq. 26. Fig. 13c provide comparisons of measured wall shear stress and wall shear stress computed from the model of Kim & Mudawar (2013b) (Eq. 24), as well as that computed from the proposed correlation for downward flow (Eq. 26). The model of

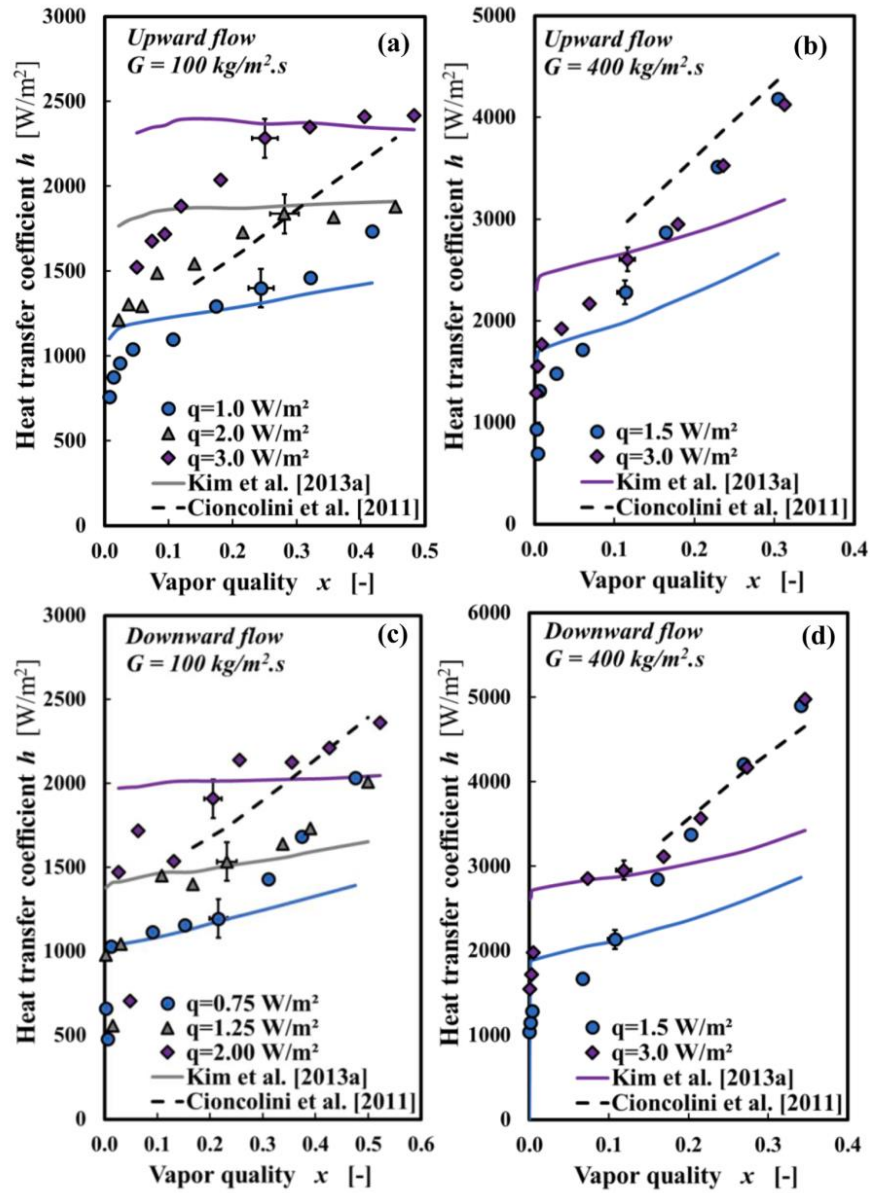


Fig. 14. Comparison between measured heat transfer coefficient with correlations of Cioncolini and Thome (2011) and Kim and Mudawar (2013a) for  $G = 100 \text{ kg/m}^2\text{s}$  (left) and  $G = 400 \text{ kg/m}^2\text{s}$  (right); experiment (symbols), prediction (lines).

Table 7

Model coefficients for  $h_{2\phi}$ .

Function	$C_1$	$C_2$	$C_3$	$C_4$	$C_5$	$C_6$	$C_7$	$C_8$	$C_9$	$C_{10}$
Kim's correlation	2345	0.70	0.38	-0.51	5.2	0.08	-0.54	3.5	0.94	0.25
Upward flow correlation	2345	0.76	0.38	-0.7	5.2	0.08	-0.54	5.1	0.71	0.13
Downward flow correlation	2345	0.76	0.38	-0.7	5.2	0.08	-0.54	5.5	0.71	0.13



**Table 8**  
Mean absolute error for selected heat transfer models.

Model/Correlation	Upward (MAE %)	Downward (MAE %)
Kandlikar (1990)	69.8	65.8
Kim and Mudawar (2013)	24.7	25.5
Kew and Cornwell (1997)	30.4	27.1
Cioncolini and Thome (2011)	14.1	17.7
Liu and Winterton (1991)	12.9	21.8
Proposed correlation	12.1	15.9

Kim & Mudawar (2013b) underpredicted and overpredicted the measured data for  $G \leq 200 \text{ kg/m}^2\text{s}$  and  $G = 400 \text{ kg/m}^2\text{s}$  respectively. The proposed correlation provided a better prediction of the measured data, particularly for  $G \geq 100 \text{ kg/m}^2\text{s}$ . The mean square error for the model of Kim & Mudawar (2013b) and that for the proposed correlation

are given in Table 6 above.

$$C_{NA} = \begin{cases} C_A [1 + 30We_l^{0.32}Bo^{0.78}] & Re_l \geq 1500 \\ C_A [1 + 400We_l^{0.52}Bo^{1.09}] & Re_l < 1500 \end{cases} \quad (26)$$

### 3.4.3. Modelling of heat transfer coefficient

As mentioned in the introduction, correlations for heat transfer based on the wall shear stress (or friction velocity) have been shown to provide good estimation of wall heat transfer. This is due to the coupling between wall heat transfer and wall shear stress. A correlation for heat transfer coefficient for annular convective flow based on the friction velocity was proposed by Cioncolini and Thome (2011). This correlation was developed from algebraic turbulent eddy diffusivity models for momentum and heat in the liquid film. The model is given by Eq. 27.

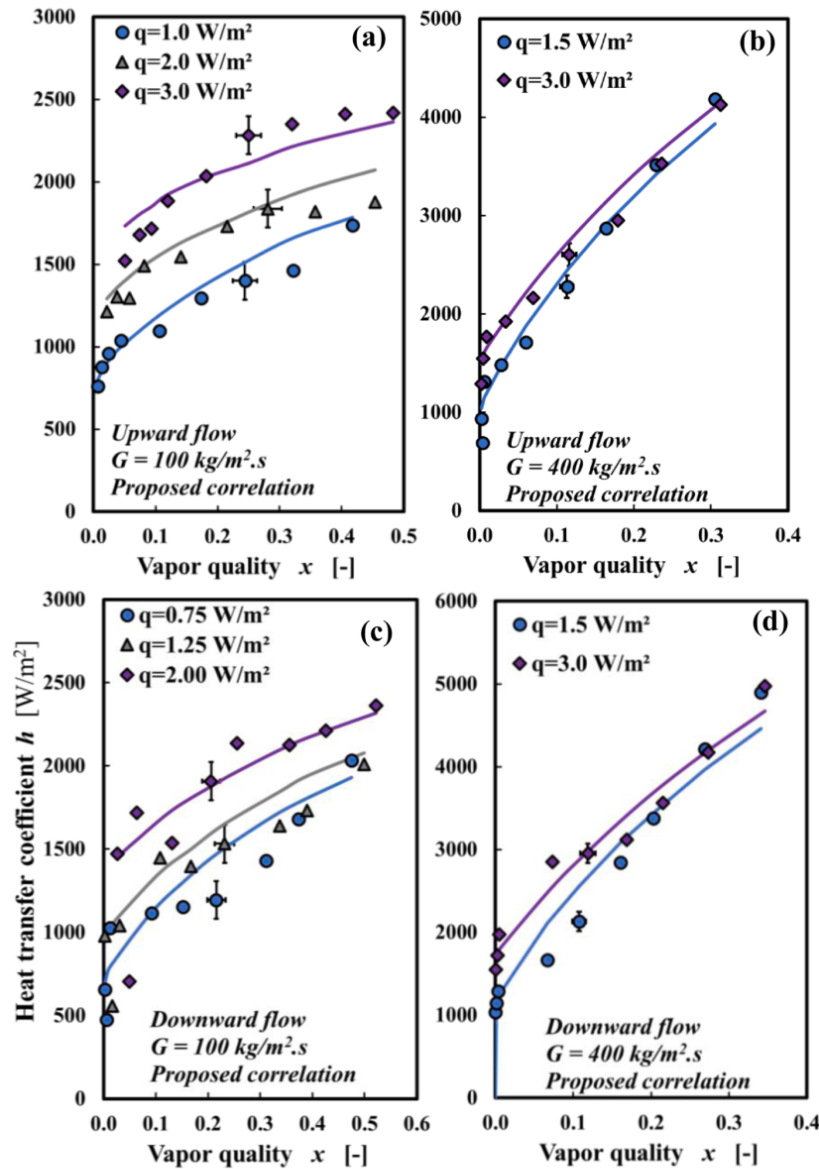


**Fig. 15.** Comparison between measured heat transfer and that predicted using the proposed correlation for  $G = 100 \text{ kg/m}^2\text{s}$  and  $G = 400 \text{ kg/m}^2\text{s}$ ; experiment (symbols), prediction (lines).

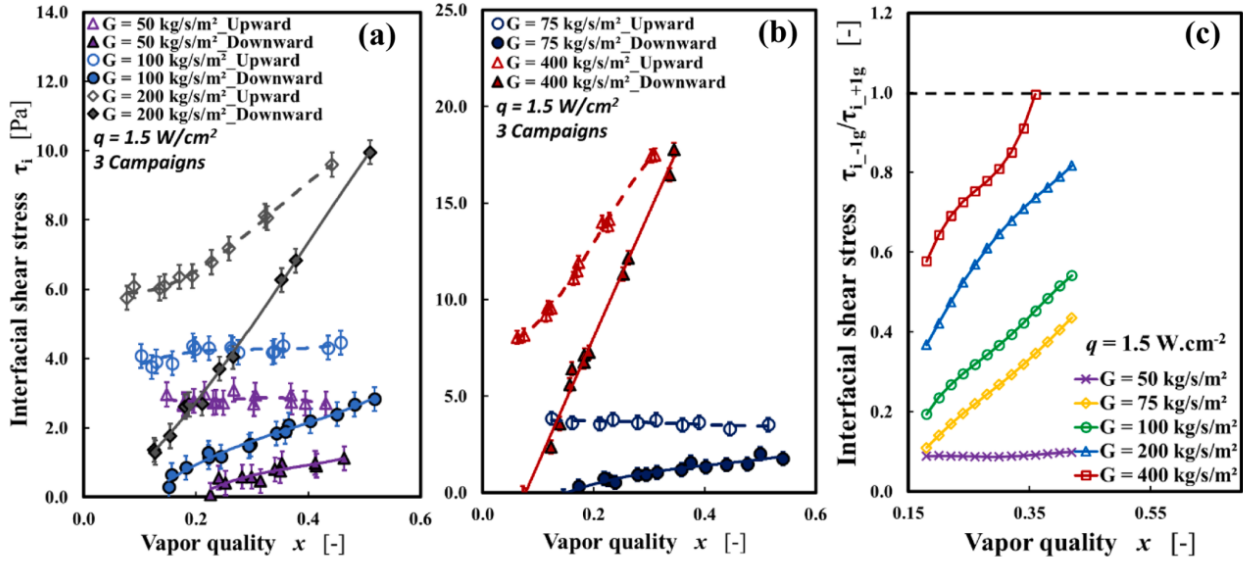


Fig. 16. Comparison between interfacial shear stress in upward and downward flow at constant heat flux. The lines are polynomial fits that provide trends: upward flow (solid lines), downward flow (dashed lines).

Table 9

Ratio of interfacial shear stress between downward and upward flows for  $q = 1.5$  and  $3.0 \text{ W/cm}^2$ .

Mass flux	$q = 1.5 \text{ W/cm}^2$		$q = 3.0 \text{ W/cm}^2$	
	$x = 0.20$	$x = 0.30$	$x = 0.10$	$x = 0.35$
$G = 50 \text{ kg/m}^2/\text{s}$	0.0895	0.0872	-	-
$G = 75 \text{ kg/m}^2/\text{s}$	0.1408	0.2680	-	-
$G = 100 \text{ kg/m}^2/\text{s}$	0.2335	0.3673	-	-
$G = 200 \text{ kg/m}^2/\text{s}$	0.4222	0.6469	0.966	0.7517
$G = 400 \text{ kg/m}^2/\text{s}$	0.6429	0.8092	0.6809	0.8854

$$h = 0.0776 \frac{\lambda_l (\delta^+)^{0.9} Pr^{0.52}}{\delta} \quad 10 < \delta^+ < 800 \quad 0.86 < Pr < 6.1 \quad (27)$$

$$\delta^+ = \frac{\delta}{y^+}, y^+ = \frac{v_l}{u^*}, u^* = \left( \frac{\tau_w}{\rho_l} \right)^{0.5}, \delta = y^+ \cdot \max \left[ \sqrt{\frac{2\Gamma_{lf}^*}{R^*}}, 0.0066 \frac{\Gamma_{lf}^*}{R^*} \right]$$

$\delta$  is the mean liquid film thickness,  $\delta^+$  is the dimensionless mean liquid film thickness,  $u^*$  is the friction velocity,  $y^+$  is the dimensionless distance from the wall,  $R^*$  is the dimensionless tube radius and  $\Gamma_{lf}^*$  is the dimensionless mass flow rate in the liquid film. The correlation is applicable to water, refrigerants and selected hydrocarbons flowing inside vertical and horizontal tube with diameter in the range of  $1.03 \leq D \leq 14.4 \text{ mm}$ . The friction velocity was obtained from the wall shear stress correlation of Cioncolini et al. (2009) (Eq. 28). The model is valid for fully convective flows and does not account for the effect of wall heat flux on heat transfer. Fig. 14 shows comparison between measured heat transfer and predicted heat transfer using correlation of Cioncolini and Thome (2011) for both upward and downward flows. The correlation gave a fairly good prediction at the highest mass flux tested ( $G = 400 \text{ kg/m}^2\text{s}$ ) where convective contribution to the heat transfer was dominant (Fig. 14b&d). It, however, fails to predict the heat transfer coefficient at lower mass fluxes where nucleate boiling is the predominant mode of heat transfer (Fig. 14a&c).

$$\left( \frac{dp}{dz} \right)_{fr} = \frac{4\tau_{w-2\phi}}{D} = 2f_{2\phi} \frac{\rho_c v_c^2}{D} \quad (28)$$

$$f_{2\phi} = 0.172 We_c^{-0.372} \quad (29)$$

$$We_c = \frac{\rho_c v_c^2 D}{\sigma} \left\{ \rho_c = \frac{x + e(1-x)}{\frac{x}{\rho_v} + \frac{e(1-x)}{\rho_l}} \right\}$$

$$e = (1 + 271.6 We_c^{-0.8395})^{-2.209}$$

where  $We_c$  is the core Weber number,  $e$  is the liquid entrainment rate and  $\rho_c$  is the core density

It is quite obvious from the foregoing that, heat transfer coefficient is influenced by wall heating in the nucleate boiling regime. This explains the poor prediction of the model of Cioncolini and Thome (2011) in the nucleate boiling regime. Kim and Mudawar (2013a) proposed an empirical correlation for predicting heat transfer coefficient which takes into account the nucleate and convective boiling contributions to the total heat transfer. The correlation, which was developed for saturated boiling regime, is given by Eqs. 30-32.

$$h_{2\phi} = \sqrt{(h_{nb}^2 + h_{cb}^2)} \quad (30)$$

$$h_{nb} = h_l \left[ C_1 Bo^{C_2} \left( \frac{P}{P_{crit}} \right)^{C_3} (1-x)^{C_4} \right] \quad (31)$$

$$h_{cb} = h_l \left[ C_5 Bo^{C_6} We_{lo}^{C_7} + C_8 \left( \frac{1}{X_{tt}} \right)^{C_9} \left( \frac{\rho_v}{\rho_l} \right)^{C_{10}} \right] \quad (32)$$

where  $C_1 - C_{10}$  are empirical constants (see Table 7),  $Bo$  is the Boiling number,  $X_{tt}$  is the Lockhart-Martinelli parameter based on turbulent liquid-turbulent vapor flows,  $We_{lo}$  is the Weber number of the liquid,  $x$  is the vapor quality,  $P/P_{crit}$  is the reduced pressure,  $h_l$  is determined from single-phase turbulent heat transfer correlation of Dittus and Boelter (1930).

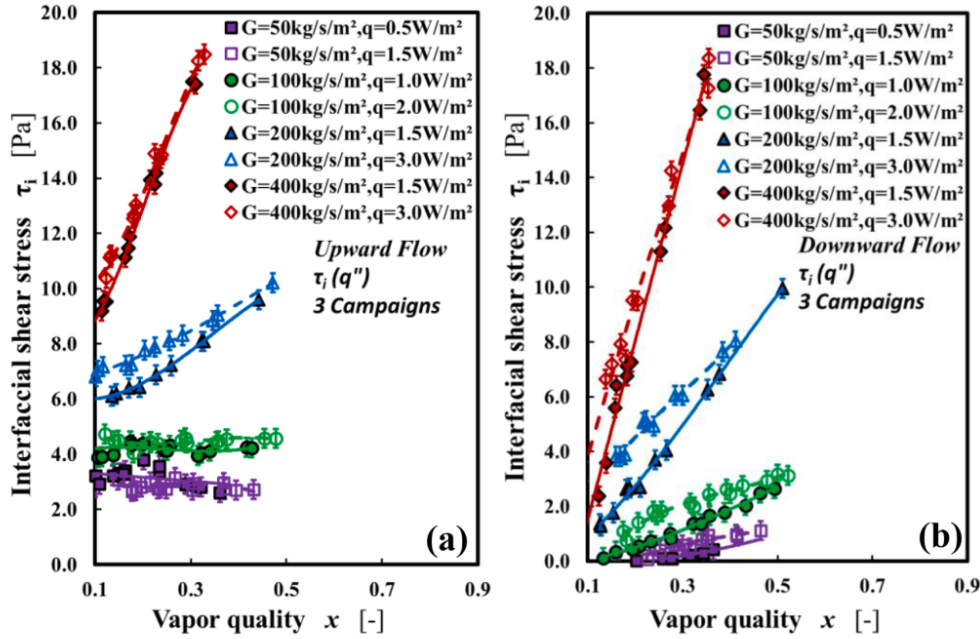


Fig. 17. Interfacial shear stress versus vapor quality at selected heat flux in a. upward flow, b. downward flow. The lines are polynomial fits that provide trends: upward flow (solid lines), downward flow (dashed lines).

$$Bo = \frac{q}{Gh_{lv}}, X_{tt} = \left( \frac{1-x}{x} \right)^{0.9} \left( \frac{\rho_v}{\rho_l} \right)^{0.5} \left( \frac{\mu_l}{\mu_v} \right)^{0.1}, We_{lo} = G^2 D / (\sigma \rho_l), h_l = 0.023 Re_l^{0.8} Pr_l^{0.4} \frac{\lambda_l}{D}$$

This correlation is applicable to refrigerants flowing inside vertical tubes of diameter 4.5 to 6.50 mm with mass flux of 100 – 500 kg/m<sup>2</sup>s. In their correlation,  $h_l$  was determined using  $Re_l = G(1-x)D/\mu_l$  not  $Re_{lo} = GD/\mu_l$ . The term  $(1-x)^{0.9}$  was introduced to account for nucleate boiling suppression, while  $We_{lo}$  accounts for the interaction between inertia and surface tension forces.

The nucleate boiling heat transfer ( $h_{nb}$ ) given by Eq. 31 is dependent of mass flux and decreases slightly with quality. The first term in the bracket in the expression of  $h_{cb}$  (Eq. 32) is generally small due to the small value of the exponent of  $Bo$ .  $h_{cb}$  increases with both mass flux and vapor quality. The correlation generally over-predicted the measured heat transfer in the nucleate boiling regime (Fig. 14) particularly for upward flow. The over-prediction in the nucleate boiling regime can be explained by the relatively fewer nucleation sites in the Sapphire tube used in the current work (relative to metallic tubes). The density of active nucleation sites was determined from high-speed video recording and was about 1 to 2 active sites per cm<sup>2</sup> for the bubbly flows with a wall superheat of 3 to 4 K (see the video in the supplementary material). An estimation of the active site density through the classical correlation of Kocamustafaogullari and Ishii (1983) gave values for metallic surfaces of around 10 sites per cm<sup>2</sup>. This difference is likely linked to the surface roughness  $R_a$ . In general, the surface roughness of sapphire substrates,  $0.3 \leq R_a \leq 0.7$  nm, (Shang Ying-Qi et al., 2017) is significantly lower than that of common copper substrates,  $0.1 \leq R_a \leq 10$  μm, (Wang et al., 2018). At high vapor quality in upward flow, their model gave good predictions of the measured heat transfer at lower mass flux ( $G \leq 100$  kg/m<sup>2</sup>s) (Fig. 14a) and under-predicted the measured heat transfer at higher mass flux ( $G \geq 200$  kg/m<sup>2</sup>s) (Fig. 14b). Furthermore, in their model, the contribution of nucleate boiling to the total heat transfer remained significant even at high mass fluxes/high vapor quality where convective heat transfer is expected to become dominant (Fig. 14b). At

high vapor quality in downward flow, their model under-predicted the measured heat transfer for all mass fluxes. Experimental data was also compared to other heat transfer models. Table 8 provides a summary of the MAE for the various models. Overall, the model of Liu and Winter-ton (1991) gave the lowest value of MAE.

Due to the limitations of the model of Kim and Mudawar (2013a) described above, a modification to their model was done to improve the performance of the correlation in relation to the current work. This was done by small modifications of some of the empirical constants in the original model of Kim and Mudawar (2013a) for upward flow. The empirical constants of the proposed correlation are provided in Table 8 along with the empirical constants of the model of Kim and Mudawar (2013a). In the proposed correlation for upward flow, the evolution of nucleate and convective boiling contributions to the total heat transfer were similar to that of Kim and Mudawar (2013). However, the nucleate boiling contribution to the total heat transfer was lower and the convective boiling contribution to the total heat transfer was higher. The proposed correlation gave good prediction of the measured heat transfer in upward flow over the entire range of mass flux, heat flux and vapor quality (Fig. 15a-b). Due to the higher liquid velocity in downward flow relative to upward flow, the proposed model for upward flow was modified by increasing the multiplier of the convective part (i.e.,  $C_8$ ) from 5.1 to 5.5 (Table 7). Fig. 15c-d give comparisons between measured and predicted heat transfer coefficient in downward flow. The model gave good prediction of the measured data over the entire measurement conditions in downward flow.

### 3.5. Interfacial shear stress and wave structures

#### 3.5.1. Interfacial shear stress

Fig. 16 provide comparisons between interfacial shear stress ( $\tau_i$ ) in upward and downward flows for various mass flux and constant heat flux.  $\tau_i$  increased with mass flux in both flow configurations and was generally higher in upward flow. This is due to higher relative velocity between the vapor and liquid phases in upward flow. A ratio of  $\tau_i$  in downward and upward flow is also provided in Table 9 to provide



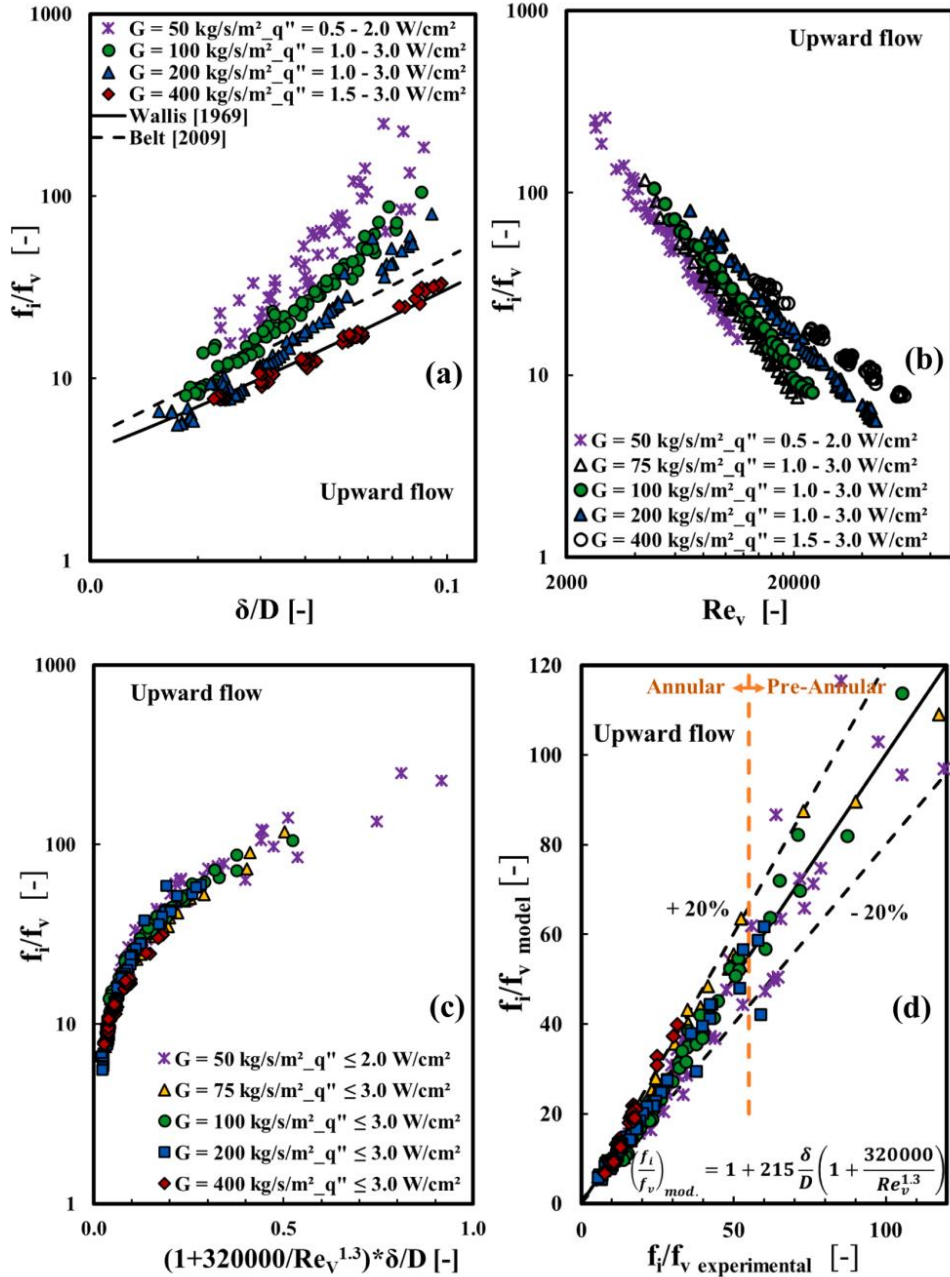


Fig. 18. a. interfacial friction factor ratio versus dimensionless liquid film thickness, b. interfacial friction factor ratio versus Reynolds number of the vapor phase, c. interfacial friction factor ratio versus model function, and d. measured interfacial friction factor ratio versus predicted interfacial friction factor ratio.

quantitative comparison. As mass flux increased, the ratio of  $\tau_i$  between both configuration increased (Fig. 16c and Table 9). Similar to wall shear stress, interfacial shear stress showed a dependence on heat flux, however, the dependence was less obvious (Fig. 17). The dependence of interfacial shear stress on wall heating was more significant downward flow (Fig. 17).

### 3.5.2. Modelling of interfacial friction factor

From the interfacial shear stress, it was possible to calculate the interfacial friction factor  $f_i$  from Eq 8 and to scale it by the friction factor

of the vapor core flow  $f_v$  (Eq. 9). The values of  $f_i/f_v$  are plotted for upward flow in Fig. 18. The relative velocity between the phases in annular two-phase upward flow is often very high, resulting in the destabilization of the interface and emergence of roll waves (Belt et al., 2009; Nancy et al., 2014). The wavy liquid surface acts as a rough wall for the gas flow. Consequently, a number of models for predicting interfacial shear stress are analogical to wall friction factor correlations in rough pipes. Wallis (1969) proposed a correlation for interfacial factor for wavy annular films which was linked to the roughness of the interface (Eq. 33). It was assumed that the vapor core flow is fully turbulent and



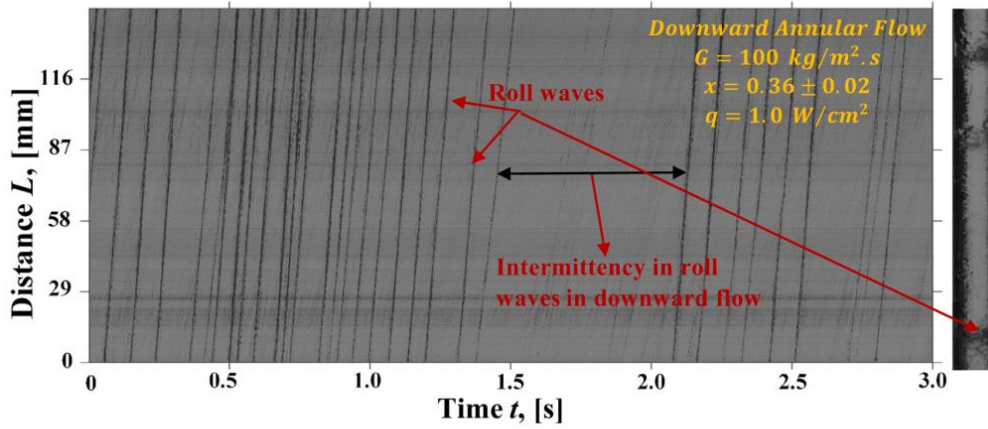


Fig. 19. Typical distance versus time plot for annular downward flow at  $G = 100 \text{ kg/m}^2\text{s}$ .

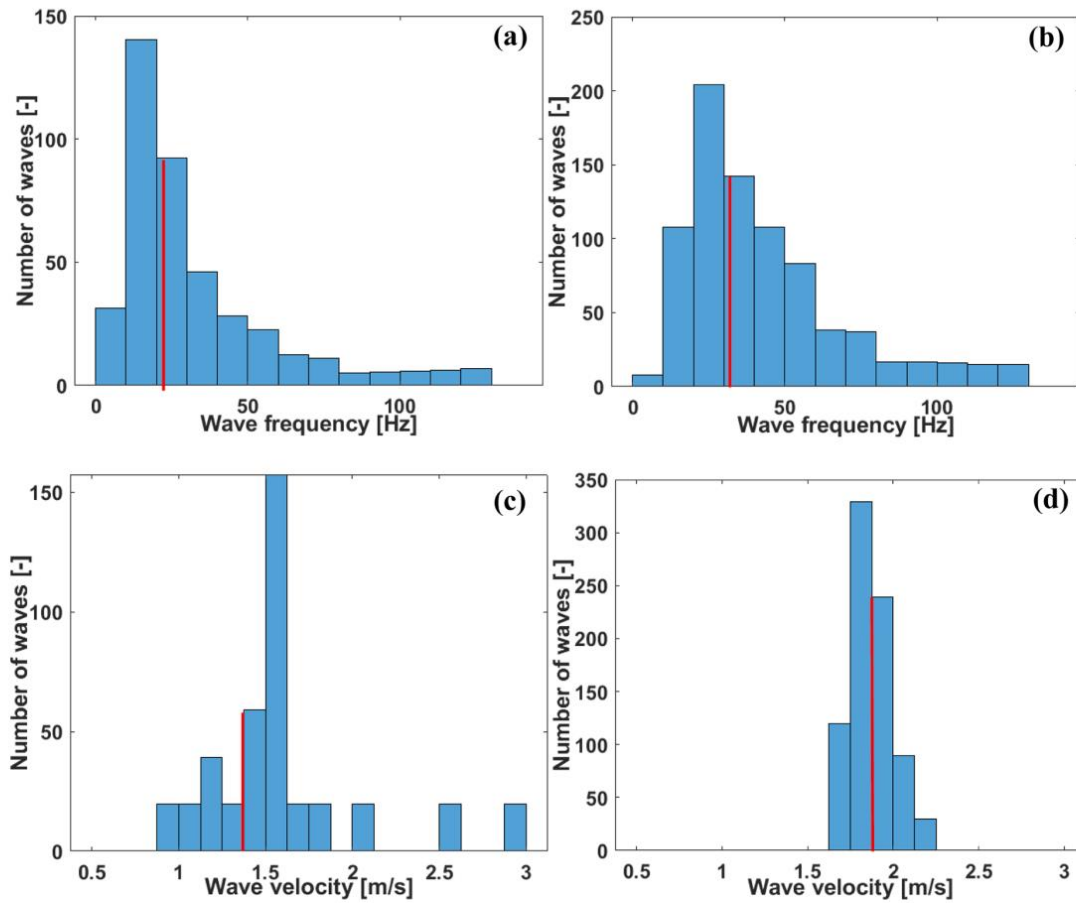


Fig. 20. PDF of a. wave frequency for  $G = 100 \text{ kg/m}^2\text{s}$ ,  $x = 0.35$ ,  $q = 1.5 \text{ W/cm}^2$ ,  $n = 413$ , b. wave frequency for  $G = 200 \text{ kg/m}^2\text{s}$ ,  $x = 0.34$ ,  $q = 1.5 \text{ W/cm}^2$ ,  $n = 807$ , c. wave velocity for  $G = 100 \text{ kg/m}^2\text{s}$ ,  $x = 0.35$ ,  $q = 1.5 \text{ W/cm}^2$ ,  $n = 413$ , d. wave velocity for  $G = 200 \text{ kg/m}^2\text{s}$ ,  $x = 0.34$ ,  $q = 1.5 \text{ W/cm}^2$ ,  $n = 807$ .  $n$  is the total number of roll waves analyzed, red line is the mean value.

the roughness of the interface was equal to the liquid film thickness ( $\delta$ ). The correlation was developed from two-phase adiabatic flow using data obtained in large diameter tube ( $D = 50 \text{ mm}$ ). In this flow configuration, the friction factor of the vapor core ( $f_v$ ) flow is  $\approx 0.005$  and quite independent of the Reynolds number of the vapor. The model provided a

good estimation of the measured interfacial friction factor ratio for  $Re_v \geq 30,000$  (see Eq. 35) corresponding to  $G = 400 \text{ kg/m}^2\text{s}$  ( $x \geq 0.16$ ) and  $G = 200 \text{ kg/m}^2\text{s}$  ( $x \geq 0.35$ ) (Fig. 18a). This flow condition was characterized by high wave velocities and high wave frequencies which resulted in a significantly rough interface. Using a similar flow

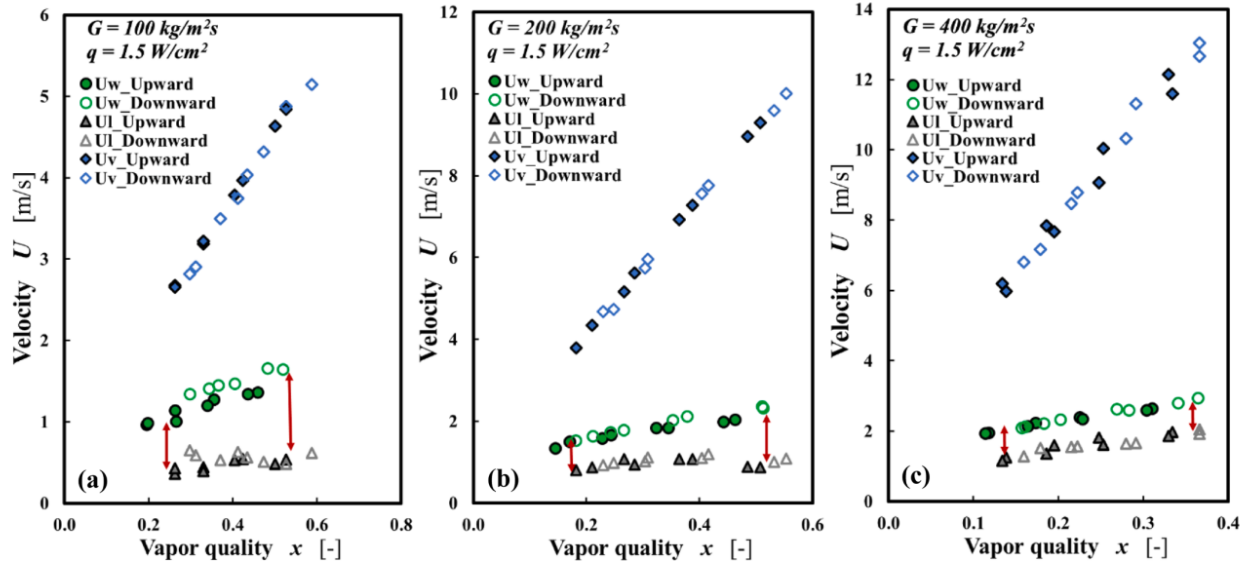


Fig. 21. Comparison between mean wave velocity, liquid velocity and vapor velocity at constant heat flux for a.  $G = 100 \text{ kg/m}^2\text{s}$ , b.  $G = 200 \text{ kg/m}^2\text{s}$  and c.  $G = 400 \text{ kg/m}^2\text{s}$ .

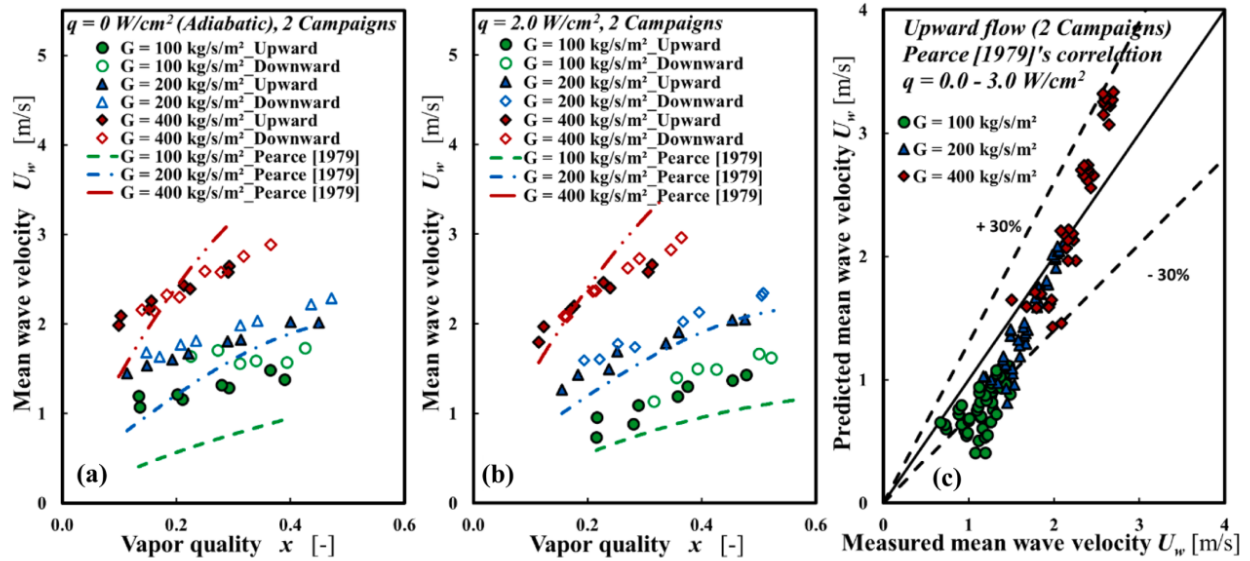


Fig. 22. Mean wave velocity versus vapor quality in upward and downward flow. a. adiabatic flow, b. non-adiabatic flow, c. predicted mean wave velocity versus measured mean wave velocity.

configuration to Wallis (1969), Belt et al. (2009) proposed a correlation given by Eq. 34. Their correlation over-predicted the friction factor ratio for  $Re_v \geq 30,000$ . Both correlations under-predicted the friction factor ratio for  $Re_v < 30,000$ . It was shown by Nancy et al. (2014) that for  $Re_v < 30,000$  the turbulence in the vapor core flow is not fully developed. This explains the poor predictions of the model of Wallis (1969) and Belt et al. (2009) for  $Re_v < 30,000$ . The regime corresponding to  $Re_v < 30,000$ , in the current work, represents a transition between smooth and fully rough turbulent regimes (Fore et al., 2000; Lopes and Dukler, 1986; Nancy et al., 2014). In the regime of transition between smooth and fully rough interface, Fore et al. (2000) highlighted the dependency of interfacial friction factor on both film thickness and Reynolds number of

the gas phase. They introduced a function  $(1 + A/Re_v)$  to the correlation of Wallis (1969) to account for the Reynolds number dependence. In the current work, the dependence of the friction factor ratio on the Reynolds number of the vapor is shown in Fig. 19b. A similar trend was also reported in the work of Nancy et al. (2014) for data acquired in an adiabatic section of the flow facility. Following similar approach to Fore et al. (2000), a function  $(1 + A/Re_v^{1.3})$  was introduced (in the current work) to the model of Wallis, (1969). The exponent of  $Re_v$  was derived from a plot of  $f_i/f_v$  versus  $Re_v$  (Fig. 18b). A plot of  $f_i/f_v$  versus  $\delta/D(1 + 320000/Re_v^{1.3})$  is shown in Fig. 18c. As can be seen from Fig. 18c, the interfacial friction factor ratios collapsed into a single curve. A correlation for  $f_i/f_v$  in upward flow was proposed in terms of  $Re_v$

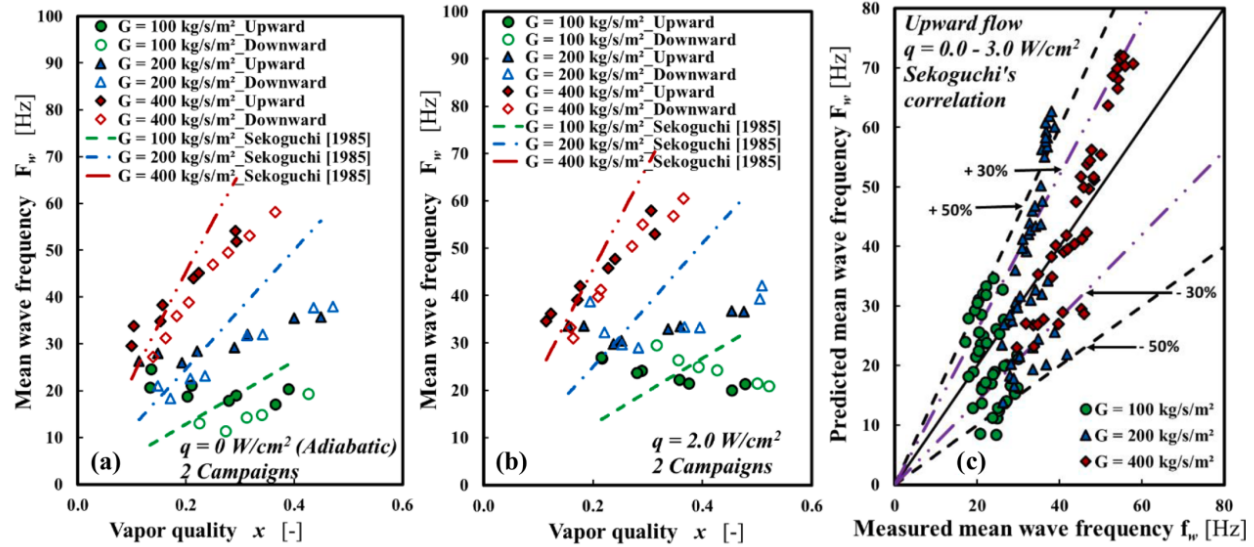


Fig. 23. Mean wave frequency versus vapor quality in upward and downward flow. a. adiabatic flow, b. non-adiabatic flow, c. predicted mean wave frequency versus measured mean wave frequency.

and  $\delta/D$  (Eq. 35). The correlation gives a good prediction of the experimental data (Fig. 18d). It should be remarked that the interfacial friction factor ratio in downward flow showed significant dependence on the wall heat flux and modelling was done in relation to wave parameters in the next section.

$$\frac{f_i}{f_v} = 1 + 300\delta/D \quad (33)$$

$$f_i = 6.826 \times 10^{-4} + 2.316\delta/D \quad (34)$$

$$\frac{f_i}{f_v} = 1 + 215\delta/D(1 + 3.2 \times 10^5/Re_v^{1.3}) \quad \left( Re_v = \frac{U_v D_c}{\nu_v}, D_c = D\sqrt{\alpha} \right) \quad (35)$$

### 3.5.3. Structure of the liquid film in annular flow: wave velocity and wave frequency

In this section, the structure of the interface, especially the velocity and the frequency of the roll waves was investigated. It is well known that the interfacial friction is directly linked to the interfacial structure. The void fraction probes used in this experiment did not have sufficient time and space resolution to measure the local real-time film thickness. Thus, the characterization of the interface was performed by image processing of high-speed visualizations and especially of the analysis of space-time diagrams.

Flow visualization revealed both roll waves and capillary waves (ripples) in upward and downward flows. The roll waves were more coherent and travelled at much higher velocities than the capillary waves. Fig. 19 show typical space-time plots obtained from the time evolution of the grey levels on an axial line of the right image in the tube center. The roll waves in upward and downward flow configurations clearly appear as dark lines in the plots. The slope of the lines gives the wave velocity ( $U_w$ ) and the intervals between them gives the period ( $T$ ). Waves of different velocities merge along the test section in both flow configurations and there is intermittency in roll waves in downward flow configuration at low mass flux.

In the current work  $\geq 20,000$  images were acquired at 1000 fps (and in some cases 1400 fps) for each flow condition corresponding to specific values of  $G$ ,  $x$  and  $q$ . The total number of waves ranged from 400 for the lowest mass flux to 1200 for the highest mass flux. Image acquisition was

carried out for two experimental campaigns at various inlet quality, mass flux and heat flux. Computed mean wave velocity and mean wave frequency from both campaigns converged within  $\pm 7.5\%$  of each other for similar flow condition. Image acquisition for each flow condition were also segmented into batches of  $\approx 2500$  images. For a given flow condition, computed wave frequency and wave velocity for each image batch were within  $\pm 5\%$  of the mean value obtained for the entire recording. The temporal interval between successive waves (period of wave) and consequently the wave frequency varied significantly. Typically range of the wave frequency was between 5 to 150 Hz. The variation of wave velocity among the individual waves (or group of 2-4 waves) was much smaller than the frequency variation (particular at higher flow rates). Fig. 20 shows typical histogram of wave frequency and wave velocity at selected flow conditions. The histogram provides further validation of data convergence.

Fig. 21 shows a comparison between the mean wave velocity, liquid velocity and vapor velocity at constant heat flux in both upward and downward flows. The mean wave velocity, liquid velocity and vapor velocity all increased with vapor quality and vapor Reynolds number. In both flow configurations, the mean wave velocity was intermediate between the mean liquid and vapor velocities and was closer to the former. The difference between the mean wave velocity and mean liquid velocity ( $U_w - U_l$ ) decreased with mass flux.  $U_w - U_l$  increased with vapor quality, but becomes independent of vapor quality at high vapor Reynolds number.

Figs. 22 and 23 show the evolution of the wave velocity and wave frequency versus the vapor quality in upward and downward flows for  $100 \leq G \leq 400 \text{ kg/m}^2\text{s}$ . At a given heat flux, both wave velocity and wave frequency increased with mass flux in both flow configurations. This is consistent with previous reports (Dasgupta et al., 2017; Kumar et al., 2002; Omebere-Iyari and Azzopardi, 2007). Wave velocity was generally higher in downward flow relative to upward flow for  $Re_v \leq 30000 \text{ kg/m}^2\text{s}$  ( $G \leq 200 \text{ kg/m}^2\text{s}$ ) but become similar in both configurations at  $Re_v > 30000 \text{ kg/m}^2\text{s}$  ( $G = 400 \text{ kg/m}^2\text{s}$ ) (Fig. 22). Gravity enhances the wave velocity in downward flow and has an opposite effect in upward flow. Conversely, at given mass flux and vapor quality, wave frequency was generally higher in upward flow relative to downward flow (Fig. 23). This is coherent with the lower interfacial shear stress measured in downward flow which in turn results in fewer roll wave formation. The difference between the mean wave frequency in upward



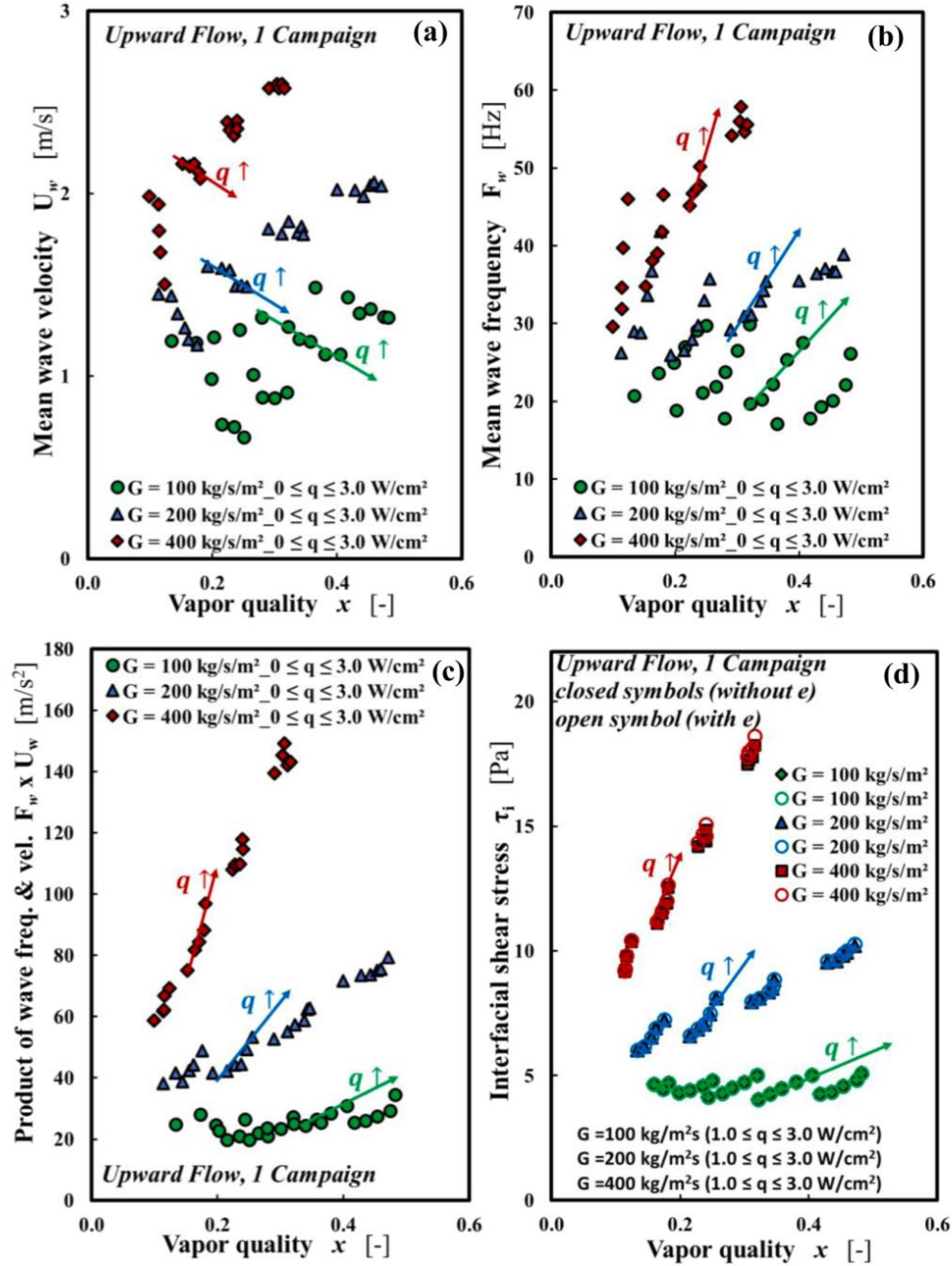


Fig. 24. a. Mean wave velocity, b. mean wave frequency, c. product of mean wave velocity and mean wave frequency, d. interfacial shear stress versus vapor quality in upward flow.

and downward flows decreased with quality and mass flux. At lower mass flux, increase in heat flux resulted in more wave formation (particularly capillary waves) in downward flow and consequently higher wave frequency in downward flow than in upward flow (Fig. 23b).

Pearce (1979) proposed a correlation for the wave velocity for adiabatic two-phase upward flow (Eq. 35). The constant  $C$  in Eq. 36 was determined to be in the range of  $0.51 \leq C \leq 0.61$  for tube diameters between  $5 \text{ mm} \leq C \leq 10 \text{ mm}$  by Omebere-Iyari and Azzopardi et al.,

(2007). Following the approach of Omebere-Iyari and Azzopardi et al., (2007), the value of the constant for the 6 mm diameter tube used for the current work is  $\approx 0.53$ . In the current work, liquid entrainment ( $e$ ) and its contribution to the calculation of the various hydrodynamic parameters was generally small across all flow configurations (see Fig. 24d). Therefore, computation of the mean liquid velocity ( $\bar{u}_l$ ) was done using Eq. 37. Pearce (1979)'s correlation reproduced the trend and provided a good estimation of the wave velocity at higher heat flux and higher mass flux (Fig. 22b-c). Similar prediction was obtained for downward flows.

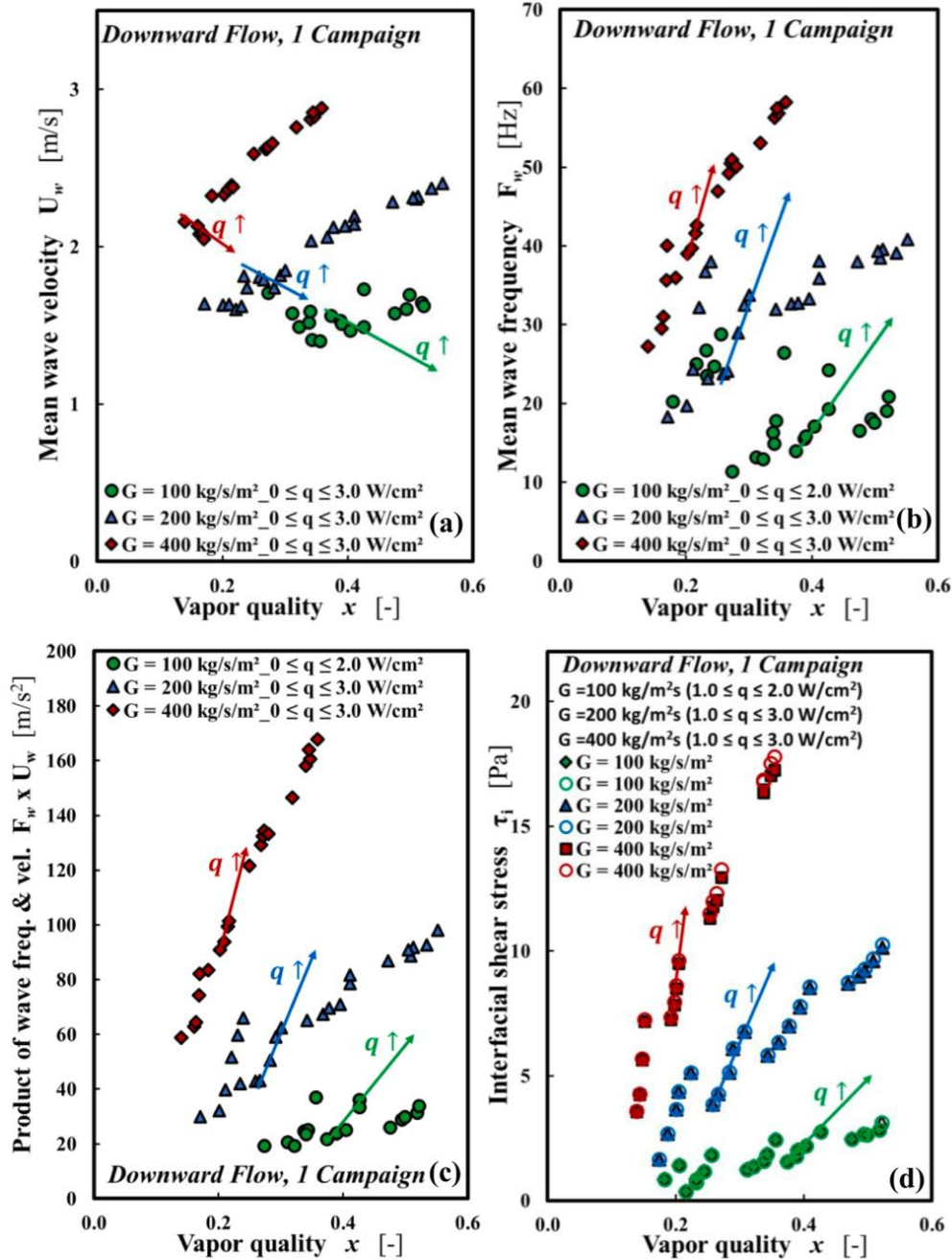


Fig. 25. a. mean wave velocity, b. mean wave frequency, c. product of mean wave velocity and mean wave frequency, d. interfacial shear stress versus vapor quality in downward flow.

$$U_w = \frac{C\bar{u}_{lf} + j_v \sqrt{\frac{\rho_v}{\rho_l}}}{C + \sqrt{\frac{\rho_v}{\rho_l}}} \quad (36)$$

$$\bar{u}_{lf} = \frac{G(1-x)}{\rho_l(1-\alpha)} \quad (37)$$

Sekoguchi et al., (1985) proposed a correlation for predicting the frequency of disturbance waves in upward flow as a function of the Eötvös number ( $Eu$ ), Reynolds number of the liquid ( $Re_l$ ) and Froude

number of the vapor ( $Fr_v$ ) (Eq. 38). The correlation predicted the measured mean wave frequency in upward flow for  $100 \leq G \leq 400$  kg/m<sup>2</sup>s within  $\pm 50\%$  and the measured mean wave frequency in upward flow for  $G = 400$  kg/m<sup>2</sup>s within  $\pm 30\%$  (Fig. 23c). Similar prediction was obtained for downward flow.

$$F_w = f_1 g_1 j_v D \quad (38)$$

where,  $f_1 = 0.5g_1 Eu^{-0.5} \ln Eu$ ,  $g_1 = 0.0076 \ln \varphi - 0.51$ ,  $Eu = \frac{gD^2(\rho_l - \rho_v)}{\sigma}$ ,  $\varphi =$

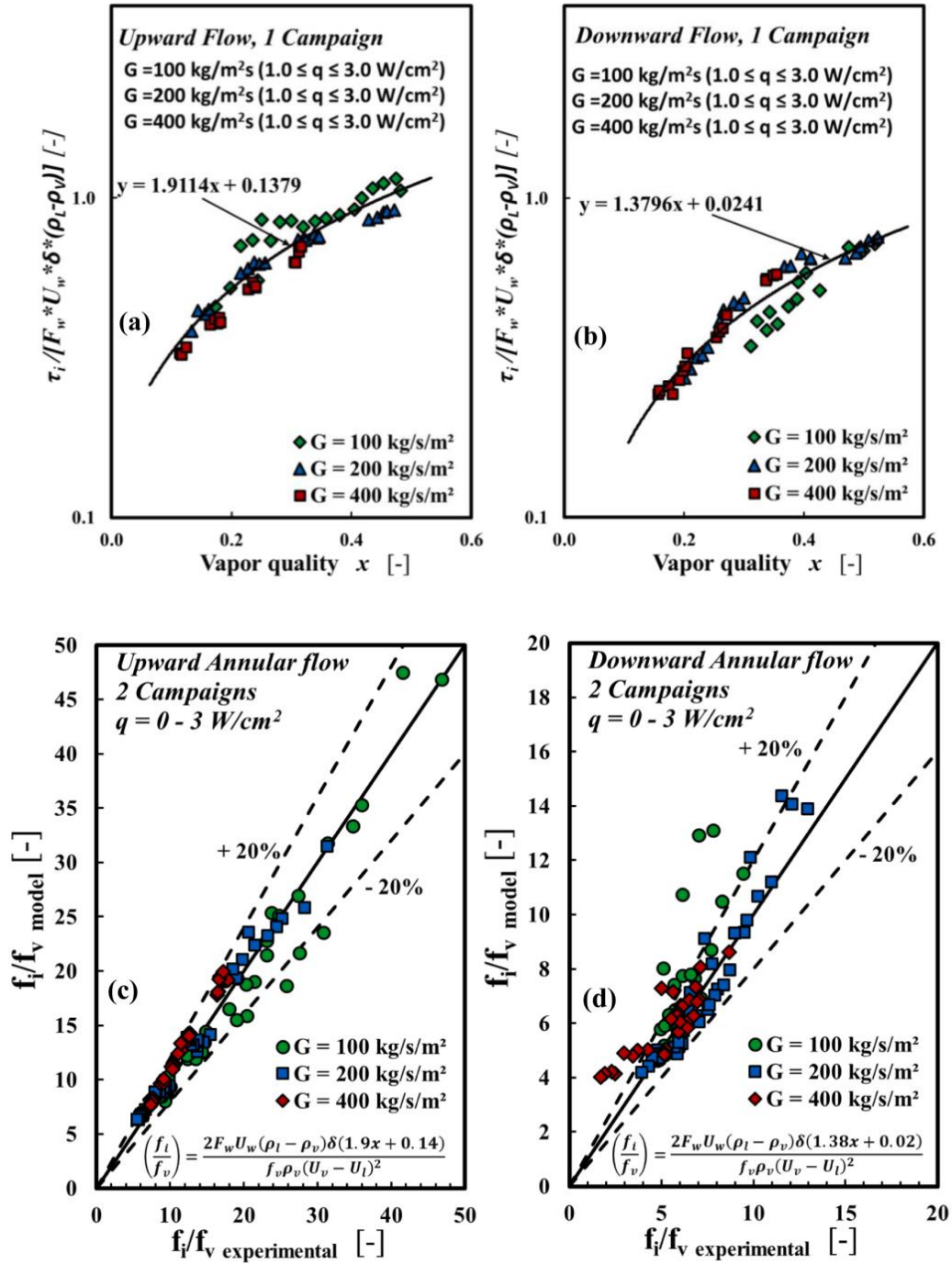


Fig. 26. Dimensionless parameter versus quality for a. upward flow, b. downward flow. Predicted interfacial friction factor ratio versus experimental interfacial friction factor ratio for c. upward flow, d. downward flow.



$$\frac{Re_{\tau}^{2.5}}{Fr_v}, Fr_v = \frac{j_v}{\sqrt{gD}}$$

The mean wave velocity and mean wave frequency showed significant dependence on wall heat flux in both flow configurations (Figs. 24 and 25). At lower vapor quality and lower mass flux, increase in wall heat flux resulted in decrease in wave velocity (Figs. 24a and 25a) and increase in wave frequency (Figs. 24b and 25b). These trends were more obvious in upward flow. Similar to mean wave frequency, the interfacial shear stress increased with wall heat flux, but at a much smaller scale (Figs. 24d and 25d). The product of mean wave velocity and mean wave frequency (Figs. 24c and 25c) also increased with wall heat flux and at a scale similar to the interfacial shear stress. It appears that effect of wall heat flux on interfacial shear stress is well captured by the product of the wave velocity and wave frequency. The results suggest that correlations for predicting interfacial shear stress in boiling flow should capture the effect of these two wave parameters (particularly in flow conditions where the effect of heat flux on the interfacial shear stress is important).

Due to the coupling between  $\tau_i$  and  $F_w \times U_w$ , a dimensionless parameter,  $\tau_i/[F_w U_w (\rho_l - \rho_v) \delta]$  was plotted against the vapor quality (Fig. 26a-b). In upward flow, data for all the mass fluxes and heat fluxes collapsed within  $\pm 10\%$  of a single curve (Fig. 26a). Similarly, in downward flow, data for all the mass fluxes and heat fluxes collapsed within  $\pm 15\%$  of a single curve (Fig. 26b). It should be remarked that the slight deviation in the profile for  $G = 100 \text{ kg/m}^2\text{s}$  in downward flow was due to lower accuracy in  $F_w \times U_w$  and difficulty in distinguishing between falling film and annular flow regimes at lower flow rates. The lower accuracy in  $F_w$  and  $U_w$  at  $G = 100 \text{ kg/m}^2\text{s}$  was due to the presence of significant number of ripples which made it difficult to analyze the roll waves independently. From the straight line fit in Fig. 26a and b, a correlation for predicting interfacial friction factor ratio in boiling flows is proposed (Eq. 39).

$$\frac{f_i}{f_v} = \frac{1}{f_v} \frac{2\tau_i}{\rho_v (U_v - U_l)^2} = \frac{1}{f_v} \frac{2F_w U_w (\rho_l - \rho_v) \delta (Ax + B)}{\rho_v (U_v - U_l)^2} \quad (39)$$

$$A \text{ and } B \approx \begin{cases} 1.9 \text{ and } 0.14 \text{ in upward flow} \\ 1.4 \text{ and } 0 \text{ in downward flow} \end{cases}, \quad 0 < q < 3W / \text{cm}^2, \quad D = 6\text{mm}$$

where  $A$  and  $B$  are constants,  $u_v$  is the vapor velocity,  $u_l$  is the liquid velocity and  $x$  is the vapor quality.

Fig. 26c and d provide comparisons between experimental interfacial friction factor ratio and that predicted by Eq. 39 for upward and downward flows respectively. For upward flow, the model predicted over 90% of the data within  $\pm 20\%$ , while for downward flow, the model predicted over 70% of the data within  $\pm 20\%$ . It should be remarked that while the values of  $B$  in Eq. 39 is expected to apply to other pipe diameters, the constant  $A$  may depend on pipe diameter. To use Eq. 39 for the prediction interfacial friction factor ratio, correlations for predicting  $F_w$  and  $U_w$  are required. The correlation of Pearce (1979) provided a reasonable prediction of  $U_w$ , particularly at higher mass flux, however, a correlation for predicting  $F_w$  is still required.

#### 4. Conclusions

This study presents a complete dataset on vertical tube flow boiling in upward and downward configurations, including void fraction, wall and interfacial shear stresses, wall heat transfer and interfacial waves characteristics in annular flow. Most of the data are compared to models and correlations of the literature and improvement of some models is proposed. The main findings of the study are the following:

1. Bubble characteristics, void fraction (& vapor velocity), wall shear stress and heat transfer coefficient showed significant sensitivity to flow direction. The aforementioned parameters were generally higher in downward flow relative to upward flow for  $G < 400 \text{ kg/m}^2\text{s}$  and  $x \leq 0.25$ .
2. The void fraction is well predicted in upward flow by the drift flux model of Rouhani and Axelsson (1970) in intermittent flow and by the model of Zuber et al. (1967) in annular flows. In downward flow the model of the Rouhani and Axelsson (1970) is in good agreement with the data in intermittent, falling film and annular flow regimes. From the void fraction values, the averaged film thickness can be estimated in annular flows using Eq. 16, since the effect of the droplet entrainment rate estimated by Cioncolini et al. (2009) is negligible.
3. There was a strong coupling between wall shear stress and heat transfer coefficient in both upward and downward flows. Wall shear stress was generally higher in boiling flow relative to adiabatic vapor-liquid two-phase flow because of the effect of bubble nucleation at the wall. The influence of wall heating on wall shear stress and heat transfer coefficient was more pronounced in downward flow relative to upward flow. Slight modifications of the correlation of Kim and Mudawar (2013b) for the wall shear stress and of the correlation of Kim and Mudawar (2013a) for the heat transfer coefficient are proposed for upward flow and extended to downward flows.
4. The interfacial shear stress increases with the mass flux, quality and wall heat flux in upward and downward flows. The effect of the heat flux is more pronounced in downward flow. In upward flow the interfacial friction factor depends on both the film thickness and the Reynolds number of the vapor core and is well predicted by Eq. 35. The interfacial shear stress is strongly related to the structure of the interfacial waves (velocity and frequency). Wave velocities and frequencies have been determined by image processing. The wave frequency increased while the wave velocity decreased with the wall heat flux. The interfacial friction factor is found to depend on the product of the wave velocity and wave frequency. Eq. 39 provides a good prediction of the friction factor subject to a good prediction of the wave velocity and the wave frequency. The correlation of Pearce (1979) gives a reasonable estimation of the mean wave velocity, but some additional work is needed for a better prediction of the wave frequency to have a fully predictive model of the interfacial friction factor.

All the experimental data presented in this manuscript can be found in the supplementary material.

#### Declaration of Competing Interest

The authors declare that they have no known competing financial interests or personal relationships that could have appeared to influence the work reported in this paper.

#### Acknowledgement

Petroleum Technology Development Fund (PTDF) is acknowledged for the PhD grant funding of P. O. Ayegba. The European Space Agency (ESA) and the French Space Agency (CNES) through the GDR MFA are acknowledged for the financial support in the building of the experimental set-up.

## Supplementary materials

Supplementary material associated with this article can be found, in the online version, at doi:[10.1016/j.ijmultiphaseflow.2022.104120](https://doi.org/10.1016/j.ijmultiphaseflow.2022.104120).

## Appendix

The uncertainties in the measured parameters are presented in this section followed by results of single-phase flow validation.

### Measurement uncertainties

Uncertainties in measured inlet and outlet vapor qualities are determined by Eq. A1 and Eq. A4. Table A1 provides a summary of uncertainties and low and high vapor qualities.

$$\delta x_{in} = \left\{ \left[ \frac{4\delta P_{ph}}{G\pi D^2 h_{lv}} \right]^2 + \left[ \frac{-4P_{ph}\delta G}{G^2\pi D^2 h_{lv}} \right]^2 + \left[ \frac{-8P_{ph}\delta D}{G\pi D^3 h_{lv}} \right]^2 + \left[ \frac{-Cp_l\delta T}{h_{lv}} \right]^2 \right\}^{0.5} \quad (A1)$$

$$\delta G = \sqrt{\left( \frac{4}{\pi D^2} \delta \dot{m} \right)^2 + \left( \frac{-8\dot{m}}{\pi D^3} \delta D \right)^2}, \delta \dot{m} = 0.5\% \times \dot{m} \quad (A2)$$

$$\delta P_{ph} = \sqrt{(U_{rms}\delta I_{rms})^2 + (I_{rms}\delta U_{rms})^2} \\ \delta I_{rms} = \pm 10 \text{ mA}, \delta U_{rms} = \pm 45 \text{ mV} \quad (A3)$$

$$\delta x_{out} = \delta x_{in} = \left\{ \left[ \frac{4L\delta q_{eff}}{GD[h_{lv} + Cp_l(T_{sat,meas} - T_z)]} \right]^2 + \left[ \frac{4q_{eff}\delta L}{GD[h_{lv} + Cp_l(T_{sat,meas} - T_z)]} \right]^2 \right. \\ \left. + \left[ \frac{-4Lq_{eff}\delta G}{G^2D[h_{lv} + Cp_l(T_{sat,meas} - T_z)]} \right]^2 \right. \\ \left. + \left[ \frac{-8Lq_{eff}\delta D}{GD^2[h_{lv} + Cp_l(T_{sat,meas} - T_z)]} \right]^2 + \left[ \frac{-Cp_l\delta T}{h_{lv} + Cp_l(T_{sat,meas} - T_z)} \right]^2 \right\}^{0.5} \quad (A4)$$

$$q_{eff} = \sqrt{\left( \frac{\delta P_{\pi O}}{\pi DL} \right)^2 + \left( \frac{-P_{\pi O}\delta D}{\pi D^2 L} \right)^2 + \left( \frac{-P_{\pi O}\delta L}{\pi DL^2} \right)^2} \quad (A5)$$

$$\delta P_{\pi O} = \sqrt{(U_{\pi O}\delta I_{\pi O})^2 + (I_{\pi O}\delta U_{\pi O})^2} \quad (A6)$$

$$\delta I_{\pi O} = \pm 10 \text{ mA}, \delta U_{\pi O} = \pm 30 \text{ mV}$$

Assuming negligible error from computed liquid entrainment, the uncertainty in the measured liquid film thickness is given by;

$$\delta(\delta) = \left[ \left( \frac{\delta D}{2} (1 - \sqrt{\alpha}) \right)^2 + \left( \frac{D}{2} \left( \frac{-\delta\alpha}{2\sqrt{\alpha}} \right) \right)^2 \right]^{0.5} \quad (\delta\alpha \approx \alpha \times 6 / 100) \quad (A7)$$

**Table A1**

Uncertainty in calculated interfacial shear stress (Pa).

	low x		high x	
	$x(-)$	$\delta x(-)$	$x(-)$	$\delta x(-)$
inlet	0.1090	0.0099(9.08%)	0.2853	0.2770(4.73%)
outlet	0.1615	0.0129(7.99%)	0.4211	0.0181(4.29%)

The mean estimated errors for low to high vapor qualities corresponding to high and low liquid film thickness is shown in Table A2. Errors in measured film thickness of up to 70% can be obtained for very high vapor qualities corresponding to very thin liquid film. (Tables A3–A5)

The uncertainty of the measured heat transfer coefficient was determined by;

**Table A2**

Error estimation for calculated liquid film thickness.

	0.10 < x < 0.20	0.20 < x < 0.35	x > 0.35
$\delta(\delta)/\delta \times 100$	3%	15%	45%



**Table A3**Uncertainty in calculated heat transfer coefficient ( $W/m^2K$ ).

	$q = 1.0 W/cm^2$ ( $T_{ow} - T_{i\infty} = 5^\circ C$ )	$q = 3.0 W/cm^2$ ( $T_{ow} - T_{i\infty} = 18^\circ C$ )
$\delta h_i$ ( $W/m^2K$ )	229.5	114.5

**Table A4**

Uncertainty in calculated wall shear stress (%).

$\tau_w$ (Pa)	$\alpha = 0.3$	$\alpha = 0.7$	$\alpha = 0.9$
3.13	$15.4 \pm 0.5\%$	$29.1 \pm 0.5\%$	$36.6 \pm 0.5\%$
9.38	$9.5 \pm 0.5\%$	$12.5 \pm 0.5\%$	$14.5 \pm 0.5\%$
15.63	$8.7 \pm 0.5\%$	$10.0 \pm 0.5\%$	$11.0 \pm 0.5\%$

**Table A5**

Uncertainty in calculated interfacial shear stress (Pa).

	$\alpha = 0.30$	$\alpha = 0.70$	$\alpha = 0.90$
$\delta \tau_i$ (Pa)	0.196	0.303	0.346

$$\delta h_i = \left[ \left( \frac{\delta q_{eff} (T_{ow} - T_{i\infty})}{T_{ow} - T_{i\infty} - \ln \left( \frac{R_o}{R_i} \right) \frac{R_o}{k} q_{eff}} \right)^2 + \left( \frac{-q_{eff} \delta T_{ow}}{(T_{ow} - T_{i\infty} - \ln \left( \frac{R_o}{R_i} \right) \frac{R_o}{k} q_{eff})^2} \right)^2 + \left( \frac{q_{eff} \delta T_{i\infty}}{(T_{ow} - T_{i\infty} - \ln \left( \frac{R_o}{R_i} \right) \frac{R_o}{k} q_{eff})^2} \right)^2 \right]^{0.5} \quad (A8)$$

$$\tau_w = \left[ (\delta \Delta P_f D / (4L))^2 + (\Delta P_f \delta D / (4L))^2 + (-\Delta P_f \delta L / (4L^2))^2 \right]^{0.5} \quad (A9)$$

Neglecting the acceleration term ( $\Delta P_f = \Delta P - [\rho_l(1 - \alpha) + \rho_v \alpha]gL$ ); the uncertainty in the measured frictional pressure drop ( $\delta \Delta P_f$ ) is given by;

$$\Delta P_f = \sqrt{(\delta \Delta P)^2 + (-\delta L [\rho_l(1 - \alpha) + \rho_v \alpha]g)^2 + ([\rho_l - \rho_v]gL \delta \alpha)^2} \quad (A10)$$

$$\delta \Delta P = \pm 0.27 \text{ mbar}$$

$$\delta \tau_i = \left[ \left( \frac{D\sqrt{\alpha}}{4L} \delta(\Delta P) \right)^2 + \left( \left( \frac{\Delta P\sqrt{\alpha}}{4L} + \frac{\rho_v g \sqrt{\alpha}}{4} \right) \delta(D) \right)^2 + \left( \frac{-\Delta P D \sqrt{\alpha}}{4L^2} \delta(L) \right)^2 + \left( \left( \frac{-\Delta P D}{8L} + \frac{\rho_v g D}{8} \right) \frac{\delta(\alpha)}{\sqrt{\alpha}} \right)^2 \right]^{0.5} \quad (A11)$$

#### Single-phase flow validation

Fig. A1 shows results of single-phase flow validation for wall friction factor and heat transfer coefficient.

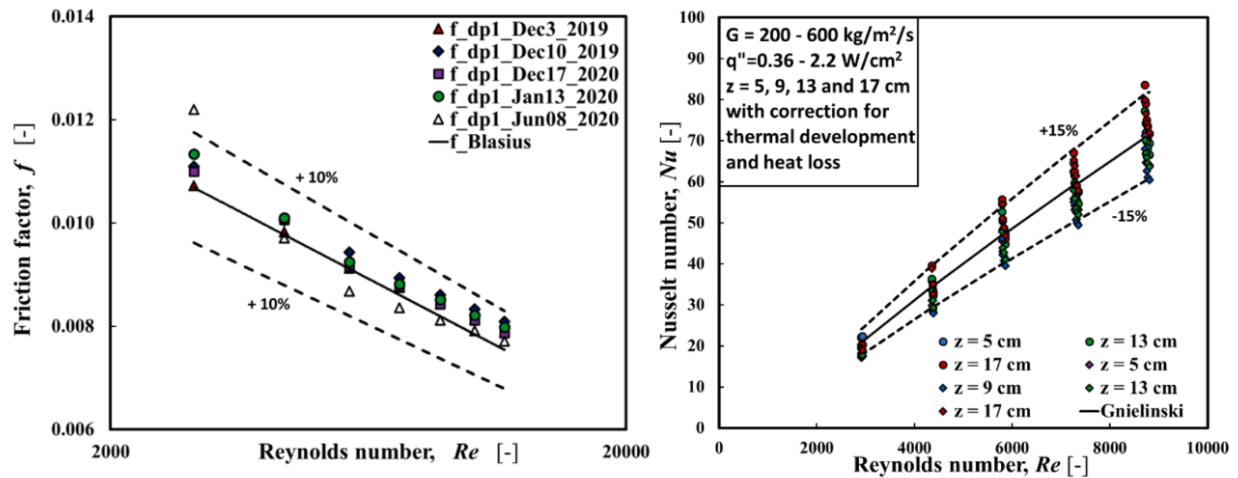


Fig. A1. Single-phase validation for wall friction factor (left) and heat transfer (right).

Comparison between wall shear stress in upward and downward non-boiling flows

Fig. A2 shows plots of wall shear stress versus quality in upward and downward flows.

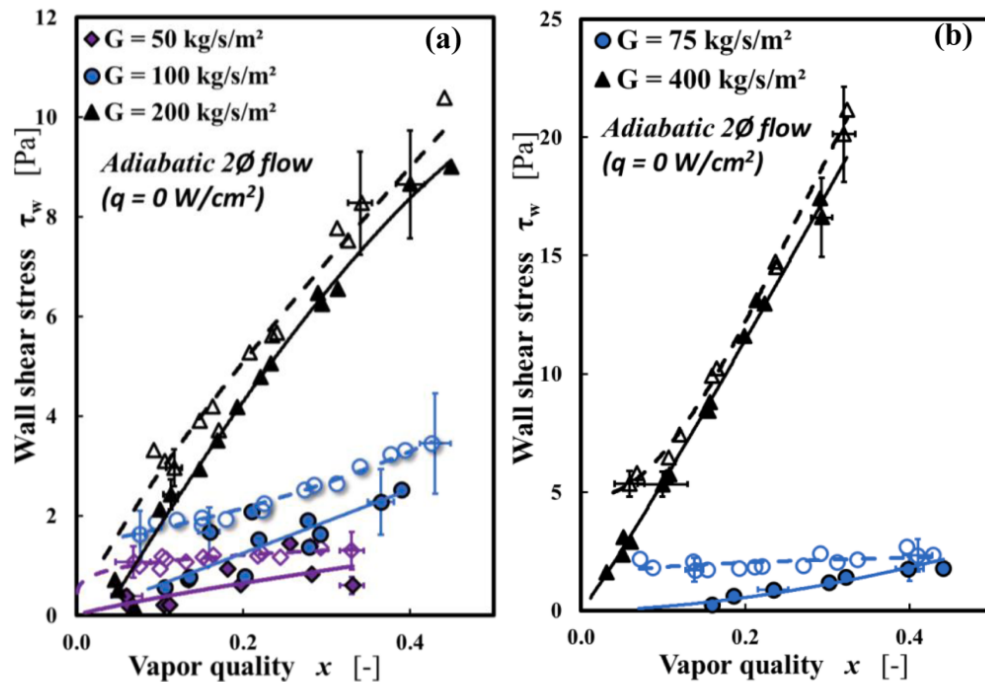


Fig. A2. Comparison of measured wall shear stress in upward and downward flow; upward flow (closed symbol), downward flow (open symbols). The lines are polynomial fits that provide trends; upward flow (solid lines), downward flow (dashed lines).

## References

- Al-Arabi, M., 1982. Turbulent heat transfer in the entrance region of a tube. *Heat Transfer Eng.* 3, 76–83.
- Almabrok, A.A., Aliyu, A.M., Lao, L., Yeung, H., 2016. Gas/liquid flow behaviours in a downward section of large diameter vertical serpentine pipes. *Int. J. Multiph. Flow* 78, 25–43.
- Asali, J.C., Hanratty, T.J., Andreussi, P., 1985. Interfacial drag and film height for vertical annular flow. *AIChE J.* 31, 895–902.
- Azzopardi, B.J., 1986. Disturbance wave frequencies, velocities and spacing in vertical annular two-phase flow. *Nucl. Eng. Des.* 92, 121–133.
- Barbosa, J.R., Hewitt, G.F., Richardson, S.M., 2003. High-speed visualisation of nucleate boiling in vertical annular flow. *Int. J. Heat Mass Transfer* 46, 5153–5160.
- Belt, R.J., Van't Westende, J.M.C., Portela, L.M., 2009. Prediction of the interfacial shear-stress in vertical annular flow. *Int. J. Multiph. Flow* 35, 689–697.
- Bhagwat, S.M., Ghajar, A.J., 2017. Experimental investigation of non-boiling gas-liquid two phase flow in downward inclined pipes. *Exp. Therm. Fluid Sci.* 89, 219–237.
- Bhagwat, S.M., Ghajar, A.J., 2015. An Empirical Model to Predict the Transition between Stratified and Nonstratified Gas-Liquid Two-Phase Flow in Horizontal and Downward Inclined Pipes. *Heat Transfer Eng.* 36, 1485–1494.
- Bhagwat, S.M., Ghajar, A.J., 2014. A flow pattern independent drift flux model based void fraction correlation for a wide range of gas-liquid two phase flow. *Int. J. Multiph. Flow* 59, 186–205.
- Bhagwat, S.M., Ghajar, A.J., 2012. Similarities and differences in the flow patterns and void fraction in vertical upward and downward two phase flow. *Exp. Therm. Fluid Sci.* 39, 213–227.
- Canière, H., T'joen, C., Willockx, A., de Paepe, M., Christians, M., van Rooyen, E., Liebenberg, L., Meyer, J.P., 2007. Horizontal two-phase flow characterization for small diameter tubes with a capacitance sensor. *Meas. Sci. Technol.* 18, 2898–2906.
- Ceccio, S.L., George, D.L., 1996. A review of electrical impedance techniques for the measurement of multiphase flows. *J. Fluids Eng.* 118, 391–399.
- Celata, G.P., Zumbo, G., 2009. Flow boiling heat transfer in microgravity: recent progress. *Multiph. Sci. Technol.* 21, 187–212.
- Chen, L., Tian, Y.S., Karayiannis, T.G., 2006. The effect of tube diameter on vertical two-phase flow regimes in small tubes. *Int. J. Heat Mass Transfer* 49, 4220–4230.
- Cicchitti, A., Lombardi, C., Silvestri, M., Soldaini, G., Zavalluilli, R., 1960. Two-phase cooling experiments-pressure drop, heat transfer and burnout measurements. *Energia Nucleare* 7, 407–425.
- Cioncolini, A., Thome, J.R., 2017. Pressure drop prediction in annular two-phase flow in macroscale tubes and channels. *Int. J. Multiph. Flow* 89, 321–330.
- Cioncolini, A., Thome, J.R., 2012. Void fraction prediction in annular two-phase flow. *Int. J. Multiph. Flow* 43, 72–84.
- Cioncolini, A., Thome, J.R., 2011. Algebraic turbulence modeling in adiabatic and evaporating annular two-phase flow. *Int. J. Heat Fluid Flow* 32, 805–817.
- Cioncolini, A., Thome, J.R., Lombardi, C., 2009. Unified macro-to-microscale method to predict two-phase frictional pressure drops of annular flows. *Int. J. Multiph. Flow* 35, 1138–1148.
- Colin, C., Fabre, J., McQuillen, J., 1996. Bubble and slug flow at microgravity conditions: state of knowledge and open questions. *Chem. Eng. Commun.* 141–142, 155–173.
- Dalkilic, A.S., Laohalertdech, S., Wongwises, S., 2008. Two-phase friction factor in vertical downward flow in high mass flux region of refrigerant HFC-134a during condensation. *Int. Commun. Heat Mass Transfer* 35, 1147–1152.
- Dasgupta, A., Chandraker, D.K., Kshirasagar, S., Reddy, B.R., Rajalakshmi, R., Nayak, A.K., Walker, S.P., Vijayan, P.K., Hewitt, G.F., 2017. Experimental investigation on dominant waves in upward air-water two-phase flow in churn and annular regime. *Exp. Therm. Fluid Sci.* 81, 147–163.
- Davis, E.J., Anderson, G.H., 1966. The incipience of nucleate boiling in forced convection flow. *AIChE J.* 12, 774–780.
- Dittus, E., Boelter, L., 1930. Experiments with fluid friction roughened pipes. *Publ. Engi.* 2, 443.
- Enoki, K., Ono, M., Okawa, T., Kristiawan, B., Wijayanta, A.T., 2020. Water flow boiling heat transfer in vertical minichannel. *Exp. Therm. Fluid Sci.* 117.
- Fore, L.B., Beus, S.G., Bauer, R.C., 2000. Interfacial friction in gas-liquid annular flow: Analogies to full and transition roughness. *Int. J. Multiph. Flow* 26, 1755–1769.
- Friedel, L., 1979. Improved friction pressure drop correlations for horizontal and vertical two-phase pipe flow. In: *European Two-Phase Flow Meeting*.
- Fukano, T., Furukawa, T., 1998. Prediction of the effects of liquid viscosity on interfacial shear stress and frictional pressure drop in vertical upward gas-liquid annular flow. *Int. J. Multiph. Flow* 24, 587–603.
- Gardenghi, A.R., Filho, E.dos S., Chagas, D.G., Scagnolatto, G., Oliveira, R.M., Tibiriçá, C.B., 2020. Overview of Void Fraction Measurement Techniques, Databases and Correlations for Two-Phase Flow in Small Diameter Channels. *Fluids* 5, 216.
- Gnielinski, V., 1976. New equations for heat and mass transfer in turbulent pipe and channel flow. *Int. J. Chem. Eng.* 16, 359–368.
- Gomyo, T., Asano, H., 2016. Void fraction characteristics of one-component gas-liquid two-phase flow in small diameter tubes. *Interfac. Phenom. Heat Transfer* 4, 1–18.

- Ishii, M., 1977. One-dimensional drift-flux model and constitutive equations for relative motion between phases in various two-phase flow regimes. *ANL-77-47*.
- Kandlikar, S.G., 1990. A general correlation for saturated two-phase flow boiling heat transfer inside horizontal and vertical tubes. *J. Heat Transfer* 112, 219–228.
- Kew, P.A., Cornwell, K., 1997. Correlations for the prediction of boiling heat transfer in small-diameter channels. *Appl. Therm. Eng.* 17, 705–715. [https://doi.org/10.1016/s1359-4311\(96\)00071-3](https://doi.org/10.1016/s1359-4311(96)00071-3).
- Kharangate, C.R., O'Neill, L.E., Mudawar, I., 2016. Effects of two-phase inlet quality, mass velocity, flow orientation, and heating perimeter on flow boiling in a rectangular channel: Part I – Two-phase flow and heat transfer results. *Int. J. Heat Mass Transfer* 103, 1261–1279.
- Khodabandeh, R., 2005. Pressure drop in riser and evaporator in an advanced two-phase thermosiphon loop. *Int. J. Refrig.* 28, 725–734.
- Kim, S., Mudawar, I., 2014. Review of databases and predictive methods for pressure drop in adiabatic, condensing and boiling mini/micro-channel flows. *Int. J. Heat Mass Transfer* 77, 74–97.
- Kim, S.M., Mudawar, I., 2013a. Universal approach to predicting saturated flow boiling heat transfer in mini/micro-channels – Part II. Two-phase heat transfer coefficient. *Int. J. Heat Mass Transfer* 64, 1239–1256.
- Kim, S.M., Mudawar, I., 2013b. Universal approach to predicting two-phase frictional pressure drop for mini/micro-channel saturated flow boiling. *Int. J. Heat Mass Transfer* 58, 718–734.
- Kim, S.M., Mudawar, I., 2012. Universal approach to predicting two-phase frictional pressure drop for adiabatic and condensing mini/micro-channel flows. *Int. J. Heat Mass Transfer* 55, 3246–3261.
- Kocamustafaogullari, G., Ishii, M., 1983. Aire interfaciale et densité de sites de nucléation dans les systèmes en ébullition. *Int. J. Heat Mass Transfer* 26, 1377–1387.
- Konishi, C., Mudawar, I., 2015. Review of flow boiling and critical heat flux in microgravity. *Int. J. Heat Mass Transfer* 80, 469–493.
- Kumar, R., Gottmann, M., Sridhar, K.R., 2002. Film thickness and wave velocity measurements in a vertical duct. *J. Fluid. Eng. Transact. ASME* 124, 634–642.
- Layssac, T., 2018. Contribution à l'étude phénoménologique de l'ébullition convective en mini-canal. Université de Lyon.
- Liu, Z., Winterton, R.H.S., 1991. A general correlation for saturated and subcooled flow boiling in tubes and annuli, based on a nucleate pool boiling equation. *Int. J. Heat Mass Transfer* 34, 2759–2766.
- Lockhart, R.W., Martinelli, R.C., 1949. Proposed correlation of data for isothermal two-phase, two-component flow in pipes. *Chem. Eng. Prog.* 45, 39–48.
- Lopes, J.C., Dukler, A.E., 1986. Droplet entrainment in vertical annular flow and its contribution to momentum transfer. *AIChE J.* 32, 1500–1515.
- Maqbool, M.H., Palm, B., Khodabandeh, R., 2012. Flow boiling of ammonia in vertical small diameter tubes: Two phase frictional pressure drop results and assessment of prediction methods. *Int. J. Therm. Sci.* 54, 1–12.
- Martin, S.C., 1976. Vertically downward two-phase slug flow. *J. Fluid. Eng. Transact. ASME* 98, 715–722.
- Mishima, K., Ishii, M., 1984. Flow regime transition criteria for upward two-phase flow in vertical tubes. *Int. J. Heat Mass Transfer* 27, 723–737.
- Muller-Steinhagen, H., Heck, K., 1986. Flow boiling in tube under normal gravity and microgravity conditions. *Chem. Eng. Process.* 20, 297–308.
- Narcy, M., de Malmazet, E., Colin, C., 2014. Flow boiling in tube under normal gravity and microgravity conditions. *Int. J. Multiph. Flow* 60, 50–63.
- Omebere-Iyari, N.K., Azzopardi, B.J., 2007. A study of flow patterns for gas/liquid flow in small diameter tubes. *Chem. Eng. Res. Des.* 85, 180–192.
- Pearce, D.L., 1979. Film waves in horizontal annular flow: space time correlator experiments. Central Electricity Research Laboratories.
- Rouhani, S.Z., Axelsson, E., 1970. Calculation of void volume fraction in the subcooled and quality boiling regions. *Int. J. Heat Mass Transfer* 13, 383–393.
- Sekoguchi, K., Takashi, U., Osamu, T., 1985. An investigation of the flow characteristics in the disturbance wave region of annular flow: 2nd report, on correlation of principal flow parameters. *Trans. Jpn. Soc. Mech. Eng.* 51, 1798–1806.
- Shang, Ying-Qi, Qi, Hong, Ma, Yun Long, Wu, Ya Lin, Zhang, Yan, Chen, Jing, 2017. Study on sapphire microstructure processing technology based on wet etching. *Int. J. Mod. Phys. B* 31.
- Taitel, Y., Bornea, D., Dukler, A.E., 1980. Modelling flow pattern transitions for steady upward gas-liquid flow in vertical tubes. *AIChE J.* 26, 345–354.
- Usui, K., 1989. Vertically downward two-phase flow, (II): Flow regime transition criteria. *J. Nucl. Sci. Technol.* 26, 1013–1022.
- Usui, K., Sato, K., 1989. Vertically downward two-phase flow, (I) void distribution and average void fraction. *J. Nucl. Sci. Technol.* 26, 670–680.
- Wallis, G., 1969. One dimensional two-phase flow. McGraw-Hill.
- Wang, M., Mei, Y., Li, X., Burgos, R., Boroyevich, D., Lu, G.Q., 2018. How to determine surface roughness of copper substrate for robust pressureless sintered silver in air. *Mater. Lett.* 228, 327–330.
- Woldesemayat, M.A., Ghajar, A.J., 2007. Comparison of void fraction correlations for different flow patterns in horizontal and upward inclined pipes. *Int. J. Multiph. Flow* 33, 347–370.
- Wu, B., Firouzi, M., Mitchell, T., Rufford, T.E., Leonardi, C., Towler, B., 2017. A critical review of flow maps for gas-liquid flows in vertical pipes and annuli. *Chem. Eng. J.*
- Zuber, N., Staub, F.W., Bijwaard, G., Kroeger, P.G., 1967. Steady State and Transient Void Fraction in Two-Phase Flow Systems. General Electric Co. Report GEAP-5417.

## 3.2 Additional Results on Hydrodynamics of Upward and Downward Flow Boiling

### 3.2.1 Liquid entrainment in the vapour core of annular flow

In this work, the liquid entrainment is estimated from the correlation of Cioncolini and Thome (2012b) (Eqs. 1.38 - 1.40). Due to implicit nature of Eqs. 1.38 - 1.40 the vapour density ( $\rho_v$ ) is used as an initial estimate for the core density ( $\rho_c$ ). This is then used to estimate the core Weber number ( $We_c$ ) and then the liquid entrainment ( $e$ ). The estimated liquid entrainment is then used to refine  $\rho_c$ . This iterative procedure is repeated until suitable convergence is achieved. The dependence of  $e$  on  $j_v$  would normally translate to higher  $e$  at higher vapour quality and higher mass flux. Figure 3.1 shows the estimated liquid entrainment as a function of vapour quality for various mass fluxes in upward and downward flows. Liquid entrainment for  $G \leq 100 \text{ kg/m}^2\text{s}$  was negligible but was significant at higher mass fluxes and increased with vapour quality. At mass flux of  $G = 400 \text{ kg/m}^2\text{s}$  and high vapour quality liquid entrainment of up to 25% was obtained.

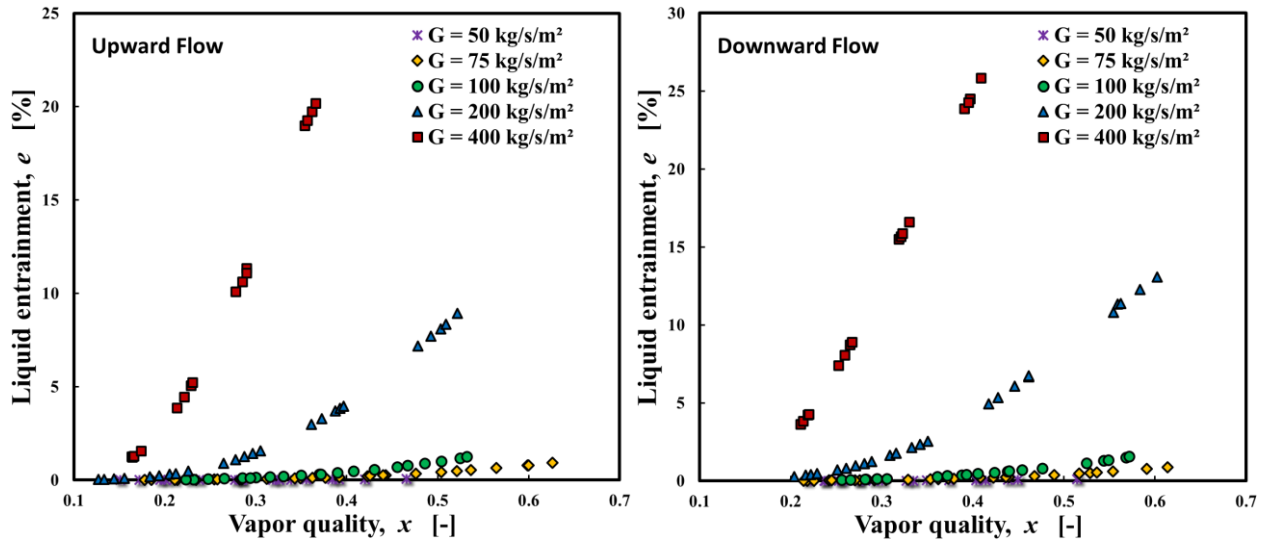


Figure 3.1: Liquid entrainment in the gas core of annular two-phase flow.

### 3.2.2 Modelling of wave structures in annular flow

As reported in Section 3.1 (journal article) the mean roll wave velocity determined from image processing was a function of the mass flux, heat flux and vapour quality. It was also shown that the model of Pearce (1979) for mean wave velocity which was developed for adiabatic two-phase flow did not provide a good prediction of the measured data in the current work. Therefore, correlations for mean roll wave velocity for upward and downward flow boiling was proposed in this work in

terms of the modified vapour Weber number ( $We_m$ ), liquid Reynolds number ( $Re_{lo}$ ) and Boiling number ( $Bo$ ). The proposed correlation is given by;

$$U_w = aRe_{lo}^b \ln We_m - c(Re_{lo}Bo)^d \quad 3.1$$

$$We_m = \frac{\rho_c j_v^2 D}{\sigma} \left( \frac{\rho_l - \rho_c}{\rho_c} \right)^{1/3} \quad 3.2$$

Table 3.1. Constants in Eq. 3.1

	a	b	c	d
Upward flow	0.0521	0.2117	0.0743	0.8506
Downward flow	0.1263	0.1112	0.1092	0.2956

Figure 3.2 shows a comparison between measured mean wave velocity and that predicted using Eq. 3.1. The correlation predicted the measured data within  $\pm 15\%$  and also recovered the heat and mass flux dependence if the mean wave velocity in both upward and downward flow.

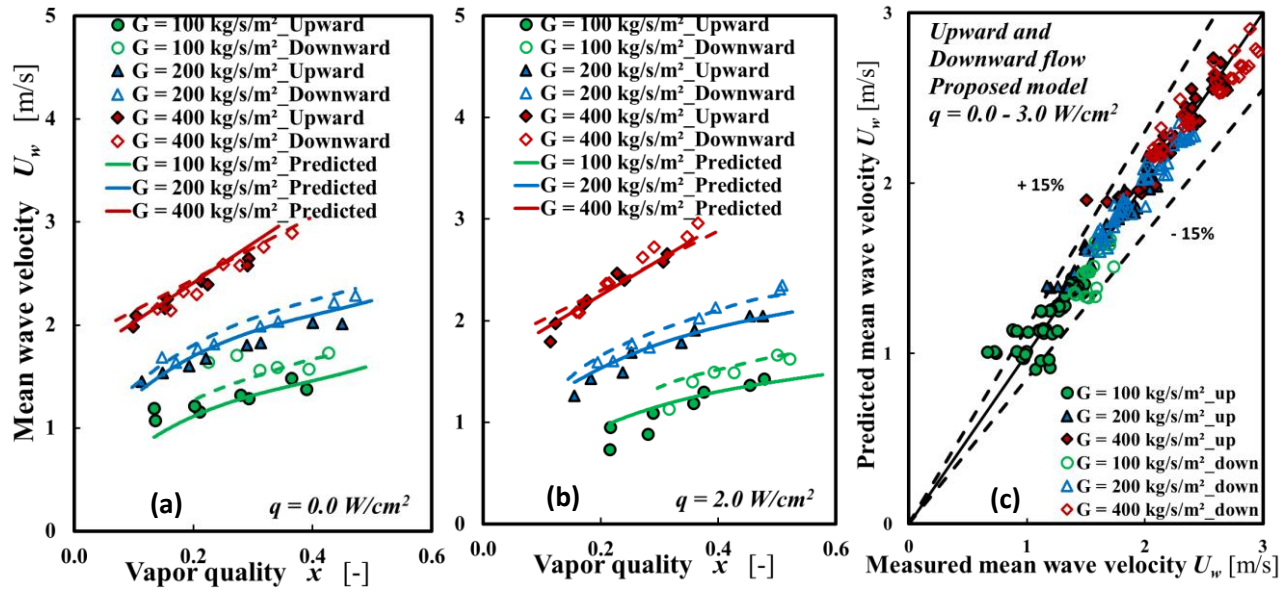


Figure 3.2: Comparison between measured and predicted mean wave velocity for upward and downward flow boiling.

Similar to mean wave velocity, measured mean wave frequency was influenced by the mass flux, heat flux and vapour quality. The predicted mean wave frequency using the correlation of Sekoguchi et al. (1985) was generally poor and as expected, for adiabatic two-phase models, it failed to highlight



the heat flux dependence of the wave frequency. In the current work, correlations for roll wave frequency for adiabatic and flow boiling were proposed. The proposed correlation is given by;

$$F_w = \sqrt{F_{w-1}^2 + F_{w-2}^2} \quad 3.3$$

$$F_{w-1} = \begin{cases} \text{Flow boiling: } [C_1 Bo^{C_2} P_R^{C_3} (1-x)^{C_4}] Re_l^{0.8} \\ \text{Adiabatic: } 0 \end{cases} \quad 3.4$$

$$F_{w-2} = \begin{cases} \text{Flow boiling: } [C_5 Bo^{C_6} We_{lo}^{C_7} + C_8 (1/X_{tt})^{C_9} (\rho_v/\rho_l)^{C_{10}}] Re_l^{0.8} \\ \text{Adiabatic: } [C_8 (1/X_{tt})^{C_9} (\rho_v/\rho_l)^{C_{10}}] Re_l^{0.8} \end{cases} \quad 3.5$$

where  $P_R$  is the reduced pressure.

Table 3.2. Constants in Eqs. 3.4 - 3.5

	$C_1$	$C_2$	$C_3$	$C_4$	$C_5$	$C_6$	$C_7$	$C_8$	$C_9$	$C_{10}$
Upward flow	41.78	1.40	-1.16	2.50	4.68	-0.09	-1.35	0.10	0.51	0.25
Downward flow	37.45	1.56	-1.62	1.39	-10.73	-0.16	-1.78	0.07	0.75	0.25

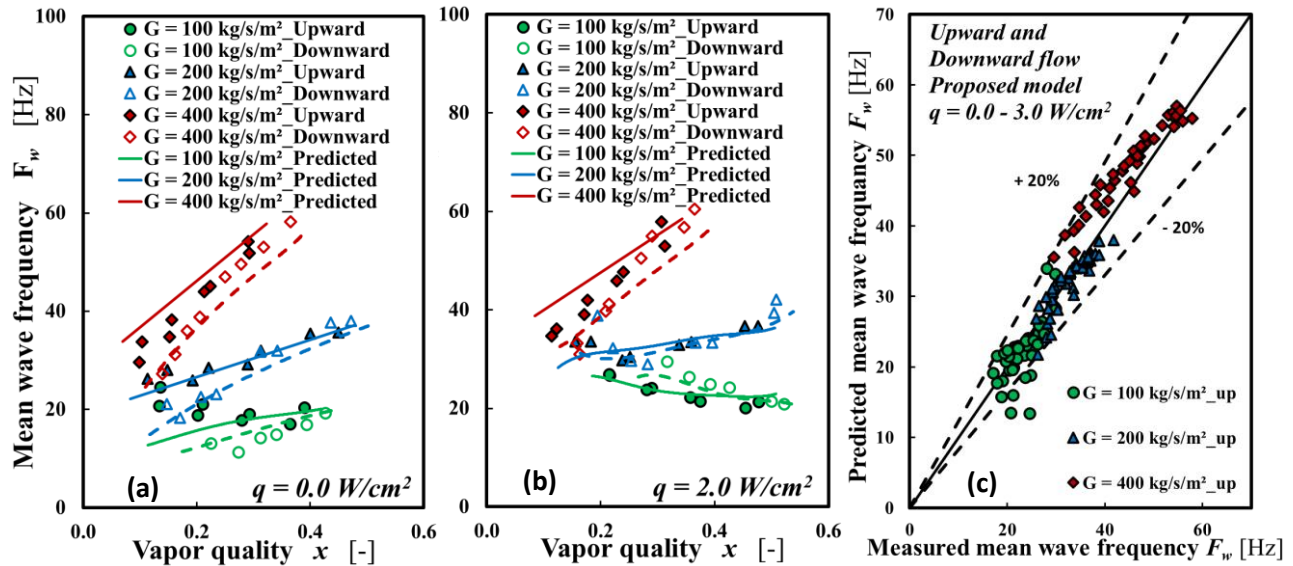


Figure 3.3: Comparison between measured and predicted mean wave velocity for upward and downward flow boiling.

Figure 3.3 shows a comparison between measured mean wave velocity and that predicted using Eq. 3.3. The correlation predicted the measured data within  $\pm 20\%$  and also recovered the heat and mass flux dependence of the mean wave velocity in both upward and downward flow.

### 3.2.3 Modelling of Interfacial Friction Factor in Annular flow

Modelling of the interfacial friction factor ratio ( $f_i/f_v$ ) for upward boiling flow was presented in section 3.1 (journal article, Eq. 35 pp 23). The focus here is to provide an interfacial friction factor model for downward flow. As reported in section 3.1 (journal article), unlike like the case of upward flow, the interfacial friction factor for downward flow was significantly influenced by the wall heat flux (Figure 3.4a-c) and less affected by the liquid film thickness (Figure 3.4d). In addition to the  $Re_v$ -dependence of  $f_i/f_v$ , its lower dependence on  $\delta$  was counted for by replacing  $\delta/D$  with  $(\delta/D)^m$  ( $m \cong 0.55$ ) and its dependence on heat flux was accounted for by the introduction of a Boiling number function.

A plot of  $f_i/f_v$  vs  $(\delta/D)^{0.55} \left\{ 1 + 3.2 \times 10^5 [1 + (Re_{lo}Bo)^6]/Re_v^{(1.62+0.116Re_{lo}Bo)} \right\}$  is shown in Figure 3.4e and it most of the data collapse into the single profile. A model for  $f_i/f_v$  given by Eq. 3.6 is therefore proposed for downward flow boiling. Figure 3.4f shows a plot of predicted versus measured interfacial friction factor ratio for downward flow boiling. The proposed correlation predicted the experimental data within  $\pm 20\%$ .

$$\frac{f_i}{f_v} = 1 + 30.5 \left( \delta/D \right)^{0.55} \left[ 1 + \frac{3.2 \times 10^5 [1 + (Re_{lo}Bo)^6]}{Re_v^{(1.62+0.116Re_{lo}Bo)}} \right] \quad 3.6$$

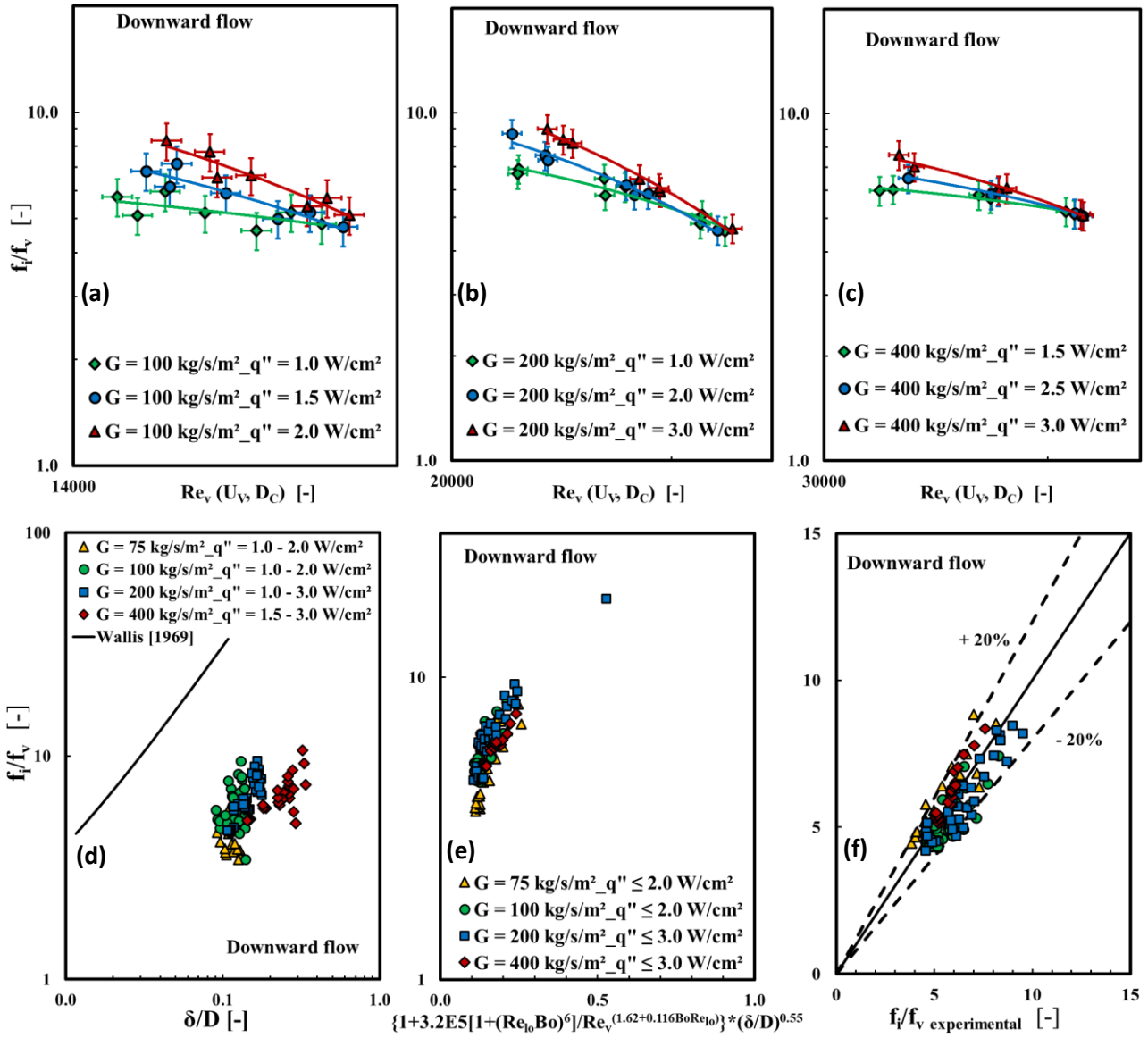


Figure 3.4: Interfacial friction factor ratio in downward flow.

### 3.3 Conclusion

Results of experimental and modelling studies of the hydrodynamics of flow boiling in upward and downward flow configurations were presented in this chapter. The flow boiling quantities of interest were flow pattern, void fraction, wave structures, wall and interfacial shear stresses as well as heat transfer coefficient. The aforementioned flow boiling quantities were influenced by the mass flux, heat flux, vapour quality and flow configuration. Void fraction, wave velocity, wall shear stress and heat transfer coefficient were higher in downward flows relative to upward flow while the converse was the case for interfacial shear stress and wave frequency. Wall shear stress, interfacial shear stress, wave velocity, wave frequency and heat transfer coefficient generally increased with mass flux. In



*both flow configurations, it was found that, wall and interfacial shear stresses were higher in flow boiling relative to adiabatic vapour-liquid two-phase flows and the difference increased with heat flux. A significant coupling was found between wall shear stress and heat transfer coefficient as well as between wave structures and interfacial shear stress. Models developed for adiabatic two-phase flows did not provide very good prediction of the flow boiling data in the current work. Correlations for predicting flow boiling wall shear stress, interfacial friction factor, wave structures and heat transfer coefficient were proposed in this chapter and the proposed correlations provided good estimates of the measured data.*

*The validity of the proposed models in the article were only tested using the experimental data acquired in this work. Future studies should test these models on other data in literature so as to increase the level of confidence in the models for industry applications.*

## **Chapter 4**

### **Results of Heat Transfer in Upward and Downward Flow Boiling**

*This section begins with a brief discussion of the measured heat transfer coefficient for the various flow regimes in both upward and downward flows. It is then followed by the theoretical modelling of heat transfer coefficient and liquid film thickness in annular upward and downward flows (as published in one of our articles) is presented.*

#### 4.1 Mechanism of Heat Transfer in Upward and Downward Flow Boiling

The effect of heat flux, mass flux and vapour quality on measured heat transfer coefficient was described in general terms in Chapter 3 (journal article, Fig. 14, pp118). In this section, a more detailed discussion of the measured heat transfer in the various flow boiling regimes is presented. Flow boiling heat transfer can be broadly categorised into subcooled and saturated boiling regimes. In the current work, the subcooled boiling regime corresponded mostly to the bubbly, slug/churn and falling film flow regimes at low vapour qualities while the saturated boiling regime corresponded mainly to the churn and annular flow regimes at intermediate to high vapour qualities. The total heat transfer coefficient consisted of nucleate boiling and convective boiling components and the magnitude of each of these components depends on the heat flux, mass flux and vapour quality.

Table 4.1 and Figure 4.1 provide a general description of the heat transfer regimes in upward flow. In general, in the nucleate boiling (NB) regime, the heat transfer coefficient increased with heat flux and was independent of the vapour quality. Whereas, in the convective boiling (CB) regime, the heat transfer coefficient increased with the vapour quality and was independent of heat flux.

For  $50 \leq G \leq 400 \text{ kg/m}^2\text{s}$ ,  $x \leq 0.1$  and  $q \geq 0.5 \text{ W/cm}^2$  (bubbly and intermittent flows) the flow was in the NB regime and the measured heat transfer coefficient increased with heat flux (Figure 4.1). At low mass fluxes ( $G = 50, 75 \text{ kg/m}^2\text{s}$ ),  $q \geq 0.5 \text{ W/cm}^2$  and  $0.1 < x \leq 0.7$  (intermittent and annular flows), the flow was also in the NB regime and heat transfer coefficient increased with heat flux but was generally independent of the vapour quality (Figure 4.1). At intermediate mass flux ( $G = 100 \text{ kg/m}^2\text{s}$ ),  $1.0 < q \leq 3.0 \text{ W/cm}^2$  and  $0.1 < x \leq 0.7$  (intermittent and annular flows) there appeared to be a transition between the NB and CB regimes (NB + CB) and the heat transfer coefficient was dependent on both heat flux and vapor quality. At high mass flux ( $G = 200, 400 \text{ kg/m}^2\text{s}$ ),  $1.5 < q \leq 3.0 \text{ W/cm}^2$  and  $0.1 < x \leq 0.25$  (intermittent and annular flows), there also appeared to be a transition between the NB and CB regimes (NB + CB) and the heat transfer coefficient was dependent on both heat flux and vapor quality (Figure 4.1). At high mass flux ( $G = 200, 400 \text{ kg/m}^2\text{s}$ ),  $q \leq 3.0 \text{ W/cm}^2$  and  $x > 0.25$  (annular flow), the flow was in the CB regime and the measured heat transfer coefficient increased with quality and was independent of the heat flux.

Table 4.1: Dominant mechanism of heat transfer in upward flow boiling

Mass flux	$x \leq 0.1$	$0.1 < x \leq 0.25$	$x > 0.25$
$G = 200, 400 \text{ kg/m}^2\text{s}$	NB	NB+CB	CB
$G = 100 \text{ kg/m}^2\text{s}$	NB	NB+CB	NB+CB
$G = 50, 75 \text{ kg/m}^2\text{s}$	NB	NB	NB

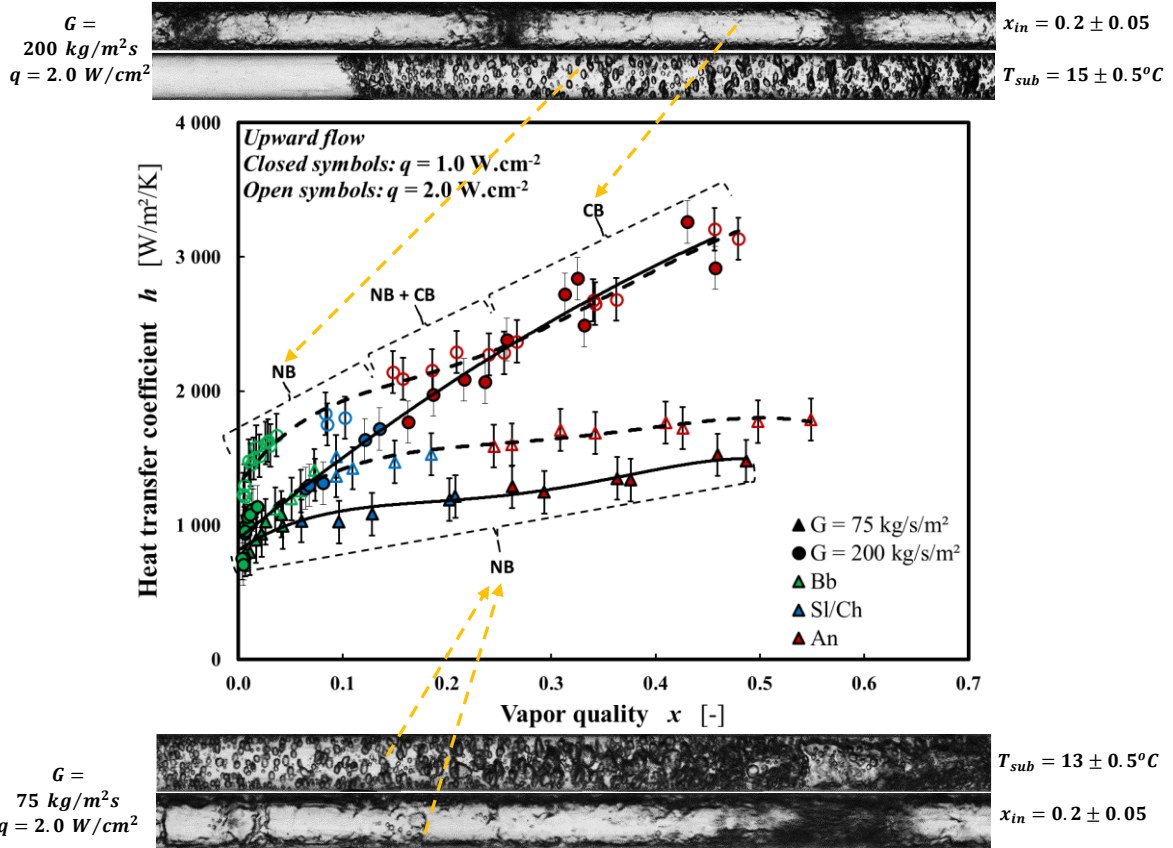


Figure 4.1: Illustration of the various heat transfer regimes for upward flow boiling.

Table 4.2 and Figure 4.2 provide a general description of the heat transfer regimes in downward flow. For  $50 \leq G \leq 400 \text{ kg/m}^2\text{s}$ ,  $x \leq 0.15$  and  $q \geq 0.5 \text{ W/cm}^2$  (bubbly, intermittent and falling-film flows) the flow was in the NB regime and the measured heat transfer coefficient increased with heat flux (Figure 4.2). At low to intermediate mass flux ( $G \leq 100 \text{ kg/m}^2\text{s}$ ),  $q \geq 0.5 \text{ W/cm}^2$  and  $0.15 < x \leq 0.7$  (falling-film and annular flows) the flow was in the NB regime and the measured heat transfer coefficient increased with heat flux but was quite independent of the vapour quality. At high mass flux ( $G \geq 200 \text{ kg/m}^2\text{s}$ ),  $1.5 \leq q \leq 3.0 \text{ W/cm}^2$  and  $0.15 < x \leq 0.3$  (intermittent and annular flows), there appeared to be a transition between the NB and CB regimes (NB + CB) and the

heat transfer coefficient was dependent on both heat flux and vapor quality. At high mass flux ( $G \geq 200 \text{ kg/m}^2\text{s}$ ),  $q \leq 3.0 \text{ W/cm}^2$  and  $x > 0.3$ , the flow was in the CB regime and the measured heat transfer coefficient increased with quality and was independent of the heat flux.

Table 4.2: Dominant mechanism of heat transfer in downward flow boiling

Mass flux	$x \leq 0.15$	$0.15 < x \leq 0.3$	$x > 0.3$
$G = 200, 400 \text{ kg/m}^2\text{s}$	NB	NB+CB	CB
$G = 50, 75, 100 \text{ kg/m}^2\text{s}$	NB	NB	NB

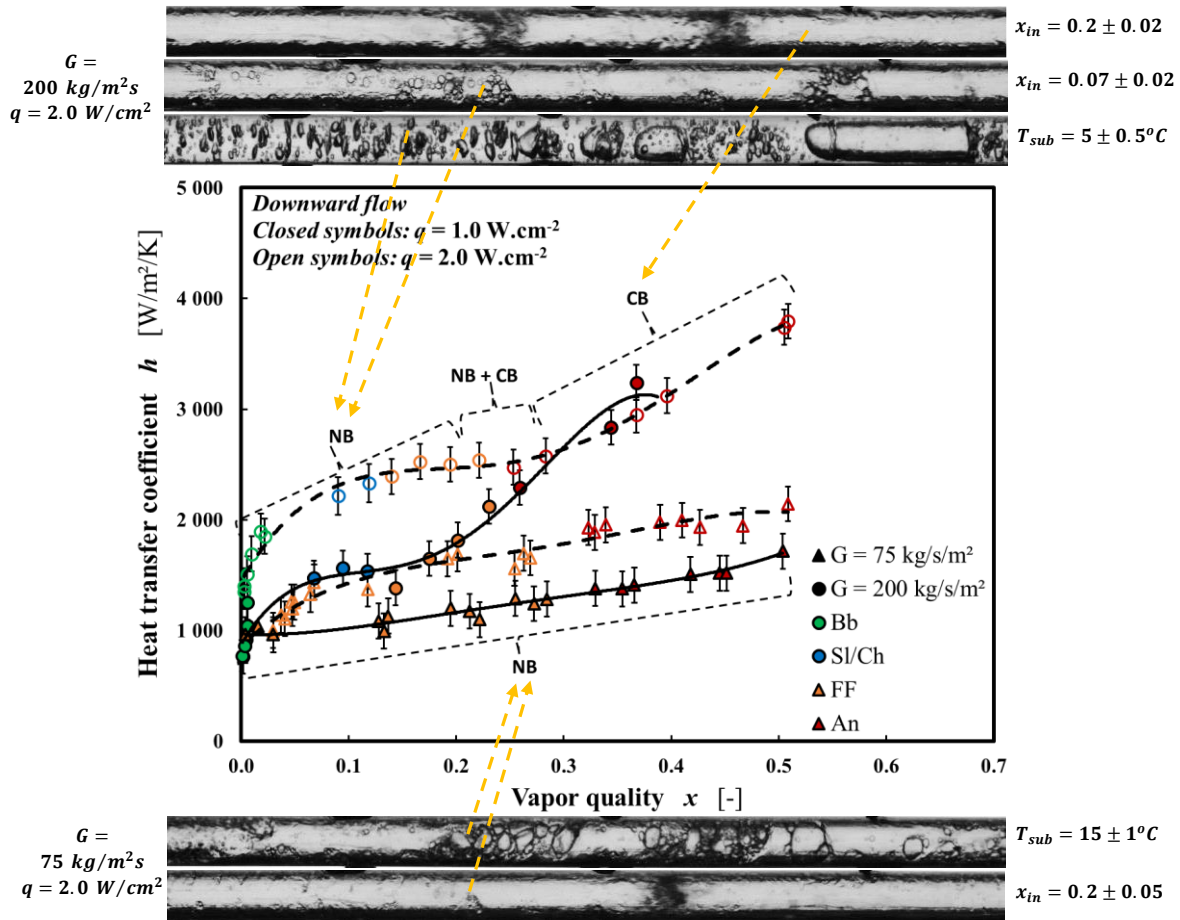


Figure 4.2: Illustration of the various heat transfer regimes for downward flow boiling.

### 4.3 Modelling of Heat Transfer Coefficient and Liquid Film Thickness in Annular Flow Boiling (accepted manuscript: *Heat Transfer Engineering*)

## Theoretical Modelling of Heat Transfer in Vertical Upward and Downward Annular Flow Boiling

*Paul Onubi Ayegba, Julien Sebilliau, Catherine Colin\**

*Institut de Mécanique des Fluides de Toulouse – Université de Toulouse – CNRS-INPT-UPS*

*Allée Camille Soula – 31400 Toulouse – France*

### Abstract

*This work entails experimental measurement and theoretical modelling of heat transfer coefficient for annular flow boiling in upward and downward flow configurations. The working fluid used was HFE-7000 and experimental measurements were carried out inside a 6 mm sapphire tube coated externally with indium-tin-oxide (ITO) for Joule heating. The range of vapour quality, mass flux and heat flux investigated were 0.15 – 0.7, 75 – 400 kg/(m<sup>2</sup>s) and 0.5 – 3.0 W/cm<sup>2</sup> respectively. Theoretical models for predicting heat transfer coefficient in upward and downward flows were developed using heat-flux-dependent wall shear stress correlations and roll-wave-velocity-based interfacial damping function. It was found that interfacial damping depends on the Reynolds number of the liquid film. The proposed models predicted over 96% of the measured heat transfer coefficient within  $\pm 20\%$  in both upward and downward flows and reproduced the heat flux dependence of the heat transfer coefficient. The models also predicted over 96% of the measured liquid film thickness within  $\pm 30\%$  in both upward and downward flows.*

\* Address correspondence to Professor Catherine COLIN, Institut de Mécanique des Fluides de Toulouse – Université de Toulouse – CNRS-INPT-UPS Allée Camille Soula – 31400 Toulouse – France. E-mail: [catherine.colin@imft.fr](mailto:catherine.colin@imft.fr).

## Introduction

Flow boiling is encountered in various applications such as in the production of electricity in nuclear power plants, energy conservation and process industries. Flow boiling thermal systems take advantage of the latent heat in phase change. Modelling studies of phase change heat transfer have mainly focused on semi-empirical correlations [1–7] and algebraic eddy viscosity models by [8–10]. Such models are generally valid for specific flow configurations and relatively narrow ranges of operating conditions. Theoretical modelling approaches are generally more robust and provide heat transfer predictions over a wider range of operating conditions [11]. Theoretical models also provide a better representation of the physics of the flow.

A common theoretical approach entails the prediction of heat transfer coefficient (*HTC*) from turbulent eddy diffusivity in the liquid film of annular flow. This modelling approach requires, among other things, closure law for interfacial shear stress ( $\tau_i$ ) or wall shear stress ( $\tau_w$ ) (for control volume analyses adjacent to the interface or adjacent to the wall respectively). The interfacial shear stress or wall shear stress is usually obtained from suitable correlations [12]. In the current work, control volume analysis was done adjacent to the wall in order to capture the effect of bubble nucleation at the wall on the wall shear stress and on the eddy viscosity and diffusivity. Most of the existing correlations for two-phase wall shear stress are applicable to adiabatic two-phase flows and in the convective dominant regime of flow boiling [13, 14]. When there is significant nucleation in the annular film, wall shear stress differs quite remarkably from adiabatic two-phase flows [15–18]. Bubble nucleation at the heated wall in flow boiling alters the velocity profile close to the wall which in turn modifies the wall shear stress and heat transfer. Nucleation in the annular film increases fluid mixing inside the film which alters the Prandtl mixing length. It is, therefore, important to use relevant modelling of wall shear stress in flow boiling to develop heat transfer models.

In theoretical modelling of eddy viscosity, it is also important to account for turbulent damping close to wall as well as damping close to the interface [12, 19]. The eddy viscosity ( $\varepsilon_m$ ) from Prandtl mixing length theory is given by:

$$\frac{\varepsilon_m}{\nu_l} = l^{+2} \frac{du^+}{dy^+} \quad (1)$$

$$l^+ = Ky^+ \quad (2)$$

$$y^+ = \frac{y}{y^*}, u^+ = \frac{u_l}{u^*}, l^+ = \frac{l}{y^*}, y^* = \frac{\mu_l}{\rho_l u^*} \text{ and } u^* = \sqrt{\frac{\tau_w}{\rho_l}}, \quad (3)$$

where  $\mu_l$  is the liquid kinematic viscosity,  $u_l$  the local liquid velocity in the film,  $\rho_l$  the liquid density,  $l^+$  is the dimensionless mixing length,  $K = 0.41$  is the von Karman constant,  $y^+$  is the dimensionless distance from the wall,  $\tau_w$  is the wall shear stress and  $u^*$  the friction velocity. To account for wall damping, Van Driest [20] proposed a modification to the dimensionless mixing length given by:

$$l^+ = Ky^+ \left[ 1 - \exp\left(-\sqrt{\frac{\tau}{\tau_w}} \frac{y^+}{A^+}\right) \right] \quad (4)$$

where the term in the square bracket is referred to as the Van Driest wall damping function.  $A^+$  is a constant and was given equal to 26 by Van Driest. Kays [21] and Kays and Crawford [22] proposed an expression for  $A^+$  which has found more general application [12, 19, 23–25] and is given by:

$$A^+ = 26X_{lam}^{-1} \left\{ X_{lam} = 1 + 30.18 \left[ \frac{\mu_l \left( \frac{dp}{dz} \right)}{\rho_l^{0.5} \tau_w^{1.5}} \right] \right\} \quad (5)$$

$X_{lam}$  is the laminarization parameter which accounts for the effect of free stream pressure gradient ( $dp/dz$ ) on the Van Driest damping function.



To account for interfacial damping of turbulent eddies due to the action of surface tension, Mudawwar and El-Masri [19] and other recent studies proposed the introduction an interfacial damping function (Eq. (6)) to the expression for eddy viscosity,  $\delta^+$  being the dimensionless liquid film thickness and  $n$  constant.

$$(1 - y^+/\delta^+)^n \text{ (Interfacial damping function)} \quad (6)$$

The surface tension damping at the interface has been linked to the suppression of small waves or ripples at the interface [19]. In general, increase in surface density and/or amplitude of small waves at the interfaces results in reduced interfacial damping [19]. The converse the case with roll waves because increase velocity and frequency of roll waves results in decreased in small waves. The value of the exponent  $n$  in the following studies are; 1.0 [19], 0.1 [4, 12, 24] and 0 [20, 23]. In these works, the value of  $n$  used was that which gave best prediction of the measured heat transfer coefficient. A small value of  $n$  (e.g.,  $n = 0.1$ ) means significant mixing or turbulence intensity close to the interface while a high value of  $n$  (e.g., 1.0) signifies significant turbulence damping or flow laminarization close to the interface. Considering the fact that velocity profile in the liquid film close to the interface is significantly influenced by interfacial wave structures, the choice of a constant value of  $n$  would at best provide an estimated mean value. Furthermore, when there is nucleation in the annular film, bubble growth and coalescence with the interface may result in interfacial disturbances. It is therefore important to determine suitable values of  $n$  based on wave structures and/or other relevant flow parameters. In this work, theoretical modelling of heat transfer in upward and downward annular flows was done using suitable modelling of the wall shear stress, eddy viscosity profile in the liquid film including damping at the interface.

In the next section the experimental set-up and measurements technics for the study of flow boiling in millimetric tubes in vertical and downward flow are briefly described. The experimental

results have been extensively reported in the paper of Ayegba et al. [17] and will be used in this work for the validation of the models. The third session of the manuscript is devoted to the presentation of the theoretical model and the last session to the comparison of the model with the experimental data.

## **Experimental Setup and Data Reduction**

### ***Experimental setup***

A detailed description of the experimental setup used for this work is available in [17]. Figure 1 is a schematic drawing of the hydraulic loop used in the current work. The experimental fluid used was 1-methoxyheptafluoropropane ( $C_3F_7OCH_3$ ) refrigerant, commonly called HFE-7000 which has a saturation temperature ( $T_{sat}$ ) of  $34^\circ C$  at 1 bar. The fluid temperature at the inlet of the preheater was set at  $T_{sat} - 10^\circ C$ . Two-phase vapour-liquid flow was generated in a series of preheaters and passes through a 22 cm long vertical adiabatic section before entering the test section. The pressure at the inlet of the test section was between 1.2 to 1.5 bar. The test section consisted of a vertical transparent sapphire tube of 0.6 cm ID, 20 cm long and 0.1 cm thick, coated externally with ITO for Joule heating. The coating was transparent allowing flow visualization. Vapour quality at the outlet of the test section was determined by enthalpy balance along the test section and was in the range of  $0.15 \leq x \leq 0.70$ . The two-phase flow at the outlet of the test section was condensed and cooled to the desired temperature at the inlet of the pump using two PID-controlled Peltier modules in the condenser. The ranges of mass and heat flux tested were  $75 \leq G \leq 400 \text{ kg}/(m^2s)$  and  $0.5 \leq q \leq 3.0 \text{ W}/cm^2$  respectively. This experimental set-up allowed the determination of void fraction and heat transfer coefficient in upward and downward vertical flow configurations. Analysis of images obtained from high-speed visualization was also used in this work to describe the interfacial wave structures. Measurement instrumentations used included Coriolis flow meter, absolute pressure transmitters (Keller PAA21), thermocouples (K- and T-type), PT100 temperature probes, void

fraction probes (capacitance type) and a high-speed camera (PCO Dimax). Description of the test section along with measurement uncertainties are available in a previous publication [17].

### **Data reduction**

In the annular flow regime, the fluid at the inlet of the test section was at saturated conditions. The vapour quality at the inlet of the test section ( $x_{in}$ ) was determined from the enthalpy balance across the preheater and adiabatic section (insulated stainless steel and flexible tube) upstream of the test section (Eq. (7)).

$$\frac{P_{ph\_eff}}{(\pi D^2/4)} = G(1 - x_{in})Cp_l T_{in} + Gx_{in}h_v - GCp_l T_{in,ph} \quad (7)$$

$T_{in}$  and  $x_{in}$  are the temperature and the vapour quality at the inlet of the test section,  $T_{in,ph}$  is the temperature at the inlet of the preheater,  $P_{ph\_eff}$  is the preheater power after correction for heat losses, which is the effective power transmitted to the fluid,  $G$  is the total mass flux,  $h_v$  is the enthalpy of the vapour and  $Cp_l$  is the specific heat capacity of the liquid. For saturated conditions at the inlet of the test section;

$$Cp_l T_{in} = h_{l,sat}, h_v = h_{v,sat} \text{ and } h_{v,sat} - h_{l,sat} = h_{lv} \quad (8)$$

$$x_{in} = \frac{4P_{ph\_eff} - GCp_l \pi D^2 (T_{in} - T_{in,ph})}{G \pi D^2 h_{lv}} \quad (9)$$

were  $h_{l,sat}$  and  $h_{v,sat}$  are the enthalpy of liquid and vapour at saturation.

The vapour quality ( $x_z$ ) at an axial position ( $z$ ) in the test section was obtained from the enthalpy balance between the inlet of the test section and the position  $z$ .

$$x_z = x_{in} + \frac{4q_{eff} \times z}{GDh_{lv}} \quad (10)$$

The effective wall heat flux ( $q_{eff}$ ) was obtained by subtracting the heat loss in the test section from the applied heat flux ( $q$ ).

Calculation of inner wall heat transfer coefficient ( $h_i$ ) was done at 4 axial locations along the test section [17]. The heat transfer coefficient at the inner wall was obtained from an energy balance between the fluid and the inner wall as follows;

$$h_i = \frac{q_{eff}}{T_{ow} - T_{i\infty} - \ln\left(\frac{R_o}{R_i}\right) \frac{R_o}{k} q_{eff}} \quad (11)$$

where  $k$  is the thermal conductivity of sapphire tube,  $R_o$  and  $R_i$  are the outer and inner tube radii of the sapphire tube,  $T_{ow}$  and  $T_{i\infty}$  are the outer wall temperature and the liquid bulk temperature.

The capacitance probes have been used to measure the void fraction  $\alpha$  at the inlet and outlet of the test section. In annular flow the liquid film thickness  $\delta$  is related to the measured value of the fraction  $\alpha$  [26].

$$\delta = 0.5D(1 - \sqrt{\alpha}) \quad (12)$$

For the mass fluxes limited to  $400 \text{ kg}/(\text{m}^2\text{s})$  the entrainment rate of the droplet estimated using the model of Cioncolini et al. [27] can be neglected in the evaluation of the film thickness [17, 26]. The wall and interfacial shear stresses in annular flow have been derived from combined measurement of the pressure drop along the test section and void fraction.

The uncertainties in the measured vapour quality, mass flux, heat flux, liquid film thickness and heat transfer coefficient are provided in [17]. The measurements of the heat transfer coefficients,

wall shear stress and film thickness will be used for the validation of the theoretical model.

## **Theoretical Modelling of Eddy Viscosity and Eddy Diffusivity**

### ***Model assumptions***

The local equations for mass, momentum and energy conservation in the liquid film will be derived under the following assumptions and integrated over a control volume (Figure 2):

1. The flow is co-current, at steady state and the liquid is incompressible.
2. The pressure is uniform in the tube cross section.
3. The flow is axisymmetric and the averaged liquid film thickness  $\delta$  is uniform around the circumference of the tube.
4. Thermo-physical properties of the phases are assumed constant and taken at saturation temperature.
5. The liquid film is supposed to be single-phase flow: interfacial mass and momentum transfer are neglected in the liquid film, except at the interface with the vapour core. The effect of the bubble nucleation is only taken into account in the modification of the wall shear stress.
6. Entrained liquid fraction in the vapour core is neglected [17, 26].
7. Axial momentum changes in the liquid film are negligible [28].

### ***Eddy viscosity modelling***

The momentum balance equation for the liquid phase in the axial direction (Figure 2) is given as;

$$\frac{1}{r} \frac{\partial}{\partial r} (r\tau) + \frac{dp}{dz} + \rho_l g \sin \theta + \frac{d}{dz} (\rho_l u_l^2) = 0 \quad (13)$$

$$[u_l]_z = [u_l(r)]_z \quad (14)$$

Integrating Eq. (13) across the liquid film (from  $r$  to  $R$ ) and assuming negligible acceleration in the liquid film gives:

$$\tau = \tau_w \frac{R}{r} + \frac{(R^2 - r^2)}{2r} \left( \frac{dp}{dz} + \rho_l g \sin \theta \right) \quad (15)$$

where  $\tau$  and  $\tau_w$  are the shear stresses in the liquid film and tube wall respectively,  $r$  and  $R$  are the radial distances of the control volume and wall respectively,  $p$  is the pressure and  $\theta$  is the inclination from the horizontal [28]. The second term in the bracket accounts is the hydrostatic pressure gradient and is zero of horizontal and microgravity flows.

In terms of the distance from the wall, Eq. (15) becomes;

$$\tau = \tau_w \frac{R}{(R - y)} + \frac{y(2R - y)}{2(R - y)} \left( \frac{dp}{dz} + \rho_l g \sin \theta \right) \quad (y = R - r) \quad (16)$$

And in dimensionless form Eq. (16) can be written;

$$\frac{\tau}{\tau_w} = \frac{R^+}{(R^+ - y^+)} + \frac{y^+(2R^+ - y^+)}{2(R^+ - y^+)} \left( \frac{y^*{}^2}{\mu_l \times u^*} \right) \left( \frac{dp}{dz} + \rho_l g \sin \theta \right) \quad (17)$$

For turbulent liquid films;

$$\tau = -\mu_l \left( 1 + \frac{\varepsilon_m}{\nu_l} \right) \frac{du_l}{dr} = \mu_l \left( 1 + \frac{\varepsilon_m}{\nu_l} \right) \frac{du_l}{dy} \quad (r = R - y, \ dr = -dy) \quad (18)$$

where  $\varepsilon_m$  is the eddy viscosity,  $\mu_l$  is the dynamic viscosity of the liquid,  $u_l$  is the velocity of the liquid which is dependent of the distance ( $y$ ) from the tube wall. In dimensionless form Eq. (18) is written

as;

$$\frac{\tau}{\tau_w} = \left(1 + \frac{\varepsilon_m}{v_l}\right) \frac{du^+}{dy^+} \quad (19)$$

Integrating Eq. (19) from 0 to  $y^+$  gives the velocity profile ( $u^+$ ) in the liquid film as follows;

$$u_l^+(y^+) = \int_0^{y^+} \frac{\tau}{\tau_w} \left(1 + \frac{\varepsilon_m}{v_l}\right)^{-1} dy^+ \quad (20)$$

For known values of total mass flux  $G$ , wall heat flux  $q_w$  ( $q_{eff}$ ), vapour quality  $x$  and fluid properties, the velocity profile in the liquid film can be determined from Eq. (20), if relations for  $dp/dz$ ,  $\tau_w$ ,  $\varepsilon_m/v_l$  and the liquid film thickness  $\delta$  are available simultaneously.

$dp/dz$  in Eqs. (15-17) may be derived from the momentum balance of the two-phase mixture:

$$\frac{dp}{dz} = -\frac{2}{R}\tau_w - \rho_m g \sin \theta - G^2 \frac{d}{dz} \left[ \frac{(1-x)^2}{\rho_l(1-\alpha)} + \frac{x^2}{\rho_v\alpha} \right] \quad (21)$$

where  $\alpha$  is the void fraction ( $\alpha \approx r_i^2/R^2 \approx (R-\delta)^2/R^2$ ),  $r_i$  is the distance between the tube centre and the interface and;

$$\rho_m = \rho_l(1-\alpha) + \rho_v\alpha \quad (22)$$

The second term in the right-hand-side is the gravitational term and the third term is the acceleration term which for constant density yields:

$$G^2 \frac{d}{dz} \left[ \frac{(1-x)^2}{\rho_l(1-\alpha)} + \frac{x^2}{\rho_v\alpha} \right] = G^2 \frac{dx}{dz} \left\{ \left[ \frac{2x}{\rho_v\alpha} - \frac{2(1-x)}{\rho_l(1-\alpha)} \right] + \frac{d\alpha}{dx} \left[ \frac{(1-x)^2}{\rho_l(1-\alpha)^2} - \frac{x^2}{\rho_v\alpha^2} \right] \right\} \quad (23)$$

Therefore Eq. (21) becomes:

$$\frac{dp}{dz} = -\frac{2}{R}\tau_w - \rho_m g \sin \theta - G^2 \frac{dx}{dz} \left\{ \left[ \frac{2x}{\rho_v \alpha} - \frac{2(1-x)}{\rho_l(1-\alpha)} \right] + \frac{d\alpha}{dx} \left[ \frac{(1-x)^2}{\rho_l(1-\alpha)^2} - \frac{x^2}{\rho_v \alpha^2} \right] \right\} \quad (24)$$

where;

$$\frac{dx}{dz} = \frac{2}{R} \frac{q}{G h_{lv}} \text{ (valid for saturated boiling)} \quad (25)$$

$h_{lv}$  is latent heat and  $\frac{d\alpha}{dx}$  is estimated from the drift flux model [17] and given by:

$$\alpha = \frac{Gx/\rho_v}{C_0[Gx/\rho_v + G(1-x)/\rho_l] + u_\infty} \quad (C_0 \approx 1.2, u_\infty \approx \pm 0.15 \text{ m/s}) \quad (26)$$

$$\frac{d\alpha}{dx} = \frac{G}{\rho_v[C_0 Gx/\rho_v + C_0 G(1-x)/\rho_l + u_\infty]} - \frac{Gx(C_0 G/\rho_v - C_0 G/\rho_l)}{\rho_v[C_0 Gx/\rho_v + C_0 G(1-x)/\rho_l + u_\infty]^2} \quad (27)$$

As discussed in the introduction, the wall shear stress ( $\tau_w$ ) in Eq. (24) may be obtained from suitable correlations. It was also highlighted in the Introduction that the wall shear stress is influenced by wall heating. Wall shear stress is generally higher in flow boiling than adiabatic two-phase flows and the difference increases with wall heat flux [15–17]. Due to the foregoing, Kim and Mudawar [16] proposed a correlation for predicting upward flow boiling wall shear stress by modifying the model for adiabatic two-phase flow proposed by Kim and Mudawar [29]. The model highlighted the heat flux dependence of the wall shear stress. Examination of the model by Ayegba et al. [17], showed some limitations of the model in both the convective and nucleate boiling dominant regimes. Furthermore, the model of Kim and Mudawar [16] was limited to upward flow. Ayegba et al. [17], proposed modifications to the expressions for  $C_A$  and  $C_{NA}$  in the model of Kim and Mudawar [16] to provide better prediction of the wall shear stress in both upward and downward boiling flows (Eqs. (28-34). The modified correlations were used for the determination of  $\tau_w$  in the current work and are valid for  $1 \leq p \leq 2 \text{ bar}$ ,  $75 \leq G \leq 200 \text{ kg/(m}^2\text{s)}$ ,  $0 \leq q \leq 3 \text{ W/cm}^2$ ,  $0.05 \leq x \leq 0.8$  and  $D =$



6 mm. A comparison of model predictions with experimental data of Ayegba et al. [17] is shown in Figure 3 for reference purpose. The model predicted over 96% of the measured data within  $\pm 15\%$  and also captured the effect of heat flux on wall shear stress.

$$\left(\frac{dp}{dz}\right)_{fr} = \frac{4\tau_{w,2\phi}}{D} = \phi_l^2 \left(\frac{dp}{dz}\right)_l \quad (28)$$

$$\phi_l^2 = 1 + \frac{C_{NA}}{X} + \frac{1}{X^2} \quad (29)$$

$$X = \left[ \left(\frac{dp}{dz}\right)_l / \left(\frac{dp}{dz}\right)_v \right]^{0.5} \quad (30)$$

$$\left(\frac{dp}{dz}\right)_l = -\frac{4}{D} f_l \frac{\rho_l j_l^2}{2} = -f_l \frac{2G^2(1-x)^2}{\rho_l D} \quad (31)$$

$$\left(\frac{dp}{dz}\right)_v = -\frac{4}{D} f_v \frac{\rho_v j_v^2}{2} = -f_v \frac{2G^2 x^2}{\rho_v D} \quad (32)$$

$$C_A = \begin{cases} 0.33 Re_{lo}^{0.03} Su_{vo}^{0.1} (\rho_l / \rho_v)^{0.35} (1/X^{0.22}), & Re_l \geq 3000, Re_v \geq 3000 \\ 0.40 Re_{lo}^{0.03} Su_{vo}^{0.1} (\rho_l / \rho_v)^{0.35} (1/X^{0.27}), & Re_l < 3000, Re_v \geq 3000 \end{cases} \quad (33)$$

$$C_{NA} = \begin{cases} C_A [1 + 30 We_l^{0.32} Bo^{0.78}] & Re_l \geq 1500 \\ C_A [1 + 320 We_{lo}^{0.52} Bo^{1.09}] & Re_l < 1500 \end{cases} \quad (34)$$

$$C_A = \begin{cases} 0.38 Re_{lo}^{0.03} Su_{vo}^{0.1} (\rho_l / \rho_v)^{0.35} (1/X^{0.22}), & Re_l \geq 3000, Re_v \geq 3000 \\ 0.47 Re_{lo}^{0.03} Su_{vo}^{0.1} (\rho_l / \rho_v)^{0.35} (1/X^{0.30}), & Re_l < 3000, Re_v \geq 3000 \end{cases} \quad (35)$$

$$C_{NA} = \begin{cases} C_A [1 + 30 We_l^{0.32} Bo^{0.78}] & Re_l \geq 1500 \\ C_A [1 + 400 We_{lo}^{0.52} Bo^{1.09}] & Re_l < 1500 \end{cases} \quad (36)$$

$$f_k = \begin{cases} 16Re_k^{-1} & Re_k < 1500 \\ 0.079Re_k^{-0.25} & 1500 \leq Re_k < 20000 \\ 0.046Re_k^{-0.2} & Re_k \geq 20000 \end{cases} \quad (37)$$

where  $k$  stands for liquid ( $l$ ) or vapour ( $v$ ),

$$Re_l = \frac{G(1-x)D}{\mu_l}, Re_{lo} = \frac{GD}{\mu_l}, Re_v = \frac{GxD}{\mu_v}, Re_{vo} = \frac{GD}{\mu_v}, \quad Su_{vo} = \frac{\rho_v \sigma D}{\mu_v^2} \quad (38)$$

$$We_l = \frac{G^2(1-x)^2D}{\rho_l \sigma}, We_{lo} = \frac{G^2D}{\rho_l \sigma}, Bo = \frac{q}{Gh_{lv}} \quad (39)$$

Several algebraic eddy diffusivities expressions have also been proposed to obtain the velocity profile  $u_l^+$  in the liquid film (Eq. (20)). Simple expressions as constant eddy viscosity [8, 9] or quadratic expression [10] were proposed and led to an analytical expression of heat transfer coefficient. However, these models do not provide a realistic shape of the velocity and temperature profiles in the liquid film and were not able to reproduce the effect of the heat flux on the heat transfer coefficient [17]. Therefore, we decided to base our analysis on the models proposed by Kim and Mudawar [12] and Mudawwar and El-Masri [19].

Substituting Eqs. (4) and (19) into Eq. (1) gives the following expression for eddy viscosity:

$$\frac{\varepsilon_m}{v_l} = -\frac{1}{2} + \frac{1}{2} \sqrt{1 + 4K^2 y^{+2} \left[ 1 - \exp\left(-\sqrt{\frac{\tau}{\tau_w}} \frac{y^+}{A^+}\right) \right]^2} \frac{\tau}{\tau_w} \quad (40)$$

To account for interfacial damping, Mudawwar and El-Masri (1986) introduced an interfacial damping function Eq. (6) to the expression for turbulent eddy diffusivity (Eq. (40)) resulting in:

$$\frac{\varepsilon_m}{v_l} = -\frac{1}{2} + \frac{1}{2} \sqrt{1 + 4K^2 y^{+2} \left[ 1 - \exp\left(-\sqrt{\frac{\tau}{\tau_w}} \frac{y^+}{A^+}\right) \right]^2 \frac{\tau}{\tau_w} \left(1 - \frac{y^+}{\delta^+}\right)^n} \quad (41)$$

$\delta^+$  is the dimensionless liquid film thickness and  $n$  is an empirical constant.

The remaining parameter for closure of Eq. (20) is the liquid film thickness ( $\delta$ ). This is accomplished using a numerical scheme involving a guess value of  $\delta$  and relevant boundary conditions. For mass conservation in the liquid film, it is required that the mass flow rate of the liquid film be;

$$\dot{m}_l = (1 - x)\dot{m} = (1 - x)G\pi R^2 = 2\pi\rho_l \int_0^\delta (R - y) * u_l dy = 2\pi\rho_l \int_r^R r * u_l dr \quad (42)$$

where  $\dot{m}$  is the total mass flow rate. Eq. (42) is used to determine if the guess value of  $\delta$  satisfies the mass conservation in the liquid film. It should be remarked that in the current work, the liquid entrainment had negligible effect on the liquid film thickness [17, 26] and is not taken into account in Eq. (42).

### ***Eddy heat diffusivity modelling***

The energy balance equation in the annular film writes:

$$\frac{1}{r} \frac{\partial}{\partial r} (rq) = 0 \quad (43)$$

where  $q$  is the local diffusive and turbulent heat flux heat, expressed using Boussinesq the assumption:

$$q = (k_l + k_t) \frac{dT}{dr} = -(k_l + k_t) \frac{dT}{dy} = -k_l \left(1 + \frac{k_t}{k_l}\right) \frac{dT}{dy} = -k_l \left(1 + \frac{Pr_l \varepsilon_m}{Pr_t v_l}\right) \frac{dT}{dy} \quad (44)$$

$$Pr_l = \frac{Cp_l \mu_l}{k_l}, \quad Pr_t = \frac{Cp_l \mu_t}{k_t}, \quad \frac{k_t}{k_l} = \frac{Pr_l \mu_t}{Pr_t \mu_l} = \frac{Pr_l \varepsilon_m}{Pr_t \nu_l} \quad (45)$$

where  $Cp_l$  is the specific heat capacity of the liquid,  $k_l$  and  $k_t$  are liquid and turbulent thermal conductivities,  $Pr_l$  and  $Pr_t$  are liquid and turbulent Prandtl numbers. Integrating Eq. (43) yields;

$$q/q_w = R/(R - y) \quad (46)$$

The dimensionless temperature in the liquid film is defined as;

$$T^+ = \rho_l Cp_l u^* (T_w - T)/q_w \quad (47)$$

In dimensionless form, Eq. (44) is given by;

$$\frac{q}{q_w} = \frac{1}{Pr_l} \left( 1 + \frac{Pr_l \varepsilon_m}{Pr_t \nu_l} \right) \frac{dT^+}{dy^+} \quad (48)$$

where;

$$dT = -(q_w/\rho_l Cp_l u^*) dT^+, \quad dy = -(\mu_l/\rho_l u^*) dy^+ \quad (49)$$

$T_w$  is the wall temperature. The turbulent Prandtl number was given by Mudawwar and El-Masri (1986) as;

$$Pr_t = 1.4 \exp(-15 y^+/\delta^+) + 0.66 \quad (50)$$

Integrating Eq. (47) from 0 to  $\delta^+$  and Eq. (48) from 0 to  $y^+$  give the heat transfer coefficient (Eq. (51)) and the dimensionless temperature profile (Eq. (52)) respectively.

$$h = \frac{q_w}{T_w - T_{sat}} = \frac{\rho_l Cp_l u^*}{T_\delta^+} = \frac{\rho_l Cp_l u^*}{\int_0^{\delta^+} \frac{q}{q_w} \left[ \frac{1}{Pr_l} \left( 1 + \frac{Pr_l \varepsilon_m}{Pr_t \nu_l} \right) \right]^{-1} dy^+} \quad (51)$$

$$T^+ = \int_0^{y^+} \frac{q}{q_w} \left[ \frac{1}{Pr_l} \left( 1 + \frac{Pr_l}{Pr_t} \frac{\varepsilon_m}{\nu_l} \right) \right]^{-1} dy^+ \quad (52)$$

### ***Solution algorithm and model validity range***

The algorithm for the resolution of the equations is depicted in Figure 4 and the numerical simulation was done using MATLAB programming. Turbulent eddy diffusivity models are generally valid for the turbulent flows. In single-phase flow in a pipe the transition from laminar to turbulent occurs for a  $Re$  number around 2000. In liquid film in annular flow, the momentum and heat diffusivity are enhanced due to the high shear at the interface and in flow boiling due to bubble nucleation at the wall which induces a significant mixing. In the works of Kim and Mudawar [11, 12], eddy diffusivity model was applied to flow boiling in mini/micro channels for  $10 \leq Re_l(\bar{u}_l, \delta) \leq 600$ ,  $Re_l(\bar{u}_l, \delta)$  being the Reynolds number based on the mean liquid velocity in the film and the film thickness. In the current work, the range of liquid film Reynolds number was  $700 \leq Re_l(\bar{u}_l, \delta) \leq 6500$ .

## **Results**

In this section, results of upward flow are presented first followed by results for downward flow. For each flow orientation, the results of eddy viscosity, liquid velocity and liquid temperature profiles are discussed for two values of  $n$ . This is followed by comparison between predicted and measured heat transfer coefficient. Afterwards, an expression for determining suitable values of  $n$  is proposed with the aim of improving heat transfer prediction. Model predictions using this  $n$ -function is then discussed. Finally, results of predicted and measured liquid film thickness is discussed.

### ***Heat transfer coefficient in upward flow***

Figure 5 shows eddy viscosity profiles as a function of dimensionless distance from the wall,

for two constant values of  $n$  (0.1 and 1.2) and a value of  $n$  ( $b.u_w$ ) that is linked to the roll wave velocity. It should be remarked that, with change in the value of  $n$ , the film thickness at which mass conservation in the liquid film is obtained changes (maximum value of  $y^+$ ). With increase in  $n$ , there is increase in the thickness of the damped layer close to the interface and a lower value of the eddy viscosity in the liquid film. Figure 6 shows predicted velocity and temperature profiles in the liquid film at selected flowrates as a function of dimensionless distance from the wall. With increasing value of  $n$ , the dimensionless velocity and temperature profiles increased and the results are in agreement with similar works in literature [11, 25, 30]. Experimental measurements of the velocity profiles in the annular liquid film have been carried out for adiabatic gas-liquid flows [31, 32]. Similar to the current work, the measured dimensionless velocity and temperature profiles were higher than single phase flow and increased with  $n$ . Experimental measurements close to the interface has not been very successful due to limitations of common diagnostics. However, the limited experimental data available also showed changes in the velocity profile as the interface is approached [31, 32].

Figure 7 and Figure 8 provide comparisons between predicted (Eq. (51)) and measured values of heat transfer coefficient in upward flow. For a  $n$  value of 0.1, the model generally over-predicts the measured heat transfer for  $G = 200 \text{ kg}/(\text{m}^2\text{s})$  ( $1700 \leq Re_l(\bar{u}_l, \delta) \leq 3000$ ) and  $G = 400 \text{ kg}/(\text{m}^2\text{s})$  ( $4600 \leq Re_l(\bar{u}_l, \delta) \leq 6500$ ). Although it also over-predicts the measured heat transfer for  $G = 75 \text{ kg}/(\text{m}^2\text{s})$  ( $700 \leq Re_l(\bar{u}_l, \delta) \leq 1000$ ) and  $G = 100 \text{ kg}/(\text{m}^2\text{s})$  ( $800 \leq Re_l(\bar{u}_l, \delta) \leq 1400$ ), the model predicted over 96% of the measured data in this mass flux range with  $\pm 30\%$ . These results are consistent with the results of Kim and Mudawar [11, 12] where a value of  $n = 0.1$  was deemed suitable for  $HTC$  prediction in the Reynold number range of  $10 \leq Re_l(\bar{u}_l, \delta) \leq 600$ . For  $n = 1.2$ , the model predicted 100% of the measured heat transfer for  $G \geq 200 \text{ kg}/(\text{m}^2\text{s})$  within  $\pm 20\%$  but under-predicted the measured heat transfer for  $G \leq 100 \text{ kg}/(\text{m}^2\text{s})$  particular for

higher wall heat fluxes. The results suggest a dependence of  $n$  on both mass flux and heat flux.

We first examine the effect of mass flux on both  $n$  and the measured heat transfer coefficient. A high value of  $n$ , signifies significant turbulence damping close to the interface of the liquid film (i.e., smoother interface) [19]. According to Mudawwar and El-Masri [19], the “*smooth-surface assumption can only be justified by the long waves (roll waves) that prevail in turbulent flows (high Reynolds number flows)*”. In other words, with increase in the Reynolds number (or mass flux); the roll waves become dominant, the interface becomes smoother (free from ripples) and consequently  $n$  increases. In the current work, as Reynolds number of the liquid (or mass flux) increased so did the mean value of  $n$  that provided best prediction of the measured heat transfer coefficient in the current work. This is in agreement with the significance of  $n$  as described by Mudawwar and El-Masri [19]. Over the range of vapour qualities, the average of the optimal values of  $n$  that gave best predictions of heat transfer coefficient in upward flow were 0.60, 0.74, 1.09, and 1.27, for  $G = 75 \text{ kg}/(\text{m}^2\text{s})$  ( $700 \leq Re_l(\bar{u}_l, \delta) \leq 1000$ ),  $G = 100 \text{ kg}/(\text{m}^2\text{s})$  ( $800 \leq Re_l(\bar{u}_l, \delta) \leq 1400$ ),  $G = 200 \text{ kg}/(\text{m}^2\text{s})$  ( $1700 \leq Re_l(\bar{u}_l, \delta) \leq 3000$ ) and  $G = 400 \text{ kg}/(\text{m}^2\text{s})$  ( $4600 \leq Re_l(\bar{u}_l, \delta) \leq 6500$ ) respectively.

Next, we examine the effect of heat flux on both  $n$  and the measured heat transfer coefficient at constant mass flux and vapour quality. While, increase in mass flux increased the dominance of roll waves over ripples (i.e., increase in  $n$ ), increase in heat flux produced the opposite effect. For  $G \leq 200 \text{ kg}/(\text{m}^2\text{s})$ , there was significant amount of bubble nucleation in the annular film which detaches from the wall and coalesce with the interface resulting in increased interfacial disturbances and reduced interfacial damping. The density and frequency of detachment of nucleated bubbles in the annular film increases with wall heat flux resulting in higher interfacial disturbances (and reduced interfacial damping or  $n$ ) with increase in heat flux. In the current work, the increased interfacial

disturbances with increase in heat flux was deduced from the increase in both the interfacial shear stress and frequency of ripples with increase in heat flux [17]. Flow visualizations showing bubble nucleation in the annular film as well as that showing the effect of heat flux on interfacial shear stress and wave frequency have been provided in Ayegba et al. [17]. The eddy viscosity (Eqs. (40) and (41)) increase with the wall and interfacial shear stresses (Figure 5) and as reported in various studies [10, 11, 19, 25, 33], the heat transfer coefficient increases with the interfacial shear stresses. This, again, is consistent with decrease in the optimal values of  $n$  (the value of  $n$  that best prediction of the measured heat transfer coefficient) with increase in heat flux.

In general, the optimal value of  $n$  was not constant but rather increased with mass flux and decreased with heat flux. The physical significant of  $n$  is seen as the modification of the interfacial shear stress by the interfacial structures. It should be remarked that changes in values of  $n$  had very limited effect on the computed liquid film thickness ( $\delta$ ).

As described above, the damping at the interface is linked to wave structures at the interface [19]. With increase in vapour Reynolds number, velocity fluctuations close the interface become increasingly dominated by inertia forces leading to increased viscous effects in the liquid sublayer close to the interface [19]. This creates a free-surface boundary layer with a liquid sublayer similar to that in the near-wall-region [19]. In the current work, the wave structure at the interface has been characterized by image processing of high-speed visualisations of the flow [17]. The roll waves velocities have been determined from space-time plots of the grey levels along an axial line (tube centre) of the image (Figure 9). Roll waves and ripples can be seen on this figure. At low value of  $G$  the ripples were clearly visible, but disappeared at higher values of  $G$  in agreement with the observations of Mudawwar and El-Masri [19] An increase in total mass flux led to an increase in the measured mean velocity of roll waves (Figure 10(a)). On the other hand, with increase in heat flux,



there was increase in bubble nucleation at the wall resulting in increased bubble coalescence with the interface as well as increased generation of ripples (Figure 9). This results in increased disturbance or mixing in the interfacial sublayer (decrease in interfacial damping) as well as reduced viscous effect in this layer. In the current work, both the measured mean velocity of roll waves and the optimal values of  $n$  for the prediction of heat transfer coefficient increased with mass flux and decreased with heat flux (Figure 10(a)). In other words, the optimal values of  $n$  for the prediction of heat transfer coefficient and the measured velocity of roll waves showed similar dependence on mass flux and heat flux. However, while the optimal values of  $n$  was generally independent of the vapour quality, the measured mean wave frequency increased with vapour quality. For this reason, a plot of optimal values of  $n$  versus measured mean velocity of roll waves did not show a clear pattern and therefore was not shown. Notwithstanding, in this work, an attempt was made to link the value of  $n$  to the wave velocity ( $u_w$ ).

According to Sawant et al. [34], if the wave velocity is correlated against the modified Weber number (Eq. (53)), the wave velocity becomes independent of the Reynolds number of the liquid. A simple correlation for wave velocity is proposed in this work (Eq. (54)). The correlation predicted around 92% of the measured wave velocity within  $\pm 20$  (Figure 10(b)). A simple expression relating  $n$  to  $u_w$  was also proposed in this work (Eq. (54)). Similar to roll wave velocity, the value of  $n$  given by Eq. (55) increases with mass flux and vapour quality and also decreased with heat flux.

$$We_m = \frac{\rho_c j_v^2 D}{\sigma} \left( \frac{\rho_l - \rho_c}{\rho_c} \right)^{1/3} \quad (53)$$

$$u_w = \frac{2.18 We_m}{55 + 1.14e5 * Bo + We_m} \quad (54)$$

$$n = b \cdot u_w \quad b = \begin{cases} 0.60 & \text{upward flow} \\ 0.40 & \text{downward flow} \end{cases} \quad (55)$$

The value of  $n$  given by Eq. (55) was used in Eq. (41) and the procedure outlined in Figure 4 was followed to determine the various parameters of interest. Predicted velocity and temperature profiles in the liquid at selected conditions are shown in Figure 6 above along with profiles obtained for  $n = 0.1$  and  $n = 1.2$ . The predicted heat transfer coefficient obtained for  $n$  given by Eq. (55) in upward flow is shown in Figure 11. The model predicted around 98% of the measured heat transfer within  $\pm 20\%$  for the range of mass and heat fluxes tested. It is important to note that 98% the values of the film thickness calculated to match the liquid mass flux (Eq. (42)) is a good agreement (within  $\pm 20\%$ ) with the measured values as shown in Figure 13(a).

### ***Heat transfer coefficient in downward flow***

In downward flow, the interfacial shear stress is much lower relative to upward flow resulting in lower frequency of roll waves. The implication of this is lower interfacial damping, greater disturbances at the interface due to bubble coalescence with the interface and higher sensitivity of the interfacial shear stress to changes in heat flux. For similar conditions of flow, the optimal value of  $n$  in downward flow was significantly smaller relative to upward flow. Over the range of vapour qualities, the average of the optimal values of  $n$  that gave best predictions of heat transfer coefficient in downward flow were 0.29, 0.74, 0.75, and 1.21, for  $G = 75 \text{ kg}/(\text{m}^2\text{s})$  ( $700 \leq Re_l(\bar{u}_l, \delta) \leq 1000$ ),  $G = 100 \text{ kg}/(\text{m}^2\text{s})$  ( $800 \leq Re_l(\bar{u}_l, \delta) \leq 1400$ ),  $G = 200 \text{ kg}/(\text{m}^2\text{s})$  ( $1700 \leq Re_l(\bar{u}_l, \delta) \leq 3000$ ) and  $G = 400 \text{ kg}/(\text{m}^2\text{s})$  ( $4600 \leq Re_l(\bar{u}_l, \delta) \leq 6500$ ), respectively. In general, the optimal value of  $n$  was not constant but rather increased with mass flux and vapour quality but decreased with heat flux. It should be remarked that in the current work, the change in flow direction had only limited effect on the wave velocity and Eq. (52) predicted around 92% of the

measured wave velocity in downward flow within  $\pm 20\%$ . The effect of change in flow direction from upward to downward flow was more obvious in the change in wave frequency and was higher in the former. For the case of downward flow, the expression for  $n$  given by Eq. (55) provided the best predictions of the measured heat transfer coefficient. Figure 12 shows measured and predicted heat transfer for  $n$  given by Eq. (55). The model predicted over 96% of the experimental data within  $\pm 20\%$  for the range of mass and heat flux tested. Furthermore, it provided a better representation of the trends in the measured data.

### ***Liquid film thickness in upward and downward flows***

In line with the solution scheme in Figure 4, the predicted liquid film thickness corresponds to the liquid film thickness for which there is mass conservation in the liquid film. In the current work, liquid film thickness was estimated from measured void fraction. The uncertainty in measured liquid film thickness is provided in [17]. Figure 13 provides a comparison between measured and predicted liquid film thickness in upward and downward flows, with some error bars to give an estimation of the measurement accuracy. The models predicted around 98% of the measured film thickness in upward (within  $\pm 20\%$ ) and downward (within  $\pm 30\%$ ) flows. The slight over-prediction in downward flow for  $G \leq 100 \text{ kg/m}^2\text{s}$  is due to the fact that, the experimental liquid film thickness under these conditions was very thin (relative to upward flow) [17]. In the current work, the experimental measurement uncertainties of the liquid film thickness for thin liquid films (high void fraction) were high ( $\Delta\delta/\delta \approx 45\%$  for  $x \geq 0.35$ ) [17]. It should be remarked that changes in  $n$  from 0.1 to 1.2 had very limited effect on the predicted liquid film thickness (Figure 14).

## Conclusion

Eddy-diffusivity-based theoretical models for predicting heat transfer coefficient in upward and downward flow boiling were developed in this work. The models were developed using heat-flux-dependent wall shear stress correlations and the interfacial damping function was modelled using wave structures. Some of the important findings include:

1. The proposed models predicted over 96% of the measured heat transfer coefficient within  $\pm 20\%$  in both upward and downward flows and also reproduced the heat flux dependence of the measured heat transfer coefficient. The heat flux dependence was particularly important for  $Re_l < 4000$  where nucleation was present in the annular liquid film [17].
2. The proposed models predicted over 96% of the measured liquid film thickness within  $\pm 30\%$  in both upward and downward flows. This was within the range of experimental uncertainty of the measured film thickness.
3. It was found that interfacial damping depends on the Reynolds number of the liquid film. A first attempt towards improving the interfacial damping function originally proposed by Mudawwar and El-Masri (1986) was carried out. The determination of optimal values of the exponent ( $n$ ) of the interfacial damping function from roll wave velocity improved model predictions from within  $\pm 30\%$  to within  $\pm 20\%$ .
4. The predicted dimensionless velocity and temperature profiles were higher than single phase flow and increased with  $n$ . These results generally agree with both experimental and modelling studies in literature (Ashwood et al., 2015; Chen et al., 2015; Kim and Mudawar, 2014a; Sun et al., 2001; Zadrazil and Markides, 2014).

# Nomenclature

$A$	cross-section area	$m^2$
$A^+$	constant	$[-]$
$Bo$	Boiling number	$[-]$
$b$	constant	$[-]$
$C$	constant	$[-]$
$C_p$	specific heat at constant pressure	$J/(kgK)$
$D$	diameter	$m$
$e$	rate of entrainment	$[-]$
$f$	friction factor	$[-]$
$G$	mass flux	$kg/(m^2s)$
$g$	acceleration due to gravity	$m/(s^2)$
$h$	heat transfer coefficient or specific enthalpy	$W/(m^2K)$ or $J/(kgK)$
$h_{l,v}$	latent heat of vaporisation	$J/kg$
$ITO$	indium-tin-oxide	$[-]$
$j$	mixture or superficial velocity	$m/s$
$K$	von Karman constant	$[-]$
$k$	thermal conductivity of sapphire tube	$W/(mK)$
$L$	length of the test section	$m$
$l^+$	dimensionless mixing length	$[-]$
$\dot{m}$	mass flow rate	$kg/s$
$Nu$	Nusselt number	$[-]$
$n$	exponent of the interfacial damping function	$[-]$
$P$	pressure	$bar$
$Pr$	Prandtl number	$[-]$
$q$	heat flux	$W/m^2$
$R$	radius	$m$
$Re$	Reynolds number	$[-]$
$r$	radial coordinate	$m$

$S$	perimeter	$m$
$Su$	Suratman number	$[-]$
$T$	temperature	$K$
$t$	time	$s$
$u$	mean velocity	$m/s$
$u^*$	friction velocity	$m/s$
$V$	volume	$m^3$
$We$	Weber number	$[-]$
$X$	Martinelli or laminarization parameter	$[-]$
$x$	vapour quality	$[-]$
$y^+$	dimensionless distance from the wall	$[-]$
$y^*$	frictional distance from the wall	$m$
$z$	axis coordinate	$m$

### Greek symbols

$\alpha$	void fraction	$[-]$
$\delta$	liquid film thickness	$m$
$\varepsilon_m$	eddy viscosity	$m^2/s$
$\phi$	Martinelli parameter	$[-]$
$\Gamma$	mass transfer	$kg/(m^3s)$
$\lambda$	thermal conductivity of liquid	$W/(mK)$
$\mu$	dynamic viscosity	$Pa.s$
$\nu$	kinematic viscosity	$m^2/s$
$\rho$	density	$kg/m^3$
$\sigma$	surface tension and dielectric constant	$N/m$
$\tau$	shear stress	$Pa$
$\theta$	inclination	$degree$

### Subscripts

$A$	adiabatic
-----	-----------

<i>c</i>	vapor core
<i>eff</i>	effective
<i>exp</i>	experimental
<i>fr</i>	frictional
<i>g</i>	gas
<i>i</i>	inner or interfacial
<i>inlet</i>	inlet conditions
<i>k</i>	phase
<i>l</i>	liquid phase
<i>lam</i>	laminar or laminarization
<i>lf</i>	liquid film
<i>lo</i>	liquid only
<i>m</i>	mixture or modified
<i>meas</i>	measured
<i>NA</i>	non-adiabatic
<i>o</i>	outer
<i>out</i>	outlet conditions
<i>ph</i>	preheater
<i>pred</i>	predicted
<i>sat</i>	saturated conditions
<i>sub</i>	subcooled conditions
<i>t</i>	turbulent or total
<i>v</i>	vapor phase
<i>vo</i>	liquid only
<i>w</i>	wall or wave
$\infty$	infinity

## **Acknowledgement**

Petroleum Technology Development Fund (PTDF) is acknowledged for the PhD grant funding of P. Ayegba. The European Space Agency (ESA) and the French Space Agency (CNES) through the GDR 2799 Micropesanteur Fondamentale et Appliquée are acknowledged for the financial support in the building of the experimental set-up.



## References

- [1] Z. Liu and R.H.S. Winterton, “A general correlation for saturated and subcooled flow boiling in tubes and annuli, based on a nucleate pool boiling equation,” *International Journal of Heat and Mass Transfer*, vol. 34, no. 11, pp. 2759–2766, 1991. DOI: 10.1016/0017-9310(91)90234-6.
- [2] K.E. Gungor and R.H.S. Winterton, “A general correlation for flow boiling in tubes and annuli,” *International Journal of Heat and Mass Transfer*, vol. 29, no. 3, pp. 351–358, 1986. DOI: 10.1016/0017-9310(86)90205-X.
- [3] S.G. Kandlikar, “A general correlation for saturated two-phase flow boiling heat transfer inside horizontal and vertical tubes,” *Journal of Heat Transfer*, vol. 112, no.1, pp. 219–228, 1990. DOI: 10.1115/1.2910348.
- [4] S.-M. Kim and I. Mudawar, “Universal approach to predicting saturated flow boiling heat transfer in mini/micro-channels – Part II, Two-phase heat transfer coefficient,” *International Journal of Heat and Mass Transfer*, vol. 64, pp. 1239–1256, 2013. DOI: 10.1016/j.ijheatmasstransfer.2013.04.014.
- [5] D. Mikielewicz and J. Mikielewicz, “A common method for calculation of flow boiling and flow condensation heat transfer coefficients in minichannels with account of nonadiabatic effects,” *Heat Transfer Engineering*, vol. 32, no. 13-14, pp. 1173–1181, 2011. DOI: 10.1080/01457632.2011.562728.
- [6] H. Wang and X. Fang, “Evaluation analysis of correlations of flow boiling heat transfer coefficients applied to ammonia,” *Heat Transfer Engineering*, vol. 37, no.1, pp. 32–44, 2016. DOI: 10.1080/01457632.2015.1025006.

- [7] O.E. Turgut, H. Genceli, M. Asker and M.T. Çoban, “Novel saturated flow boiling correlations for R600a and R717 refrigerants,” *Heat Transfer Engineering*, vol. 43, no. 18, pp. 1579-1609, 2022. DOI: 10.1080/01457632.2021.1989843.
- [8] A. Cioncolini, J.R. Thome and C. Lombardi, “Algebraic turbulence modeling in adiabatic gas-liquid annular two-phase flow,” *International Journal of Multiphase Flow*, vol. 35, no.6 pp. 580–596, 2009. DOI: 10.1016/j.ijmultiphaseflow.2009.02.002.
- [9] A. Cioncolini and J.R. Thome, “Algebraic turbulence modeling in adiabatic and evaporating annular two-phase flow,” *International Journal of Heat and Fluid Flow*, vol. 32, no. 4, pp. 805–817, 2011. DOI: 10.1016/j.ijheatfluidflow.2011.05.006.
- [10] H. Ohta, “Microgravity heat transfer in flow boiling,” in *Advances in Heat Transfer*, vol. 37, 1st ed., J.P. Hartnett, T.F. Irvine, Y.I. Cho and G.A. Greene, Eds. California, USA: Elsevier, 2003, pp. 1–75.
- [11] S.-M. Kim and I. Mudawar, “Theoretical model for local heat transfer coefficient for annular flow boiling in circular mini/micro-channels,” *International Journal of Heat and Mass Transfer*, vol. 73, pp. 731–742, 2014. DOI: 10.1016/j.ijheatmasstransfer.2014.02.055.
- [12] S.-M. Kim and I. Mudawar, “Theoretical model for annular flow condensation in rectangular micro-channels,” *International Journal of Heat and Mass Transfer*, vol. 55, no. 4, pp. 958–970, 2012. DOI: 10.1016/j.ijheatmasstransfer.2011.10.014.
- [13] A. Cioncolini and J.R. Thome, “Pressure drop prediction in annular two-phase flow in macroscale tubes and channels,” *International Journal of Multiphase Flow*, vol. 89, pp. 321–330, 2017. DOI: 10.1016/j.ijmultiphaseflow.2016.11.003.
- [14] S.-M. Kim and I. Mudawar, “Review of databases and predictive methods for pressure drop in adiabatic, condensing and boiling mini/micro-channel flows,” *International Journal of*

- Heat and Mass Transfer*, vol. 77, pp. 74–97, 2014. DOI: 10.1016/j.ijheatmasstransfer.2014.04.035.
- [15] T. Layssac, “Contribution à l’étude phénoménologique de l’ébullition convective en mini-canal,” Ph.D. thesis, Université de Lyon, Lyon, France, 2018.
- [16] S.-M. Kim and I. Mudawar, “Universal approach to predicting two-phase frictional pressure drop for mini/micro-channel saturated flow boiling,” *International Journal of Heat and Mass Transfer*, vol. 58, no. 1-2, pp. 718–734, 2013. DOI: 10.1016/j.ijheatmasstransfer.2012.11.045.
- [17] P.O. Ayegba, J. Sebilliau and C. Colin, “Hydrodynamics of vertical upward and downward flow boiling in a millimetric tube,” *International Journal of Multiphase Flow*, vol. 153, pp. 1-31, 2022. DOI: 10.1016/j.ijmultiphaseflow.2022.104120.
- [18] C.B. Tibiriçá, G. Ribatski and C.B. Tibiriçá, “Two-phase frictional pressure drop and flow boiling heat transfer for R245fa in a 2.32-mm tube,” *Heat Transfer Engineering*, vol. 32, no. 13-14, pp. 1139–1149, 2011. DOI: 10.1080/01457632.2011.562725.
- [19] I.A. Mudawwar and M.A. El-Masri, “Momentum and heat transfer across freely-falling turbulent liquid films,” *International Journal of Multiphase Flow*, vol. 12, no. 5, pp. 771–790, 1986. DOI: 10.1016/0301-9322(86)90051-0.
- [20] E.R. van DRIEST, “On turbulent flow near a wall,” *Journal of the Aeronautical Sciences*, vol. 23, pp. 1007–1011, 1956. DOI: 10.2514/8.3713.
- [21] W.M. Kays, “Heat transfer to the transpired turbulent boundary layer,” *International Journal of Heat and Mass Transfer*, vol. 15, no. 5, pp. 1023–1044, 1972. DOI: 10.1016/0017-9310(72)90237-2.
- [22] W.M. Kays and M.E. Crawford, *Convective Heat and Mass Transfer*, 3rd ed. New York, NY, USA: McGraw-Hill, 1980.

- [23] S. Lee and I. Mudawar, “Enhanced model for annular flow in micro-channel heat sinks, including effects of droplet entrainment/deposition and core turbulence,” *International Journal of Heat and Mass Transfer*, vol. 133, pp. 510–530, 2019. DOI: 10.1016/j.ijheatmasstransfer.2018.12.074.
- [24] S.-M. Kim and I. Mudawar, “Theoretical model for local heat transfer coefficient for annular flow boiling in circular mini/micro-channels,” *International Journal of Heat and Mass Transfer*, vol. 73, pp. 731–742, 2014. DOI: 10.1016/j.ijheatmasstransfer.2014.02.055.
- [25] C. Chen *et al.*, “Theoretical calculation of the characteristics of annular flow in a rectangular narrow channel,” *Annals of Nuclear Energy*, vol. 85, pp. 259–270, 2015. DOI: 10.1016/j.anucene.2015.05.027.
- [26] M. Narcy, E. de Malmazet and C. Colin, “Flow boiling in tube under normal gravity and microgravity conditions,” *International Journal of Multiphase Flow*, vol. 60, pp. 50–63, 2014. DOI: 10.1016/j.ijmultiphaseflow.2013.11.011.
- [27] A. Cioncolini, J.R. Thome and C. Lombardi, “Unified macro-to-microscale method to predict two-phase frictional pressure drops of annular flows,” *International Journal of Multiphase Flow*, vol. 35, no. 12, pp. 1138–1148, 2009. DOI: 10.1016/j.ijmultiphaseflow.2009.07.005.
- [28] G.F. Hewitt and N.S. Hall-Taylor, *Annular Two-Phase Flow*, 1st ed. Oxford, UK: Pergamon Press Ltd., 1970.
- [29] S.-M. Kim and I. Mudawar, “Universal approach to predicting two-phase frictional pressure drop for adiabatic and condensing mini/micro-channel flows,” *International Journal of Heat and Mass Transfer*, vol. 55, no. 11-12, pp. 3246–3261, 2012. DOI: 10.1016/j.ijheatmasstransfer.2012.02.047.

- [30] S. Sun, Y. Wu and R. Zhao, "The numerical calculation of heat transfer performance for annular flow of liquid nitrogen in a vertical annular channel," *Cryogenics*, vol. 41, no.4, pp. 231–237, 2001. DOI: 10.1016/S0011-2275(01)00058-3.
- [31] I. Zadrazil and C.N. Markides, "An experimental characterization of liquid films in downwards co-current gas-liquid annular flow by particle image and tracking velocimetry," *International Journal of Multiphase Flow*, vol. 67, pp. 42–53, 2014. DOI: 10.1016/j.ijmultiphaseflow.2014.08.007.
- [32] A.C. Ashwood *et al.*, "A multiphase, micro-scale PIV measurement technique for liquid film velocity measurements in annular two-phase flow," *International Journal of Multiphase Flow*, vol. 68, January, pp. 27–39, 2015. DOI: 10.1016/j.ijmultiphaseflow.2014.09.003.
- [33] F. Fu and J.F. Klausner, "A separated flow model for predicting two-phase pressure drop and evaporative heat transfer for vertical annular flow," *International Journal of Heat and Fluid Flow*, vol. 18, no. 6, pp 541–549, 1997. DOI: 10.1016/S0142-727X(97)00001-5.
- [34] P. Sawant, M. Ishii, T. Hazuku, T. Takamasa and M. Mori, "Properties of disturbance waves in vertical annular two-phase flow," *Nuclear Engineering and Design*, vol. 238, no. 12, pp 3528–3541, 2008. DOI: 10.1016/j.nucengdes.2008.06.013.

## List of Figure Captions

Figure 1. Experimental set-up (adapted from [17]).

Figure 2. Control volume analysis in the liquid film of annular flow.

Figure 3. Wall shear stress versus quality for upward (left) and downward (right) annular flows; measured data (symbols), correlation of Ayegba et al. [17] (lines).

Figure 4. Numerical solution scheme.

Figure 5. Eddy viscosity versus dimensionless distance from the wall in upward flow.

Figure 6. (a) and (b) dimensionless velocity profile versus dimensionless distance from the wall in upward flow, (c) and (d) dimensionless temperature profiles versus dimensionless distance from the wall in upward flow.

Figure 7. Predicted heat transfer versus measured heat transfer in upward flow, (a) and (c)  $n=0.1$  (b) and (d)  $n=1.2$ .

Figure 8. Measured and predicted heat transfer versus vapour quality in upward flow, (a) and (c)  $n=0.1$  (b) and (d)  $n=1.2$ .

Figure 9. Time-space plot of the grey levels in the tube center line.

Figure 10. (a) measured mean roll wave velocity versus vapour quality, (b) predicted (Eq. (54)) versus measured mean roll wave velocity.

Figure 11. (a) and (b) predicted heat transfer coefficient versus measured heat transfer in upward flow, (c) and (d) measured and predicted heat transfer coefficient versus vapour quality in upward

flow.

Figure 12. (a) and (b) predicted heat transfer coefficient versus measured heat transfer in downward flow, (c) and (d) measured and predicted heat transfer coefficient versus vapour quality in downward flow.

Figure 13. Predicted versus measured film thickness in the annular flow regime, (a) upward flow, (b) downward flow.

Figure 14. Predicted versus measured film thickness in the annular flow regime, (a) and (b) upward flow, (c) and (d) downward flow. (a) and (c)  $n=0.1$ , (b) and (d)  $n=1.2$ .

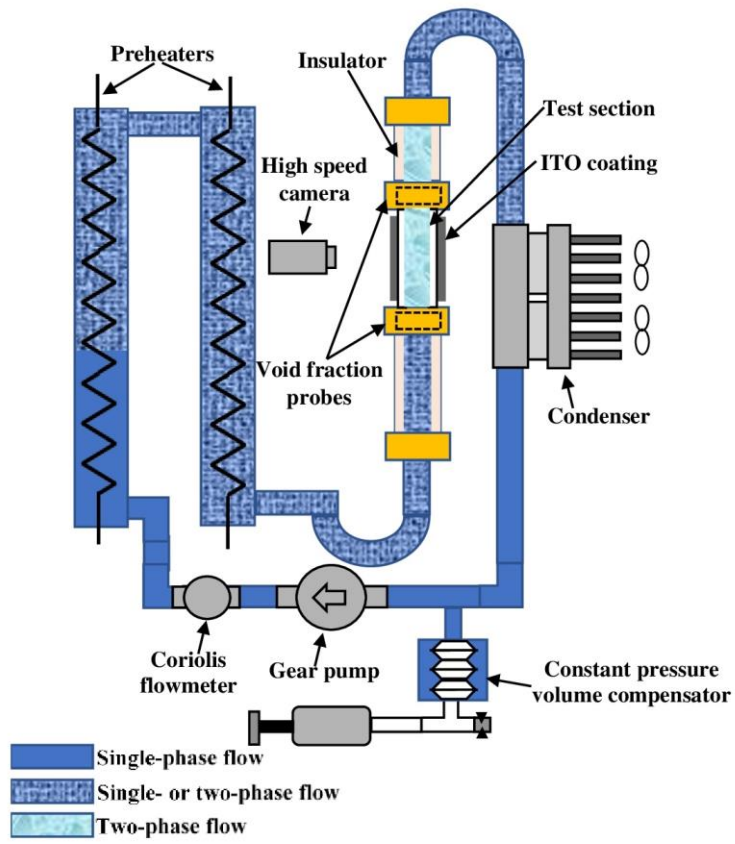


Figure 1. Experimental set-up (adapted from [17]).

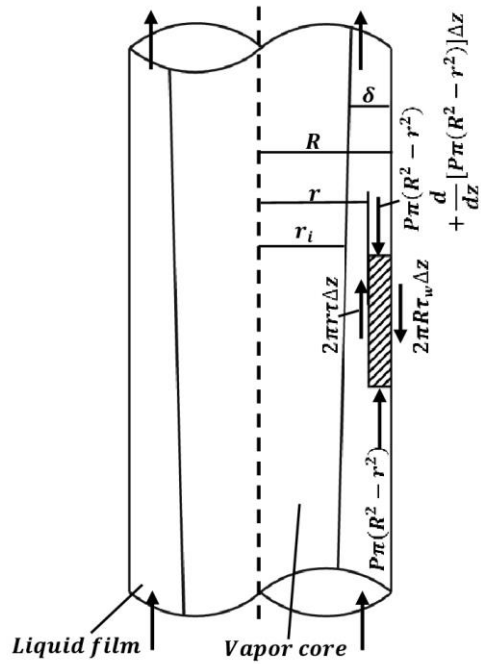


Figure 2. Control volume analysis in the liquid film of annular flow.



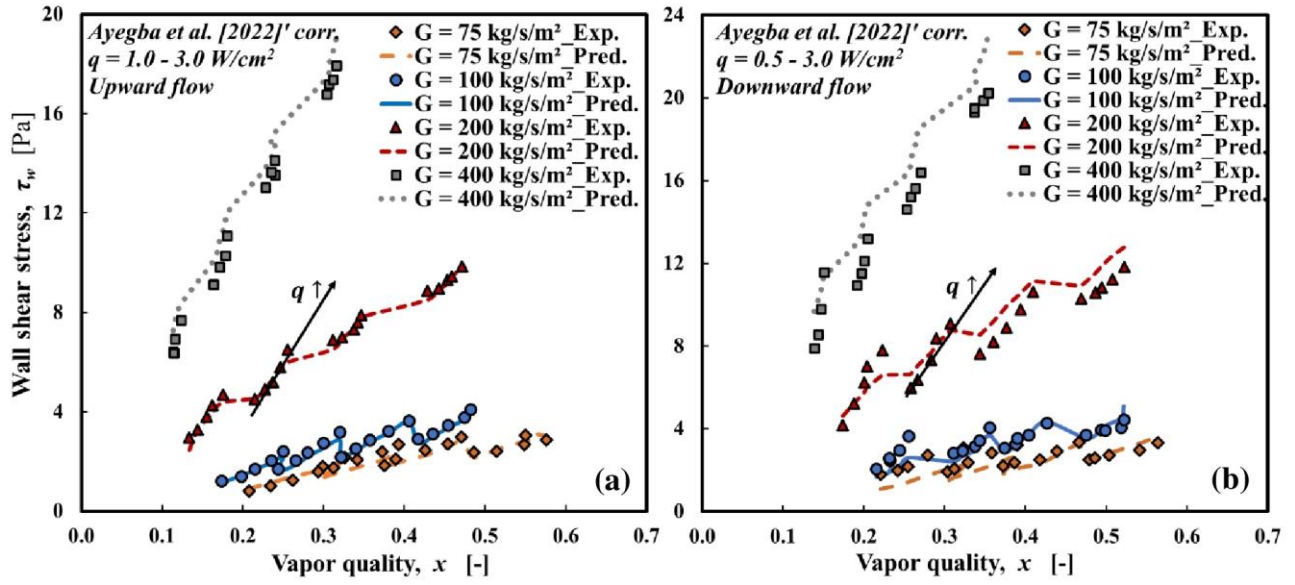


Figure 3. Wall shear stress versus quality for (a) upward and (b) downward annular flows; measured data (symbols), correlation of Ayegba et al. [17] (lines).

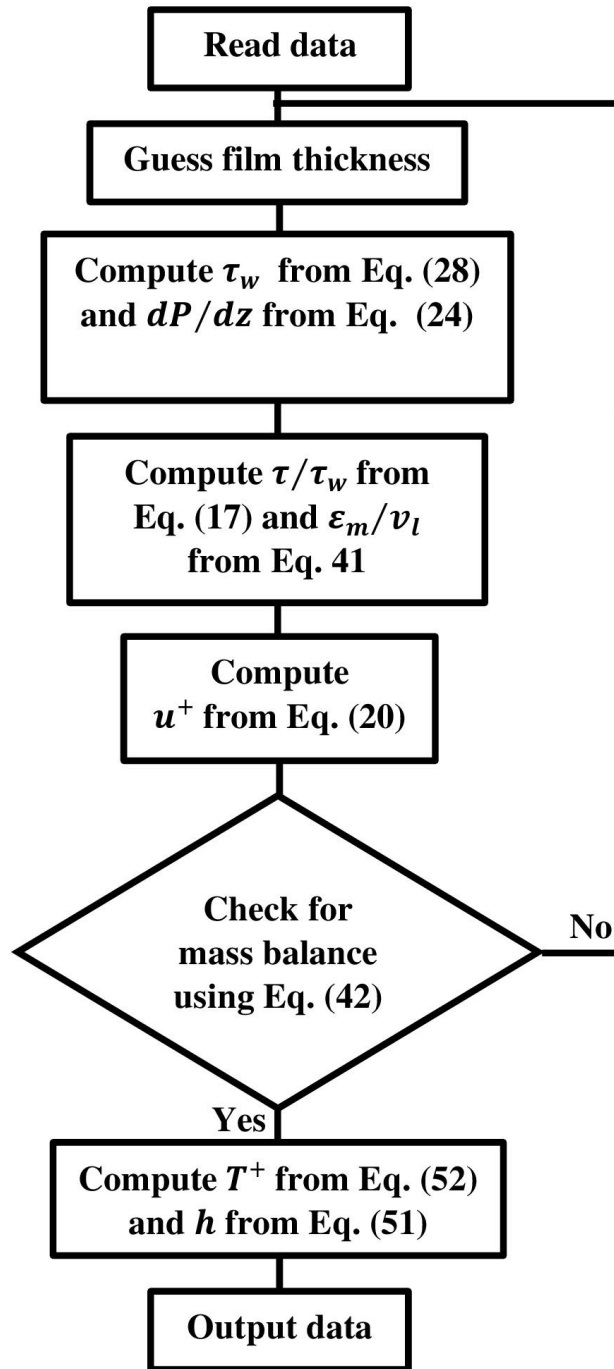


Figure 4. Numerical solution scheme.

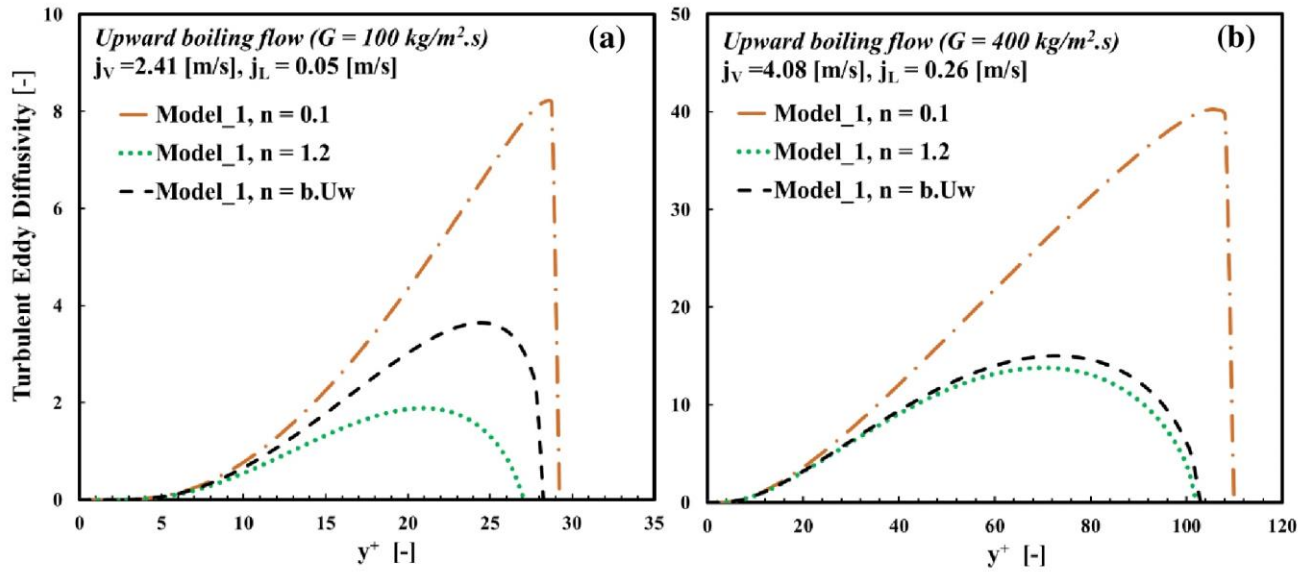


Figure 5. Eddy viscosity versus dimensionless distance from the wall in upward flow. (a)  $G = 100 \text{ kg/(m}^2\text{s)}$ , (b)  $G = 400 \text{ kg/(m}^2\text{s)}$ .

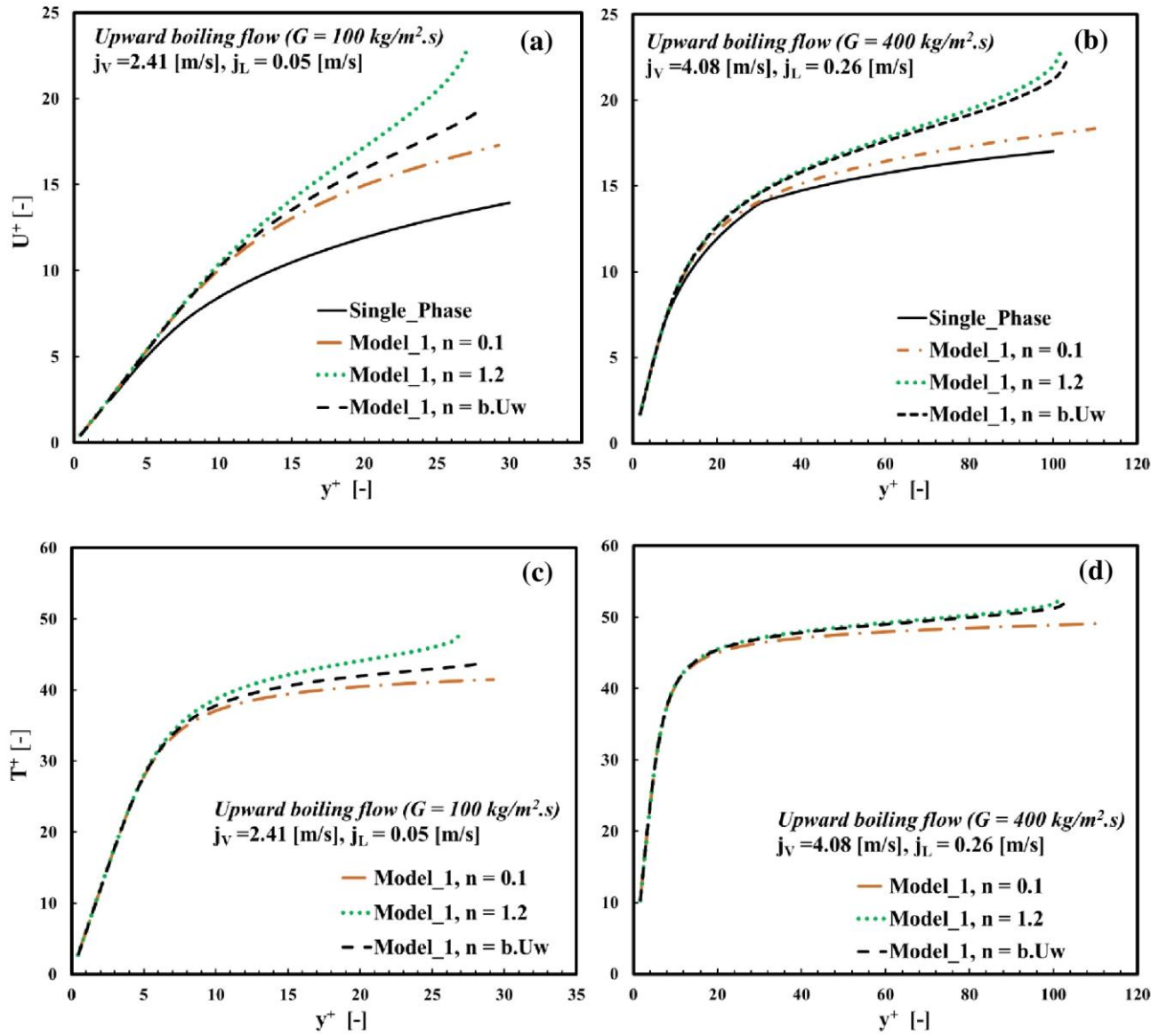


Figure 6. (a) and (b) dimensionless velocity profile versus dimensionless distance from the wall in upward flow, (c) and (d) dimensionless temperature profiles versus dimensionless distance from the wall in upward flow.

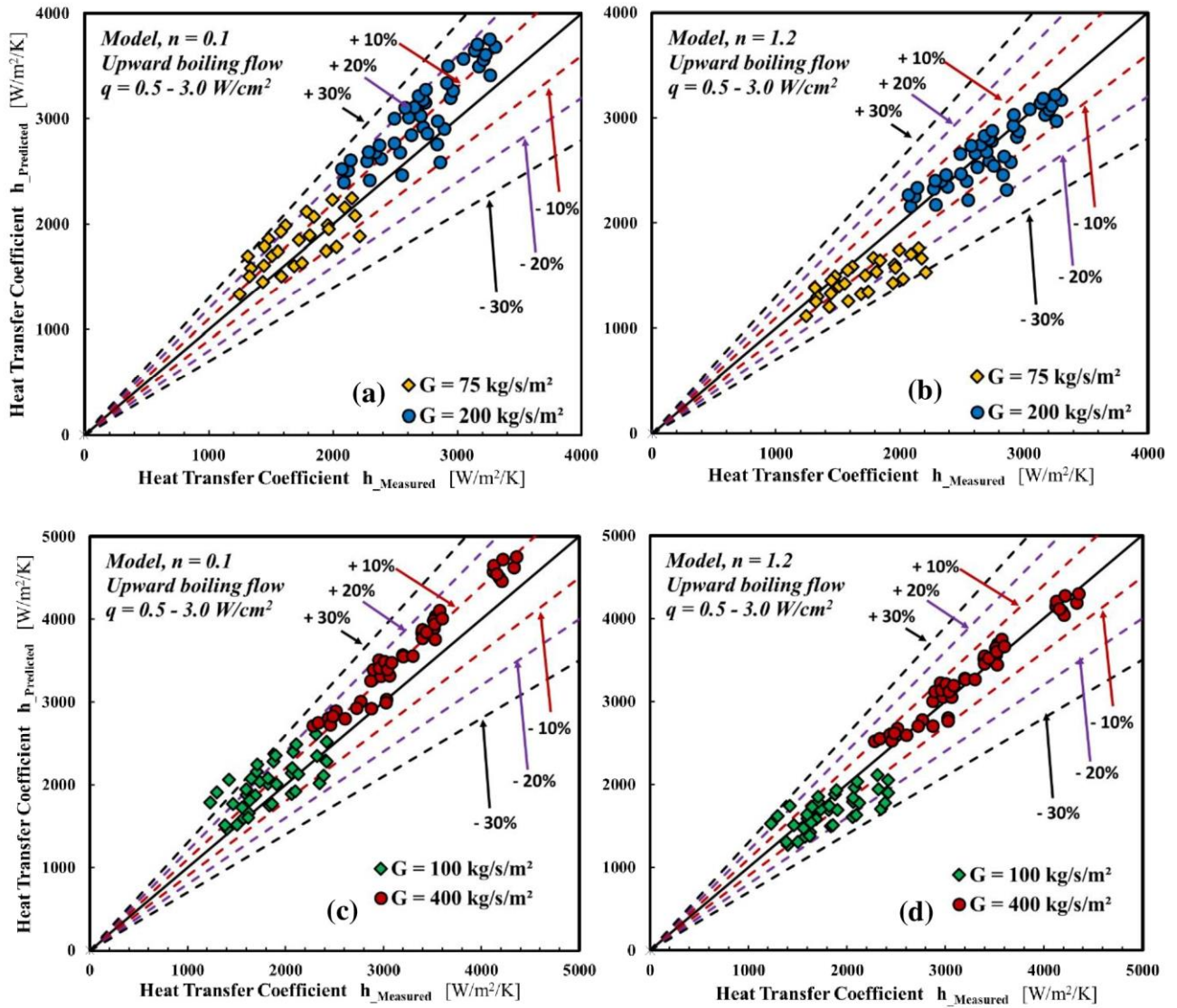


Figure 7. Predicted heat transfer versus measured heat transfer in upward flow, (a) and (c)  $n = 0.1$  (b) and (d)  $n = 1.2$ .

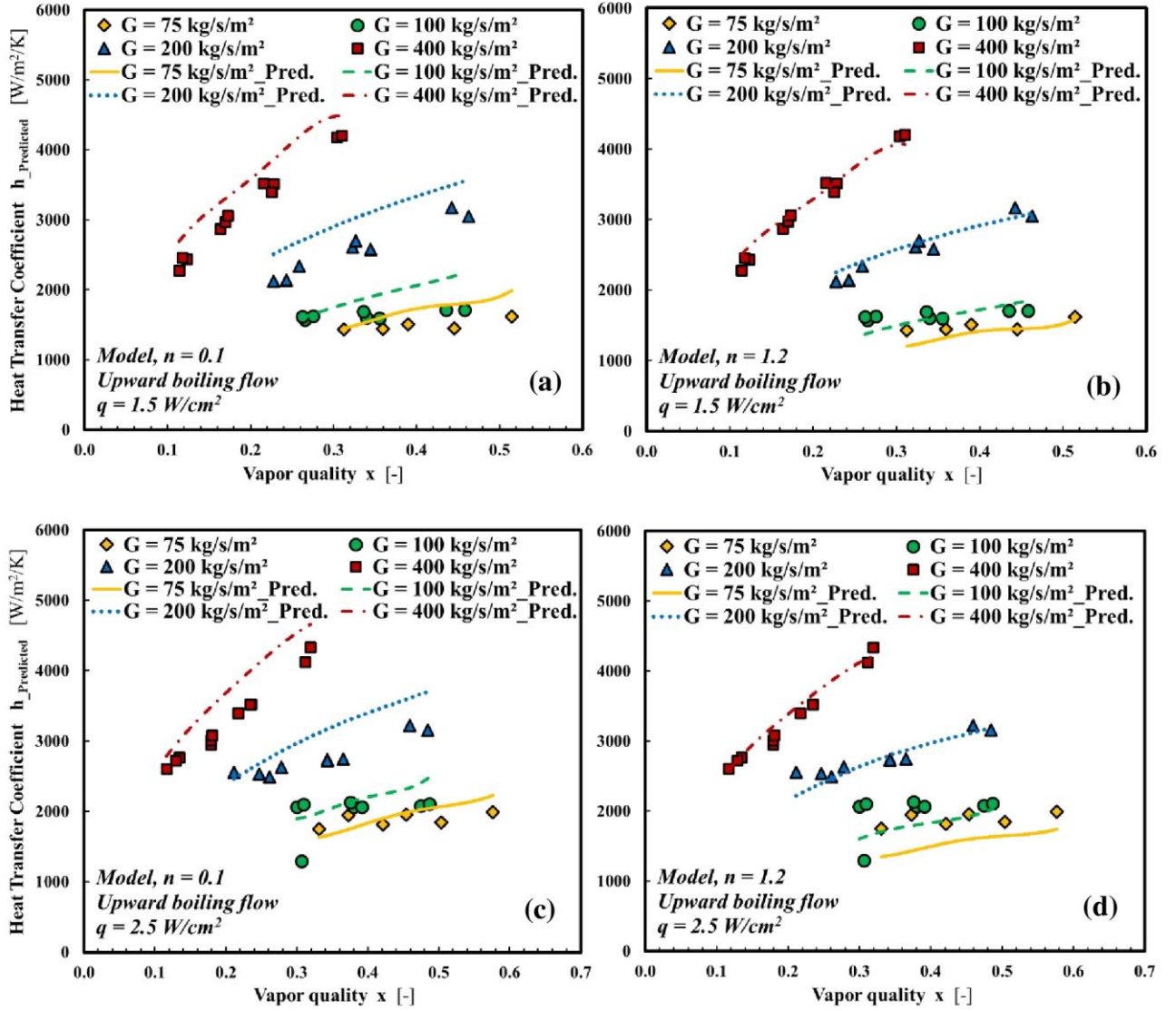


Figure 8. Measured and predicted heat transfer versus vapour quality in upward flow, (a) and (c)  $n = 0.1$  (b) and (d)  $n = 1.2$ .



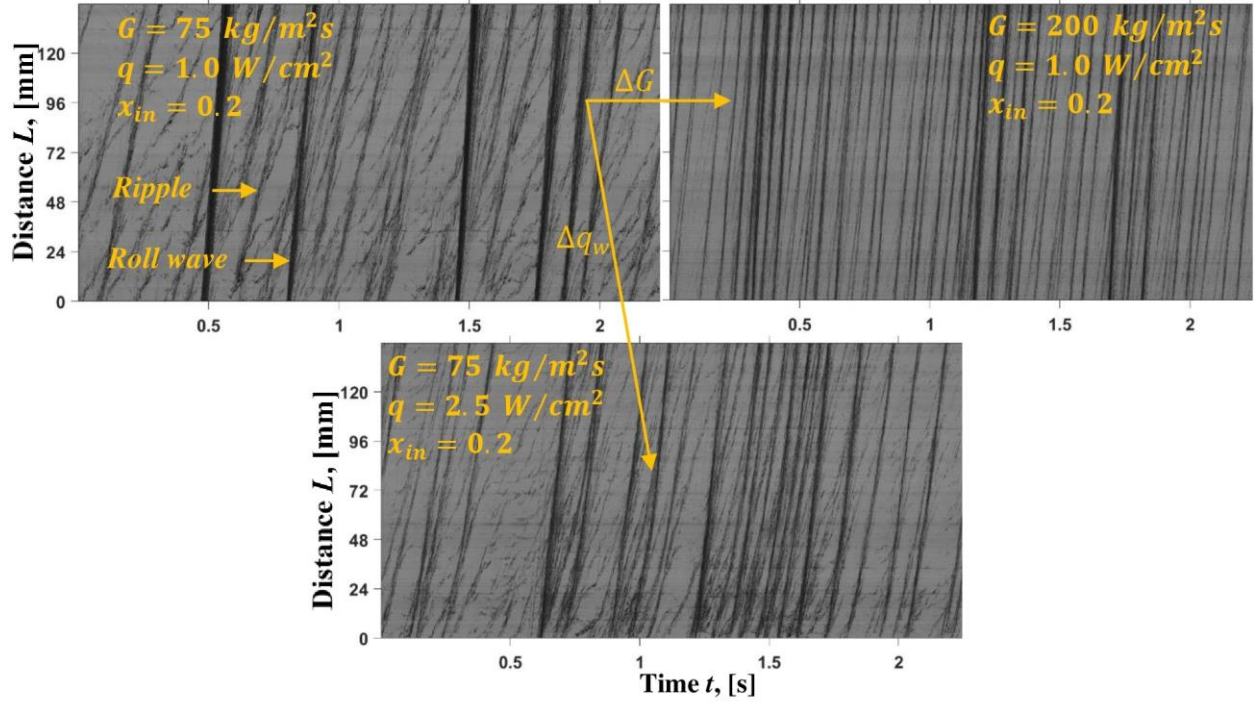


Figure 9. Time-space plot of the grey levels in the tube center line.

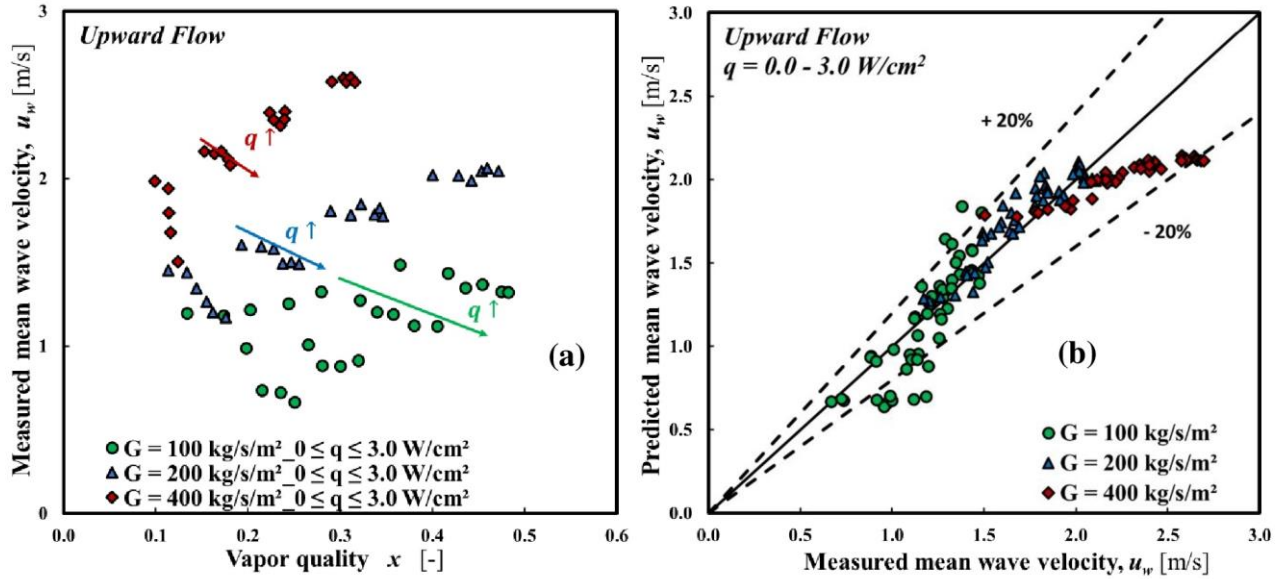


Figure 10. (a) measured mean roll wave velocity versus vapour quality, (b) predicted (Eq. (54)) versus measured mean roll wave velocity.

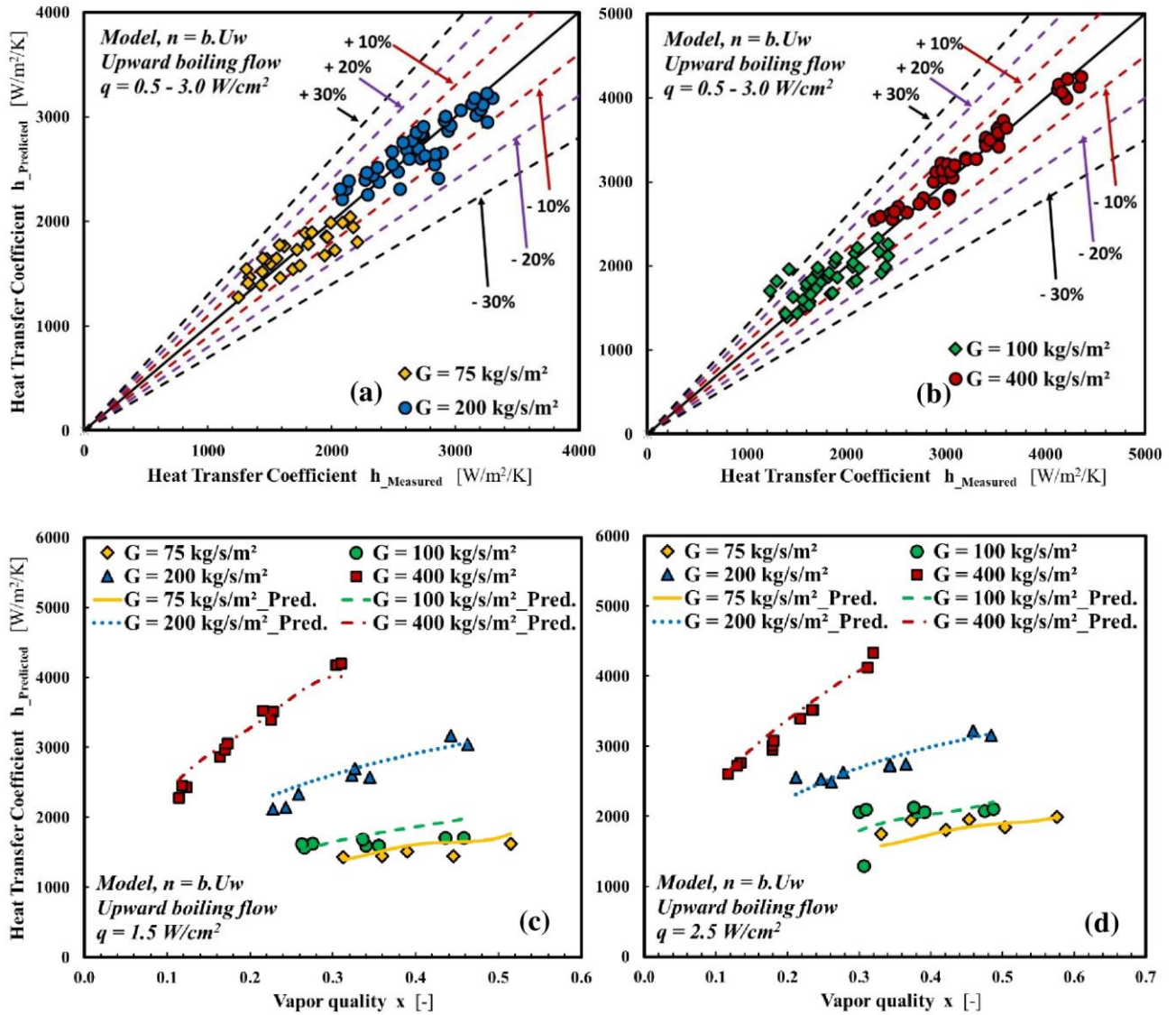


Figure 11. (a) and (b) predicted heat transfer coefficient versus measured heat transfer in upward flow, (c) and (d) measured and predicted heat transfer coefficient versus vapour quality in upward flow.



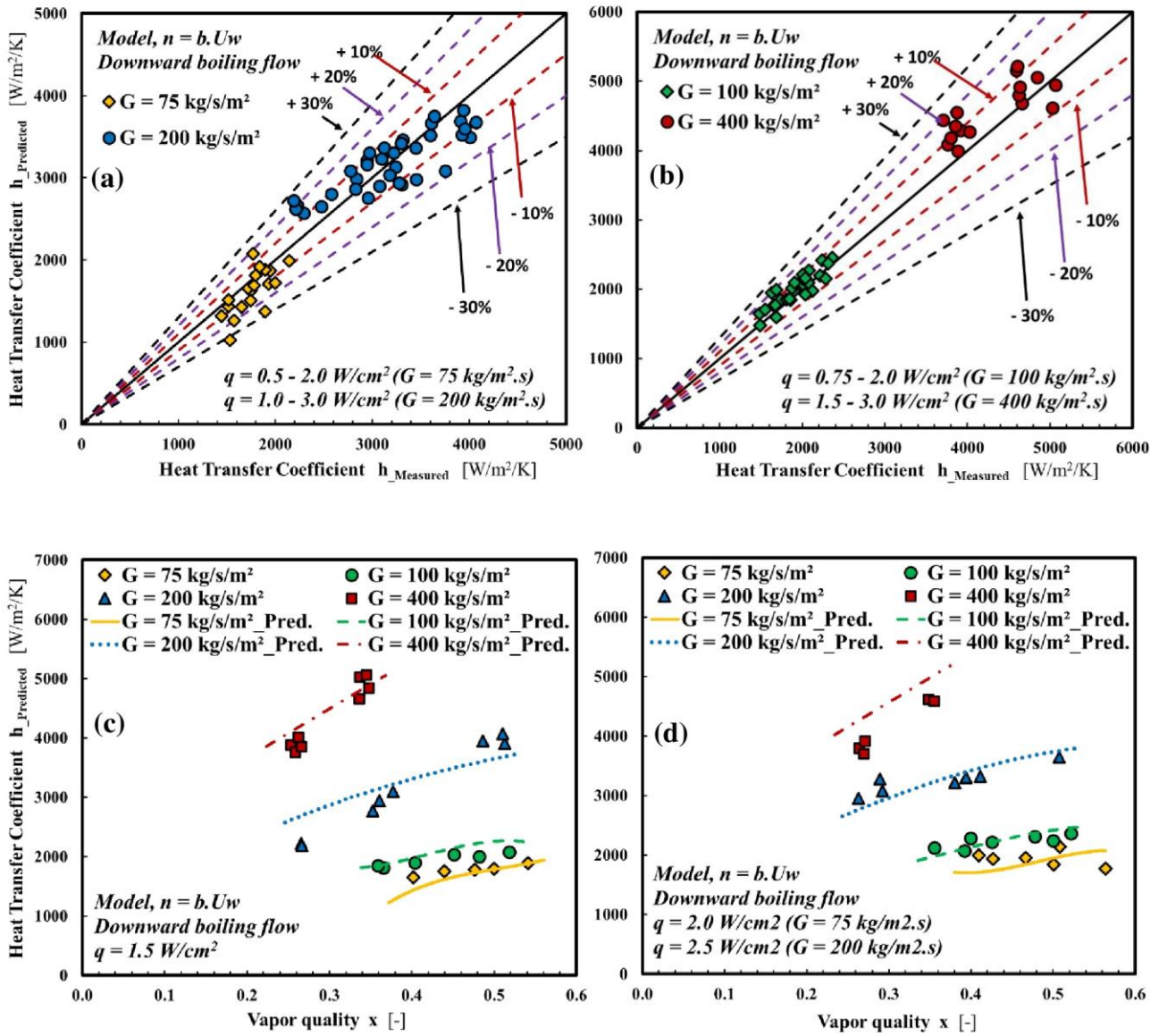


Figure 12. (a) and (b) predicted heat transfer coefficient versus measured heat transfer in downward flow, (c) and (d) measured and predicted heat transfer coefficient versus vapour quality in downward flow.

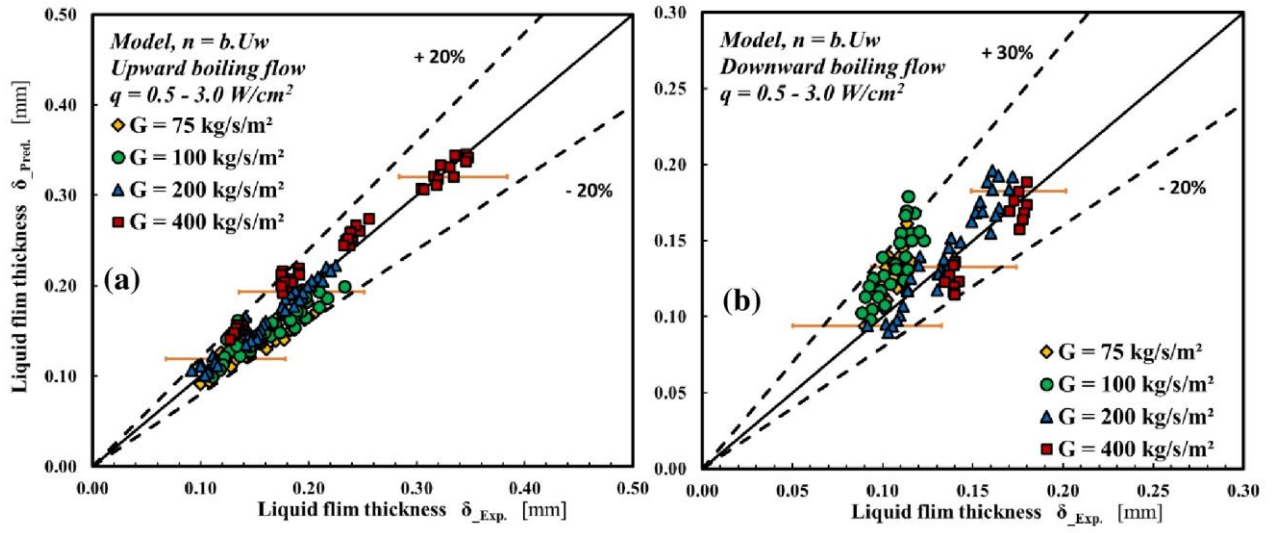


Figure 13. Predicted versus measured film thickness in the annular flow regime, (a) upward flow, (b) downward flow.

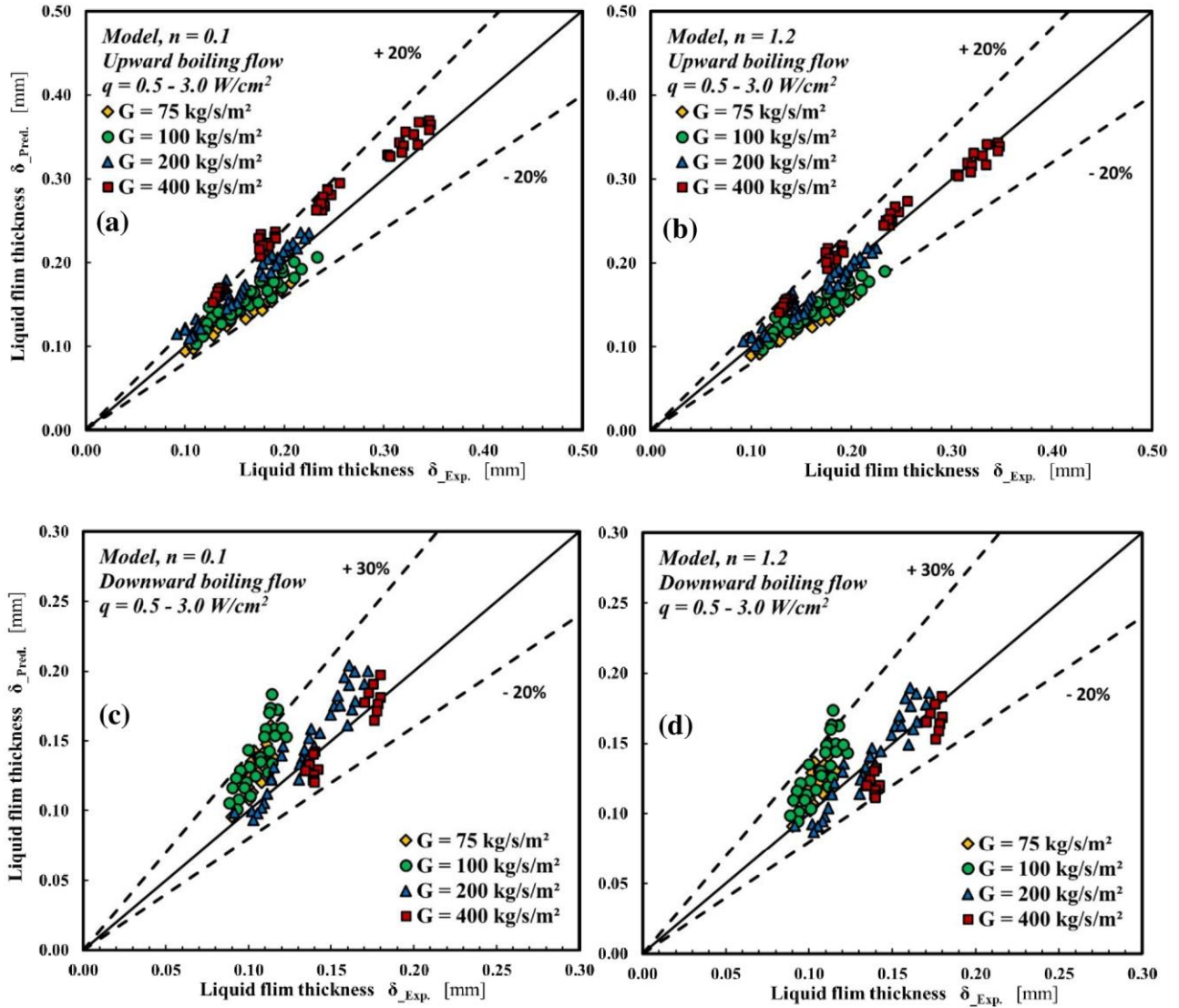


Figure 14. Predicted versus measured film thickness in the annular flow regime, (a) and (b) upward flow, (c) and (d) downward flow. (a) and (c)  $n = 0.1$ , (b) and (d)  $n = 1.2$ .

#### 4.4 Conclusion

*Experimental results showed that heat transfer was strongly influenced by the flow patterns and the evolution of heat transfer coefficient was determined by the dominant mechanism of heat transfer nucleate boiling NB or convective boiling CB. In the NB dominant regime, the heat transfer coefficient increased significantly with heat flux and was quite independent of vapour quality. In the NB+CB dominant regime the heat transfer coefficient increased with both heat flux and vapour quality while in the CB dominant regime the heat transfer coefficient was independent of heat flux but increased with vapour quality. Theoretical eddy viscosity and diffusivity models for predicting the flow velocity in the liquid film and the heat transfer coefficient were proposed in this chapter based on heat flux dependent wall shear stress models and an interfacial damping function. The proposed models gave good estimate of the measured heat transfer and liquid film thickness in both upward and downward flow configurations.*

## **Chapter 5**

### **Results of Microgravity Flow Boiling**

*In this section, experimental results of microgravity experiments carried out using the COSMO flow loop are discussed along with comparisons with normal gravity experiments. The quantities investigated are flow pattern, void fraction, bubble characteristics, vapour velocity, wave structures and heat transfer coefficient. A correlation for predicting heat transfer coefficient for microgravity flow boiling was also proposed in this chapter. The influence of the gravity level and orientation on the heat transfer coefficient is also discussed.*

## 5.1 Flow Pattern, Flow Pattern Transition and Bubble Geometry in Normal and Microgravity

In Chapter 3 the various flow patterns observed in upward and downward flows were described. Furthermore, flow pattern transition obtained from flow visualisation in upward and downward flows were compared to selected flow pattern transition criteria in literature. A similar approach is followed in this section for experiments carried out using the COSMO loop at  $\mu g$  and  $+1g$ . Furthermore, bubble size distribution in the heated section was determined using image processing technique.

### 5.1.1 Flow patterns in normal and microgravity

Similar to upward flow ( $+1g$ ), the observed flow patterns in microgravity ( $\mu g$ ) were bubbly (Bb), intermittent (Sl/Ch) and annular (An) flow patterns (Figure 5.1). Figure 5.1 shows selected flow visualisations in the heated section for  $\mu g$  and  $+1g$ . Over the range of heat flux tested, bubbly flow was observed at subcooled inlet conditions while the intermittent flow regime was observed at low subcooling or low inlet quality. The annular flow regime was observed at saturated inlet conditions corresponding to inlet vapour quality  $x_{in} \geq 0.15$ .

Flow visualisations were also carried out at the downstream visualisation section consisting of a rectangular visualisation box which served to minimise optical distortion of flow images. The absence of buoyancy forces in  $\mu g$ -flows results in zero relative velocity between the continuous liquid phase and the entrained bubbles. Consequently, dimensionless numbers such as Weber and Capillary numbers (based on this relative velocity) characterising the effect of inertia and viscosity by comparison to surface tension are very small, resulting in fairly spherical bubble shapes (Figure 5.2a). For  $+1g$ -flow, the action of buoyancy on the bubbles results in higher bubble velocity relative to the velocity of the continuous liquid phase and a higher deformation (Figure 5.2a). In both the test section and visualisation section, the bubble size was generally higher in microgravity relative to normal gravity. Furthermore, significant coalescence along the flow path resulted in larger bubbles in the downstream visualisation section (Figure 5.2a) relative to the test section (Figure 5.1a). Results of bubble size and bubble eccentricity which were obtained from image processing is presented subsequently.

Figure 5.2b and Figure 5.2c show flow visualisations carried out at the visualisation section in the slug and annular flow regimes respectively. Flow images revealed sharper nose of the Taylor bubbles in  $+1g$  relative to  $\mu g$  and this, again, is attributed to the lower relative velocity between the phases

in the later. The Taylor bubbles were also less distorted with lower density of small bubbles surrounding the vapour slug in  $\mu g$ . In general, it appeared that the width of the vapour bubble was larger in  $\mu g$  relative to  $+1g$  but no definite conclusion could be drawn on the relative size of the vapour bubble due to limitations of image acquisition. In the annular flow regime, although there was some noticeable difference in the structure of the roll waves, no other clear difference was found between  $\mu g$  and  $+1g$  flows.

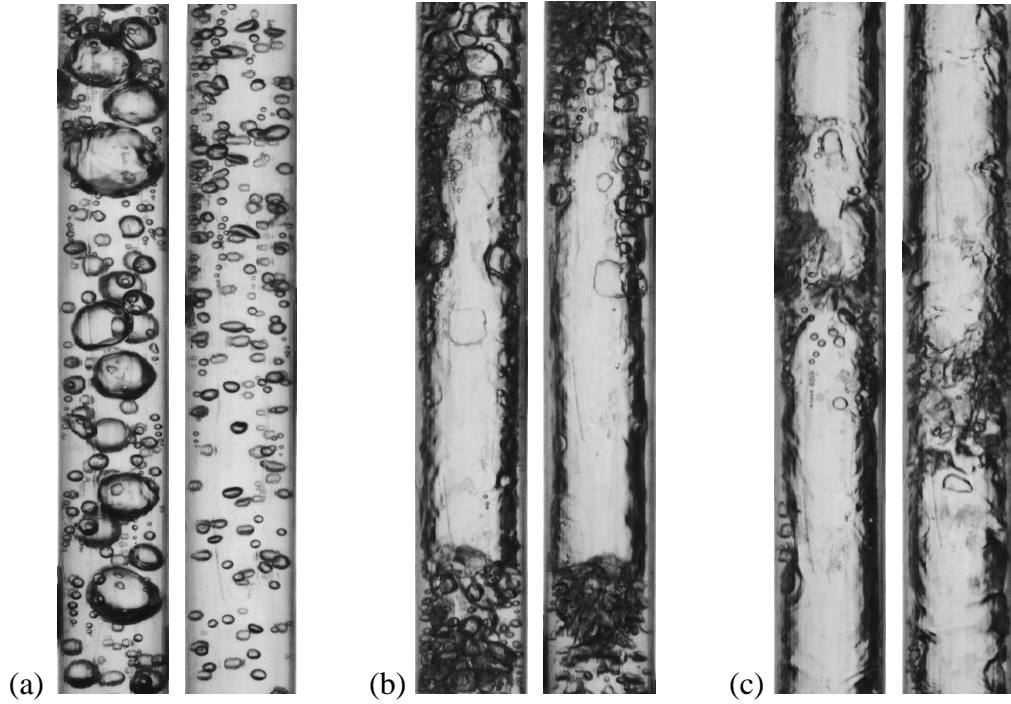


Figure 5.1: Flow visualisation in the sapphire tube in normal and microgravity for  $G = 100 \text{ kg/m}^2\text{s}$  and a.  $T_{sub} = 7.0^\circ\text{C} \pm 0.5^\circ\text{C}$ , b.  $T_{sub} = 0.0^\circ\text{C} \pm 0.5^\circ\text{C}$ , c.  $x = 0.20 \pm 0.02$ :  $\mu g$  (left),  $+1g$  (right).

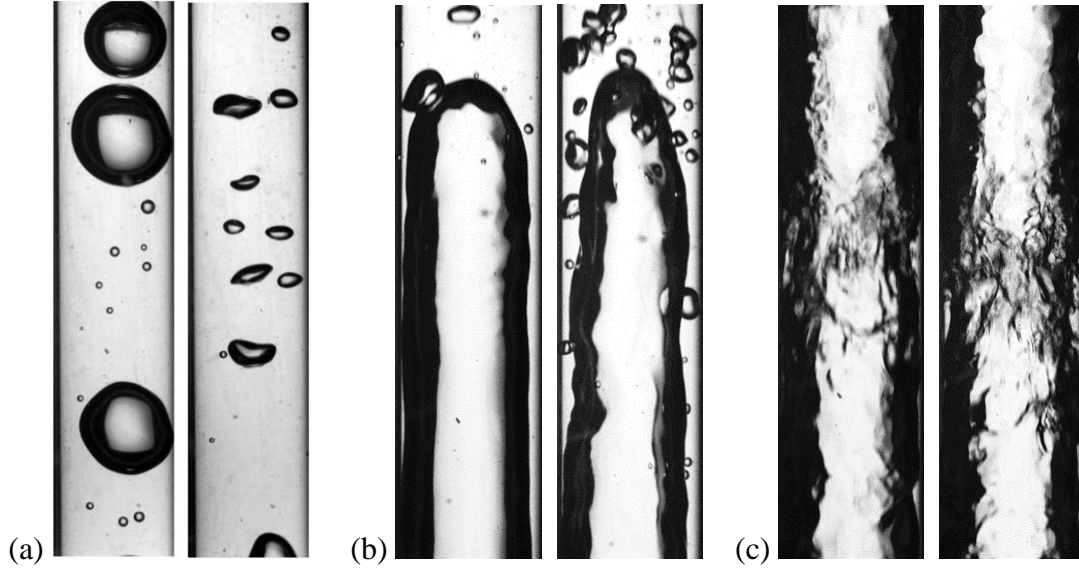


Figure 5.2: Flow visualisation in the visualisation test section in normal and microgravity for  $G = 100 \text{ kg/m}^2\text{s}$  and a.  $T_{sub} = 7.0^\circ\text{C} \pm 0.5^\circ\text{C}$ , b.  $T_{sub} = 0.0^\circ\text{C} \pm 0.5^\circ\text{C}$ , c.  $x = 0.20 \pm 0.02$ :  $\mu g$  (left),  $+1g$  (right).

### 5.1.2 Flow pattern map and flow pattern transition

The various flow patterns obtained from flow visualisation are presented in a flow pattern map in terms of the superficial velocities of the phase (Figure 5.3). Although, there were small difference in the transition region, the flow pattern map for both  $\mu g$ - and  $+1g$ -flows were generally similar.



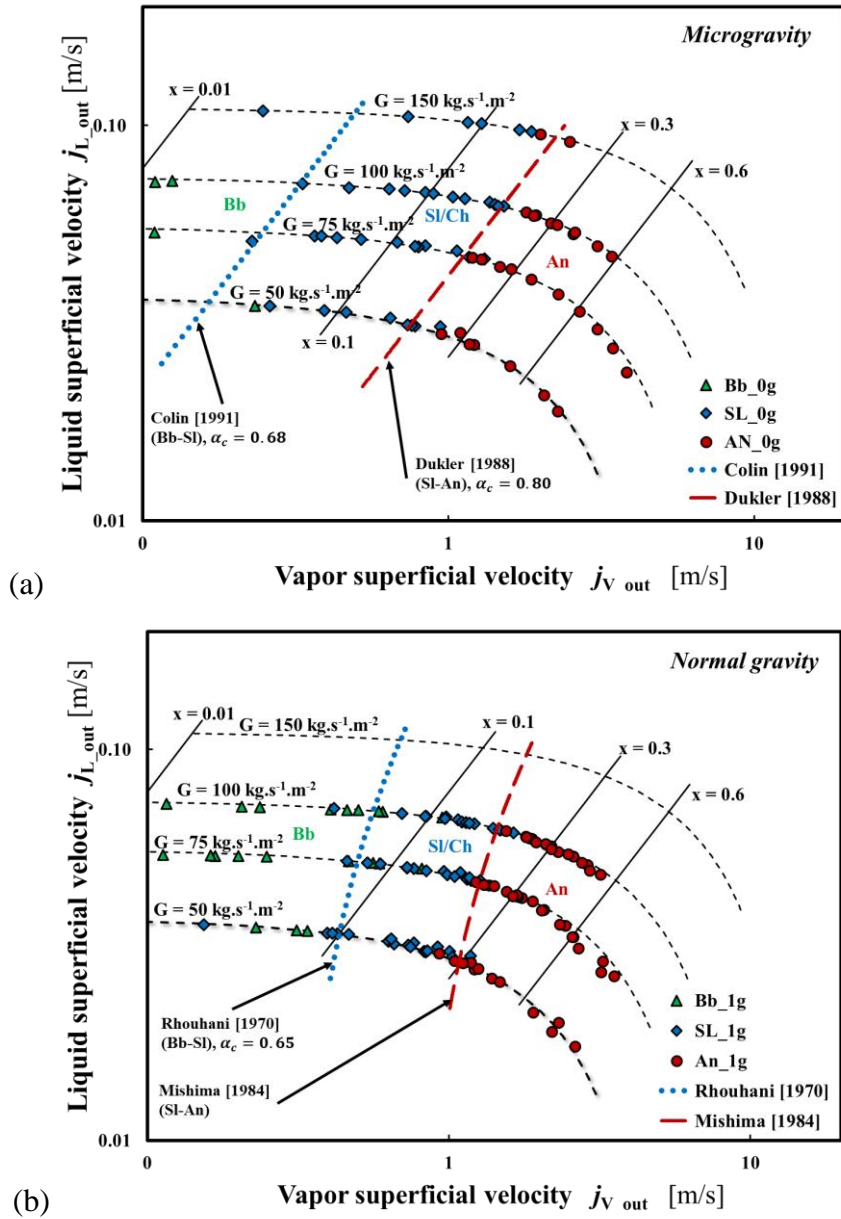


Figure 5.3: Flow pattern maps; a. microgravity, b. normal gravity.

Transition from bubbly to slug/Churn flow is due to bubble coalescence and both regimes represent a continuum of the same physical process. For developed adiabatic two-phase flows, bubbly-slug transition in microgravity based on critical void fraction ( $\alpha_c$ ) has been proposed based on the Ohnesorge number  $Oh = Re_l^2 / We_l$  (Colin et al., 1991/1996).

$$\alpha_c = \begin{cases} 0.45 & Oh > 8.2 \times 10^{-4} \\ 0.20 & Oh < 7.6 \times 10^{-4} \end{cases} \quad 5.1$$

For developing flows, in the heated section, Narcy et al. (2014) reported a critical void fraction ( $\alpha_c$ )

for bubbly-slug transition of  $\approx 0.70$  while Celata and Zummo (2009a), reported  $\alpha_c$  of 0.74. In the current work the mean void fractions at transition from bubbly to slug flow were  $\approx 0.68$  and  $\approx 0.64$  for  $\mu g$ - and  $+1g$ -flows respectively. It should be remarked that, the Ohnesorge number in the current work was  $\approx 1.1 \times 10^{-3}$  characteristic of a strong effect of bubble coalescence.

Based on experimental data of vertical gas-liquid adiabatic flow in a 40 mmID tube, Colin et al. (1991), proposed a bubbly-slug transition criteria from the drift model with  $C_0$  of 1.2 and  $\alpha_c$  of 0.45. In microgravity, the drift flux model is given by Eq. 5.2 or Eq. 5.3 and  $x_c$  is given by Eq. 5.4.

$$u_v = C_0 j \quad 5.2$$

$$j_l = \frac{1 - C_0 \alpha_c}{C_0 \alpha_c} j_v \quad 5.3$$

$$x_c = \frac{1}{1 + \frac{1 - C_0 \alpha_c}{C_0 \alpha_c} \frac{\rho_l}{\rho_v}} \quad 5.4$$

Following the approach Colin et al. (1991) (i.e.,  $C_0 = 1.2$ ) and using  $\alpha_c = 0.68$  (obtained from flow visualisation in the current work),  $x_c$  is determined from Eq. 5.3 and the resulting transition boundary is shown by dotted lines in Figure 5.3a. The line provides a good prediction of the observed transition from bubbly to slug flow for microgravity flow.

A similar approach was followed for  $+1g$ -flow but using the drift flux model of Rouhani and Axelsson (1970) (Chapter 3, Fig. 4, pp107). In the case of  $+1g$ -flow,  $x_c$  was determined from Eq. 5.5 and  $\alpha_c = 0.65$  (obtained from flow visualisation in the current work). The predicted transition boundary is shown by dashed line in Figure 5.3a. The curve provides a good prediction of the observed transition from bubbly to slug flow in normal gravity.

$$x_c = \frac{\frac{G}{\rho_l} + \frac{u_\infty}{C_0}}{\frac{G(1 - C_0 \alpha_c)}{\rho_v C_0 \alpha_c} + \frac{G}{\rho_l}} \quad 5.5$$

By equating the void fraction computed from the slug flow model and that computed from the annular flow model, Dukler et al. (1988) proposed a critical void fraction ( $\alpha_c$ ) at transition from slug to annular flow in microgravity of 0.8. For  $\mu g$ -flow,  $x_c$  was determined from Eq. 5.4,  $C_0 = 1.2$  (Dukler

et al., 1988) and the predicted transition boundary is shown by dotted curve in Figure 5.3b. The curve provides a good prediction of the observed transition from intermittent to annular flow in microgravity. In the case of  $+1g$ -flow, the transition criteria proposed by Mishima and Ishii (1984) (see Chapter 3, journal article, Eq. 13, pp110) provided a good prediction of the observed transition from intermittent to annular flow in normal gravity (dashed curve in Figure 5.3b).

### 5.1.3 Bubble size distribution in normal and microgravity

Image processing was used to estimate the bubble geometry in the heated section for  $\mu g$ - and  $+1g$ -bubbly-flows. It should be remarked that the image resolution in the heated section was low and there was significant image distortion close to the wall due to tube circularity. Therefore, the results of image processing in normal and microgravity are discussed in qualitative terms. Figure 5.4 - Figure 5.5 provide comparison of bubble geometry for  $\mu g$ - and  $+1g$ -bubbly-flows at selected conditions. In general, the mean bubble diameter was higher in microgravity relative to normal gravity flows. Furthermore, while most of the bubbles in normal gravity had diameter below  $2\text{ mm}$ , a significant number of bubbles in microgravity had diameters between  $2 - 6\text{ mm}$ . The bubble distribution in upward flow followed a log normal distribution. In microgravity, the bubble size distribution is rather bi-modal, with a large number of very small bubbles nucleated at the wall and larger bubbles resulting from coalescence. The bubbles were also more spherical in microgravity relative to normal gravity as determined by the lower eccentricity in the former (not shown).

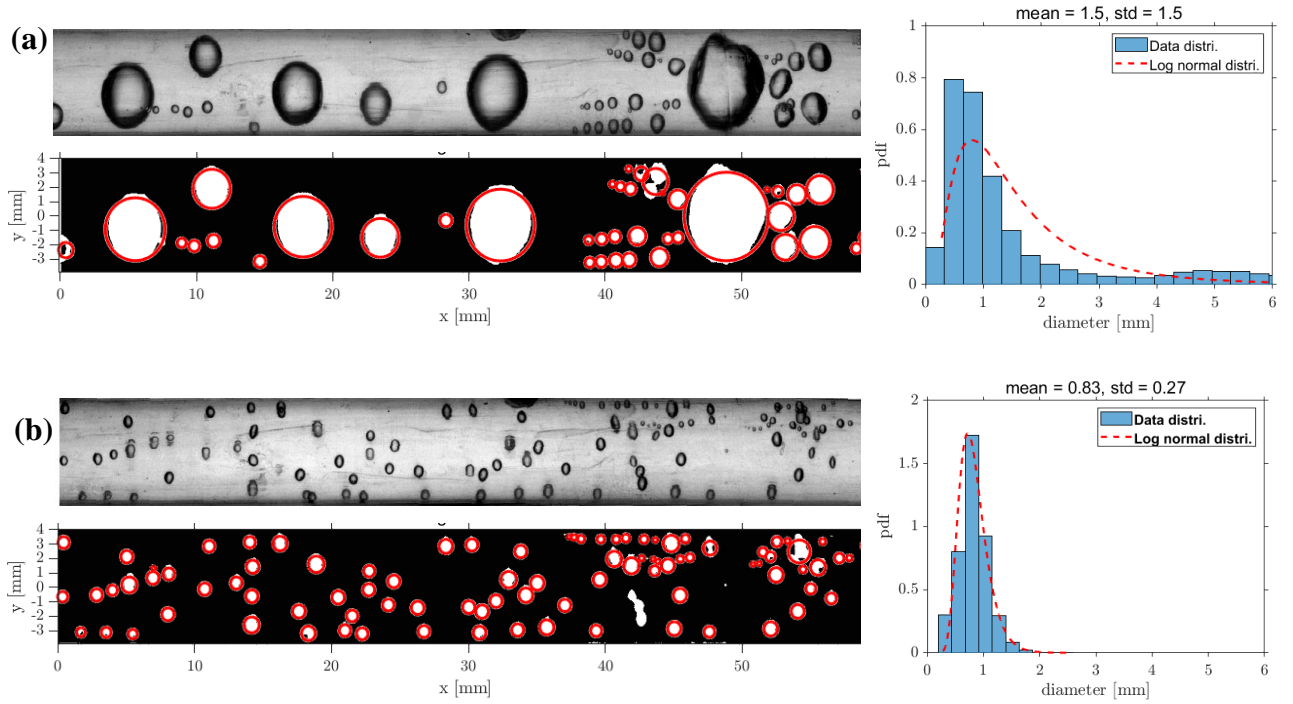


Figure 5.4. Comparison of bubble size and bubble eccentricity between microgravity and normal gravity flows. a.  $\mu g$ ,  $G = 50 \text{ kg/m}^2\text{s}$ ,  $T_{sub} = 14^\circ\text{C} \pm 0.5^\circ\text{C}$ , b.  $+1g$ ,  $G = 50 \text{ kg/m}^2\text{s}$ ,  $T_{sub} = 14^\circ\text{C} \pm 0.5^\circ\text{C}$ .

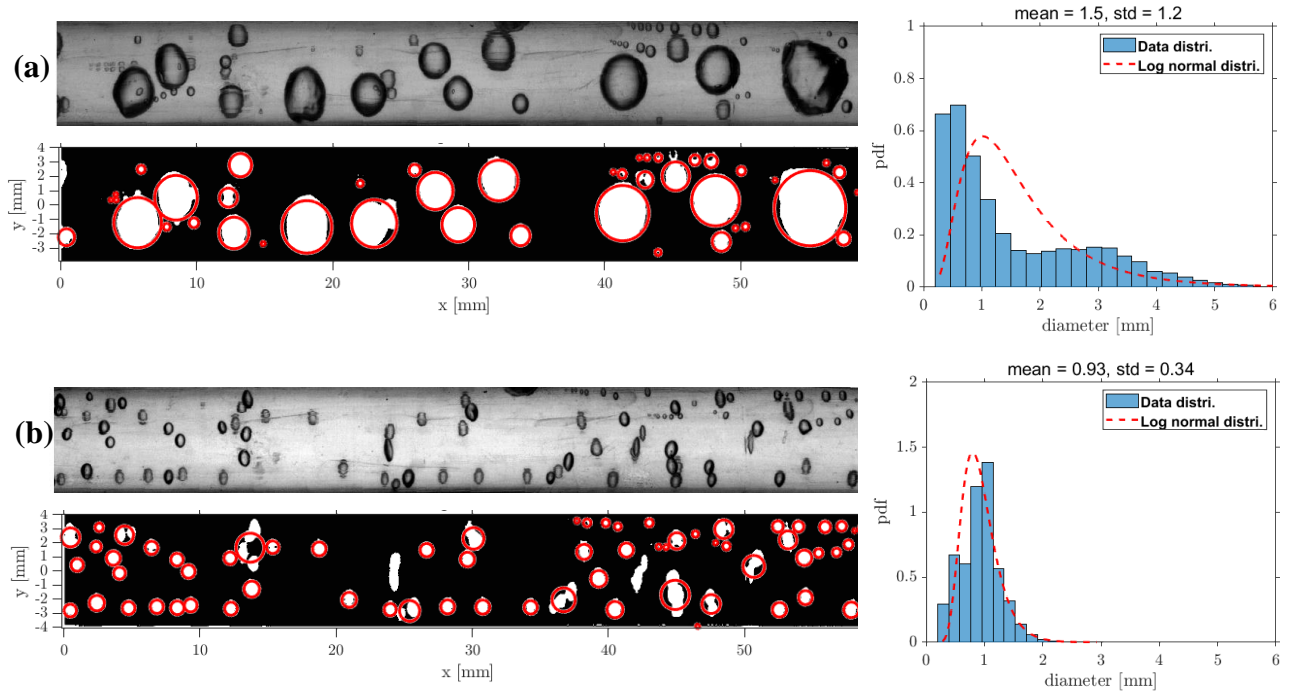


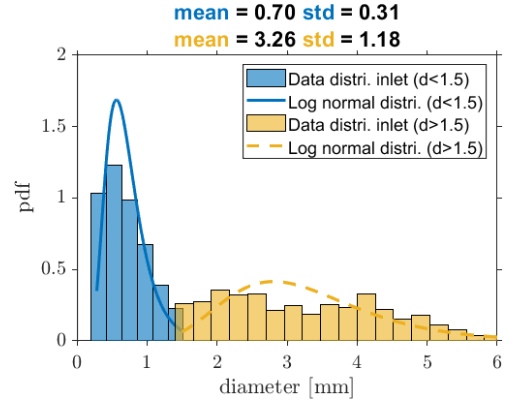
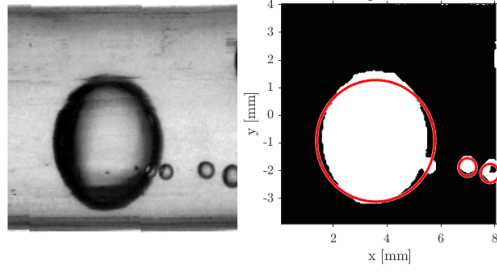
Figure 5.5. Comparison of bubble size and bubble eccentricity between microgravity and normal gravity flows. a.  $\mu g$ ,  $G = 100 \text{ kg/m}^2\text{s}$ ,  $T_{sub} = 10^\circ\text{C} \pm 0.5^\circ\text{C}$  and b.  $\mu g$ ,  $G = 100 \text{ kg/m}^2\text{s}$ ,  $T_{sub} = 9^\circ\text{C} \pm 0.5^\circ\text{C}$ .

#### 5.1.4 Bubble size evolution in normal and microgravity

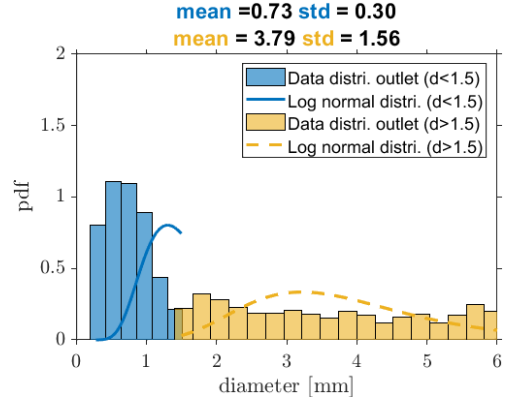
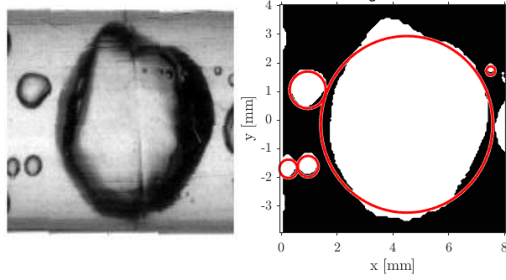
Bubble size evolution along the test section results from, bubble compressibility, phase change, bubble coalescence and bubble nucleation (Colin et al., 2004; Kamp et al., 2001; Legendre et al., 1998; Morel and Laviéville, 2008). Figure 5.7 shows flow visualisation close to the inlet and outlet of the test section's field of view (71 mm) along with the corresponding probability density functions (PDF) of bubble diameter determined from image processing. The PDF was split into two sections so as to separate bubbles due to nucleation at the wall (smaller bubbles with mean diameter  $< 1.5$  mm) from existing bubbles in the liquid.

Both flow visualisation and results of image processing show an increase in mean bubble diameter from inlet to outlet particularly for  $\mu g$ -flows (Figure 5.6 - Figure 5.7). The left part of the PDF corresponding to the smallest bubbles does not evolve much between the inlet and the outlet of the tube, because several bubble nucleation occurs along the tube. A stronger evolution of the right part of the PDF (in yellow on the graphs) is observed. The bubble growth within the field of view was between 1 – 6% in normal gravity and 14 – 22% in microgravity over the range of test conditions. The higher growth rate in microgravity relative to normal gravity is attributed to higher levels of bubble coalescence in the former. The rate of bubble coalescence is larger at the lowest mass flux because of a longer residence time of the bubbles in the tube. The evolution of the bubble size could be in future be compared to the results of coalescence models as developed by Colin et al. (2008) for microgravity flows. From these visualisations, the growth rate of the bubbles due to phase change could be also evaluated.

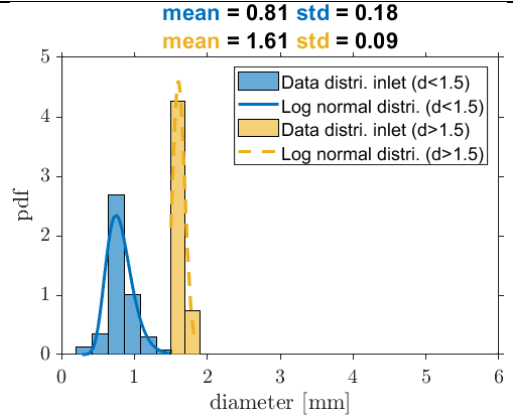
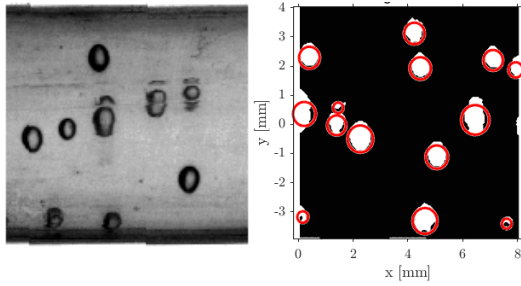
(a) Inlet



(a) Outlet



(b) Inlet



(b) Outlet

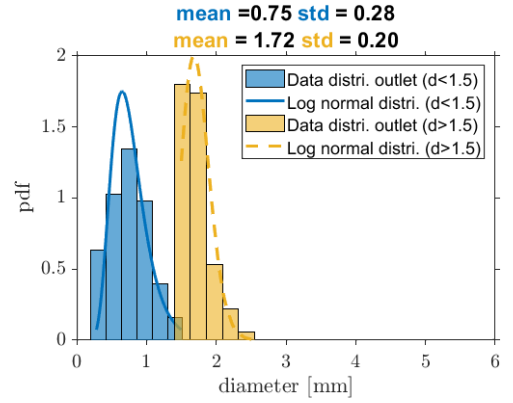
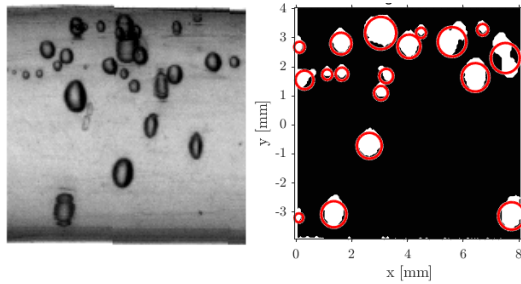
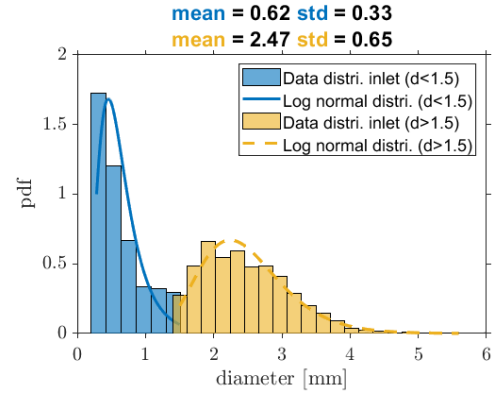
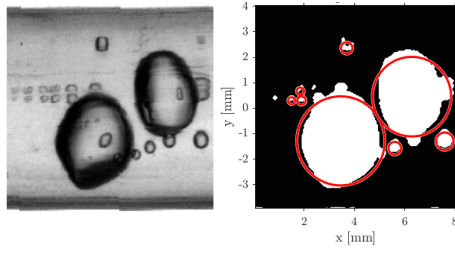
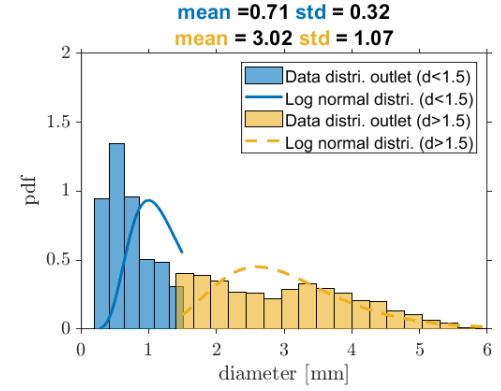
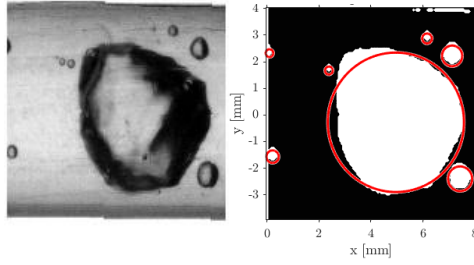


Figure 5.6. Bubble size evolution in microgravity and normal gravity flows. a.  $\mu g$ ,  $G = 50 \text{ kg/m}^2\text{s}$ ,  $T_{sub} = 14^\circ\text{C} \pm 0.5^\circ\text{C}$ , b.  $+1g$ ,  $G = 50 \text{ kg/m}^2\text{s}$ ,  $T_{sub} = 14^\circ\text{C} \pm 0.5^\circ\text{C}$ .

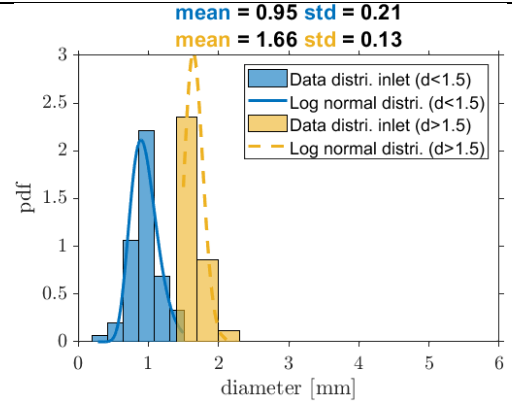
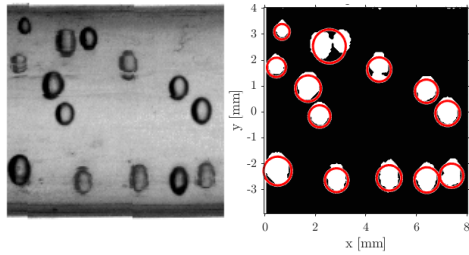
(a) Inlet



(a) Outlet



(b) Inlet



Outlet

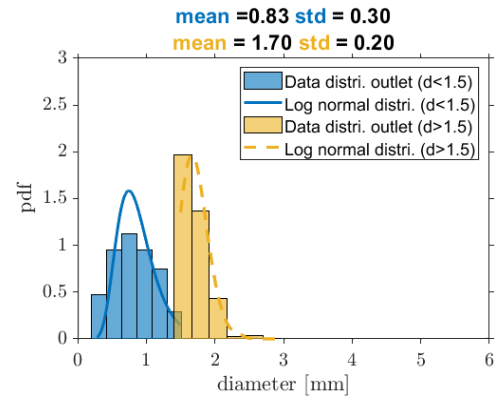
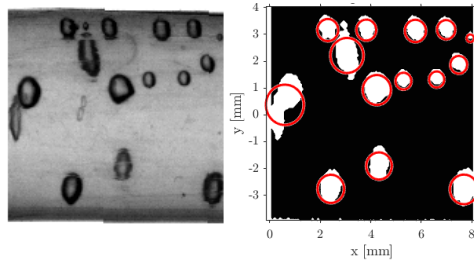


Figure 5.7. Bubble size evolution in microgravity and normal gravity flows. a.  $\mu g$ ,  $G = 100 \text{ kg/m}^2\text{s}$ ,  $T_{sub} = 10^\circ\text{C} \pm 0.5^\circ\text{C}$  and b.  $\mu g$ ,  $G = 100 \text{ kg/m}^2\text{s}$ ,  $T_{sub} = 9^\circ\text{C} \pm 0.5^\circ\text{C}$ .

## 5.2 Void Fraction and Vapour Velocity in Microgravity

Figure 5.8 shows the measured void fraction at the outlet of the test section for both  $\mu g$ - and  $+1g$ -flows. As expected, the measured void fraction for  $\mu g$ -flows evolved with vapour quality and showed no obvious dependence on mass flux (Figure 5.8a). The latter is due to the near-zero value of the drift velocity in microgravity. It should be remarked that, the scatter in the measured void fraction in microgravity was due to limited number of measurements of liquid capacitances which are required to correct for changes in measured void fraction with changes in the temperature of the electronics. In normal gravity (ground experiments), measured void fraction for each mass flux showed more regular profiles due to sufficient number of measurements of the liquid capacitance in between various two-phase measurements (Figure 5.8b). Similar, to measured void fraction in  $+1g$ -flows reported in Chapter 3 (BRASIL), the measured void fraction for  $+1g$ -flows (COSMO) evolved with quality and increased slightly with mass flux. A comparison between measured void at selected mass fluxes obtained from the two experimental setups for  $+1g$ -flows is shown in Figure 5.8c-d. Measurements from both facilities showed good agreement despite differences in the types of preheaters used and differences in the location of the preheaters relative to the test section in BRASIL and COSMO loops. Similar measurement accuracies apply to measured void fraction in both loops and details of this can be found in Chapter 3 as well as in the work of Narcy et al. (2014).

Measured void fraction was generally higher in  $\mu g$ - relative to  $+1g$ -flows, particularly in the bubbly and intermittent flow regimes ( $x \leq 0.2$ ). This is due to longer residence time of the bubbles in the test section for  $\mu g$ - relative to  $+1g$ -flows (Figure 5.8c-d). Figure 5.8c-d also provides comparisons of measured fraction in all three flow configurations ( $\mu g$ ,  $+1g$  and  $-1g$ ). For  $x \leq 0.2$ , the measured void fraction was highest in  $-1g$  and lowest in  $+1g$  following the trend of residence time of bubbles in the test section.



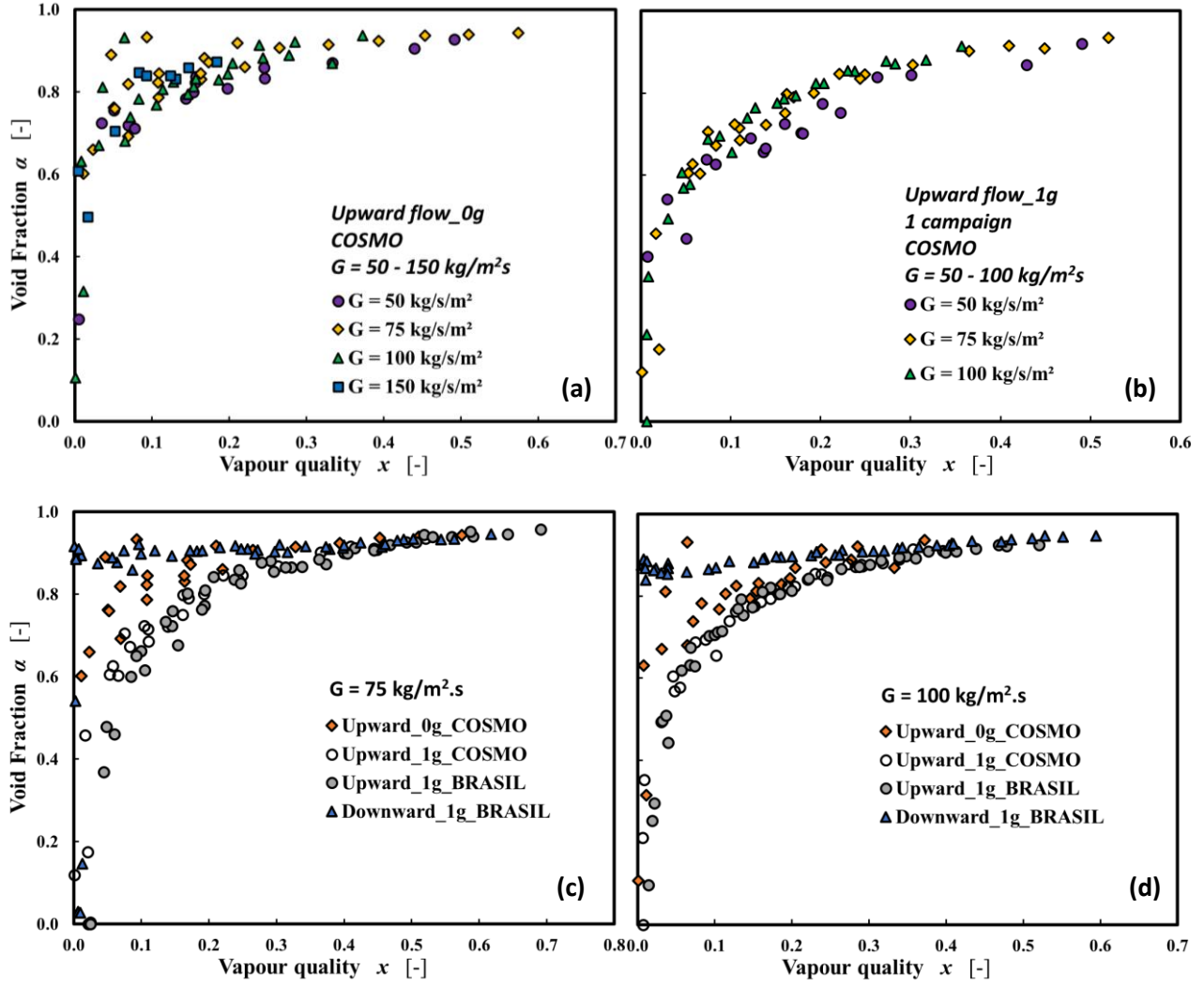


Figure 5.8: Measured void fraction at the outlet of the test sections; a. microgravity ( $\mu g \approx 0g$ ), b. normal gravity ( $+1g$ ), c. & d.  $\mu g$ ,  $+1g$  and  $-1g$  flows.

The measured void fraction in microgravity was used to determine the vapour velocity ( $u_v = j_v/\alpha$ ). Figure 5.9 shows computed vapour velocities in terms of mixture velocity for  $\mu g$ - and  $+1g$  flows. In the bubbly and intermittent flow regimes of  $\mu g$  flow, the experimental data gave values of  $C_0$  and  $u_\infty$  of 1.15 and 0 respectively (Figure 5.9a), while these parameters were 1.14 and 0.18 respectively for  $+1g$  flow (Figure 5.9c). Unlike fully developed adiabatic two-phase microgravity flows where bubbles are concentrated at the centre of the tube ( $1.2 \leq C_0 \leq 1.3$ ), there is significant concentration of bubbles close to the wall due to nucleation in the heated section of flow boiling. This may explain the lower values of  $C_0$  ( $\approx 1.14$ ) from current measurements (Figure 5.9a). The computed value of  $u_\infty \approx 0$  is in agreement with theory of microgravity two-phase flows. For  $+1g$  flow, the computed

$C_0$  and  $u_\infty$  in the bubbly and intermittent flow regimes are in general agreement with common drift flux models (see Chapter 3, journal article, Table 2, pp110). In the annular flow regime of microgravity two-phase flows, the pressure gradient results in a positive drift in relative velocity of the phase in both microgravity and normal gravity (Figure 5.9b & d). The results in the annular flow regime also show higher drift velocity in  $+1g$  flow relative to  $\mu g$  flow. This is due to higher buoyancy forces in  $+1g$  flow relative to  $\mu g$  flow.

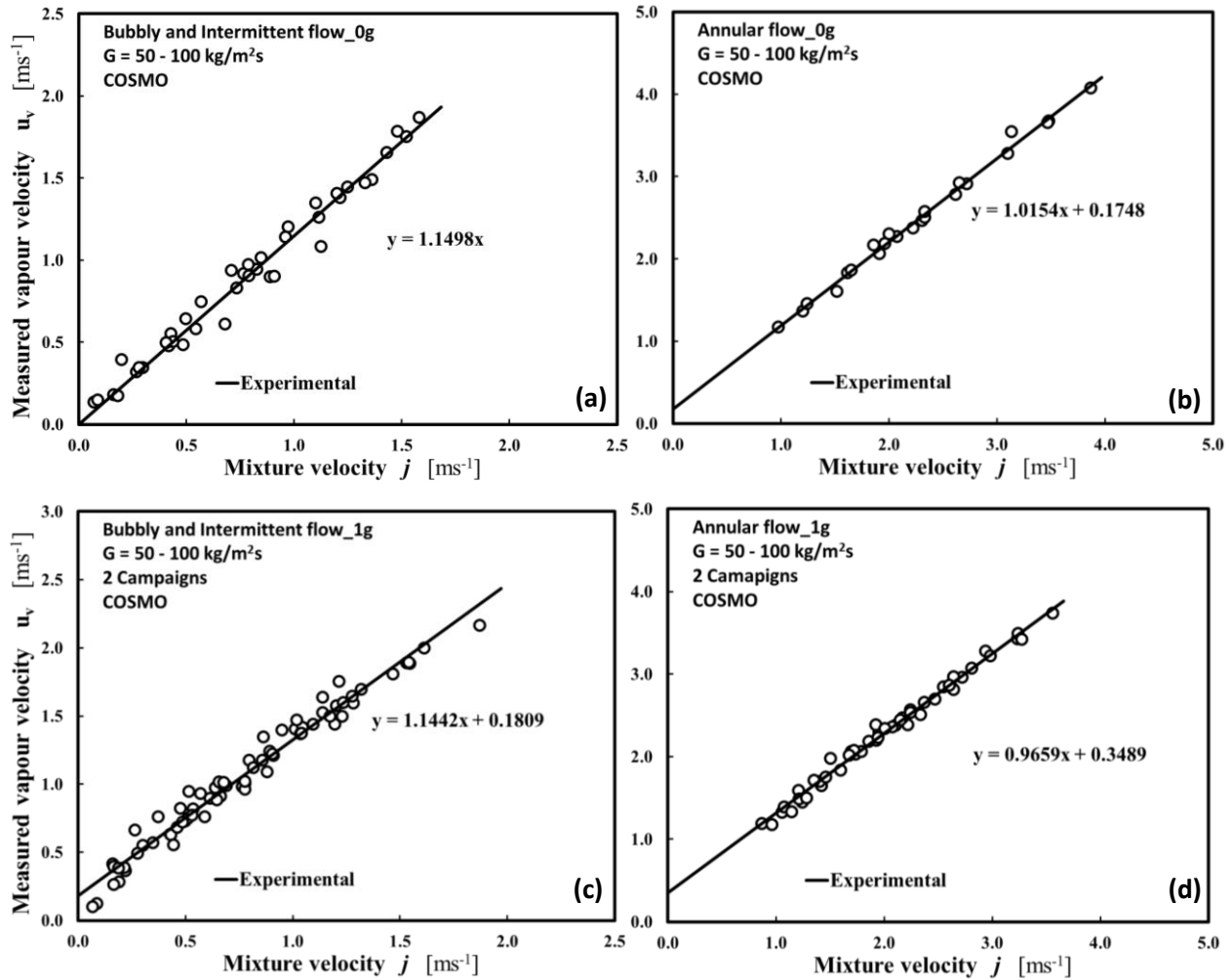


Figure 5.9: Vapour velocity computed from measured void fraction versus mixture velocity: microgravity (top), normal gravity (bottom).

In the slug flow regime of  $\mu g$  flow, the velocity of Taylor bubble at the outlet of the test section was also determined from image processing of space-time diagrams. Figure 5.10 shows a typical space-time diagram obtained from the time evolution of the grey levels on an axial centre line of the image to the right. The nose and rear of each Taylor bubble clearly appear as a pair of dark lines in the plot.

The slope of the lines gives the bubble velocity ( $u_b \equiv u_v$ ).

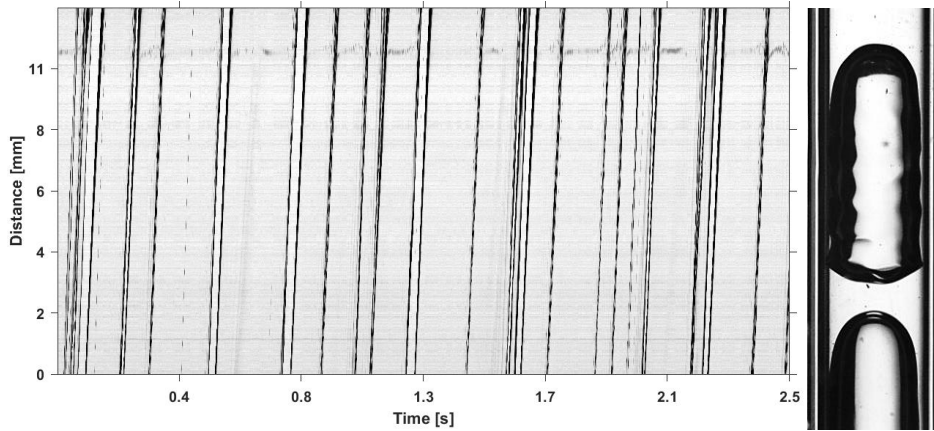


Figure 5.10: Typical distance versus time diagram for  $\mu g$  slug flow in the downstream adiabatic section at  $G = 50 \text{ kg/m}^2\text{s}$ ,  $x_{out} = 0.051$ .

During parabolic manoeuvres vibrations were transmitted from the base of the aircraft to the experimental loop. This resulted in small oscillation of the test section about the vertical axis. To limit the effect of vibration on the tracking of the tube centreline, the location of the edge of the tube was determined for each image frame. Figure 5.11 shows grey scale plots of the tube cross section at selected conditions. The location of the largest peak corresponds to the mean position of the nose of the Taylor bubbles. Its mean location was generally within  $\pm 5\%$  of the tube centre and this provides validation to the edge detection algorithm used. The peaks close to the wall represent liquid flow adjacent to the wall.

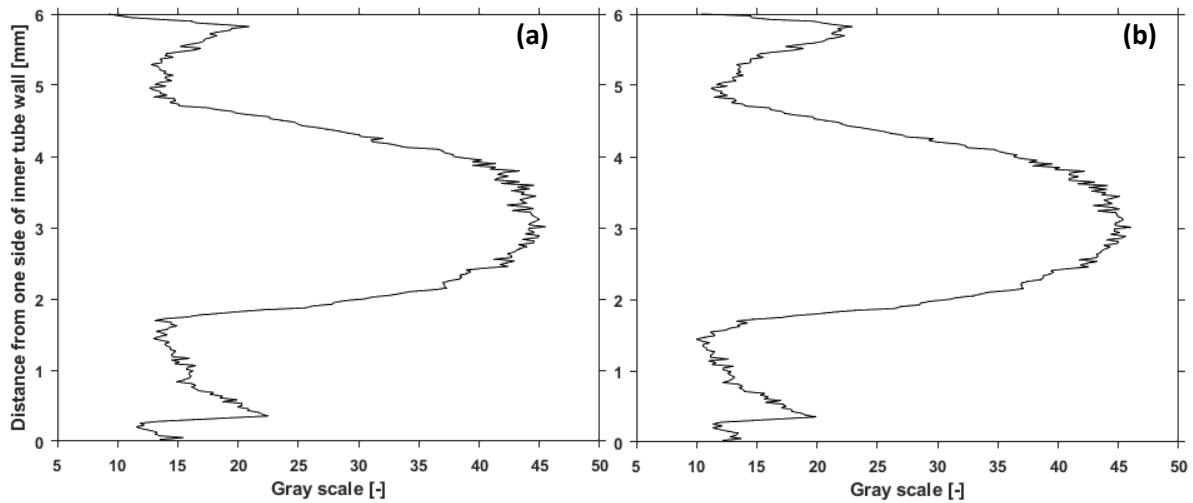


Figure 5.11: Gray scale plots of the tube cross section for  $\mu g$ -slug flow in the downstream adiabatic section; a.  $G = 50 \text{ kg/m}^2\text{s}$ ,  $x_{out} = 0.051$ , b.  $G = 100 \text{ kg/m}^2\text{s}$ ,  $x_{out} = 0.082$ .

The region of transition between bubbly and slug flow regime was often characterised by shorter slugs and bubble distribution around the centreline was sometimes asymmetric. Figure 5.12 shows space-time diagram of the tube cross section at an axial distance of  $L_{FV}/2$  ( $L_{FV}$  is the length of the field of view). Only cases where the bubble distribution was symmetric (within  $\pm 5\%$ ) about the centreline were considered for determination of Taylor bubble velocity via image processing.

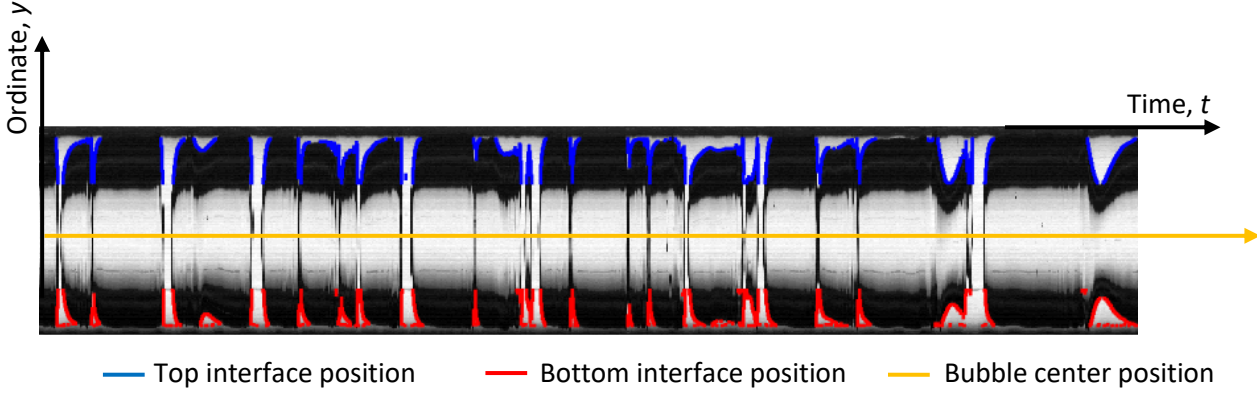


Figure 5.12: Space-time diagram of tube cross section for  $\mu g$ -slug flow in the downstream adiabatic section;  $G = 50 \text{ kg/m}^2\text{s}$ ,  $x = 0.051$ .

In the current work,  $\approx 6,000$  images were acquired at 400 fps for each flow condition corresponding to specific values of  $G$ ,  $x$  and  $q$ . The velocity variation among the individual bubbles were generally with  $\pm 50\%$  of the mean value. Figure 5.13 shows typical histograms of Taylor bubble velocity at selected flow conditions. The width of the histogram can be explained by the hydrodynamics interactions between two consecutive bubbles. The histograms were well represented by a normal distribution and this provides validation of data convergence.

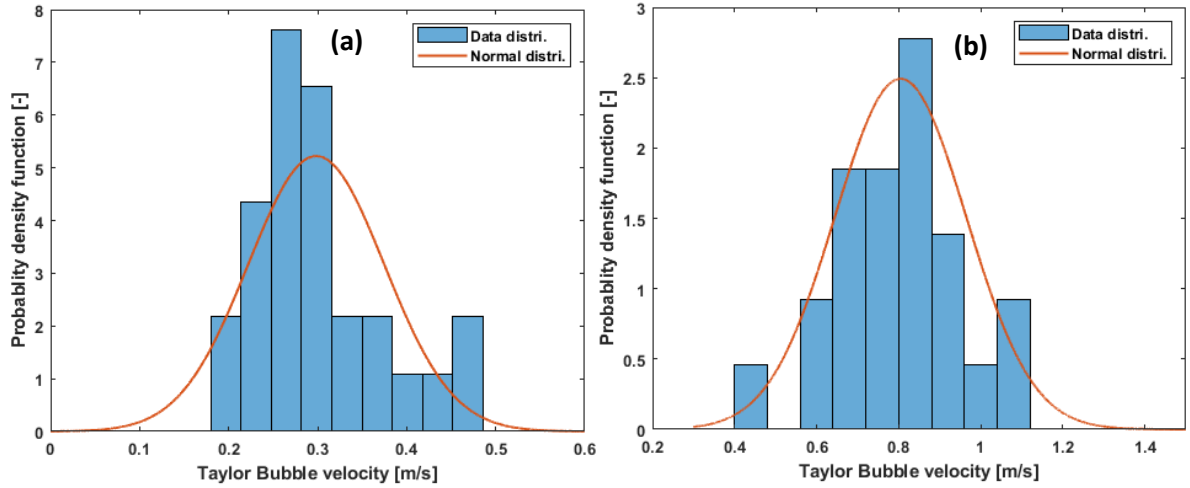


Figure 5.13: Probability density function of Taylor bubble velocity for  $\mu g$  slug flow in the downstream adiabatic section; a.  $G = 50 \text{ kg/m}^2\text{s}$ ,  $x_{out} = 0.051$ , b.  $G = 100 \text{ kg/m}^2\text{s}$ ,  $x_{out} = 0.072$ .

Figure 5.14 shows a comparison between the Taylor bubble velocity obtained from image processing and that computed from the measured void fraction ( $u_v = j_v/\alpha$ ). A fairly good agreement was found considering that the uncertainty in the vapour quality in the bubbly and slug flow regimes can be as high as 50%. The estimated uncertainties of the calculated vapour velocity is provided in Table 2.7 and shown as horizontal error bars in Figure 5.14. The Vertical errors bars represent the standard deviation for all the Taylor bubbles averaged over the entire range of test conditions ( $\approx 0.076$ ).

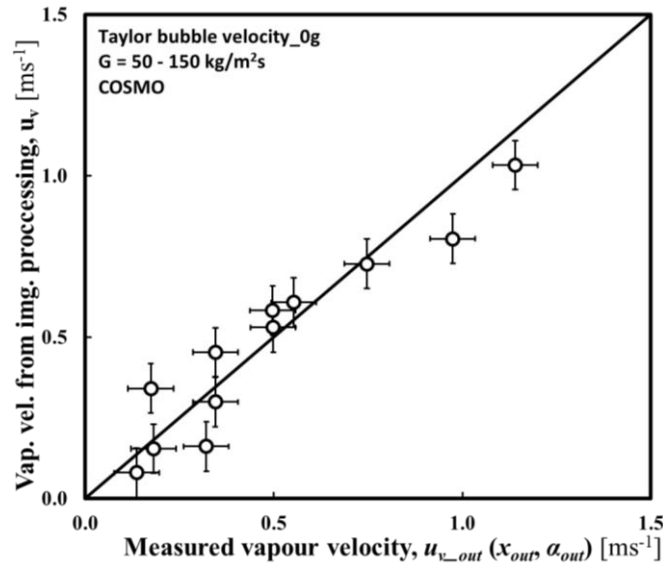


Figure 5.14: Comparison between Taylor bubble velocity obtained from image processing and that computed using the measured void fraction.

### 5.3 Wave structures in microgravity

Similar to Chapter 3 and following the image processing steps outlined in Chapter 2, the velocity and frequency of roll waves were determined for  $\mu g$ - and  $+1g$ -flows for data obtained using the COSMO setup. It should be remarked that, only very limited runs were carried out in the annular flow regime and the length of video recordings were also short relative to the BRASIL experiments. 6662 images ( $\geq 20,000$  for BRASIL) recorded at 400 fps were analysed for each run in the annular flow regime and the total number of roll waves were between 45 to 250 (400 – 1200 for BRASIL). Figure 5.15 shows a histogram of wave velocity and wave frequency for  $\mu g$ -flow. The histograms show a fairly good convergence in the wave velocity and wave frequency particularly for the former.

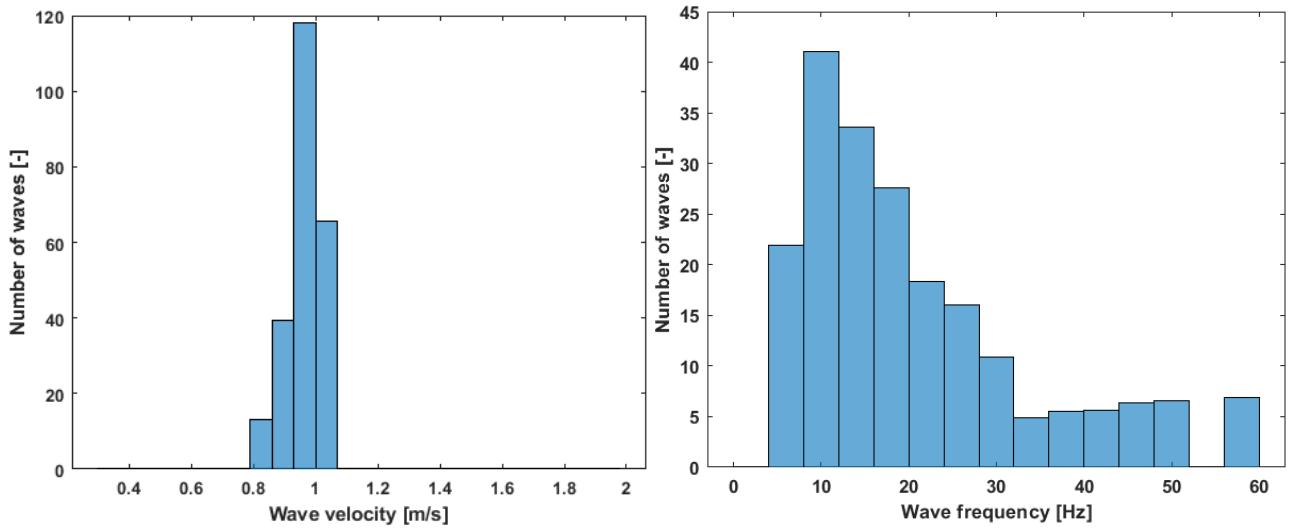


Figure 5.15: Histogram of a. wave velocity, b. wave frequency in  $\mu g$ -flow for  $G = 100 \text{ kg/m}^2\text{s}$ ,  $x = 0.19$ .

Figure 5.16a-b show comparisons between mean vapour velocity, mean liquid velocity and mean wave velocity for  $\mu g$ - and  $+1g$ -flows. Due to the limited data in the annular flow regime, results could not be presented in terms of specific heat fluxes. As expected, the mean wave velocity was smaller than the mean vapour velocity and higher than the mean liquid velocity. In general, the mean wave velocity was higher for  $\mu g$ -flow relative to  $+1g$ -flow. This is due to the higher mean liquid velocity and the absence of buoyancy forces on the roll waves in  $\mu g$ -flow. The results are consistent with other published literature (Asano et al., 2019; Trejo-Peimbert et al., 2019). The mean wave velocity obtained using both experimental facilities were also compared (Figure 5.16c) and there was a good agreement between both results.

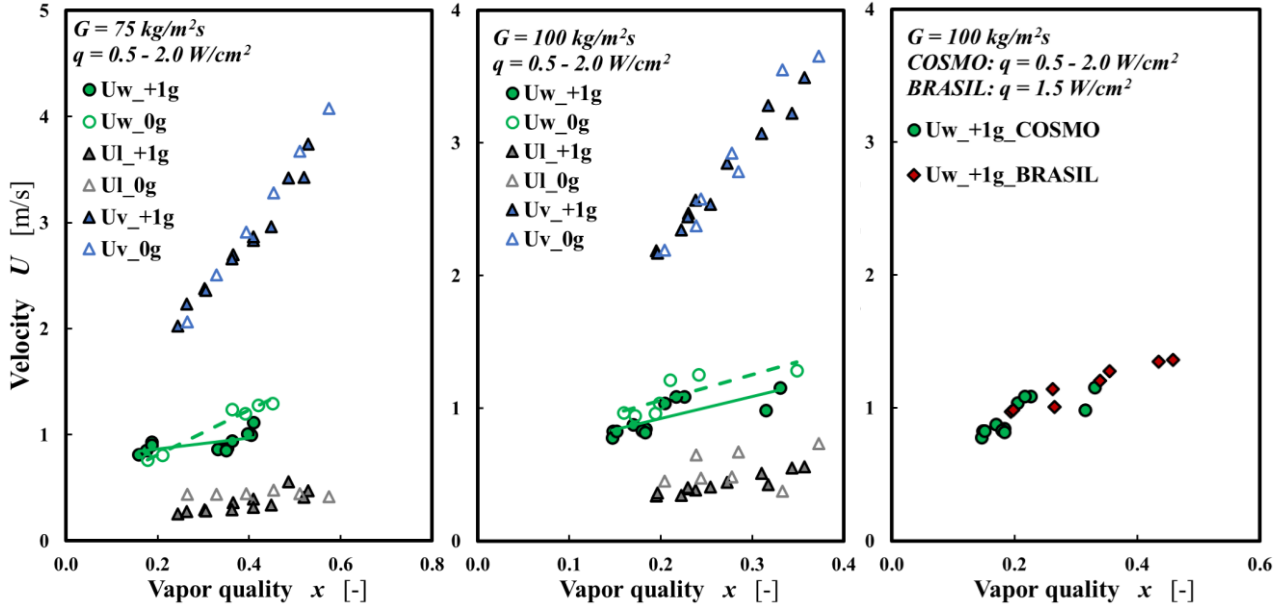


Figure 5.16: a-b. Comparison between mean wave velocity, liquid velocity and vapor velocity for  $\mu g$ - and  $+1g$ -flows obtained using the COSMO setup for  $G = 75 \text{ kg/m}^2\text{s}$  and  $G = 100 \text{ kg/m}^2\text{s}$ . c. Comparison between mean wave velocities in  $+1g$ -flows determined using BRASIL and COSMO setups for  $G = 100 \text{ kg/m}^2\text{s}$ .

Figure 5.17a-b provide comparisons between mean wave frequency for  $\mu g$ - and  $+1g$ -flows. The mean wave frequency was generally lower in  $\mu g$ -flow relative to  $+1g$ -flow due to the lower interfacial shear stress in the former. A comparison between the mean wave frequency obtained from both experimental setups is provide in Figure 5.17c. A fairly good agreement was found between both results.

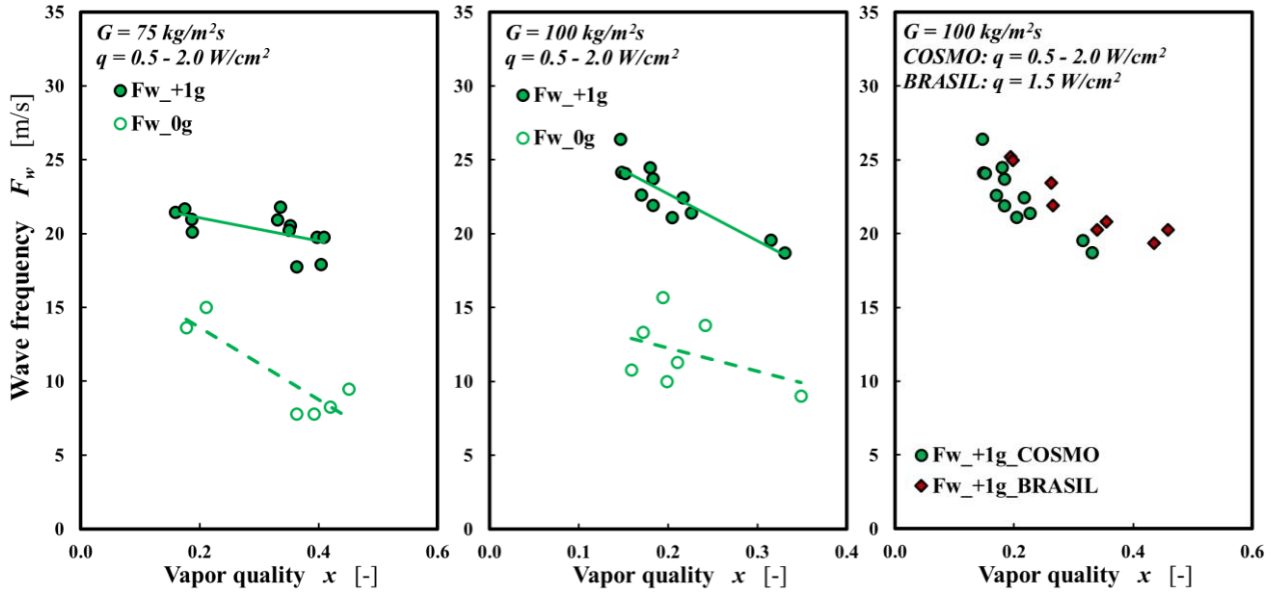


Figure 5.17: a-b. Comparison of mean wave frequency between for  $\mu g$ - and  $+1g$ -flows obtained using the COSMO setup for  $G = 75 \text{ kg/m}^2\text{s}$  and  $G = 100 \text{ kg/m}^2\text{s}$ , c. Comparison between mean wave frequency in  $+1g$ -flows determined using BRASIL and COSMO setups for  $G = 100 \text{ kg/m}^2\text{s}$ .

## 5.4 Heat Transfer Coefficient in Microgravity

In this section, experimental results as well as modelling of microgravity flow boiling heat transfer is presented. First, the effect of mass flux, flow pattern and heat flux on microgravity heat transfer coefficient is discussed. Results of microgravity heat transfer is then compared to heat transfer in upward flow. Finally, a model for predicting heat transfer coefficient in microgravity flow boiling is proposed.

### 5.4.1 Experimental results of heat transfer coefficient in microgravity

Result of measured heat transfer coefficient are presented in terms of vapour quality. Figure 5.18 shows measured heat transfer coefficient for two mass fluxes in microgravity. In general, the measured heat transfer coefficient increased with mass flux over the range of measurement conditions. Figure 5.19 shows the influence of heat flux on the measured heat transfer coefficient in microgravity flow. For  $50 \leq G \leq 150 \text{ kg/m}^2\text{s}$ ,  $0 \leq x \leq 0.7$  and  $q \geq 0.5 \text{ W/cm}^2$  (bubbly flow, intermittent and annular flows) the flow was in the NB regime and the measured heat transfer coefficient increased with heat flux (Figure 5.19).



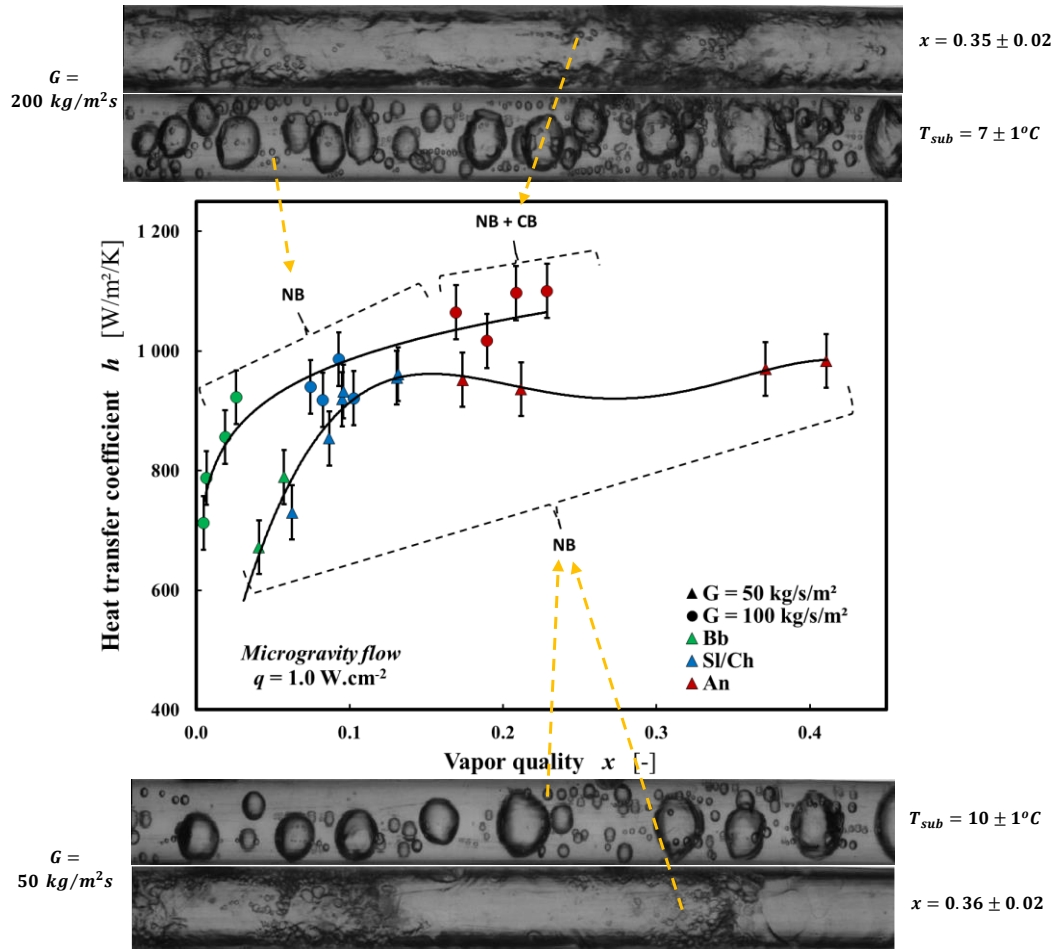


Figure 5.18: Illustration of the various heat transfer regimes for microgravity flow boiling.

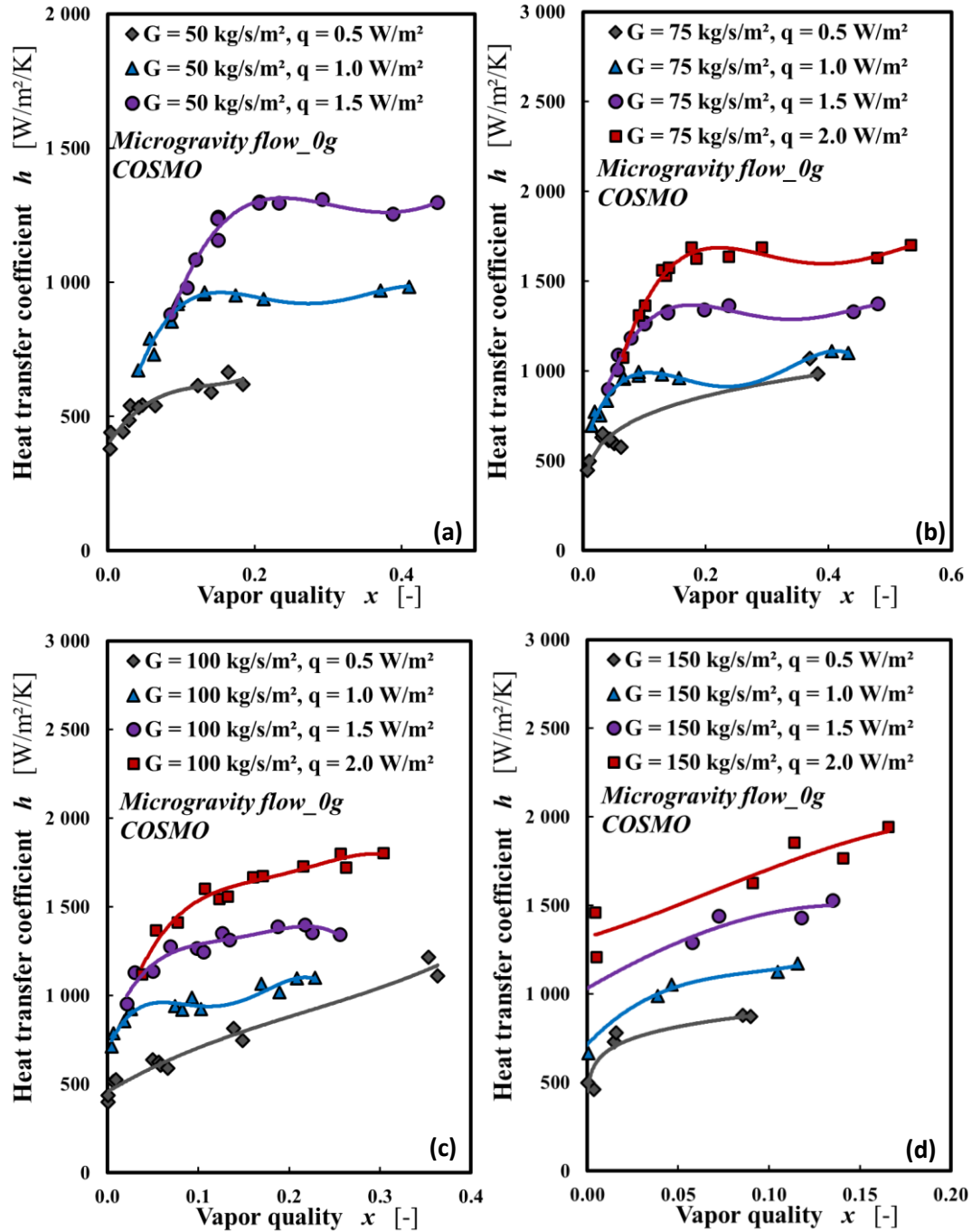


Figure 5.19: Measured heat transfer coefficient versus vapour quality at selected heat fluxes in microgravity; a.  $G = 50$  kg/m<sup>2</sup>s, b.  $G = 75$  kg/m<sup>2</sup>s, c.  $G = 100$  kg/m<sup>2</sup>s, d.  $G = 150$  kg/m<sup>2</sup>s. The lines are trend lines of the experimental data and serve to provide clarity on the trends.

Selected results of measured heat transfer coefficient in normal gravity obtained using the same experimental facility (COSMO) are also shown for reference (Figure 5.20). Similar trends and parameter dependence as with microgravity were recorded in normal gravity (Figure 5.20a-c). Heat

transfer measurements in normal gravity obtained using both experimental facilities were also in agreement (Figure 5.20d).

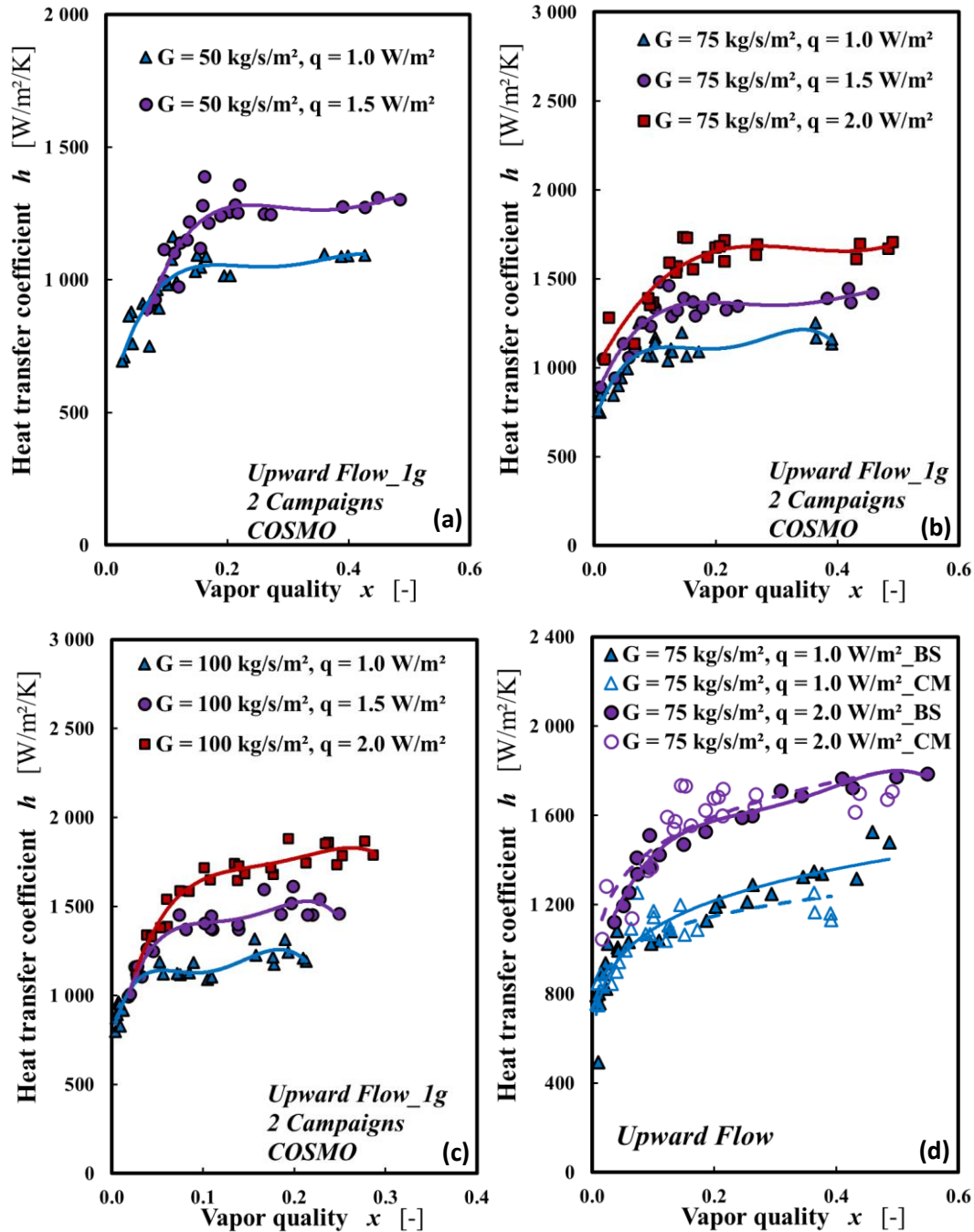


Figure 5.20: Measured heat transfer coefficient versus vapour quality at selected heat fluxes in normal gravity; a.  $G = 50 \text{ kg/m}^2\text{s}$ , b.  $G = 75 \text{ kg/m}^2\text{s}$ , c.  $G = 100 \text{ kg/m}^2\text{s}$ , d.  $G = 75 \text{ kg/m}^2\text{s}$  (BRASIL and COSMO). The lines are trend lines of the experimental data and serve to provide clarity on the trends.

### 5.4.2 Modelling of heat transfer coefficient in microgravity and downward flow

The measured heat transfer in  $\mu g$  showed higher dependence on the wall heat flux relative to  $+1g$  (see Figure 5.19 and Figure 5.23). The nucleate boiling ( $h_{nb}$ ) enhancement in  $\mu g$  also results in the suppression of a purely convective boiling regime ( $h_{cb}$ ). In Chapter 3 (journal article, Eq. 32, pp120), modifications to the model of Kim and Mudawar (2013b) was done to provide correlations for predicting heat transfer coefficient in upward ( $+1g$ ) and downward ( $-1g$ ) flow boiling. To predict heat transfer coefficient in  $\mu g$ , modifications to selected coefficients in the proposed correlations for  $+1g$  was done in line with the foregoing discussion (i.e., enhancement of  $h_{nb}$  and suppression of  $h_{cb}$ ). The proposed correlation for predicting heat transfer coefficient in  $\mu g$  is given by Eqs. 5.6 - 5.8 and the coefficients are provided in Table 5.1. The overall enhancement in  $h_{nb}$  and/or higher dependence on  $Bo$  was accounted for by changes to  $C_2$  and  $C_6$ , while the suppression of  $h_{cb}$  and/or lower dependence on  $x$  was accounted for by changes to  $C_8$  and  $C_9$ . The proposed correlation gave good predictions over the entire range of measurement and the mean absolute error is 6.8% (Figure 5.21).

In Chapter 3 (journal article, Eq. 32, pp120), a correlation for predicting heat transfer coefficient in downward flow was proposed by increasing the value of the coefficient  $C_8$  in upward flow from 5.1 to 5.5. This was done to account for the higher liquid velocity in downward flow. The proposed correlation was tested for  $G \geq 100 \text{ kg/m}^2\text{s}$  and gave an MAE of 15.9. As shall be discussed later, the heat flux dependence of  $h_{-1g}$  is significantly higher than for  $h_{+1g}$  and of similar order of magnitude as  $h_{\mu g}$ . Similar to  $h_{\mu g}$ , this higher heat flux dependence in  $h_{-1g}$  relative to  $h_{+1g}$  was accounted for by changes to  $C_2$  and  $C_6$  (particularly  $C_6$ ). While the value of  $C_8 = 5.5$  from the previous model for  $h_{-1g}$  was maintained,  $C_9$  was increased from 0.71 to .74 (Table 5.1). These modifications were particularly important for lower mass fluxes ( $G \leq 100 \text{ kg/m}^2\text{s}$ ). The new correlation gave better prediction of  $h_{-1g}$  with and MAE of 12.5%. The new correlation also produced a better representation of the mass and heat flux dependence of  $h_{-1g}$  (Figure 5.22).

The validity of the proposed heat transfer models for upward, microgravity and downward flows were only tested using the experimental data acquired in this work. Future studies should test these models on other data in literature so as to increase the level of confidence in the models for industry applications.

$$h_{2\emptyset} = \sqrt{(h_{nb}^2 + h_{cb}^2)} \quad 5.6$$

$$h_{nb} = h_l \left[ C_1 Bo^{C_2} \left( \frac{P}{P_{crit}} \right)^{C_3} (1-x)^{C_4} \right] \quad 5.7$$

$$h_{cb} = h_l \left[ C_5 Bo^{C_6} We_{lo}^{C_7} + C_8 \left( \frac{1}{X_{tt}} \right)^{C_9} \left( \frac{\rho_v}{\rho_l} \right)^{C_{10}} \right] \quad 5.8$$

Table 5.1. Model coefficients for  $h_{2\emptyset}$  in normal and microgravity.

Function	$C_1$	$C_2$	$C_3$	$C_4$	$C_5$	$C_6$	$C_7$	$C_8$	$C_9$	$C_{10}$
Upward flow (+1g )	2345	0.76	0.38	-0.7	5.2	0.08	-0.54	5.1	0.71	0.13
Microgravity ( $\mu g$ )	2345	0.73	0.38	-0.7	5.2	0.32	-0.54	3.5	0.63	0.13
Downward flow (-1g)	2345	0.75	0.38	-0.7	5.2	0.32	-0.54	5.5	0.74	0.13

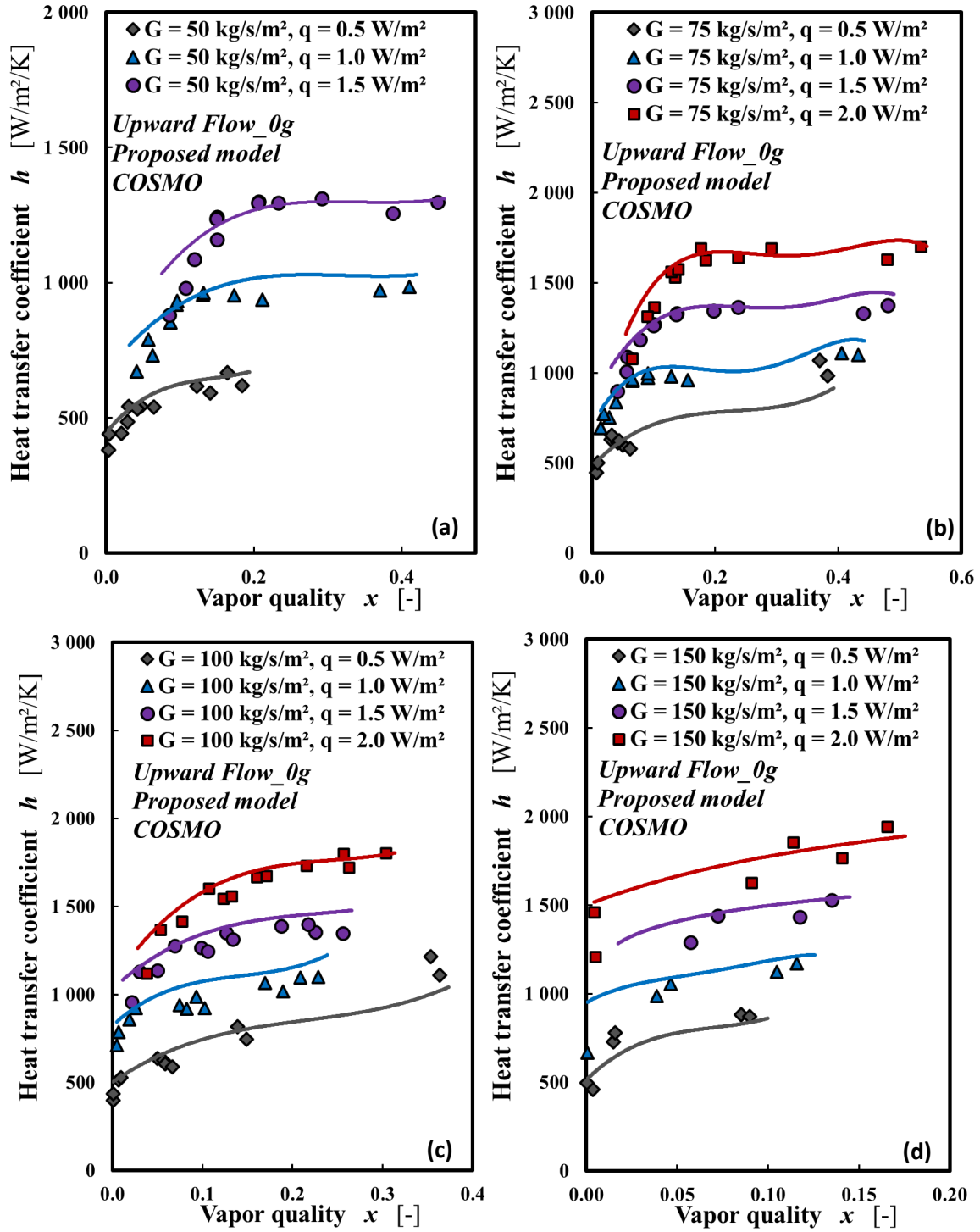


Figure 5.21: Heat transfer coefficient versus vapour quality at selected heat fluxes in microgravity; a.  $G = 50 \text{ kg/m}^2\text{s}$ , b.  $G = 75 \text{ kg/m}^2\text{s}$ , c.  $G = 100 \text{ kg/m}^2\text{s}$ , d.  $G = 150 \text{ kg/m}^2\text{s}$ . Measured (markers), Correlation (solid lines).

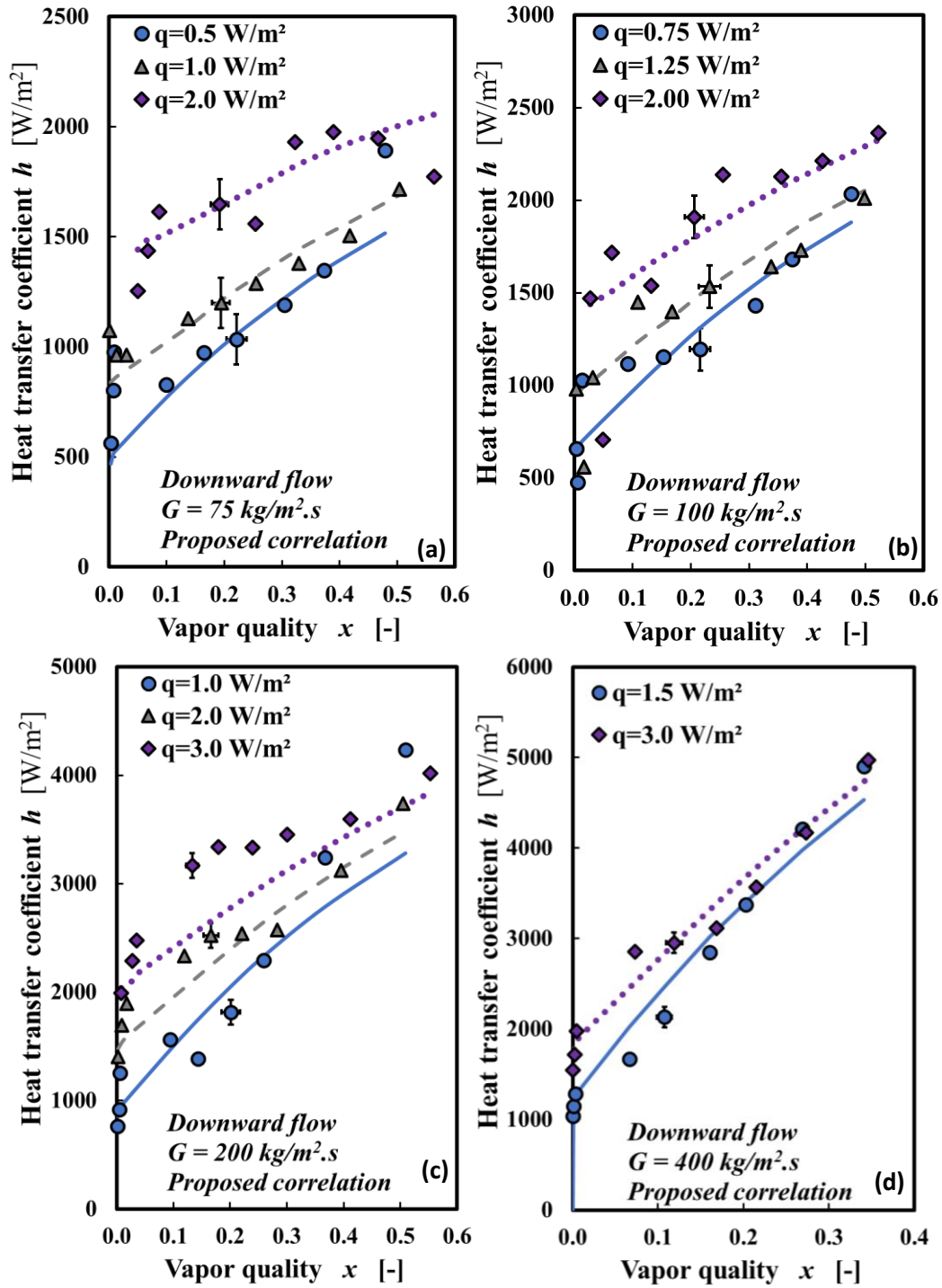


Figure 5.22: Heat transfer coefficient versus vapour quality at selected heat fluxes downward flow; a.  $G = 75 \text{ kg/m}^2\text{s}$ , b.  $G = 100 \text{ kg/m}^2\text{s}$ , c.  $G = 200 \text{ kg/m}^2\text{s}$ , d.  $G = 400 \text{ kg/m}^2\text{s}$ . Measured (markers), Correlation (lines).

### 5.4.3 Effect gravity level on measured heat transfer

Figure 5.23 provides a comparison between heat transfer coefficient in normal and microgravity. Two inferences can be made from the results:

1. At low heat flux ( $Bo \leq 0.002$ ) and for  $1/X_{tt} \leq 10$ , corresponding to low density of nucleated bubbles and limited interaction among nucleated bubbles, the frequency of bubble detachment from the heated wall was significantly influenced by gravity (buoyancy) and was higher in normal gravity relative to microgravity. Consequently, the measured heat transfer coefficient was higher in normal gravity relative to microgravity. This result is generally consistent with other results in literature (Lebon et al., 2019; Ohta et al., 2013).
2. At high heat flux ( $Bo > 0.002$ ) and for  $1/X_{tt} \leq 10$ , corresponding to high density of nucleated bubbles and significant interaction among nucleated, the frequency of bubble detachment from the heated wall was more influenced by bubble interaction and less influenced by gravity (buoyancy). Consequently, both the bubble detachment frequency and the measured heat transfer coefficient were similar in normal and microgravity. This is generally consistent with the flow regime map of Ohta et al. (2013) (Figure 1.17).

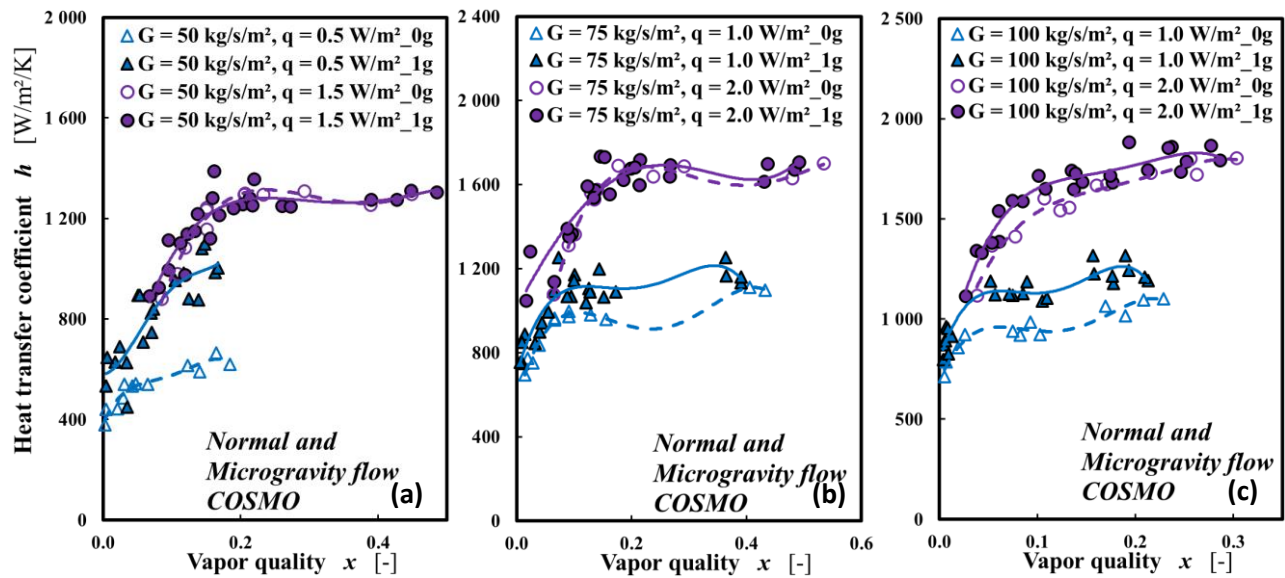


Figure 5.23: Comparison between heat transfer coefficient in normal and microgravity.

Result of measured heat transfer coefficient was also presented in terms of ratio of heat transfer coefficient in microgravity ( $h_{\mu g}$ ) to heat transfer coefficient in normal gravity ( $h_{+1g}$ ) (Figure 5.24).



At the lowest heat flux tested, the heat transfer coefficient was significantly higher in  $+1g$ -flow relative to  $\mu g$ -flow (Figure 5.24a). With increase in heat flux, the heat transfer coefficient increased more abruptly in  $\mu g$ -flow (particularly at the lowest heat flux), and the ratio of  $h_{\mu g}$  to  $h_{+1g}$  tends to 1.

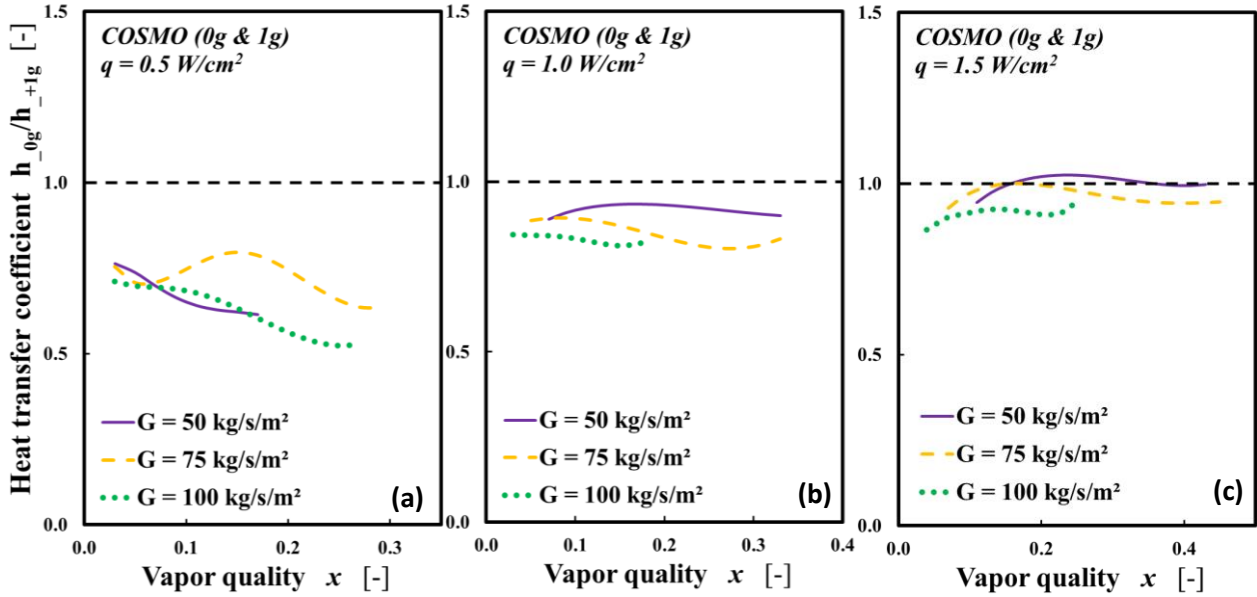


Figure 5.24: Ratio of heat transfer coefficient between  $\mu g$ - and  $+1g$ -flows.

Figure 5.25 shows results of measured heat transfer coefficient in terms of vapour quality in all three flow configurations while Figure 5.26 provides plots of  $h_{-1g}/h_{+1g}$  in terms of vapour quality at selected conditions. Measurement of heat transfer in microgravity was limited to mass flux of  $G \leq 150 \text{ kg/m}^2\text{s}$  and heat flux of  $q \leq 2.0 \text{ W/cm}^2$ . For  $75 \leq G \leq 400 \text{ kg/m}^2\text{s}$ , and  $q \leq 1.0 \text{ W/cm}^2$   $h_{-1g} \approx h_{+1g} \geq h_{\mu g}$  (Figure 5.25) while for  $G = 50 \text{ kg/m}^2\text{s}$  and  $q \leq 1.0 \text{ W/cm}^2$   $h_{\mu g} \leq h_{-1g} \leq h_{+1g}$  (Figure 5.24 and Figure 5.26). With increase in heat flux, the heat transfer coefficient increased more abruptly in both  $h_{-1g}$  and  $h_{\mu g}$  relative to  $h_{+1g}$ . Consequently,  $h_{\mu g}$  generally approached  $h_{+1g}$ , while  $h_{-1g}$  generally became higher than  $h_{+1g}$  for  $75 \leq G \leq 400 \text{ kg/m}^2\text{s}$ . For  $75 \leq G \leq 400 \text{ kg/m}^2\text{s}$ , and  $q \geq 1.5 \text{ W/cm}^2$   $h_{-1g} > h_{+1g} \approx h_{\mu g}$  (Figure 5.25) while for  $G = 50 \text{ kg/m}^2\text{s}$  and  $q \geq 1.5 \text{ W/cm}^2$   $h_{\mu g} \approx h_{-1g} \approx h_{+1g}$  (Figure 5.24 and Figure 5.26). At mass flux  $G \geq 200 \text{ kg/m}^2\text{s}$  the ratio,  $h_{-1g}/h_{+1g}$  also decreased with vapour quality (Figure 5.26c). The flow in this regime was predominantly convective and heat flux dependence was reduced. Overall, although the effect of gravity diminished significantly with mass flux, gravity still influenced the heat transfer

coefficient even at the highest mass flux (particular higher heat flux).

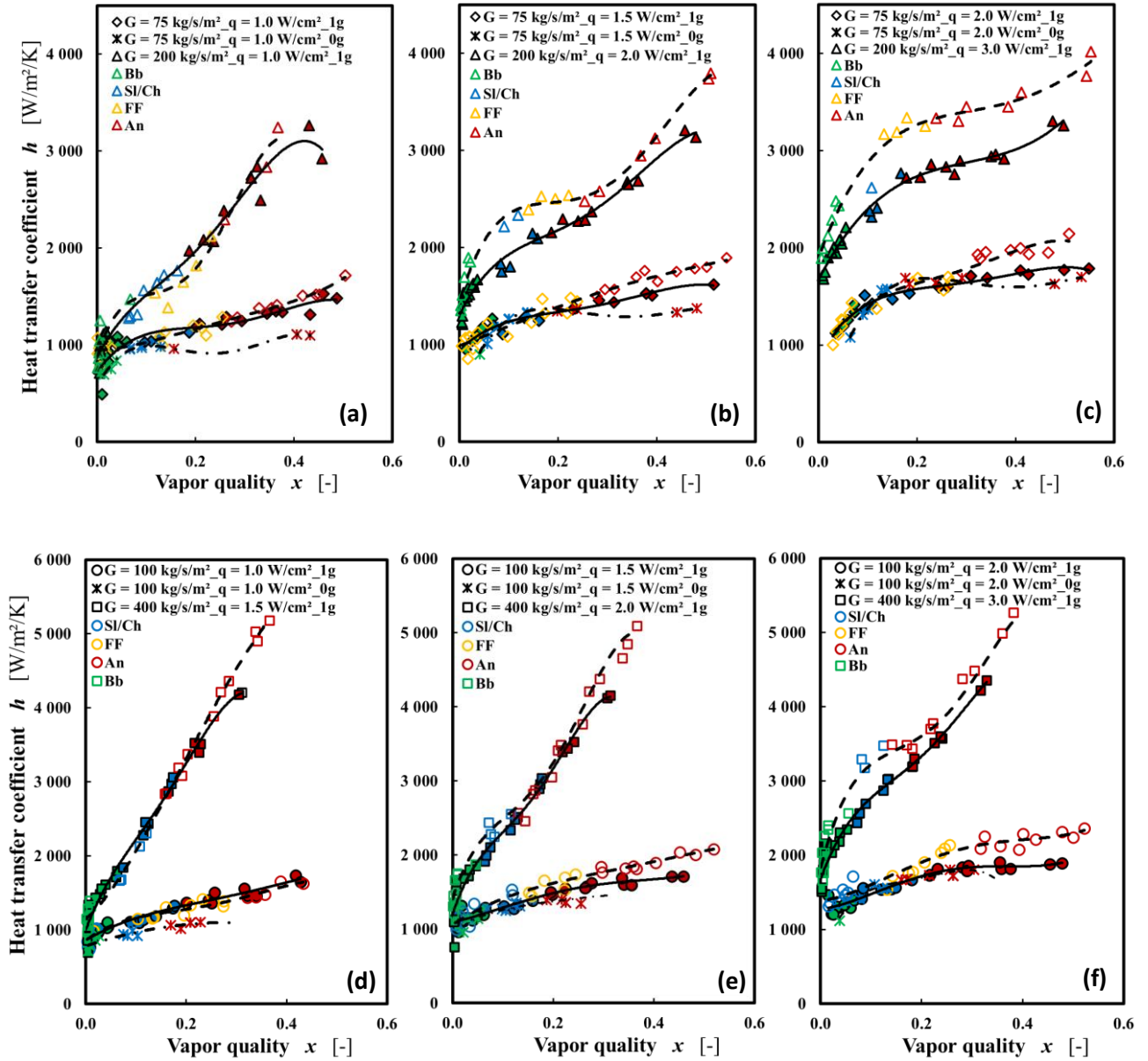


Figure 5.25: Comparison between heat transfer coefficient among  $+1g$ ,  $-1g$  and  $\mu g$ -flows.  $+1g$  (closed symbols),  $-1g$  (open symbols) and  $\mu g$  (\*).

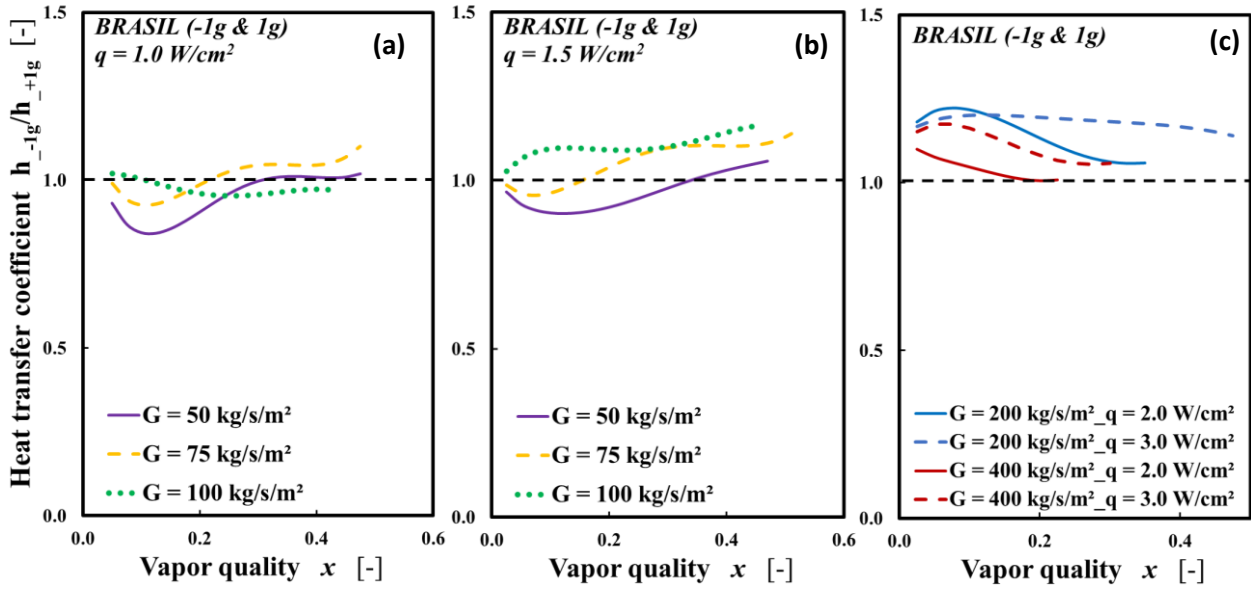


Figure 5.26: Ratio of heat transfer coefficient between  $-1g$ - and  $+1g$ -flows.

It has been well documented that when flow inertia is dominant over buoyancy and surface tension forces, the effect of gravity on various flow boiling quantities is negligible (Baba et al., 2012; Narcy et al., 2014; Narcy and Colin, 2015). In the current work, the range of normal-gravity mixture Froude number ( $Fr = \sqrt{G^2 / \rho_m(\rho_l - \rho_v)gD}$ ) were  $0.13 \leq Fr \leq 0.48$  for  $G = 50 \text{ kg/m}^2\text{s}$  ( $0.05 \leq x \leq 0.70$ ) and  $1.61 \leq Fr \leq 2.9$  for  $G = 400 \text{ kg/m}^2\text{s}$  ( $0.05 \leq x \leq 0.40$ ). In this measurement range, (Figure 1.16) the effect of gravity on the heat transfer coefficient is expected to remain significant (Baba et al., 2012). However, the results above show that the effect of gravity is strongly linked to the applied wall heat flux. Lebon et al. (2019) proposed a regime map showing the transition from gravity-dependent to gravity-independent region at some threshold value of heat flux depending on the mass flux (Figure 1.18). Although their study was limited to subcooled boiling conditions, the proposed map showed that at sufficiently high heat fluxes, the effect of gravity level ( $h_{\mu g}$  relative to  $h_{+1g}$ ) is negated (Figure 1.18). This in general agreement with the results of the current studies for  $h_{+1g}$ - and  $h_{\mu g}$ -flows. In the current work,  $h_{\mu g} \approx h_{+1g}$  for boiling number  $Bo \geq 0.002$ . It should be remarked that, the proposed regime map suggests that a lower threshold value of heat flux is required at higher mass fluxes (Figure 1.18). This is contrary to the results of the current study, where the threshold heat flux ( $h_{\mu g} \approx h_{+1g}$ ) increased with mass flux (Figure 5.23). In the current study, this threshold heat flux for  $G = 50$  and  $G = 75 \text{ kg/m}^2\text{s}$  were  $q = 1.5$  ( $Bo = 0.0021$ ) and  $q = 2.0 \text{ W/cm}^2$  ( $Bo = 0.002$ ) respectively. The proposed map could not explain the results for  $h_{-1g}$ -

flow relative to  $h_{+1g}$ -flow. In the current work, the effect of flow orientation relative to gravity was negligible ( $h_{-1g} \approx h_{+1g}$ ) at  $q \leq 1.0 \text{ W/cm}^2$  ( $Bo = 0.001$ ) and  $q = 1.5 \text{ W/cm}^2$  ( $Bo = 0.0003$ ) for  $G = 75$  and  $G = 400 \text{ kg/m}^2\text{s}$  respectively. Table 5.2 and

Table 5.3 provide summaries of gravity dependence observed in the current work.

## 5.5 Conclusion

*Results of flow pattern, bubble geometry, void fraction, vapor velocity and heat transfer showed significant dependence on gravity level. Bubble size were generally higher in microgravity flow relative to normal gravity flow. Furthermore, bubbles were more spherical in microgravity due the absence of drift velocity. The measured void fraction was highest in downward flow and lowest in upward flow. Heat transfer in all three flow regimes showed significant dependence on mass and heat flux. Measured heat transfer coefficient was higher in normal gravity relative to microgravity for  $Bo < 0.002$  but the effect of gravity level was negligible for  $Bo \geq 0.002$ . For  $75 \leq G \leq 400 \text{ kg/m}^2\text{s}$  and  $Bo > 0.001$ , the measured heat transfer coefficient in downward was higher than that of upward flow but the effect of flow orientation relative to gravity becomes negligible for  $Bo < 0.001$ . Measured heat transfer coefficient was generally highest in downward flow and lowest in microgravity particularly for  $0.001 < Bo < 0.002$ . A correlation for predicting heat transfer coefficient in microgravity was proposed along with an improvement to the proposed model for heat transfer in downward flow reported in Chapter 3. The proposed correlations gave good predictions of the measured data over the entire range of measurement.*

Table 5.2. Gravity dependence  $h_{\mu g} \approx h_{+1g}$    $h_{\mu g} < h_{+1g}$

Mixture Froude number	Mass flux	Boiling number $Bo < 0.002$	Boiling number $Bo \geq 0.002$
$0.13 \leq Fr \leq 0.48$	$G = 50 \text{ kg/m}^2\text{s}$		
$0.70 \leq Fr \leq 0.92$	$G = 100 \text{ kg/m}^2\text{s}$		

Table 5.3. Gravity dependence  $h_{-1g} \approx h_{+1g}$    $h_{-1g} < h_{+1g}$    $h_{-1g} \geq h_{+1g}$

Mixture Froude number	Mass flux	Boiling number $Bo < 0.001$	Boiling number $Bo \geq 0.001$
$0.13 \leq Fr \leq 0.48$	$G = 50 \text{ kg/m}^2\text{s}$	<span style="background-color: #008000; border: 1px solid black; display: inline-block; width: 100%; height: 100%;"></span>	<span style="background-color: #800080; border: 1px solid black; display: inline-block; width: 100%; height: 100%;"></span>
$0.70 \leq Fr \leq 0.92$	$G = 100 \text{ kg/m}^2\text{s}$	<span style="background-color: #FF8C00; border: 1px solid black; display: inline-block; width: 100%; height: 100%;"></span>	<span style="background-color: #800080; border: 1px solid black; display: inline-block; width: 100%; height: 100%;"></span>
$1.61 \leq Fr \leq 2.90$	$G = 400 \text{ kg/m}^2\text{s}$	<span style="background-color: #FF8C00; border: 1px solid black; display: inline-block; width: 100%; height: 100%;"></span>	<span style="background-color: #800080; border: 1px solid black; display: inline-block; width: 100%; height: 100%;"></span>

## Conclusion and Perspective

*In this section, a summary of the objectives, methodology and results of this PhD Thesis is provided along with perspectives for future research.*

The goal of this work was to investigate the effect of gravity, wall heat flux and inlet conditions on several flow boiling quantities using both experimental and modelling approaches. Experimental measurements were carried out using two separate flow facilities (BRASIL and COSMO). Both facilities consisted of a vertical 6 mm sapphire tube coated externally with indium-tin-oxide (ITO) for Joule heating. The working fluid used for the experimental campaigns was HFE-7000. Upward (+1g), downward (−1g) and microgravity ( $\mu g$ ) flow boiling experiments were carried out over mass flux, heat flux and vapor quality ranges of  $50 \leq G \leq 400 \text{ kg/m}^2 \cdot \text{s}$ ,  $0 \leq q \leq 3 \text{ W/cm}^2$  and  $0 \leq x \leq 0.7$  respectively. The COSMO loop was built in perspective of future implementation in the International Space Station and has to be accommodated in a much smaller space than the BRASIL experiment. Nevertheless, despite some difference in the preheating systems, void fraction probes similar results are obtained with the 2 loops.

### Flow patterns

High speed cameras were used for flow visualisation and MATLAB image processing toolbox was used to determine bubble geometry. Bubbly, intermittent (slug and churn) and annular flow patterns were observed for upward (+1g) and microgravity ( $\mu g$ ) flows over the entire measurement ranges. Falling film and annular flow patterns were observed in downward flow (−1g) for  $50 \leq G \leq 100 \text{ kg/m}^2 \cdot \text{s}$ . At  $G = 200 \text{ kg/m}^2 \cdot \text{s}$ , bubbly, intermittent, falling film and annular flow patterns were observed in downward flow while at  $G = 400 \text{ kg/m}^2 \cdot \text{s}$ , bubbly, intermittent and annular flow patterns were observed in downward flow. Flow patterns became independent of flow orientation relative to gravity at  $G = 400 \text{ kg/m}^2 \cdot \text{s}$ .

In the bubbly flow regime, the mean bubble diameter in the heated section was higher in  $\mu g$  relative to +1g due to higher bubble coalescence in microgravity relative to upward flow (Colin et al., 2008). In both microgravity and upward flows (particularly for the former), there was an evolution of the mean bubble size from the inlet to the outlet of the test section due to coalescence and phase change. Bubbly flow did not occur in downward flow for  $G \leq 100 \text{ kg/m}^2 \cdot \text{s}$  because stagnated or counter-

current bubbles continued to grow in the test section resulting in falling film flow pattern. In the intermittent flow regime, the size of the Taylor bubbles was highest in downward flow and lowest in upward flow. This is due to the longer residence time of Taylor bubbles in the test section in downward flow relative to upward and microgravity flows. The longer residence time in downward flow allows the Taylor bubbles to continue to grow by evaporation. In the annular flow regime, the liquid film thickness (as estimated from void fraction measurements) was highest in downward flow and lowest in upward flow.

In upward flow, bubbly to intermittent flow regime transition occurred for measured values of the void fraction of about 0.65 and the drift flux model of Rouhani and Axelsson (1970) gave a good prediction of the bubbly to intermittent transition boundary. In microgravity flow, bubbly to intermittent flow regime transition occurred for measured values of the void fraction of about 0.68 and the transition criteria of Colin et al. (1991) gave a good prediction of the bubbly to intermittent transition boundary. In downward flow and for  $G \geq 200 \text{ kg/m}^2\text{s}$ , bubbly to intermittent flow transition occurred at void fraction of  $\approx 0.75$  and the drift flux correlation of Usui (1989) gave a good prediction of the bubbly to intermittent flow transition in downward flow. The intermittent to annular flow transition occurred at a void fraction of  $\approx 0.8$  in all three flow configurations and the intermittent to annular flow transition boundaries for upward, microgravity and downward flows were well predicted by the transition criteria of Mishima and Ishii (1984), Dukler et al. (1988) and Usui (1989) respectively.

### **Void fraction and liquid film thickness**

Void fraction measurements were carried out using capacitance probes. Void fraction was dependent on vapour quality, mass flux and gravity condition. In general, measured void fraction was highest in downward flow and lowest in upward flow and the influence of gravity was predominant at  $x \leq 0.3$  and  $G \leq 200 \text{ kg/m}^2\text{s}$ . Similar values of void fraction were obtained in upward and downward flow at  $G = 400 \text{ kg/m}^2\text{s}$ . In upward flow, void fraction increased with mass flux particularly at  $x \leq 0.3$  while the opposite was the case in downward flow. Measured void fraction showed negligible influence of mass flux in microgravity flow.

In upward flow, the measured void fraction in the bubbly/intermittent and annular flow regimes were well predicted by the models of Rouhani and Axelsson (1970) and Zuber et al. (1967) respectively.

In downward flow, the measured void fraction for all the flow patterns was well predicted by the drift flux model of Rouhani and Axelsson (1970) with negative drift velocity.

Liquid film thickness in the annular flow regimes was estimated from the measured void fraction. The liquid film thickness was highest in upward flow and lowest in downward flows. The liquid film thickness upward and downward flows were well predicted by the models of Zuber et al. (1967) and Rouhani and Axelsson (1970) respectively. In the current work, theoretical eddy viscosity models were also developed for the simultaneous prediction of liquid film thickness and heat transfer coefficient in upward and downward flows. The proposed models gave good predictions of the measured liquid film thickness within  $\pm 20\%$ .

### **Wall and interfacial shear stresses**

Differential pressure measurements across the heated tube test section as well as void fraction measurements at the inlet and outlet of the test section were used to determine the wall and interfacial shear stresses in upward and downward flows. Wall and interfacial shear stresses could not be determined for microgravity conditions due to entry of vapour into the pressure lines during the parabolic flight campaign.

In both upward and downward flows, wall shear stress was generally higher in boiling flow relative to adiabatic vapor-liquid two-phase flow and wall shear stress increased with wall heat flux. This wall shear stress enhancement due to heat flux was first reported by Klausner et al. (1990) and was attributed to turbulence enhancement. The influence of wall heat flux on wall shear stress was more pronounced in downward flow relative to upward flow and was predominant in the nucleate boiling regime. In general, the measured wall shear stress was higher in downward flow relative upward flow and the difference increased with heat flux and decreased with mass flux. At  $G = 400 \text{ kg/m}^2\text{s}$  and  $q \leq 1.5 \text{ W/cm}^2$  similar values of wall shear stress were recorded in both flow configurations.

Measured wall shear stress was compared to several models available in literature and the model of Cioncolini and Thome (2017) gave the best prediction of the measured wall shear stress. The model, however, failed to capture the heat flux dependence of the measured wall shear stress. In this work, modifications to the correlations of Kim & Mudawar (2012b) and Kim & Mudawar (2013b) were proposed for the prediction of the wall shear stress for adiabatic vapour-liquid flow and flow boiling respectively. The proposed correlations gave good predictions of the measured wall shear stress



within  $\pm 20\%$  and also reproduced the heat flux dependence of the wall shear stress for the latter.

In both upward and downward flows, the interfacial shear stress increased with mass flux and also depended on the vapour quality. Similar to wall shear stress, the measured interfacial shear stress increased with wall heat flux, albeit to a lower degree. The effect of wall heat flux on the interfacial shear stress was higher in downward flow relative to upward flow. Interfacial shear stress was significantly higher in upward flow relative to downward flow but the difference decreased with mass flux. The lower interfacial shear stress in downward flow is due to the lower relative velocity between the phases in downward flow relative to upward flow. Interfacial friction factor was computed from the measured interfacial shear stress and it decreased with quality.

The interfacial friction factor ( $f_i$ ) in upward flow was compared to selected correlations and the correlation of Wallis (1969) gave a good prediction of the experimental data for vapour Reynolds number  $Re_v \geq 30,000$  corresponding to fully turbulent vapour core. For lower  $Re_v$  values, the model over-estimated the interfacial friction factor. Suitable correlations for predicting  $f_i$  in downward flow boiling are lacking in literature. Correlations for predicting  $f_i$  in both upward and downward flow boiling were proposed in this work in terms of  $Re_v$  and the liquid film thickness. The proposed correlations gave good predictions of the experimental data within  $\pm 20\%$ . Additional correlations for predicting  $f_i$  in upward and downward flow boiling were proposed in this work in terms of mean roll wave velocity and mean wave frequency. The correlations also gave good prediction of the experimental data.

### **Wave structures**

In all three configurations, the mean wave velocity and mean wave frequency increased with mass flux and was influenced by heat flux, vapour quality and gravity. Mean wave velocity generally increased with vapour quality but decreased with heat flux. Mean wave frequency increased with quality for  $G \geq 200 \text{ kg/m}^2\text{s}$  and also increased with heat flux. The product of wave velocity and wave frequency showed similar dependence on mass flux, heat flux and vapour quality as the interfacial shear stress. The mean wave velocities were higher in microgravity and downward flow relative to upward flow. This is attributed to the higher liquid velocities in microgravity and downward flow relative to upward flow. The mean wave frequency was highest in upward flow and lowest in downward flow. This is attributed to the low interfacial shear stress in downward flow and

high interfacial shear stress in upward flow.

Measured wave velocity and wave frequency were compared to correlations in literature. The models of Pearce (1979) and Sekoguchi et al., (1985) predicted the mean wave velocity and mean wave frequency with  $\pm 30\%$  and  $\pm 50\%$  respectively. These models were developed for adiabatic two-phase flows and could not capture the heat flux dependence of the wave structures. In this work, correlations for predicting mean wave velocities in upward and downward flows were proposed in terms of the modified Weber number of the vapour core and the boiling number. The proposed correlations predicted the experimental data within  $\pm 15\%$  and also captured the heat flux dependence of the mean wave velocity. Furthermore, correlations for predicting mean wave frequencies in upward and downward flows were proposed in this work in terms of  $Bo$ ,  $We_{lo}$ ,  $X_{tt}$ ,  $\rho_v$ ,  $\rho_l$  and  $Re_l$ . The correlations predicted the mean wave frequency within  $\pm 20\%$  and also captured the heat flux dependence of the wave frequency. Due to the limited data in the annular flow regime, no correlation was developed for predicting wave structures in microgravity.

### **Heat transfer coefficient**

In all three configurations, the measured heat transfer increased with both mass flux and heat flux and was also influenced by the vapour quality and gravity. The heat flux dependence of the heat transfer coefficient was highest in microgravity and lowest in upward flow. Measured heat transfer coefficient was higher in upward flow relative to microgravity for Boiling numbers  $Bo < 0.002$  but the effect of gravity level was negligible for  $Bo \geq 0.002$ . For  $75 \leq G \leq 400 \text{ kg/m}^2\text{s}$  and  $Bo > 0.001$ , the measured heat transfer coefficient in downward was higher than that of upward flow but the effect of flow orientation relative to gravity becomes negligible for  $Bo < 0.001$ . With increase in mass flux and vapour quality, the effect of flow orientation relative to gravity diminishes. Measured heat transfer coefficient was generally highest in downward flow and lowest in microgravity particularly for  $0.001 < Bo < 0.002$ .

Measured heat transfer were compared to selected correlations in literature and the models of Liu and Winterton (1991) and Cioncolini and Thome (2011) gave the best prediction of the measured data in terms of the mean absolute error. In this work, modifications to the model of Kim and Mudawar (2013) were done to provide suitable correlations for the prediction of heat transfer coefficient in all three configurations. The proposed correlations predicted the experimental data in all three

configurations within  $\pm 15\%$ . Furthermore, the proposed correlations for wall shear stress in upward and downward flows were used to develop theoretical eddy viscosity models for the simultaneous prediction of heat transfer coefficient and liquid film thickness in annular flow. The proposed models predicted the measured heat transfer within  $\pm 20\%$ .

## Perspectives

Although, extensive measurements of several parameters were carried out for flow boiling in upward and downward configuration, only limited measurements were carried out in microgravity. Microgravity experiments done in parabolic flights are limited by duration of measurements, number of parabolas and complexity of in-flight data acquisition. Some focus areas for future studies are listed as follows;

- The limitations of the experimental facilities used in the current work did not allow for investigation of flow boiling critical heat flux. Experimental and modelling studies of critical heat flux (CHF) would provide a more complete description of flow boiling.
- The limited camera resolution as well as optical distortion, prevented the measurement of the liquid film thickness in the annular flow regime. Future studies using more advanced diagnostics in the test section would improve measurement of this important parameter.
- Additional modelling is required, particularly for downward and microgravity flows. Modelling of waves structures in microgravity one of the areas that require attention. The proposed models in this work should be tested on flow boiling data available in literature.
- Investigations into methods of flow boiling heat transfer enhancement and the use of test sections with different wall roughness could also provide interesting information on flow boiling characteristics.
- The susceptibility of the ITO coating to scratch and the difficulty in taking wall temperature measurements also impacted on measurement accuracies. The measurements with pt100 probes were localised at 4 points of the test section. The possibility to measure local time resolved heat flux along the tube by infrared thermography could be investigated.
- Considering the possibility to accommodate COSMO in the International Space Station, it could be possible to use heated test section with much higher thermal inertia as metallic tubes.

## References

- Akers, W.W., Deans, H.A., O.K. Crosser, 1958. Condensing heat transfer within horizontal tubes. *Chemical Engineering Progress* 54, 89–90.
- Al-Arabi, M., 1982. Turbulent heat transfer in the entrance region of a tube. *Heat Transfer Engineering* 3, 76–83.
- Aliyu, A.M., Lao, L., Almabrok, A.A., Yeung, H., 2016. Interfacial shear in adiabatic downward gas/liquid co-current annular flow in pipes. *Experimental Thermal and Fluid Science* 72, 75–87.
- Almabrok, A.A., Aliyu, A.M., Lao, L., Yeung, H., 2016. Gas/liquid flow behaviours in a downward section of large diameter vertical serpentine pipes. *International Journal of Multiphase Flow* 78, 25–43.
- Asano, H., Nakase, H., Kawanami, O., Inoue, K., Suzuki, K., Imai, R., Matsumoto, S., H. Ohta, 2019. Liquid film structure of annular flows under microgravity - Results of TPF experiments onboard International Space Station, in: *26th European Low Gravity Research Association Biennial Symposium and General Assembly 14th International Conference on "Two-Phase Systems for Space and Ground Applications" European Space Agency Topical Teams Meetings*. pp. 202–203.
- Awad, M.M., Muzychka, Y.S., 2014. Bounds on two-phase frictional pressure gradient and void fraction in circular pipes. *Advances in Mechanical Engineering* 2014, 1–9.
- Azzopardi, B.J., 1986. Disturbance wave frequencies, velocities and spacing in vertical annular two-phase flow. *Nuclear Engineering and Design* 92, 121–133.
- Baba, S., Ohtani, N., Kawanami, O., Inoue, K., Ohta, H., 2012. Experiments on dominant force regimes in flow boiling using mini-tubes. *Frontiers in Heat and Mass Transfer* 3, 1–8.
- Baldassari, C., Marengo, M., 2013. Flow boiling in microchannels and microgravity. *Progress in Energy and Combustion Science* 39, 1–36.
- Baltis, C., Celata, G.P., Cumo, M., Saraceno, L., Zummo, G., 2012. Gravity influence on heat transfer rate in flow boiling. *Microgravity Science and Technology* 24, 203–213.

- Barbosa, J.R., Hewitt, G.F., Richardson, S.M., 2003. High-speed visualisation of nucleate boiling in vertical annular flow. *International Journal of Heat and Mass Transfer* 46, 5153–5160.
- Beattie, D.R.H., Whalley, P.B., 1982. A simple two-phase frictional pressure drop calculation method. *International Journal of Multiphase Flow* 8, 83–87.
- Belt, R.J., Van't Westende, J.M.C., Portela, L.M., 2009. Prediction of the interfacial shear-stress in vertical annular flow. *International Journal of Multiphase Flow* 35, 689–697.
- Bennett, D.L., Chen, J.C., 1980. Forced convective boiling in vertical tubes for saturated pure components and binary mixtures. *AIChE Journal* 26, 454–461.
- Bhagwat, S.M., Ghajar, A.J., 2017. Experimental investigation of non-boiling gas-liquid two phase flow in downward inclined pipes. *Experimental Thermal and Fluid Science* 89, 219–237.
- Bhagwat, S.M., Ghajar, A.J., 2015. An Empirical Model to Predict the Transition between Stratified and Nonstratified Gas-Liquid Two-Phase Flow in Horizontal and Downward Inclined Pipes. *Heat Transfer Engineering* 36, 1485–1494.
- Bhagwat, S.M., Ghajar, A.J., 2012. Similarities and differences in the flow patterns and void fraction in vertical upward and downward two phase flow. *Experimental Thermal and Fluid Science* 39, 213–227.
- Bousman, W., Dukler, A., 1993. Studies of gas-liquid flow in microgravity: void fraction, pressure drop and flow pattern, in: *Proceedings of the 1993 ASME Winter Meeting*. pp. 174–175.
- Brutin, D., Ajaev, V.S., Tadrist, L., 2013. Pressure drop and void fraction during flow boiling in rectangular minichannels in weightlessness. *Applied Thermal Engineering* 51, 1317–1327.
- Canière, H., T'joen, C., Willockx, A., de Paepe, M., Christians, M., van Rooyen, E., Liebenberg, L., Meyer, J.P., 2007. Horizontal two-phase flow characterization for small diameter tubes with a capacitance sensor. *Measurement Science and Technology* 18, 2898–2906.
- Ceccio, S.L., George, D.L., 1996. A Review of Electrical Impedance Techniques for the *Measurement of Multiphase Flows*. *Journal of Fluids Engineering* 118, 391–399.
- Celata, G.P., 2007. Flow boiling heat transfer in microgravity: Recent results. *Microgravity Science and Technology* 19, 13–17.

- Celata, G.P., Zummo, G., 2009a. Flow boiling heat transfer in microgravity: recent progress. *Multiphase Science and Technology* 21, 187–212.
- Celata, G.P., Zummo, G., 2009b. Flow boiling heat transfer in micro-gravity, in: *Proceedings of ECI International Conference on Boiling Heat Transfer, Floriano'polis, Brazil*. pp. 1–13.
- Chen, C., Gao, P.Z., Tan, S.C., Chen, H.Y., Xu, C., Yu, Z.T., 2015. Theoretical calculation of the characteristics of annular flow in a rectangular narrow channel. *Annals of Nuclear Energy* 85, 259–270.
- Chen, I., Downing, R., Keshock, E.G., Al-Sharif, M., 1991. Measurements and correlation of two-phase pressure drop under microgravity conditions. *Journal of Thermophysics and Heat Transfer* 5, 514–523.
- Chen, J.C., 1966. Correlation for boiling heat transfer to saturated fluids in convective flow. *Industrial and Engineering Chemistry Process Design and Development* 5, 322–329.
- Chiaromonte, F.P., Joshi, J.A., 2004. Workshop on critical issues in microgravity fluids, transport, and reaction processes in advanced human support technology – *final report, NASA TM-2004-212940*.
- Chisholm, D., 1973. Pressure gradient due to friction during the flow of evaporating two-phase mixtures in smooth tubes and channels. *International Journal of Heat and Mass Transfer* 16, 347–358.
- Chisholm, D., Heat, A., Division, T., Kilbride, E., 1967. A theoretical basis for the lockhart-martinelli correlation for twophase flow. *International Journal of Heat and Mass Transfer* 10, 1767–1778.
- Cicchitti, A., Lombardi, C., Silvestri, M., Soldaini, G., Zavalluilli, R., 1960. Two-phase cooling experiments-pressure drop, heat transfer and burnout measurements. *Energia Nucleare* 7, 407–425.
- Cioncolini, A., Thome, J.R., 2017. Pressure drop prediction in annular two-phase flow in macroscale tubes and channels. *International Journal of Multiphase Flow* 89, 321–330.
- Cioncolini, A., Thome, J.R., 2012a. Void fraction prediction in annular two-phase flow. *International Journal of Multiphase Flow* 43, 72–84.

- Cioncolini, A., Thome, J.R., 2012b. Entrained liquid fraction prediction in adiabatic and evaporating annular two-phase flow. *Nuclear Engineering and Design* 243, 200–213.
- Cioncolini, A., Thome, J.R., 2011. Algebraic turbulence modeling in adiabatic and evaporating annular two-phase flow. *International Journal of Heat and Fluid Flow* 32, 805–817.
- Cioncolini, A., Thome, J.R., Lombardi, C., 2009a. Unified macro-to-microscale method to predict two-phase frictional pressure drops of annular flows. *International Journal of Multiphase Flow* 35, 1138–1148.
- Cioncolini, A., Thome, J.R., Lombardi, C., 2009b. Algebraic turbulence modeling in adiabatic gas-liquid annular two-phase flow. *International Journal of Multiphase Flow* 35, 580–596.
- Colebrook, C., White, C., 1937. Experiments with fluid friction roughened pipes, in: *Proceedings of the Royal Society of London, Series A, Mathematical and Physical Sciences*. pp. 161(906):367–381.
- Colin, C., Fabre, J., 1995. Gas-liquid pipe flow under microgravity conditions: flow patterns and pressure drops. *Advances in Space Research* 16, 137–142.
- Colin, C., Fabre, J., Dukler, A.E., 1991. Gas-liquid flow at microgravity conditions-I. Dispersed bubble and slug flow. *International Journal of Multiphase Flow* 17, 533–544.
- Colin, C., Riou, X., Fabre, J., 2008. Bubble coalescence in gas-liquid flow at microgravity conditions. *Microgravity Science and Technology* 20, 243–246.
- Colin, C., Riou, X., Fabre, J., 2004. Turbulence and shear-induced coalescence in gas-liquid pipe flows, in: *5th International Conference on Multiphase Flow. ICMF*, Yokohama, Japan, pp. 1–13.
- Cooper, M.G., 1984. Saturation nucleate pool boiling, a simple correlation, in: *First U.K. National Conference on Heat Transfer*.
- Dasgupta, A., Chandraker, D.K., Kshirasagar, S., Reddy, B.R., Rajalakshmi, R., Nayak, A.K., Walker, S.P., Vijayan, P.K., Hewitt, G.F., 2017. Experimental investigation on dominant waves in upward air-water two-phase flow in churn and annular regime. *Experimental Thermal and Fluid Science* 81, 147–163.

- Devahdhanush, V.S., Darges, S.J., Mudawar, I., Nahra, H.K., Balasubramaniam, R., Hasan, M.M., Mackey, J.R., 2022. Flow visualization, heat transfer, and critical heat flux of flow boiling in Earth gravity with saturated liquid-vapor mixture inlet conditions – In preparation for experiments onboard the International Space Station. *International Journal of Heat and Mass Transfer* 192, 1-28.
- Di Marco, P., 2012. Influence of force fields and flow patterns on boiling heat transfer performance: A review. *Journal of Heat Transfer* 134(3), 030801.
- Dittus, E., Boelter, L., 1930. Experiments with fluid friction roughened pipes. *Publication on Engineering* 2, 443.
- Dukler, A.E., Fabre, J.A., McQuillen, J.B., Vernon, R., 1988. Gas-liquid flow at microgravity conditions: Flow patterns and their transitions. *International Journal of Multiphase Flow* 14, 389–400.
- Dukler, A.E., Wicks, M., R.G. Cleaveland, 1964. Pressure drop and hold up in two-phase flow. *AIChE Journal* 10, 38–51.
- Fang, X., Xu, Y., 2013. Correlations for two-phase friction pressure drop under microgravity. *International Journal of Heat and Mass Transfer* 56, 594–605.
- Fang, X., Zhang, H., Xu, Y., Su, X., 2012. Evaluation of using two-phase frictional pressure drop correlations for normal gravity to microgravity and reduced gravity. *Advances in Space Research* 49, 351–364.
- Fore, L.B., Beus, S.G., Bauer, R.C., 2000. Interfacial friction in gas-liquid annular flow: Analogies to full and transition roughness. *International Journal of Multiphase Flow* 26, 1755–1769.
- Forster, H.K., Zuber, N., 1955. Dynamics of vapor bubbles and boiling heat transfer. *AIChE Journal* 1, 531–535.
- Friedel, L., 1979. Improved friction pressure drop correlations for horizontal and vertical two-phase pipe flow, in: *European Two-Phase Flow Meeting*.
- Fu, F., Klausner, J.F., 1997. A separated flow model for predicting two-phase pressure drop and evaporative heat transfer for vertical annular flow. *International Journal of Heat and Fluid Flow* 18, 541–549.



- Gardenghi, Á.R., Filho, E. dos S., Chagas, D.G., Scagnolatto, G., Oliveira, R.M., Tibiriçá, C.B., 2020. Overview of void fraction measurement techniques, databases and correlations for two-phase flow in small diameter channels. *Fluids* 5, 216.
- Gnielinski, V., 1976. New equations for heat and mass transfer in turbulent pipe and channel flow. *International Journal of Chemical Engineering* 16, 359–368.
- Godbole, P. v, Tang, C.C., Ghajar, A.J., 2011. Comparison of void fraction correlations for different flow patterns in upward vertical two-phase flow. *Heat Transfer Engineering* 32, 843–860.
- Gomyo, T., Asano, H., 2016. Void fraction characteristics of one-component gas-liquid two-phase flow in small diameter tubes. *Interfacial Phenomena and Heat Transfer* 4, 1–18.
- Gungor, K.E., Winterton, R.H.S., 1986. A general correlation for flow boiling in tubes and annuli. *International Journal of Heat and Mass Transfer* 29, 351–358.
- Han, H., Gabriel, K.S., 2006. The influence of flow pressure gradient on interfacial wave properties in annular two-phase flow at microgravity and normal gravity conditions, in: *FDMP* 2 (4). pp. 287–295.
- Harmathy, T.Z., 1960. Velocity of large drops and bubbles in media of infinite or restricted extent. *AIChE Journal* 6, 281–288.
- Heppner, D.B., King, C.D., Littles, J.W., 1975. Zero-G experiments in two phase fluids flow patterns, in: *Intersociety Conference on Environmental Systems. ASME* 9 p, San Francisco, California.
- Hewitt, G.F., Hall-Taylor, N.S., 1970. Annular two-phase flow, 1st ed.
- Hurlbert, K.M., Witte, L.C., Best, F.R., Kurwitz, C., 2004. Scaling two-phase flows to Mars and Moon gravity conditions. *International Journal of Multiphase Flow* 30, 351–368.
- Iceri, D. M., Ribatski G., Saraceno, L., Zummo, G., 2017. Flow boiling heat transfer and flow pattern at normal gravity, hypergravity, and microgravity conditions, in: *9th World Conference on Experimental Heat Transfer, Fluid Mechanics and Thermodynamics. Iguazu Falls*.
- Inoue, K., Ohta, H., Asano, H., Kawanami, O., Imai, R., Suzuki, K., Shinmoto, Y., Kurimoto, T., Matsumoto, S., 2021. Heat loss analysis of flow boiling experiments onboard international

space station with unclear thermal environmental conditions (2nd report: liquid-vapor two-phase flow conditions at test section inlet). *Microgravity Science and Technology* 33.

Ishii, M., 1977. One-dimensional drift-flux model and constitutive equations for relative motion between phases in various two-phase flow regimes, *ANL-77-47*.

J. R. Lamarsh, 1983. Introduction to Nuclear Reactor Theory, 2nd Edition. ed. *Addison-Wesley, Reading*.

Jayawardena, S.S., Balakotaiah, V., Witte, L.C., 1997. Flow pattern transition maps for microgravity two-phase flows. *AIChE Journal* 43, 1637–1640.

Kamp, A.M., Chesters, A.K., Colin, C., Fabre, J., 2001. Bubble coalescence in turbulent flows: A mechanistic model for turbulence-induced coalescence applied to microgravity bubbly pipe flow, *International Journal of Multiphase Flow* 27(8), 1363-1396.

Kandlikar, S.G., 1990. A general correlation for saturated two-phase flow boiling heat transfer inside horizontal and vertical tubes. *Journal of Heat Transfer* 112, 219–228.

Kew, P.A., Cornwell, K., 1997. Correlations for the prediction of boiling heat transfer in small-diameter channels. *Applied Thermal Engineering* 17, 705–715.

Kharangate, C.R., O'Neill, L.E., Mudawar, I., 2016. Effects of two-phase inlet quality, mass velocity, flow orientation, and heating perimeter on flow boiling in a rectangular channel: Part 1 – Two-phase flow and heat transfer results. *International Journal of Heat and Mass Transfer* 103, 1261–1279.

Kim, S.-M., Mudawar, I., 2014. Review of databases and predictive methods for pressure drop in adiabatic, condensing and boiling mini/micro-channel flows. *International Journal of Heat and Mass Transfer* 77, 74–97.

Kim, S.M., Mudawar, I., 2014. Theoretical model for local heat transfer coefficient for annular flow boiling in circular mini/micro-channels. *International Journal of Heat and Mass Transfer* 73, 731–742.

Kim, S.M., Mudawar, I., 2013a. Universal approach to predicting two-phase frictional pressure drop for mini/micro-channel saturated flow boiling. *International Journal of Heat and Mass Transfer* 58, 718–734.

- Kim, S.M., Mudawar, I., 2013b. Universal approach to predicting saturated flow boiling heat transfer in mini/micro-channels – Part II. Two-phase heat transfer coefficient. *International Journal of Heat and Mass Transfer* 64, 1239–1256.
- Kim, S.M., Mudawar, I., 2012a. Universal approach to predicting two-phase frictional pressure drop for adiabatic and condensing mini/micro-channel flows. *International Journal of Heat and Mass Transfer* 55, 3246–3261.
- Kim, S.M., Mudawar, I., 2012b. Theoretical model for annular flow condensation in rectangular micro-channels. *International Journal of Heat and Mass Transfer* 55, 958–970.
- Klausner, J.F., Chao, B.T., Soo, S.L., 1990. An improved method for simultaneous determination of frictional pressure drop and vapor volume fraction in vertical flow boiling. *Experimental Thermal and Fluid Science* 3, 404–415.
- Konishi, C., Lee, H., Mudawar, I., Hasan, M.M., Nahra, H.K., Hall, N.R., Wagner, J.D., May, R.L., Mackey, J.R., 2015. Flow boiling in microgravity: Part 1 - Interfacial behavior and experimental heat transfer results. *International Journal of Heat and Mass Transfer* 81, 705–720.
- Konishi, C., Mudawar, I., 2015. Review of flow boiling and critical heat flux in microgravity. *International Journal of Heat and Mass Transfer* 80, 469–493.
- Layssac, T., 2018. Contribution à l'étude phénoménologique de l'ébullition convective en mini-canal (PhD). Université de Lyon.
- Lebon, M.T., Hammer, C.F., Kim, J., 2019. Gravity effects on subcooled flow boiling heat transfer. *International Journal of Heat and Mass Transfer* 128, 700–714.
- Lee, S., Mudawar, I., 2019. Enhanced model for annular flow in micro-channel heat sinks, including effects of droplet entrainment/deposition and core turbulence. *International Journal of Heat and Mass Transfer* 133, 510–530.
- Legendre, D., Boré, J., Magnaudet, J., 1998. Thermal and dynamic evolution of a spherical bubble moving steadily in a superheated or subcooled liquid. *Physics of Fluids* 10, 1256–1272.

- Liao, Y., Lucas, D., Krepper, E., Schmidtke, M., 2011. Development of a generalized coalescence and breakup closure for the inhomogeneous MUSIG model. *Nuclear Engineering and Design* 241, 1024–1033.
- Lin, S., Kwok, C.C.K., Li, R.Y., Chen, Z.H., Chen, Z.Y., 1991. Local frictional pressure drop during vaporization of R-12 through capillary tubes. *Int. J. Multiphase Flow* 17, 95–102.
- Liu, Z., Winterton, R.H.S., 1991. A general correlation for saturated and subcooled flow boiling in tubes and annuli, based on a nucleate pool boiling equation. *International Journal of Heat and Mass Transfer* 34, 2759–2766.
- Lockhart, R.W., Martinelli, R.C., 1949. Proposed correlation of data for isothermal two-phase, two-component flow in pipes. *Chem. Eng. Prog.* 45, 39–48.
- Lu, Q., Chen, D., Li, C., He, X., 2017. Experimental investigation on flow boiling heat transfer in conventional and mini vertical channels. *International Journal of Heat and Mass Transfer* 107, 225–243.
- Luciani, S., Brutin, D., Le Niliot, C., Rahli, O., Tadrist, L., 2008. Flow boiling in minichannels under normal, hyper-, and microgravity: Local heat transfer analysis using inverse methods. *Journal of Heat Transfer* 130, 101502.
- Luciani, S., Brutin, D., Le Niliot, C., Tadrist, L., Rahli, O., 2009. Boiling heat transfer in a vertical microchannel: Local estimation during flow boiling with a non intrusive method. *Multiphase Science and Technology* 21, 297–328.
- Lui, R., Kawaji, M., Ogushi, T., 1994. An Experimental investigation of subcooled flow boiling heat transfer under microgravity conditions, in: *Proc. 10th Int. Heat Transfer Conf., Brighton, UK*. 497–502.
- Ma, Y., Chung, J.N., 2001. A study of bubble dynamics in reduced gravity forced-convection boiling. *International Journal of Heat and Mass Transfer* 44, 399–415.
- Ma, Y., Chung, J.N., 1998. An experimental study of forced convection boiling in microgravity. *Int. Journal of Heat and Mass Transfer* 41, 2371–2382.
- Martin, S.C., 1976. Vertically downward two-phase slug flow. *Journal of Fluids Engineering, Transactions of the ASME* 98, 715–722.

- McAdams, W.H., Woods, W.K., Heroman, L.C., 1942. Vaporization inside horizontal tubes – II: Benzene–oil mixture. *Transactions ASME* 64, 193–200.
- Mishima, K., Ishii, M., 1984. Flow regime transition criteria for upward two-phase flow in vertical tubes. *International Journal of Heat and Mass Transfer* 27, 723–737.
- Morel, C., Laviéville, J.M., 2008. Modeling of multi-size bubbly flow and application to the simulation of boiling flows with the NEPTUNE\_CFD Code. *Science and Technology of Nuclear Installations* 2009, 1–8.
- Mudawwar, I.A., El-Masri, M.A., 1986. Momentum and heat transfer across freely-falling turbulent liquid films. *International Journal of Multiphase Flow* 12, 771–790.
- Muller-Steinhagen, H., Heck, K., 1986. Flow boiling in tube under normal gravity and microgravity conditions. *Chemical Engineering and Processing: Process Intensification* 20, 297–308.
- Narcy, M., 2014. Doctorat de l’université de toulouse. Institut National Polytechnique de Toulouse.
- Narcy, M., Colin, C., 2015. Two-phase pipe flow in microgravity with and without phase change: Recent progress and future prospects. *Interfacial Phenomena and Heat Transfer* 3, 1–17.
- Narcy, M., de Malmazet, E., Colin, C., 2014. Flow boiling in tube under normal gravity and microgravity conditions. *International Journal of Multiphase Flow* 60, 50–63.
- Nicklin, D.J., 1962. Two-phase bubble flow, *Chemical Engineering Science*. Pergamon Press Ltd., London. Primed in Great Britain.
- Ohta, H., 2003. Microgravity heat transfer in flow boiling. *Advances in Heat Transfer* 37, 1–75.
- Ohta, H., 1997. Experiments on microgravity boiling heat transfer by using transparent heaters. *Nuclear Engineering and Design* 175, 167–180.
- Ohta, H., Baba, A., Gabriel, K., 2002. Review of existing research on microgravity boiling and two-phase flow. *Annals of the New York Academy of Sciences* 974, 410–427.
- Ohta, H., Baba, S., Asano, H., Kawanami, O., Suzuki, K., Fujii, K., 2013. Subjects to be clarified in flow boiling experiments on board International Space Station, in: *8th International Conference on Multiphase Flow ICMF 2013, Jeju, Korea*. pp. 1–13.

- Owens, W.L., 1961. Two-phase pressure gradient, in: *International Developments in Heat Transfer, Pt. II, ASME, New York.*
- Pearce, D.L., 1979. Film waves in horizontal annular flow: space time correlator experiments, *Central Electricity Research Laboratories.*
- Reynolds, W.C., S.M.A. and S.H.M., 1964. Capillary hydrostatics and hydrodynamics at low g.
- Rouhani, S.Z., Axelsson, E., 1970. Calculation of void volume fraction in the subcooled and quality boiling regions. *International Journal of Heat and Mass Transfer* 13, 383–393.
- Saito, M., Yamaoka, N., Miyazaki, K., Kinoshita, M., Abe, Y., 1994. Boiling two-phase flow under microgravity. *Nuclear Engineering and Design* 146, 451–461.
- Sekoguchi, K., Takashi, U., Osamu, T., 1985. An investigation of the flow characteristics in the disturbance wave region of annular flow: 2nd report, on correlation of principal flow parameters. *Transactions of the Japan Society of Mechanical Engineers.* 51, 1798–1806.
- Takamasa, T., Iguchi, T., Hazuku, T., Hibiki, T., Ishii, M., 2003. Interfacial area transport of bubbly flow under microgravity environment. *International Journal of Multiphase Flow* 29, 291–304.
- Trejo-Peimbert, E., 2018. Dynamics and transfers in two phase flows with phase change in normal and microgravity conditions. PhD Thesis INP-Toulouse.
- Trejo-Peimbert, E., Achour, N., Colin, C., Sebilleau, J., Hammer, C., Kim, J., 2019. Dynamics and heat transfer in flow boiling in tube in normal and microgravity conditions, in: *10th International Conference on Multiphase Flow, ICMF 2019, Rio de Janeiro, Brazil, May 19 – 24.* p. OC.126.
- Usui, K., 1989. Vertically downward two-phase flow, (II): Flow regime transition criteria. *Journal of Nuclear Science and Technology* 26, 1013–1022.
- van DRIEST, E.R., 1956. On turbulent flow near a wall. *Journal of the Aeronautical Sciences* 23, 1007–1011.
- van P. Carey, 1992. Liquid-vapor phase-change phenomena. *Taylor and Francis.*
- Vlachou, M.C., Lioumbas, J.S., Kostoglou, M., David, K., Chasapis, D., Schwarz, C., van Loon, J.J.W.A., Karapantsios, T.D., 2019. Subcooled flow boiling in horizontal and vertical macro-

channel under earth-gravity and hyper-gravity conditions. *International Journal of Heat and Mass Transfer* 133, 36–51.

Wallis, G., 1969. One dimensional two-phase flow. McGraw-Hill.

Westheimer, D.T., Peterson, G.P.B., 2001. Visualization of Flow Boiling in an Annular Heat Exchanger Under Microgravity Conditions. *Journal of Thermophysics and Heat Transfer* 15, 333–339.

Woldeesemayat, M.A., Ghajar, A.J., 2007. Comparison of void fraction correlations for different flow patterns in horizontal and upward inclined pipes. *International Journal of Multiphase Flow* 33, 347–370.

Zhao, J. fu, 2010. Two-phase flow and pool boiling heat transfer in microgravity. *International Journal of Multiphase Flow* 36, 135–143.

Zhao, L., Rezkallah, K.S., 1995. Pressure drop in gas-liquid flow at microgravity conditions. *International Journal of Multiphase Flow* 21, 837–849.

Zhao, L., Rezkallah, K.S., 1993. Gas-liquid flow patterns at microgravity conditions. *International Journal of Multiphase Flow* 19, 751–763.

Zuber, N., Findlay, J., 1965. Average volumetric concentration in two-phase systems. *Journal of Heat Transfer* 453–468.

Zuber, N., Staub, F.W., Bijwaard, G., Kroeger, P.G., 1967. Steady state and transient void fraction in two-phase flow systems. *General Electric Co. Report GEAP-5417*.